NUMERICAL MODELING OF A LATERALLY HETEROGENEOUS LITHOSPHERE UNDER EXTENSION: STRENGTH CONTRASTS AND RIFTING OF A METASOMATIZED CRATON

by

Stefanie Wenker

Submitted in partial fulfilment of the requirements
for the degree of Master of Science

at

Dalhousie University
Halifax, Nova Scotia
August 2015

Table of Contents

List of Tables

List of Figures

Abstract

The heterogeneous composition of the lithosphere affects the way it deforms under extension. This thesis investigates the effects of heterogeneities that introduce compositional, thermal, and thickness contrasts within an extending lithosphere using 2D-numerical thermal-mechanically coupled finite element methods. Rifting in the absence of large quantities of melt (magma-poor rifting) is the result of the initiation and growth of necking instabilities. Two main factors that determine the growth rate of necking instabilities are the brittle vs. viscous (approximately stiff vs. pliable behavior) of lithospheric layers and the rate of deformation (strain rate) applied. In a laterally homogeneous lithosphere the stiff vs. pliable behavior determines the location of localization and the timing of rifting, because the strain rate is equally distributed laterally throughout the layers and does not preferentially enhance growth of any individual necking instability. On the other hand, where a lateral contrast is introduced the strain rate is no longer equally distributed throughout the layers and this may alter the location of lithospheric breakup to the location of the necking instability under the highest strain rate. The first part of the thesis investigates the competition between growing necking instabilities in a vertically layered lithosphere with models where a vertical lithospheric boundary is present. The strength of the crust and mantle changes across this vertical boundary and creates a strain rate contrast. Localization occurs in the higher strain rate lithosphere in most model configurations. Only where the background strain rates are near equal can localization in a stiff layer overtake necking instabilities in layers with higher strain rates. The results are applied to: 1) the formation of asymmetric rifted margins where strain localizes at the boundary between contrasting lithospheres, but deformation is mostly distributed throughout the lithosphere under a higher strain rate, and; 2) the preservation of strong cratons, where they are protected by surrounding younger and weaker lithospheres affected by a higher strain rate. In the second part of the thesis, more complex models, with thermal, compositional, and thickness contrasts, are employed to expand on the second application and show that craton rifting requires significant weakening of the cratonic lithosphere. Weakening of the craton is accomplished by melt metasomatism. Melt injected into the cratonic mantle lithosphere effectively increases the density from 3335 kg m^{-3} to 3378 kg m^{-3}, increases the temperature from the heat released by melt as it cools and crystallizes, and decreases the viscosity by rehydration. Especially important is the increase in temperature, which decreases the viscosity and strength of the craton so that it becomes weaker than the surrounding lithosphere. In particular, a craton can be rifted when its mantle lithosphere is thinned and heated just below the Moho. In this case, the craton is weaker than the younger lithosphere, the roles are reversed, and the craton protects the younger lithosphere from rifting. The heterogeneity introduced in the models presented throughout this thesis illustrates the complex way in which the lithosphere is affected by inherited structures and contrasts, and provides a new understanding of the role these heterogeneities may have in altering the location of localization in an extending lithosphere.

List of Abbreviations and Symbols Used

General Abbreviations	
Abbreviation	Description
ALE	Arbitrary Lagrangian Eulerian
Ga	Billions of Years
CAMP	Central Atlantic Magmatic Province
C-MWZ	Central Mantle Weak Zone
CMB	Central Mobile Belt
CBL	Chemical Boundary Layer
COB	Continent-Ocean Boundary
CML	Cratonic Mantle Lithosphere
CWZ	Crustal Weak Zone
E	Episode
EDC	Edge-driven Convection
h	Elevation Change
HREE	Heavy Rare Earth Elements
L-MWZ	Left Mantle Weak Zone
LREE	Light Rare Earth Elements
Mg#	Magnesium Number
ML	Mantle Lithosphere
MWZ	Mantle Weak Zone
Ma	Millions of Years
NE	Northeast
P	Pliable
P	Phase
Vp	Primary Seismic Velocity
R-MWZ	Right Mantle Weak Zone
SW	Southwest
S	Stiff
SL	Standard Lithosphere
SLM	Sublithospheric Mantle
TBL	Thermal Boundary Layer
2D	Two-dimensional
U	Unconformity
WOl	Wet Olivine
WQz	Wet Quartzite

Roman Symbols		
Symbol	Description	Units
A	Pre-exponential Scaling Factor	$MPa^{-n}\ s^{-1}$
A_r	Radiogenic Heat Production	$\mu W\ m^{-3}$
C	Cohesion	Pa
C_p	Specific Heat Capacity	$J\ g^{-1}\ K^{-1}$
d_S	Depth of Sediments	km
d_{ML}	Thickness of Cratonic Mantle Lithosphere	km
f	Scaling Factor	-
g	Gravitational Acceleration	$m\ s^{-2}$
$\dot{I}_2'$	Second Invariant of the Deviatoric Strain Rate	s^{-2}
J_2'	Square Root of the Second Invariant of the Deviatoric Stress	Pa
K	Thermal Conductivity	$W\ m^{-1}K^{-1}$
L	Latent Heat of Crystallization/Fusion	J
n	Power-law Exponent	-
P	Pressure	Pa
P_f	Pore-fluid Pressure	Pa
q	Heat Flow	$W\ m^{-2}$
Q	Activation Energy	$kJ\ mol^{-1}$
Q_2	Heat Released by Melt	$kJ\ kg^{-1}$
r	Ratio Between Actual Temperature Change and Total Temperature Change	-
R	Universal Gas Constant	$J\ mol^{-1}\ K^{-1}$
t	Time	s
T_{Moho}	Moho Temperature	°C
T_K	Absolute Temperature	K
V^*	Activation Volume	$m^{-3}\ mol^{-1}$
ΔV	Fractional Melt Volume	-
X_2	Melt Fraction	-

Greek Symbols		
Symbol	Description	Units
α	Thermal expansivity	K^{-1}
$\Delta\rho$	Change in Density	$kg\ m^{-3}$
$\dot{\varepsilon}$	Strain Rate	s^{-1}
$\dot{\epsilon}_{ij}'$	Strain Rate Tensor	s^{-1}
ϕ_{eff}	Angle of Internal Friction	°
η_{eff}	Effective Viscosity	Pa s
ρ	Density	$kg\ m^{-3}$
σ	Stress	Pa
σ_{ij}	Deviatoric Stress Tensor	Pa

Acknowledgements

First and foremost I have to thank my supervisor, Chris, who gave me the opportunity to complete my Master at Dalhousie, always guided me in the right direction through interesting discussions, made me feel part of a valuable collaboration, and provided financial support. I would also like to thank my supervisory committee. Becky Jamieson for reading and correcting countless drafts of chapters, papers and 6300 assignments, Charlotte Keen for valuable comments on my thesis drafts and papers, and finally Nick Culshaw for asking the big picture questions. Many thanks to Douglas Guptill for his technical support and late night code changes.

I would like to thank my family for their support and encouraging Skype calls. Above all, I need to thank my husband, Eric Standing, who followed me to the East Coast and is my home, wherever we are.

Lastly, the work presented in this thesis would not have been completed with such enjoyment if it had been completed without the support and friendship of my fellow graduate students.

Chapter 1 Introduction

1.1 Motivation

Plate tectonics, one of the fundamental theories of the earth sciences, describes how the outer lithospheric shell of the Earth moves and deforms through interaction with the deeper mantle. During the tectonic cycle, supercontinents are formed through major continent-continent collisional events; the resulting suture zones can later become the location of supercontinent breakup. Continental breakup starts by the initiation of a continental rift where the lithosphere is under extensional stress and strain localizes into faults. If rifting is successful the rifted continental margins will be separated by an oceanic spreading center. Thus, research focused on understanding the formation of continental rifts and their development into rifted margins is an integral part of understanding how the Earth deforms as a whole. Furthermore, the sedimentary basins that form in continental rifts and rifted margins contain 60% of Earth's giant hydrocarbon fields and are of major interest to the petroleum industry (Mann et al. 2001, Fraser et al. 2007). Knowledge of the dynamics of rift and rifted margin development gives insight into the timing of basin formation, sedimentation, trap formation, and heat flow evolution which are crucial for efficient hydrocarbon exploration.

As a result of the broad interest in rifted margins, many kinematic, analogue and simple dynamic modeling studies have been undertaken to explain observed features at continental rifts and rifted margins. These models are mainly constrained by seismic reflection and refraction data, with the addition of gravity, magnetics, well log, geochemical and xenolith data. As a result, it is generally accepted that the final geometry of the rift (e.g. the character of lithospheric thinning, distribution of normal faults, the exposure of lower crust and/or upper mantle lithosphere, and the symmetry) depends largely on intrinsic properties of the lithosphere such as the rheology and temperature. For example, extension of a "hot" lithosphere generally results in a wide rift, whereas extension of a "cold" lithosphere results in a narrow rift.

The complex and diverse nature of rifted margins remains difficult to explain, suggesting that other factors need to be taken into account. For instance, inherited weak faults are

regularly invoked to explain rift geometry (Wilson 1966, Ebinger 1989, Magnavita et al. 1994, Tommasi and Vauchez 2001), but their exact role in localizing necking instabilities is not well studied. In addition, lateral lithospheric-scale heterogeneity is introduced by terrane accretion, continent-continent collision, and transcurrent shearing, all of which can juxtapose contrasting lithospheres. Consequently, distinct lithospheric terranes are separated by sutures that can remain weak and be reactivated as sites of localization. Even if the suture itself is not weak, the dynamics of rifting will change as a consequence of any inherited lithospheric thermal, rheological, or thickness contrasts between the terranes. In spite of the general acknowledgement that lithospheric-scale heterogeneities can change the way the lithosphere deforms as a whole, their effects have not been studied in detail.

This thesis focuses on lithospheric rifting in magma-poor settings, where rifting is dictated by the growth rate of necking instabilities (regions that preferentially thin) in the presence of a lateral lithospheric contrast. I use 2D geodynamic models with a vertical lithospheric boundary to investigate how: 1) a strength contrast across the boundary changes localization and the growth rates of necking instabilities by creating a non-uniform background strain rate, and; 2) the weakening of a thick, cold and strong craton can eventually result in localization of necking instabilities in the craton. This chapter gives an overview of general rift and rifted margin characteristics, and reviews studies that explain the controls on large-scale rift geometry. Lastly, evidence for the heterogeneity of continents is reviewed.

1.2 Continental Rifts and Rifted Margins

1.2.1 Characteristics of Rifts and Rifted Margins

Continental rifts are the result of extensional forces, which cause the lithosphere to fault, stretch and thin. Extension may eventually result in continental breakup and the formation of new oceanic lithosphere, leaving the two sides of the continental rift behind as conjugate rifted margins (e.g. Péron-Pinvidic and Manatschal 2008). Regional extension can be caused by far-field plate movements (e.g. breakup of Pangea; Olsen 1997), back-arc extension (e.g. Aegean; Jolivet et al. 2010, Huet et al. 2011), post-orogenic extension (e.g. Basin and Range; Jones et al. 1992, Parsons 1995) and mantle plumes or hotspots (e.g. Ethiopian rift;

Ziegler and Cloetingh 2004, Chorowicz 2005). Extension rates can increase where voluminous magma is intruded at volcanic margins (Buck 2004, Geoffroy 2005). This thesis focuses on magma-poor rifts to avoid the complexities associated with the effects of magmatism on rifting, many of which are only partly understood (Ziegler and Cloetingh 2004, Simon 2007). At magma-poor rifts extension is the result of far-field plate motions. Rifts have general characteristics that allow them to be categorized broadly as either narrow or wide (e.g. Buck 1991, Kearey et al. 2009). The similarities in rift geometry within each group suggests that similar geodynamic processes were involved in creating them. The main differences lie in the distribution of sedimentary rift basins formed during extension.

Narrow rifts consist of an elongated series of asymmetric rift basins flanked on one side by steeply dipping normal faults (Kearey et al. 2009). Thinning and weakening of the lithosphere is focused at the rift axis, which is evident from localized thinning of the seismogenic layer (depth distribution of earthquakes). Earthquakes can occur to depths of 30

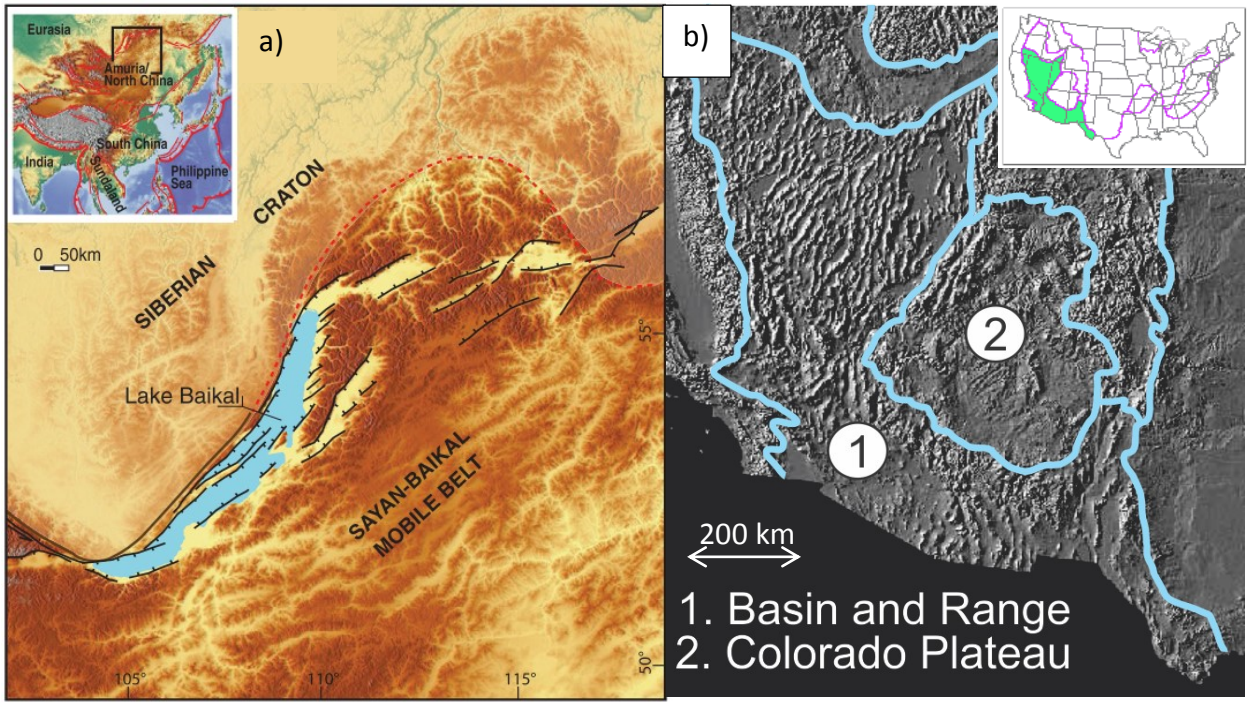

Figure 1.1. Examples of a narrow and wide continental rift. a) The Baikal rift in Asia lies on the border between the Siberian Craton and the Sayan-Baikal mobile Belt. Black lines represent normal faults, the interpreted boundary of the craton is shown in red (Corti et al. 2013a). b) Shaded relief map of the southwestern United States. The ridges and valleys are visible within the Basin and Range. The tectonic provinces are outlined in blue. From http://geomaps.wr.usgs.gov/

km in the rift flanks, but are generally shallow (12-15 km) at the rift axis. An example of a narrow rift is the Baikal rift in Asia (Figure 1.1a). It has a maximum width of 100 km and consists of linked asymmetric basins bounded by steeply dipping faults that extend over 1500 km in a NE-SW direction (Delvaux et al. 1995, 1997). Although the southern and northern parts of the rifts are characterized by more distributed deformation owing to transtension, the central Baikal rift system has undergone orthogonal extension, resulting in deep asymmetric rift basins (Logatchev and Florensov 1978, Delvaux et al. 1995, 1997, Petit and Déverchère 2006). The deepest basin hosts Lake Baikal and has a 9 km deep depocentre (Delvaux et al. 1997). Heat flow measurements on the Siberian craton and in the Sayan-Baikal mobile belt (40-60 mW m^{-2}) indicate they are cooler than in the center of the rift (60-80 mW m^{-2}), but a lack of volcanism in the rift axis combined with data from off-axis xenoliths, suggests that the lithosphere is still over 70 km thick (Ionov et al. 1995, Petit and Déverchère 2006). Other examples of narrow rifts can be found in the western branch of the East African rift system (Ebinger 1989, 2005, Foster and Ebinger 1997) and the northern Rio Grande rift (Olsen et al. 1987, Baldridge et al. 1995, Keller and Baldridge 1999, Wilson et al. 2005).

On the other hand, wide continental rifts exhibit broadly distributed deformation accommodated by regularly spaced, near-parallel, normal faults. The majority of these faults accommodate only a small amount of extension (<10 km; Jones et al. 1992). The remainder of the extension is accomplished by shallowly dipping large-scale detachment faults that can have displacements of up to 50 km (Axen 2004, Wernicke 2009). The offset on these detachment faults can create core complexes where the lower or middle crust is exposed at the surface (Wernicke 1985). A prime example of a wide rift is the Basin and Range province of the southwestern USA. It is estimated to have extended by 200% of its original width (Figure 1.1b) and contains over 30 core complexes (Coney 1980, Jones et al. 1992, Snow and Wernicke 2000, Wernicke et al. 2008, Whitney et al. 2012). The rift is 800 km wide and consists of basins bounded by shallowly dipping normal faults, separated at intervals of ca. 30 km by largely undeformed blocks (Figure 1.1b). A weak viscous lower crust is inferred from the presence of core complexes and a shallow seismogenic layer (15-17 km deep in Utah and Nevada; Pancha et al. 2006). Furthermore, low seismic velocities suggest an adiabatic mantle temperature of

1300°C at depths around 50 km (Jones et al. 1992, Zandt et al. 1995, Goes and Lee 2002). This high geothermal gradient is further supported by heat flow measurements that range from 63-105 mW m^{-2} (Parsons 1995), and granulite xenoliths from near the Moho that indicate a minimum metamorphic temperature of 950-1100°C achieved at less than 30 Ma (Hayob et al. 1989). Other wide rifts include the Carnarvon Basin in northwest Australia (Gartrell 2000) and the West Antarctica rift (Behrendt et al. 1991).

It is not surprising that rifted margins show similar wide vs. narrow characteristics, since rifted margins are the final result of successful continental rifting. As more seismic, magnetic, and gravity data have become available it is clear that rifted margins are as diverse as continental rifts (e.g. Ziegler and Cloetingh 2004, Reston 2009, Mohriak and Leroy 2012). Narrow rifted margins such as the Flemish Cap margin (Bassi et al. 1993, Gerlings et al. 2011, Welford et al. 2012), the west Greenland margin (Chalmers 1997, Chalmers and Pulvertaft 2001, Skaarup et al. 2006) and the Camamu margin in the South Atlantic (Blaich et al. 2011) have a narrow necking zone. That is, seismic reflection data show that the crust thins abruptly from a normal thickness (~30 km) to less than 5 km over a distance of 50 km. In contrast, wide margins exhibit gradually thinning continental crust over a distance of >100 km. For example, thinning at the Gabon margin extends over a distance of over 150 km (Blaich et al. 2011). Conjugate margin pairs can be asymmetric, with a narrow margin facing a wide margin as its conjugate (e.g. Camamu-Gabon; Blaich et al. 2011; Labrador-SW Greenland; Chian et al. 1995).

Furthermore, the width of continental rifts and rifted margins is far from constant along their strike. This change in distribution of deformation along the rift has been explained by the temperature of the pre-rift lithosphere, the direction of extension, and the diachronous nature of rifting (e.g. Ziegler and Cloetingh 2004, Reston 2009). In addition, the boundary between narrow and wide rifts and margins can in many places be linked to a change in geology. For example, the northern Rio Grande rift is located between the strong and tectonically stable Great Plains and Colorado Plateau (Baldridge et al. 1995, West et al. 2004). The northern rift is <100 km wide and has characteristics of a narrow rift, whereas the southern region (<34°N) shows distributed deformation and has similar characteristics to the wide and hot Basin and Range (Olsen et al. 1987, Baldridge et al. 1995, Keller and Baldridge 1999, Wilson et al. 2005).

An example of an abruptly changing rifted margin is along the northeastern Brazilian margin in the South Atlantic. In the Camamu region, the margin is less than 100 km wide, yet further south at the Espirito-Santo margin the width increases to ~200 km (Davison 1997, Mohriak et al. 2008, Blaich et al. 2008, 2011). This change in width is accompanied by a gravity low that abruptly changes into a gravity high at the onshore border between the Sao-Francisco craton and the Proterozoic mobile belt (Blaich et al. 2010, 2011), suggesting that a spatial change in pre-rift lithospheric properties may be responsible for the changing margin width. The narrow margins border the Sao-Francisco craton, which was colder and necked more rapidly than the Proterozoic mobile belt to the south, where the wider margins are located (Blaich et al. 2008, 2011, 2013).

This thesis focuses on the evolution of magma-poor rifts in a complex lithosphere with a lithospheric boundary across which the strength distribution, temperature, and thickness of the lithosphere change. The first part of the thesis is focused on the growth of necking instabilities at inherited finite weak zones in a non-homogeneous lithosphere in which only the strength changes across a vertical lithospheric boundary. The second part of the thesis is specific to cratons. Additional to the effect of a strength contrast, the effects of contrasts in lithospheric thickness and temperature are also investigated in the second part. The rest of this chapter presents an overview of the advancement in our knowledge concerning the formation of rifted margins, from rift initiation to ocean floor formation, and explains the growth of necking instabilities in a layered lithosphere. Section 1.3 outlines the effect of weak zones and larger scale contrasts on the growth rate of necking instabilities.

1.2.2 Rifting a Complex Layered Lithosphere

The first models of rifted margins consisted of rotated fault blocks overlying a uniformly thinned lower continental crust and mantle lithosphere with a sharp transition to ocean floor (e.g. Peron-Pinvidic et al. 2013). The formation of sedimentary basins on extended continental crust (e.g. North Sea) and in back-arcs (e.g. Aegean) was explained by uniform thinning (pure shear; Figure 1.2a) as suggested by McKenzie (1978). In this model, the amount of thinning is uniform with depth throughout the lithosphere. The difference in thickness between the original and thinned lithosphere is balanced by upwelling asthenosphere, bringing it closer to

the surface and causing subsidence if the crust was initially thicker than 18 km, and uplift if the crust was thinner than 18 km (McKenzie 1978). Further subsidence follows as the hot lithosphere and asthenosphere cool and contract.

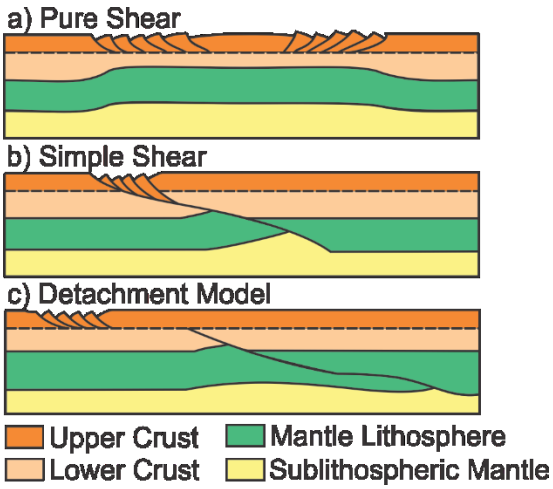

Figure 1.2. Kinematic models of lithospheric stretching , after Lister et al. (1986). a) Pure shear (McKenzie 1978). b) Simple shear (Wernicke 1985) c) Detachment model of Lister et al. (1986).

The pure shear stretching model was applied to the Nova Scotia margin by Royden and Keen (1980). Their results showed that the sedimentation observed in well data could satisfactorily be explained by subsidence curves calculated using uniform thinning. However, this model did not fit the thermal subsidence history interpreted for the Labrador margin (Royden and Keen 1980). Instead, a better fit with thermal and subsidence data can be found if the mantle lithosphere has undergone more thinning than the crust. In this type of case, known as depth-dependent extension (Royden and Keen 1980), either the mantle lithosphere or crust thins faster and more extensively than the other, resulting in a more complicated subsidence history.

The views and models of the structure of rifted margins evolved as more seismic, gravity, magnetic and well-log data became available (Ziegler and Cloetingh 2004, Péron-Pinvidic and Manatschal 2008, Reston 2009). For example, neither the existence of exhumed serpentinized mantle lithosphere like that found at the Galicia margin (Boillot et al. 1980, 1987) nor the asymmetric nature of many conjugate margins could be explained using pure shear models (e.g. Lister et al. 1986). For this reason, Lister et al. (1986) adapted the simple shear

model (Figure 1.2b; Wernicke 1985), which was developed to explain the formation of core complexes in the Basin and Range, to the formation of rifted margins. According to the Lister et al. (1986) model, extension is accommodated on shallowly dipping faults offset by horizontal detachments in the more viscous parts of the lithosphere, essentially decoupling deformation in the crust and mantle lithosphere (Figure 1.2c). Like the simple shear model, the detachment model predicts inherent asymmetry in rifted conjugate margin geometry and is compatible with depth-dependent extension. Seismic data from the Iberia-Newfoundland conjugate margins reveal continentward dipping reflectors interpreted to support the existence of detachment faults in the lower crust (Pickup et al. 1996, Boillot and Froitzheim 2001).

Depth-dependent extension is still a favored model, but the complexity of continental rifts and rifted margins is inadequately explained by simple kinematic models, which neglect the geodynamical processes involved in creating rifts. In fact, analogue (e.g. Benes and Davy 1996, Brun 2002 and references therein) and numerical models (e.g. Bassi 1991, 1995, Buck 1991, Bassi et al. 1993, Huismans and Beaumont 2003, 2014, Rosenbaum et al. 2010) are interpreted to suggest that both the intrinsic properties of the pre-rift lithosphere and the extension rate influence the diversity of rifts and rifted margins. These factors change how the lithosphere behaves under stress applied by far-field plate motions.

The mechanism for rift initiation will always be the one that requires the least amount of force or energy (Buck 2004, Huismans and Beaumont 2007). While the lowest energy option for magma-rich rifts is intrusion of basalt into the lower crust (Buck 2004), for magma-poor rifts, where melt is not abundant, rifts evolve through the initiation and growth of necking instabilities (Bassi 1991, 1995). Necking instabilities are regions that thin faster than their surroundings as a result of a positive feedback between strain rate and viscosity in materials that strain soften (Smith 1977, Emerman and Turcotte 1984, Schmalholz et al. 2008). In this case, an increase in strain rate results in a decrease in effective viscosity, which leads to a further increase in strain rate. This feedback dictates the growth rate of necking instabilities in any non-Newtonian power-law fluid with a power-law exponent (n) >1 (equation 1.1). The flow laws are experimentally determined and depend on the minerals present in rocks. The feedback

follows from the formulation of these flow laws that describe the effective viscosity of rheologies in the lithosphere (e.g. "Wet" Olivine has n = 3; Karato and Wu 1993) in combination with its relation to stress (Equation 1.2).

$$\eta_{eff} = A^{-1/n}(\dot{\varepsilon})^{\frac{1-n}{2n}} \exp\left(\frac{Q + PV^*}{nRT_K}\right) \quad (1.1)$$

$$\sigma = \eta_{eff}(\dot{\varepsilon}) \cdot 2\dot{\varepsilon} \quad (1.2)$$

Using Equation 1.1, the effective viscosity η_{eff} can be calculated using the laboratory-determined pre-exponential scaling factor (A), activation volume (V^*), activation energy (Q) and the power-law exponent (n) for a certain temperature (T_K), pressure (P) and strain rate ($\dot{\varepsilon}$). R is the universal gas constant. Equation 1.2 relates the strain rate and effective viscosity to the stress (σ). Although necking instabilities are technically associated with viscous deformation, frictional-plastic behavior, or brittle “necking”, can be approximated by using a large power-law exponent (n > 1000; Fletcher and Hallet 1983, Zuber and Parmentier 1986), thereby increasing the growth rate of the necking instability. In light of this approximation, we define “stiff” materials to be those with n >1000 (brittle) and which therefore neck much faster than “pliable” materials with n ~ 2-5 (viscous). A single pliable layer necks more slowly and requires more extension to breakup than a single stiff layer of equal thickness (Figure 1.3a). This is analogous to a Mars Caramel bar (Figure 1.3b), which has stiff chocolate on the outside, and pliable caramel inside. Under extension, the chocolate (stiff) will break rapidly, but it will take longer for the caramel (pliable) to pull apart. The structure and composition of the lithosphere are more complex than a Mars Caramel bar, and it is the competition between necking instabilities in a layered lithosphere composed of multiple stiff or pliable layers that determines rift geometry (Bassi 1991, 1995, Bassi et al. 1993, Davis and Kusznir 2004, Huismans and Beaumont 2008, 2011, 2014).

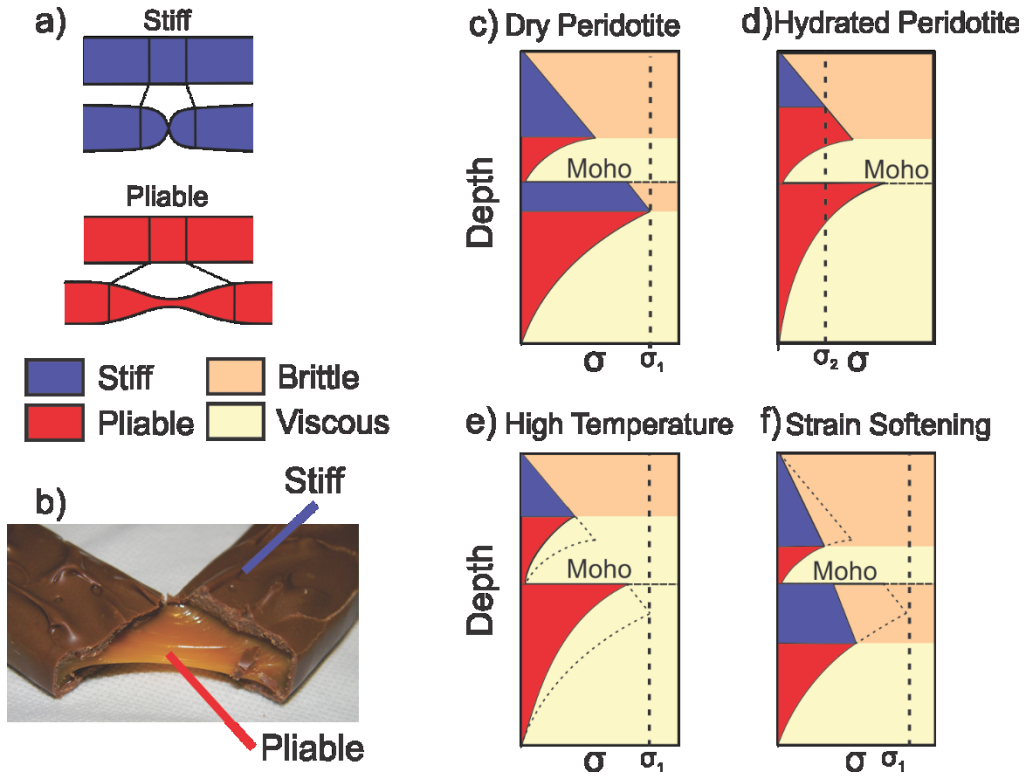

Figure 1.3. Necking of a layered lithosphere. a) Necking of a single stiff layer requires less extension than necking in a pliable layer until the layer breaks up. b) Mars Caramel bar. The chocolate is stiff and breaks apart rapidly, whereas the pliable caramel takes longer to break up. c) Yield strength profile for a lithosphere with a dry peridotite mantle lithosphere. d) Yield strength profile for a lithosphere with a mantle lithosphere composed of hydrated peridotite. The stiff part of the crust is thinner than the brittle part of the crust, because at a low strain rate and stress (σ_2) the lower part of the crust is not at yield. e) Yield strength profile of a higher temperature lithosphere (solid profile) as compared to the lithosphere shown in (a) (dashed profile). A hot geotherm results in thicker viscous layers. f) Yield strength profile of a strain softened lithosphere (solid profile) as compared to the lithosphere shown in (a) (dashed profile). The thickness of both the brittle and stiff layers has increased as the yield strength decreases through strain softening.

A simplified yield stress profile for a typical continental lithosphere consists of a brittle upper crust, a viscous lower crust, an upper mantle lithosphere that can be viscous or brittle and finally a viscous lower mantle lithosphere (Figure 1.3c,d) (Goetze and Evans 1979, Burov 2011). Although the distribution of viscous and brittle layers may not be entirely equivalent to the distribution of stiff and pliable layers, it is a useful approximation to understand the stiff and pliable behavior of the lithosphere because many modeling studies include yield strength profiles. Only the part of the brittle layer that is at yield (stress is equal to the yield stress as determined by the strength envelope) is stiff and will grow necking instabilities rapidly (Figure 1.3d). For example, where the lithosphere is under a high strain rate ($\dot{\varepsilon} = 10^{-13}\,s^{-1}$), the stress in

each layer is high (σ_1 in Figure 1.3c). In this case, stiff necking dominates over pliable necking because it is faster (Kusznir and Park 1987, Bassi 1995). This will result in a narrow rift. Conversely, a low strain rate ($\dot{\varepsilon} = 10^{-16}\,s^{-1}$) does not cause fast necking instabilities in the brittle layers, as they are not entirely at failure and only partly stiff (σ_2 in Figure 1.3d). This allows slower necking instabilities to grow in the pliable layers (Kusznir and Park 1987, Bassi 1995). As necking takes longer multiple necking instabilities may localize deformation, especially where there is significant cooling (Van Wijk and Cloetingh 2002). This results in a wide rift (Buck 1991, Chenin and Beaumont 2013).

In addition to the strain rate, the behavior of a lithosphere under extension is also subject to the character of the yield strength profile. For instance, depending on the rheology, the upper mantle lithosphere can have an upper brittle zone (e.g. dry peridotite; Figure 1.3c) or be completely viscous (e.g. hydrated peridotite, Figure 1.3d). On the other hand, a high geothermal gradient decreases the strength of the lithosphere as a whole, increasing the proportion of viscous layers (Figure 1.3e) (Bassi 1991, Buck 1991, Bassi et al. 1993). Slow necking in a hot lithosphere leads to distributed deformation and produces wide rifts, whereas a colder lithosphere necks rapidly and produces a narrow rift (Bassi 1991, Buck 1991, Bassi et al. 1993). The geothermal gradient can be related to the time of the last tectonic disturbance. This can explain the difference between the Basin and Range and the Baikal rift. The pre-rift lithosphere in the Basin and Range was thickened during the Laramide orogeny about 40-50 Ma, resulting in a high geothermal gradient (Sonder and Jones 1999). Post-orogenic extension started soon after, and the main phase of Basin and Range extension started only 10 Ma after the tectonic thickening, when the plate boundary between North America and the Pacific changed from a subduction to a strike-slip zone (29 Ma) (Parsons 1995). Conversely, the area surrounding the Baikal Rift was tectonically stable from the Proterozoic until ca. 27 Ma when rifting was initiated, and had a much longer time to cool (Delvaux et al. 1995). Frictional strain-softening also changes the distribution of brittle and viscous layers and increases the part of the lithosphere that is on yield (Figure 1.3f)

Especially important for rift geometry is the thickness of viscous middle or lower crust. Not only does this change the thickness of the stiff regions in the crust, it also determines the

degree of coupling between the crust and mantle lithosphere. Huismans and Beaumont (2014) built on previous modeling studies (Davis and Kusznir 2004, Kusznir and Karner 2007, Huismans and Beaumont 2008, 2011, Chenin and Beaumont 2013) to show that two end-member rift geometries can be produced by having either a coupled or decoupled crust and mantle. Their Type l model has only a ~5-km thick viscous lower crust effectively coupling deformation in a brittle crust to a brittle upper mantle lithosphere. The stiff crust necks rapidly and over a short distance (narrow margins) and breaks up before the mantle lithosphere. The continental mantle lithosphere or depleted cratonic mantle lithosphere is still thinning when the crust breaks apart in the Type l model, and ends up being exposed at the surface between thinned continental crust and newly formed oceanic crust. The Type ll model represents the other end member, where a 20 km thick viscous lower crust decouples the crust from the mantle lithosphere. Furthermore, this model has a mainly pliable crust that necks slower than the stiff upper mantle lithosphere. No mantle lithosphere is exposed when the crust finally breaks apart after the slow necking of the pliable crust. The Type ll model, with its prolonged crustal necking, results in wide conjugate rifted margins.

The models presented in Huismans and Beaumont (2014) and other studies referenced above provide a solid foundation for our understanding of the extensional behavior of a uniform 2D lithosphere under extensional velocity boundary conditions. We now appreciate that the intrinsic properties of the lithosphere play a role in determining how and where rifts develop, from their initiation to ocean crust formation. In particular, the complex distribution of viscous and brittle layers is a large factor in determining varying rift geometries. Even so, these models do not explain why margins can change abruptly along strike. The next section will illustrate how inherited heterogeneities ranging from infinitesimal perturbations to lithospheric-scale contrasts affect the localization and growth of necking instabilities and need to be considered in models designed to investigate rifted margin diversity.

1.3 Rifting Heterogeneous Continents

1.3.1 Complex Lithospheres

Weak zones are often interpreted to localize deformation in the lithosphere (e.g. Dunbar and Sawyer 1989, Manatschal et al. 2015). Orogenic, transcurrent and subduction events can leave behind mechanically weak structures such as thrusts and foliations that can be reactivated in favorable conditions. For example, in the western branch of the East African rift, Proterozoic faults were reactivated in the Miocene as bounding faults for asymmetric basins (Ebinger 1989, Versfelt and Rosendahl 1989, Theunissen et al. 1996, Corti et al. 2007). Although reactivation of inherited faults is widely recognized at a local scale, their importance for regional-scale rift development is less clear (Manatschal et al. 2015). For this reason we focus on sutures, which may act on a regional scale because they represent lithospheric boundaries (Griffin et al. 1999, Vaughan et al. 2005, Manatschal et al. 2015). They can extend through the brittle upper crust and all the way into the viscous lower crust and upper mantle as mylonitic shear zones (Ring 1994, Griffin et al. 1999, 2009a, Tommasi and Vauchez 2001).

Sutures mark the boundaries between crustal blocks or terranes with contrasting geological histories, and are typically marked on the surface by thrust fronts, foliations, ophiolites, and exhumed metamorphic rocks (Ebinger 1989, Vauchez et al. 1998, Magnani et al. 2004, Ziegler and Cloetingh 2004, Manatschal et al. 2015). For example, the Appalachian orogen records Neoproterozoic rifting of Laurentia and subsequent closure of the Iapetus and Rheic oceans; multiple phases of Paleozoic terrane accretion can be identified (Figure 1.4a) (Williams 1964, 1978, Wilson 1966, Hibbard and Waldron 2009, van Staal et al. 2012). The remnants of these tectonic events can still be identified and introduce heterogeneity into the lithosphere. A seismic line through Newfoundland (Figure 1.4b, c) has been interpreted to show the Devonian subduction zone that led to the accretion of Ganderia and Avalonia (van der Velden et al. 2004). A near-vertical strike slip boundary can also be seen between Laurentia and outboard accreted terranes, now comprising the Central Mobile Belt (CMB; Figure 1.4b,c) (Williams 1964, van der Velden et al. 2004).

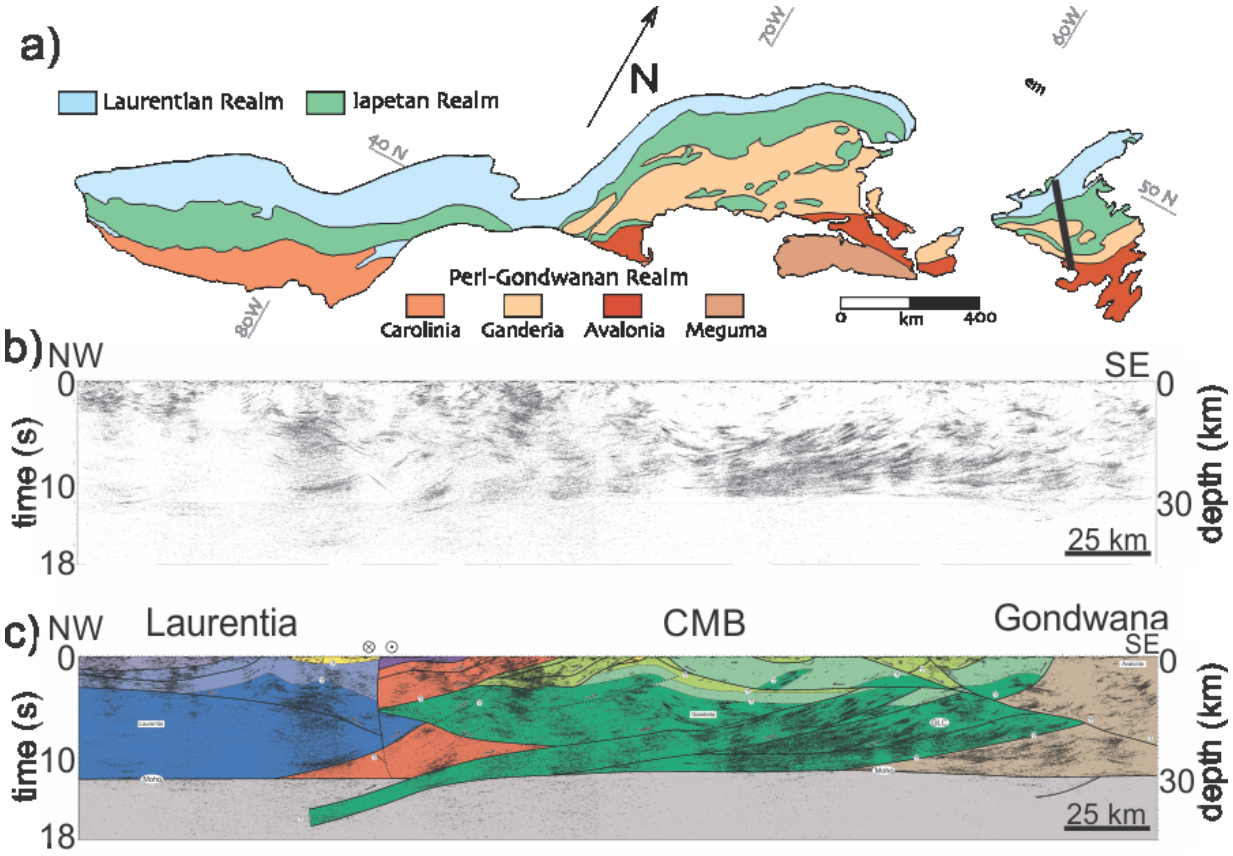

Figure 1.4. Terrane distribution in the Appalachian orogen. a) Terrane map of the Appalachians (Hibbard and Waldron 2009). b) Seismic reflection profile through Newfoundland (black line in panel a). c) Interpreted seismic section showing the boundaries between Laurentia, the Central Mobile Belt (CMB) and Avalonia, which originated from Gondwana (van der Velden et al. 2004)

Further south in the Appalachians, similar faults within the Appalachian suture zones were reactivated during the Mesozoic opening of the Atlantic. This created a series of sedimentary basins offset from the main locus of rifting including the Fundy Basin in Nova Scotia and the Newark, Gettysburg, Culpeper and Scottville basins in the eastern United States (Withjack and Schlische 2005), and similar basins can be found on the conjugate Moroccan margin (Laville et al. 2004). The formation of these basins along ancient fault zones provides evidence that suture zones may remain weak. This can be the result of cohesion loss in the upper crust (Buck 1993), fluid pressure variation (Sibson 1990), the formation of hydrous minerals (Bos and Spiers 2002), and/or grain size reduction (Karato et al. 1986) for brittle and viscous regions.

Weak suture zones are not the only heterogeneity inherited from terrane accretion. Each terrane comes with its own geological heritage; terranes can be ribbon continents, volcanic arcs, accretionary prisms, oceanic domains, and combinations of these, which may have traveled several thousand kilometers before being accreted to a continent (Vaughan et al. 2005). The lithologies, thicknesses and geotherms may be different from terrane to terrane. The resulting heterogeneity (Figure 1.5) can greatly affect the strength distribution of the lithosphere. Not only does each terrane have potentially different viscous and brittle layer distributions, their juxtaposition affects the distribution of stress and therefore the distribution of stiff and pliable layers. Sutures may be responsible for many lithospheric-scale thermal, compositional and thickness contrasts, but they are not the only heterogeneities in the lithosphere. I investigate the hypothesis that lateral lithospheric-scale contrasts affect the localization of deformation and may change the location of final breakup. Weak zones and lateral contrasts in the lithosphere alter the location and growth rates of necking instabilities. The next section reviews the existing modeling studies focused on understanding where a weak zone will localize a necking instability and how this may be affected by the presence of lateral contrasts.

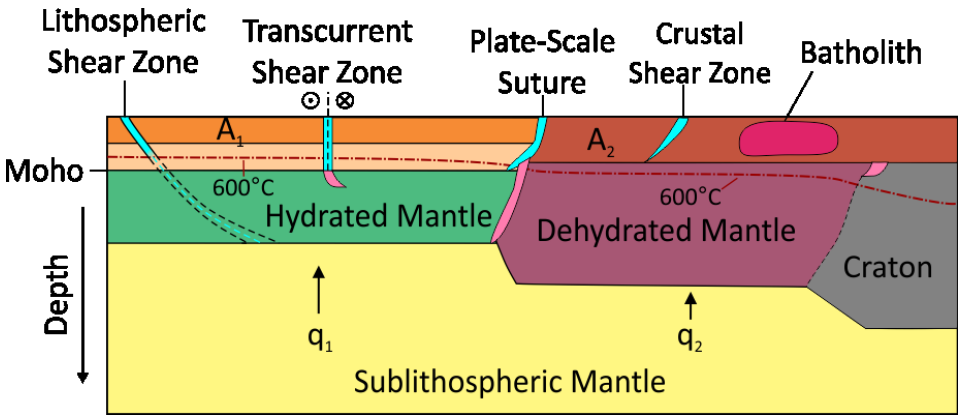

Figure 1.5. Schematic diagram illustrating types of lithospheric heterogeneities. Structural heterogeneities such as shear zones may be mechanically weak. Thermal contrasts result from variable basal heat flow (q_1 and q_2) and radiogenic heat production (A_1 and A_2) in the crust. Generally, a lithosphere that has formed or undergone a major tectonic event recently will be hotter than a lithosphere that has remained largely undisturbed. Rheological contrasts are inherent in lithosphere of different ages (e.g. Archean vs. Phanerozoic) and can also be the result of magmatic additions, varying degrees of depletion, dehydration, thickness and compositional differences.

1.3.2 Growth of Necking Instabilities in a Heterogeneous Lithosphere

Necking instabilities are the result of a small perturbation or flaw within a material that causes one location to have a higher strain rate than its surroundings (Smith 1977, Emerman and Turcotte 1984). Smith (1977) was the first to show that small-scale features such as boudins and mullions observed in nature could only be described by using a non-Newtonian flow with strain-softening properties. The analysis was simplified by Emerman and Turcotte (1984) for a single layer embedded in a medium with a large viscosity contrast under uniaxial stress and strain. With these assumptions, the growth rate of an initial thickness perturbation can be calculated knowing only the size of the perturbation, the initial and final thickness of the layer and the power-law exponent, n. For example, if n = 3 and the layer is twice its original length, a perturbation would have grown by a factor of 8 (2^3). Perturbations or heterogeneities in a layered lithosphere have a similar effect. For example, Fletcher and Hallet (1983) showed that a two-layer lithosphere can be unstable under extension where a small thickness perturbation is present in a plastic layer overlying a pliable layer with a high geothermal gradient and n = 3. The strain rate is higher in the perturbed area than in the adjacent extending layer and a necking instability is initiated (Fletcher and Hallet 1983, Zuber and Parmentier 1986). In particular, the multiple necking zones developed in the unstable model were used to explain the uniformly spaced normal faults in the Basin and Range (Fletcher and Hallet 1983)

In ceramics, plastics, and metals, heterogeneities such as small surface defects, anisotropic crystals, and pores, can act as perturbations and may start a necking instability (e.g. Ghosh 1977, Korhonen 1978). At the site of the defect, or weakness, the yield strength is lower, leading to failure (Figure 1.3). Previous modeling studies have used this approach to localize strain in a specified area of the model (Huismans and Beaumont 2003, 2008, 2014), However, studies including only one weak zone do not give insight into the competition among necking instabilities where multiple weak zones are present, as is likely in the lithosphere.

Chenin and Beaumont (2013) used 2D numerical models to investigate the competition between a mantle weak zone in the upper mantle lithosphere and offset weak zones (offset

equidistant from the center of the model) in the upper crust in an otherwise laterally homogenous lithosphere. Their results showed that the distribution of stiff and pliable layers in which weak zones are embedded strongly influences the localization of deformation in the lithosphere (Figure 1.6). In their models, a rapidly growing necking instability in the stiff upper mantle lithosphere precludes the formation of offset sedimentary basins at the offset weak zones (Figure 1.6). Conversely, where the upper mantle lithosphere is pliable the necking instability in the upper mantle lithosphere initiates and grows more slowly. In this case offset basins (e.g. eastern North America, Section 1.3.1) may form at the offset crustal weak zones and in some cases even become the locus of breakup (Figure 1.6).

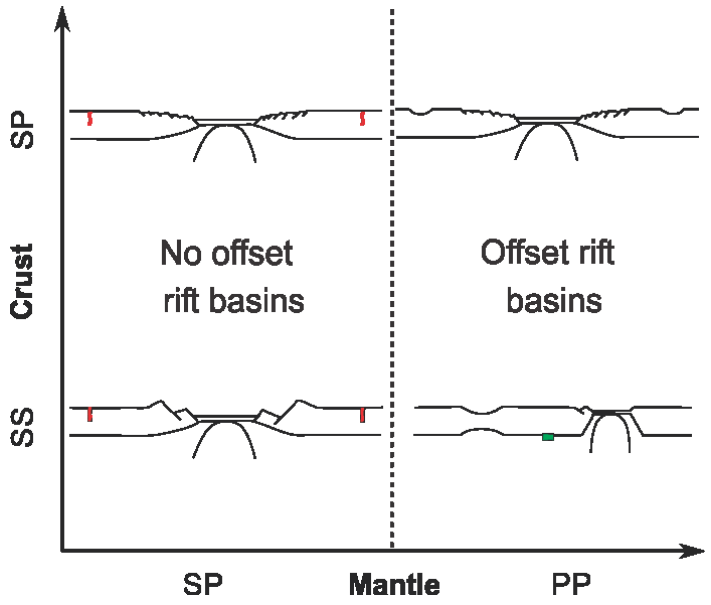

Figure 1.6. Rift style dependence on the stiff (S) and pliable (P) layering in the lithosphere (Chenin and Beaumont 2013). The axes describe the layering of the lithosphere. For example the bottom left corner describes a SS-SP model, which has a stiff upper and lower crust, a stiff upper mantle lithosphere and a pliable lower mantle lithosphere. Crustal weak zones are shown in red and the mantle weak zone, which is initially at the center of all models, is green. No offset rift basins are formed where the upper mantle lithosphere is stiff, because necking in this strong layer is rapid and there is no time for necking instabilities in the crust to grow. Where the upper mantle lithosphere is completely pliable offset rift basins will form. If the crust is stiff (SS-PP) and the mantle totally pliable rapid necking occurs at an inherited weak zone in the crust and it becomes the locus of breakup

The models presented in Chenin and Beaumont (2013) form the basis for the work presented in this thesis. The distribution of stiff and pliable layers is more complex in a laterally heterogeneous lithosphere. Since the presence of amalgamated terranes with different yield

strength distributions affects the distribution of stress, it also affects the distribution of stiff and pliable layers.

Whether through reactivated shear zones or contrasts in strength, regions with different properties affect the location and geometry of rifts and rifted margins. Therefore, the next step in understanding the development of rifted margins is to consider the effects of lithospheric-scale lateral heterogeneities in numerical models of magma-poor rifting.

1.4 Objectives and Summary of Thesis Content

Since the general acceptance of plate tectonics, many studies have contributed to our understanding of the diverse rifts and rifted margins that can be produced by varying the intrinsic properties of a laterally homogeneous lithosphere. It is clear that in a laterally homogeneous lithosphere, the distribution of strength with depth is a major control on rift development. More effort needs to be focused on understanding the effects of large-scale contrasts within the lithosphere, which also alter the distribution of strength, both vertically and laterally. The modeling work in this thesis expands on recent numerical studies that included finite weak zones representing sutures, and analogue studies that included a lateral lithospheric-scale strength contrast.

Chapter 2 presents 2D numerical rifting models that illustrate how the behavior of a laterally heterogeneous lithosphere is distinctly different from that of a homogeneous lithosphere. It develops the work of Chenin and Beaumont (2013) by considering the growth of necking instabilities around finite weak zones in a lithosphere with a strength contrast across a vertical lithospheric boundary. The distribution of brittle and viscous layers (stiff and pliable behavior) of the lithosphere is no longer the dominant control on rift development. Instead, the strain rate contrast resulting from juxtaposition of lithospheres with different strength distributions, is shown to be the primary control on the location of breakup for a range of lithospheric properties. This chapter has been submitted for publication to the *Journal of Geophysical Research*.

Chapters 3 and 4 expand on one of the implications of the results of Chapter 2, which indicate that cratons are protected by surrounding weaker lithospheres. The cratonic

lithosphere in the models presented here is not only stronger, but also thicker and colder than the standard lithosphere next to it. Chapter 3 reviews the characteristics of cratons that generally make them nearly impossible to rift and how these characteristics can be altered by metasomatic weakening, in some cases enough to initiate rifting.

Chapter 4 presents detailed models where melt metasomatism reduces the strength of a cratonic lithosphere. The main objective is to determine the amount of weakening that is needed to rift a craton. Some simplified models are presented to illustrate the effects of refertilization (increase in density), an increase in temperature (decrease in viscosity) and rehydration (decrease in viscosity) on the stability of cratonic mantle lithosphere. Weakening may result in convective removal of part of the cratonic lithosphere. This chapter is in preparation for submission to *Earth and Planetary Science Letters.*

Chapter 5 reviews the effect of lateral contrasts in the lithosphere on the stiff and pliable layer distribution and the strain rate using examples from both Part 1 and Part 2 of the thesis. It presents the conclusion from these studies and provides suggestions for further research.

Chapter 2 Effects of Lateral Strength Contrasts and Inherited Heterogeneities on Necking and Rifting of Continents

2.1 Preface

This chapter has been submitted to the *Journal of Geophysical Research: Solid Earth*. It has been accepted for submission with major revisions, which will be submitted by the end of September 2015. The revisions include reorganization and a more thorough explanation of the results within the large parameter space. S. Wenker expanded on the work done by Chenin and Beaumont (2013) by including an additional lithospheric boundary in numerical models. S. Wenker did part of the model design and conducted all model experiments. Result were interpreted with the aid of C. Beaumont and compiled and written into the manuscript by S. Wenker. The manuscript was a collaboration between C. Beaumont and S. Wenker.

2.2 Abstract

Besides the intrinsic rheological layering of the lithosphere and its thermal structure, inherited heterogeneities may play an important role in strain localization during continental extension. This is similar to the role that defects play in the failure and necking of other materials. Here, we consider both inherited small-scale weak zones and the effects of lateral juxtaposition of two lithospheres with differing properties as mechanisms to localize deformation and initiate necking instabilities. Using 2D finite-element models that contain lateral lithospheric boundaries, alone and in combination with smaller scale heterogeneities, we illustrate that two controls determine how necking instabilities grow and thus lead to varying styles of rifting: Control 1, the stiff/pliable nature of the lithosphere and Control 2, the background strain rate in the lithosphere. Control 1 depends on the lithospheric rheology, such that necking instabilities grow faster in materials with high power-law flow exponents (stiff, brittle lithosphere) than in those with low power-law flow exponents (pliable, viscous lithosphere). Control 2 prevails in lithosphere where background strain rate contrasts are highest. This happens because necking amplifies the background strain rate in power-law materials, leading to faster necking where strain rates are highest. The model results show that Control 2 determines the location of localization, unless the background strain rate is equal or near equal in both lithospheres, in which case Control 1 wins. These results explain why rifting

does not localize in cratons even though they contain heterogeneities. The results also provide a mechanism for the formation of asymmetric rifted margins.

2.3 Introduction

The diverse nature of continental rifts and rifted margins is poorly explained by simple kinematic models such as pure shear (McKenzie 1978) and simple shear (Wernicke 1985). Possible reasons for the observed complex nature of rifts and rifted margins include the inherent rheological layering and thermal structure of the lithosphere and their effects on the way it extends. These factors can result in depth-dependent extension where either the crust or mantle lithosphere preferentially thins (e.g. Royden and Keen 1980, Zuber and Parmentier 1986, Huismans and Beaumont 2003, 2014, Weinberg et al. 2007, Kusznir and Karner 2007, Nagel and Buck 2007).

In addition to rheology, inherited heterogeneities may serve to localize extension, which in some instances can lead to the development of necking instabilities in a similar manner to failure owing to defects in ceramics, metals and plastics. Inherited fabric and heterogeneities are attractive targets for research because they have the potential to explain the complexities of rifted margins including the abrupt spatial changes in their character along strike. In this study, we focus on reactivated suture zones. These heterogeneities are inherited from previous tectonic processes such as terrane accretion, continent-continent collision, and transcurrent shearing. At the surface they are represented by faults, foliations, and thrust fronts, as well as sediments, ophiolites and exhumed metamorphic rocks (Ebinger 1989, Vauchez et al. 1998, Magnani et al. 2004, Ziegler and Cloetingh 2004, Manatschal et al. 2015).

Examples of reactivated suture zones can be found all along the North Atlantic rifted margins, where they are commonly associated with sedimentary basins offset from the main locus of Triassic to Cretaceous rifting which formed the North Atlantic Ocean. These include the Rockall, Porcupine (Lefort and Max 1984, Dore et al. 1997), Jeanne d'Arc, Fundy, Newark (Withjack and Schlische 2005, Chenin and Beaumont 2013), and equivalent basins further south in the Appalachians and on the conjugate margin (Figure 2.1a). The South Atlantic margins have several examples of reactivated sutures, some resulting in offset basins (e.g. Reconcavo, Jatoba

and Tucano; Ussami et al. 1986, Castro 1987, Magnavita et al. 1994), while others that developed along the boundary between cratonic and younger lithosphere became the main locus of rifting (e.g. Camamu - Gabon Margin; Chang et al. 1992, Blaich et al. 2010).

Sutures also commonly coincide with lateral lithospheric boundaries across which a contrast in properties is present (Figure 2.1b). Even if the suture itself is not weak, this contrast will change the way the lithosphere deforms as a whole by creating a non-uniform distribution of the background strain rate. Contrasting properties can result from one or more of the following: different lithospheric compositions, difference in thermal regime (e.g. craton vs. orogenic belt, or difference in radiogenic heat production); rheological differences (e.g. resulting from contrasts in metamorphism, depletion and dehydration); and changing crustal (e.g. orogenic belt vs pre-existing extensional basin) (Dunbar and Sawyer 1989, Vauchez et al. 1998, Manatschal et al. 2015), or mantle lithosphere thickness (e.g. craton vs. young continental lithosphere).

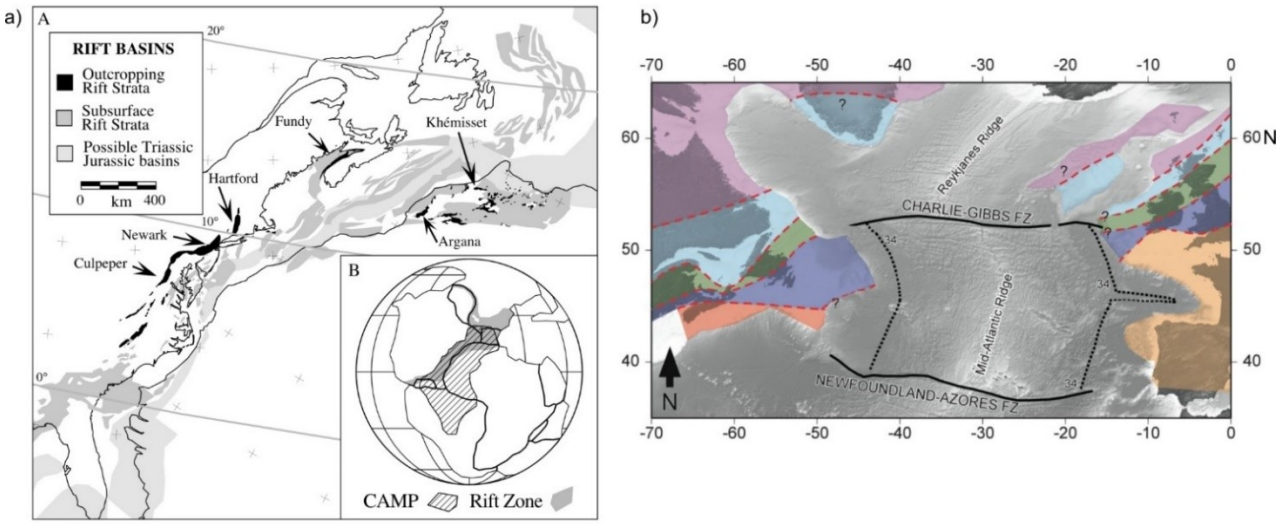

Figure 2.1. Rifting in heterogeneous lithosphere. a) Rift Basins on both sides of the North Atlantic offset from the main locus of rifting shown at their paleogeographic position at ~225 Ma (Olsen et al. 2003). b) Rifting across the terranes of the North Atlantic crosscuts multiple terranes and sutures. (Welford et al. 2012). CAMP is the Central Atlantic Magmatic Province.

Where heterogeneities are present, extension of the lithosphere involves a positive feedback loop between the initial focusing of instabilities at heterogeneities and the way

necking instabilities are amplified by the lithospheric rheology and the background strain rate (Chenin and Beaumont 2013). As we explain in Section 2.4, the growth rate of necking instabilities depends on the deformation mechanism. In particular, the growth rate increases with the power-law exponent, n, which means frictional-plastic (brittle) necking (n > 1000) will develop much faster than power-law viscous (viscous) necking (n ~ 2-5). We refer to lithospheric layers with these properties as 'stiff' (n >1000) and 'pliable' (n ~ 2-5) respectively. This terminology is used in the sense that it applies to viscous-plastic, not elastic, materials. The stratification of the lithosphere into stiff and pliable layers will depend on the composition, temperature and strain rate variation laterally and with depth. These factors determine whether deformation is plastic or viscous, the n-value that is applicable, and the stiff-pliable layer distribution (Section 2.4).

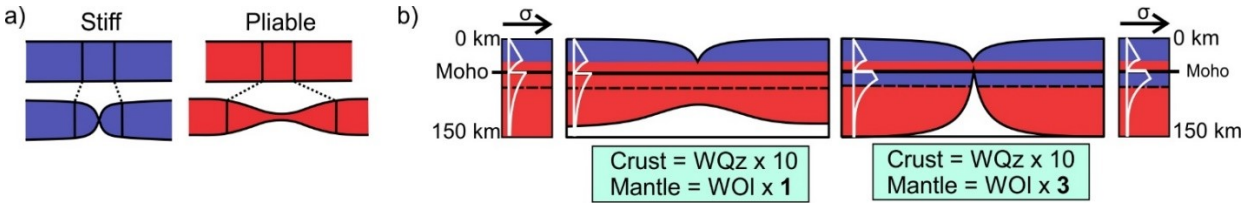

Figure 2.2. Stiff and pliable behavior. a) a pliable material (red) deforms in the viscous regime and requires a larger amount of extension to break it than a stiff material (blue), which deforms in the brittle regime and necks rapidly. b) The lithosphere consists of layers which can be stiff or pliable. The upper crust is always stiff because of cool surface termperatures and the lower mantle lithosphere is always pliable because of a high temperature. The stiff and pliable behavior of the models is changed by using a scaling factor in the viscous flow law, where WQz = "Wet" Quartzite and WOl = "Wet" Olivine. By changing the mantle lithosphere from WOl x 1 on the left to WOl x 3, and effectively changing the strength of the mantle lithosphere, we change the stiff and pliable behavior of the upper mantle lithosphere.

In the following sections we outline how necking instabilities develop, define stiff and pliable layers (Section 2.5), and propose that there are 2 primary controls on the style of rifting (Section 2.6): Control 1, the distribution of stiff and pliable layers within the lithosphere, and Control 2, the background strain rate in the lithosphere. We demonstrate these controls by using geometrically simple 2D thermo-mechanical numerical models that include small-scale inherited heterogeneities (weak zones) and/or a lateral lithospheric boundary across which a strength contrast exists (Section 2.7).

Four model types with varying placement of Mantle Weak Zones (MWZ) and Crustal Weak Zones (CWZ) were designed and used to test how the uniform or non-uniform background strain rate influences the activation of embedded finite weak zones, and whether Control 1 or 2 dominates where a lateral strength contrast is present. The model results (Section 2.8) are presented in three series to demonstrate respectively: 1) the stiff versus pliable competition in the absence of a lateral strength contrast; 2) the same competition where there is a lateral boundary, and; 3) under which circumstances the background strain rate controls the necking characteristics. Lastly, we discuss application of the results to craton preservation and asymmetric continental margins.

2.4 Growth of Lithospheric Necking Instabilities

We adopt the view that magma-poor rifted margins evolve through the growth of lithospheric necking instabilities leading to lithospheric breakup. The necking growth rate determines the timescale for lithospheric breakup, the amount of extension required, and the final geometry - wide, narrow, or complex - of the resulting rifted margin (Bassi 1991, 1995, Buck 1991, Ziegler and Cloetingh 2004). Furthermore, depth-dependent extension (Royden and Keen 1980, Zuber and Parmentier 1986) is also a manifestation of necking with different growth rates of necking instabilities in the crust and mantle lithosphere (Huismans and Beaumont 2003, 2014, Weinberg et al. 2007, Kusznir and Karner 2007, Nagel and Buck 2007, Chenin and Beaumont 2013). Our goal is to investigate the feedback between lithospheric rheology and necking instabilities, in particular, those that localize at inherited heterogeneities.

2.4.1 Understanding Necking Instabilities

We start by considering necking instabilities, which for a single layer range from wide to narrow (Figure 2.2). For continental lithosphere the behavior is more complex owing to the layering. For example, the reference continental lithosphere (Figure 2.2b) has a vertical strength profile comprising brittle and viscous crustal layers, an uppermost mantle lithosphere that can either be brittle or viscous, and a lower lithosphere that is viscous (e.g. Burov 2011, Chen et al. 2012). The whole lithosphere is extending under constant velocity boundary conditions. Although this is a complex layered system, the growth rates of necking instabilities in the individual layers can be understood by the approximation that deformation in each layer

is governed by viscous power-law flow of its material (Figure 2.3b). Necking can then be calculated using parameters derived from laboratory experiments (e.g. Karato and Wu 1993, Gleason and Tullis 1995).

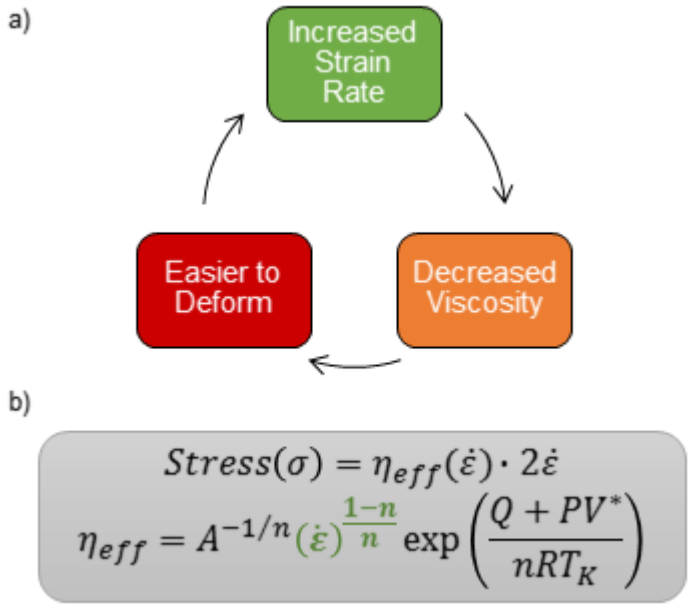

Figure 2.3. Rheological feedback a) Feedback between deformation and the power-law exponent (n), the strain rate ($\dot{\varepsilon}$) and viscosity (η_{eff}). b) This feedback follows from the power-law of fluid flow, which mainly depends on the power-law exponent (n), and the strain rate ($\dot{\varepsilon}$). A, Q and V^* are experimentally determined constants. R is the universal gas constant, TK the absolute temperature, and P is pressure.

During power-law viscous flow with an exponent (n) greater than 1, there is a positive feedback between the effective viscosity and strain rate, such that any increase in strain rate leads to a decrease in effective viscosity, which further enhances the strain rate (Figure 2.3a) (Smith 1977, Emerman and Turcotte 1984, Schmalholz et al. 2008). This means that processes that locally enhance strain rate, such as deformation at an inherited weak heterogeneity, can start this positive feedback loop and lead to a necking instability localized at the heterogeneity.

In our layered lithosphere the growth rate of necking instabilities in each layer depends on the power law exponent for that layer. During viscous flow the power-law exponent for rocks is in the range 2-5 (Gleason and Tullis 1995, Karato 2010). In contrast, plastic/brittle deformation (where we mean mechanically plastic, not crystal plastic) is an end-member

power-law flow in which the power-law exponent n tends to infinity, or in a practical sense n >1000 (Fletcher and Hallet 1983). This means that the growth rate is a maximum for plastic layers (high n) and minimum for viscous layers (n ~2-5). In our models, and probably nature, this results in an initial distribution of plastic and viscous layers that evolves as the viscosity changes dynamically in response to strain softening and temperature (Figure 2.2, blue-red layers respectively). Rapid growth of necking instabilities for high n viscous layers, used to approximate plastic layers, has been demonstrated in a number of analytical perturbation studies (e.g. Fletcher and Hallet 1983, Zuber and Parmentier 1986, Martinod and Davy 1992).

2.5 Stiff and Pliable Stratification and Necking of the Lithosphere

As we are interested in the rate at which necking instabilities grow, we adopt the stiff/pliable terminology used by Chenin and Beaumont (2013). A material is stiff and necks rapidly where the power-law exponent is large (n > 1000-10,000), approximating brittle deformation (Nye 1953, Fletcher and Hallet 1983, Zuber and Parmentier 1986, Regenauer-Lieb and Yuen 2003). A material is pliable, and necks slowly, where the exponent is small ($n \approx$ 2-5), as noted above. The total amount of extension, and therefore time, needed to neck a stiff material completely is far less than the extension needed for a pliable material (Figure 2.2a) (Chenin and Beaumont 2013).

The stiff-pliable stratification of our reference laterally homogeneous lithosphere (Figure 2.2b, blue-red layers) depends on its compositional layering, the variation of temperature with depth, and the strain rate (Bassi 1991, 1995). If we assume a Moho temperature of 600˚C, a relatively strong crust, a peridotite mantle lithosphere controlled by the flow of wet olivine, and moderate strain rates (total rifting velocity of 1 cm a^{-1}), the stratification has a single surface stiff layer and the remaining lithosphere is pliable (Figure 2.2b left). In contrast, if the mantle lithosphere is somewhat stronger, the uppermost mantle becomes stiff (Figure 2.2b right). This difference produces a wide and slowly necking pliable region in the mantle lithosphere in the first case, but a much narrower, faster necking stiff region in the second case. We show the model results (Section 2.8) in a similar manner with blue and red indicating the stiff and pliable regions, respectively.

The distribution of stiff and pliable layers is more complicated in a lithosphere that contains a lateral boundary between two regions with differing properties. There must be an overall force balance between the two regions, which results in contrasting distributions of stress and strain rate with depth in the two sides. For example, where a lithosphere with a strong crust and strong mantle lithosphere is juxtaposed against a lithosphere with both a weak crust and weak mantle lithosphere, the strong crust and mantle can both remain pliable because the force in the weaker juxtaposed region is low.

2.6 Proposed Controls on Rifting

Based on the feedback loop that governs the growth rate of necking instabilities in the lithosphere, we propose two dominant controls on rift development and the eventual geometry of rifted margins: Control 1, the distribution of stiff and pliable layers within the lithosphere, and Control 2, the background strain rate in the lithosphere.

As explained above, Control 1 depends on the deformation mechanism, such that necking instabilities grow faster in stiff lithospheric layers than in pliable ones. This control was investigated by Chenin and Beaumont (2013). Control 2 is important where a contrast in properties across a lithospheric boundary influences the distribution of the background strain rate on either side of the boundary. We define the background strain rate as the strain rate that exists in the two lithospheric regions on either side of the boundary where there are no other inherited heterogeneities. Since necking is a mechanism that amplifies the background strain rate, everything else being equal the lithosphere will neck fastest where background strain rates are highest (Figure 2.3b). Where combined with Control 1, this means that necking in a pliable layer that has a high background strain rate may outcompete necking in a stiff layer on the other side of the lithospheric boundary where the background stain rate is less. Our goal is to determine the circumstances where either Control 1 or 2 wins.

2.7 Methods

We investigate three series of models in order to demonstrate Controls 1 and 2 and the competition between them. The first series is laterally uniform, like those used by Chenin and Beaumont (2013). The second and third series juxtapose lithospheres with different strengths

and respectively illustrate examples where either Control 1 or Control 2 wins. These models are classified according to their inherited weak zones (Figure 2.4a): Type 1, no weak zones; Type 2, a mantle weak zone (MWZ) at the lithospheric boundary; Type 3, two MWZ symmetrically offset from the lithospheric boundary, and; Type 4, two crustal weak zones (CWZ) symmetrically offset from the lithospheric boundary and a MWZ at the lithospheric boundary.

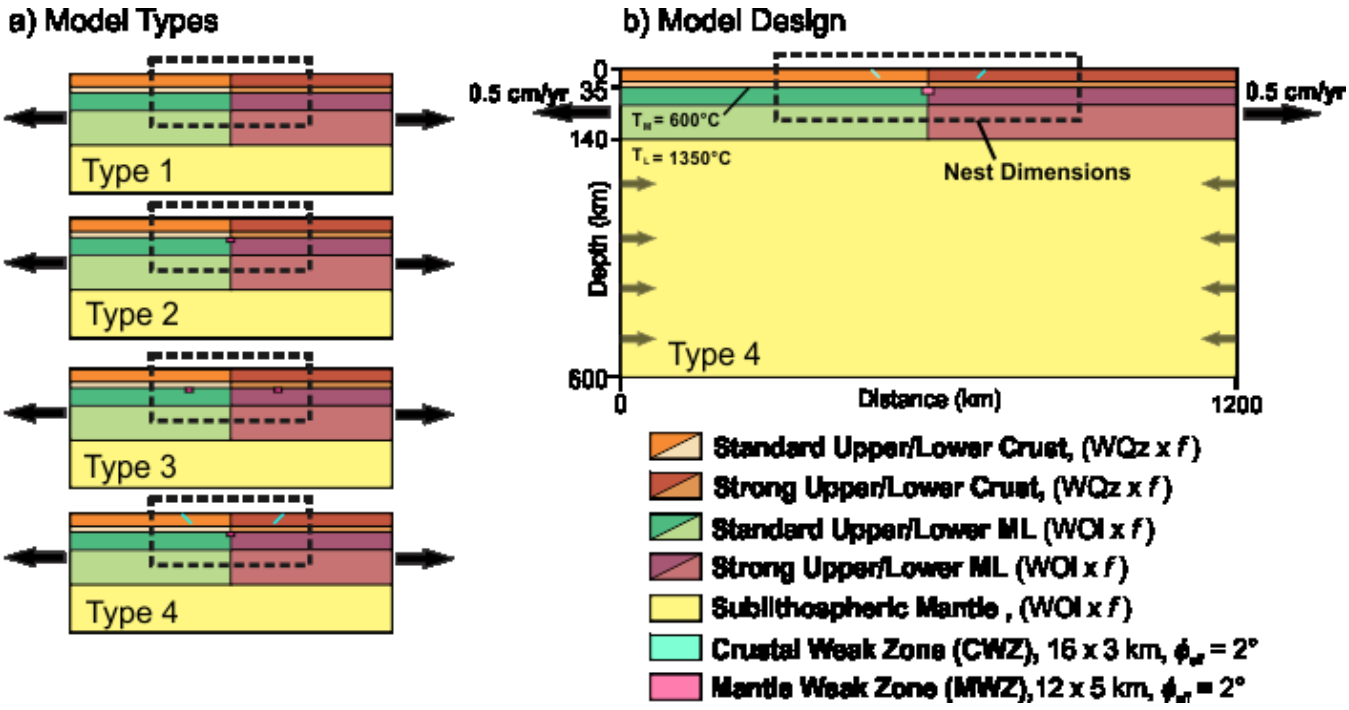

Figure 2.4. Model design and types. a) Type 1: no weak zones. Type 2, central mantle weak zone. Type 3, two symmetrically offset mantle weak zones. Type 4, two symmetrically offset crustal weak zones and a central mantle weak zone. b) Model design of Type 4 model. Other model types have the same temperature regime, large-scale geometry and boundary conditions. Only the placement and presence of weak zones changes among model types. Element dimensions change with depth: 0-50 km: 3km x 1 km (width x height); 50-360 km: 3 km x 2km; 360-600 km: 3 km x 8 km. For Type 3 models: 0-50 km: 3km x 1 km (width x height); 50-148 km: 3 km x 2km; 148-344 km: 3 km x 4 km; 344-600 km: 3 x 8 km. The small-scale nested models (dashed region) have a resolution 4 times higher in the horizontal and 3 times higher in the vertical and extend to 100 km depth.

2.7.1 SOPALE-nested

Calculations are made using SOPALE-nested (Fullsack 1995, Beaumont et al. 2009), an Arbitrary-Lagrangian-Eulerian (ALE) finite element software, which can accommodate large amounts of deformation. The code solves thermo-mechanically coupled, incompressible viscous-plastic creeping (Stokes) flow equations and has thermally activated power-law viscous

rheologies. The force balance equations for quasi-static incompressible creeping flow are solved in two dimensions for each time step (Equations 2.1 and 2.2) and are coupled to the energy balance equation (2.3) through the temperature-dependent viscosity and density.

$$\frac{\partial \sigma_{ij}}{\partial x_i} - \frac{\partial P}{\partial x_i} + \rho g = 0 \qquad i,j = 1,2 \tag{2.1}$$

$$\frac{\partial v_i}{\partial x_i} = 0 \qquad i = 1,2 \tag{2.2}$$

$$\rho C_p \left(\frac{\partial T_K}{\partial t} + \frac{\partial T_K}{\partial x_i}\right) = K(T_K)\frac{\partial^2 T_K}{\partial x_i^2} + A_R + v_2\, \alpha\, g T_K \rho \quad i = 1,2 \tag{2.3}$$

where σ_{ij} is the deviatoric stress tensor, x_i are the spatial coordinates, P is the dynamical pressure, ρ the density, g the gravitational acceleration, v_i are the components of velocity, C_p the specific heat, T_K the absolute temperature, t the time, K the thermal conductivity, A_R radioactive heat production per unit volume, and α the volumetric thermal expansivity.

The deformation mechanism is subject to the state of stress in the flow; flow will be viscous (Equation 2.4) where stress is lower than the frictional-plastic yield stress described by equation (2.5). Where stress is on the frictional-plastic yield envelope described by the pressure-dependent Drucker-Prager yield criterion (Equation 2.5), deformation is frictional-plastic and the material behaves in a stiff manner.

$$\eta = f\, A^{-1/n} (\dot{\mathrm{I}}_2')^{\frac{1-n}{2n}} \exp\left(\frac{Q + PV^*}{nRT_K}\right) \tag{2.4}$$

$$J_2' = P \sin\phi_{\text{eff}} + C \cos\phi_{\text{eff}} \tag{2.5}$$

In power-law flow (Equation 2.4), A is the pre-exponential scaling factor, $\dot{\mathrm{I}}_2' = \left(\frac{1}{2}\dot{\epsilon}_{ij}'\dot{\epsilon}_{ij}'\right)$ is the second invariant of the deviatoric strain tensor, n is the power law exponent, Q is the activation energy, V^* is the activation volume, *R* is the universal gas constant, $\dot{\epsilon}_{ij}'$ is the strain rate tensor, and *f* is the scaling factor, explained below, used to modify the relative strength of viscous materials with respect to the reference flow law. In equation (2.5), $J_2' = \left(\frac{1}{2}\sigma_{ij}'\sigma_{ij}'\right)^{1/2}$ is the square root of the second invariant of the deviatoric stress, C is the cohesion, ϕ_{eff} is the effective internal angle of friction taking account of hydrostatic fluid pressure (using

$P sin\,\phi_{\text{eff}} = (P - P_f) sin\,\phi$ where P_f is the pore-fluid pressure), which gives $\phi_{\text{eff}} \sim 15^\circ$ where $\phi = 30°$, and σ'_{ij} is the deviatoric stress tensor. Parameter values are given in Table 2.1.

The method adopted for the calculations requires explanation. In Section 2.5 we described stiff and pliable deformation in terms of respectively high and low power-law exponent flows. This is the same approach used in analytical perturbation methods, where plasticity is explicitly included as high n power-law flow (Equation 2.4) (e.g. Fletcher and Hallet 1983, Martinod and Davy 1992). However, for our numerical calculations we adopt an equivalent approach in which plastic yield is pressure-sensitive (Equation 2.5) and plastic flow is calculated by the Levy-Mises pseudo-viscous formulation in which the effective viscosity is iteratively rescaled to place the stress on yield (Malvern 1969, Willett 1992). This has exactly the same effect of rapidly reducing the effective pseudo-viscosity as in high-n power-law exponent flow.

2.7.2 Model Design

All models are 1200 km wide and extend to a depth of 600 km from the surface (Figure 2.4b). The large-scale domain is 1200 km x 600 km (400 x 140 elements) and contains a small-scale domain (nested model) with a higher grid resolution. The nest encompasses an area from 300–900 km horizontally and 0-100 km vertically (800 x 225 elements). The large-scale model has basal boundaries with free slip in the horizontal and vertical directions. Extension of the lithosphere is defined by horizontal velocities of 0.5 cm a^{-1} on the right and left horizontal boundaries (total 1 cm a^{-1}). A small horizontal flux of materials into the sub-lithospheric mantle allows for conservation of mass; there is no material flux through the base.

A MWZ of 12 x 5 km is embedded in the upper mantle lithosphere in most models. It has a reduced internal angle of friction of 2˚ to represent inherited strain softening. Offset CWZ of 3 x 16 km are included in the crust of the Type 4 models to represent shear zones or sutures. The CWZ are 150 km away from the MWZ and dip towards it at 45˚; previous studies suggest rift geometries are relatively insensitive to the dip of the CWZ (Chenin and Beaumont 2013). We choose these small weak zones on the basis that they are residual and restricted to cold lithosphere.

Property	Symbol	Value
Frictional-plastic parameters		
Internal angle of friction (˚)	ϕ_{eff}	15 → 2
Over strain rate range (%)		50 → 150
Crust cohesion (Pa)	C_{Crust}	$1 \cdot 10^{7}$
Mantle cohesion (Pa)	C_{Mantle}	$2 \cdot 10^{6}$
Crust: Wet Quartzite	WQz	
Power law exponent	n_{Crust}	4
Activation energy (J mol^{-1})	Q	$223 \cdot 10^{3}$
Initial constant (tensor invariant) ($Pa^{-n}s^{-1}$)	A	$8.574 \cdot 10^{-28}$
Scaling factor	f_{Crust}	variable
Crustal density (kg m^{-3})	ρ_S	2800
Mantle: Wet Olivine	WOl	
Power law exponent	$n_{ML} = n_{SML}$	3
Activation energy (J mol^{-1})	Q	$430 \cdot 10^{3}$
Activation Volume (m^3 mol^{-1})	V^*	$12 \cdot 10^{-6}$
Initial constant (tensor invariant) ($Pa^{-n}s^{-1}$)	A	$1.7578 \cdot 10^{-14}$
Mantle lithosphere density (kg m^{-3})	ρ_{UML1}	3350
Sub-lithospheric mantle density (kg m^{-3})	ρ_{SLM}	3370
Standard Moho temperature (˚C)	T_{Moho}	600
Base of lithosphere temperature (˚C)	T_L	1350
Basal heat flux (mW m^{-2})	q	22
Surface heat flux (mW m^{-2})	q_s	63.5
Radiogenic Heat Production	A_R	
Upper crust (µW m^{-3})	$A_{R_{UCS}}$	1.5
Lower crust (µW m^{-3})	$A_{R_{LCS}}$	0.5
Coefficient of thermal expansion (˚C^{-1})	$\alpha(T)$	$3.2 \cdot 10^{-5}$ → $3.9 \cdot 10^{-5}$
Over temperature range (˚C)		500-2000
Crust thermal conductivity (W m^{-1}˚C^{-1})	K_{Crust}	2.25
Mantle lithosphere thermal conductivity (W m^{-1}˚C^{-1})	$K_{MLS}(T)$	5 → 3
Over temperature range (˚C)		0-777
Sub-lithospheric mantle thermal conductivity (W m^{-1}˚C^{-1})	$K_{SLM}(T)$	3-40
Over temperature range (˚C)		1323-1423

Table 2.1. Model parameters

Elsewhere, annealing in the hotter viscous parts of the lithosphere (Yamasaki et al. 2006), where grain regrowth is efficient, will have removed strength contrasts associated with grain size reduction in lithospheric-scale sutures, although some form of heterogeneity (e.g compositional) may remain (Vauchez et al. 2012).

2.7.3 Mechanical Material Properties

Materials are defined by one laboratory-determined flow-law chosen for each representative lithology. We use "Wet" Quartzite (WQz) (Gleason and Tullis 1995) for the crust and "Wet" Olivine (WOl) (Karato and Wu 1993) for the mantle lithosphere and sub-lithospheric mantle. These are scaled with a scaling factor *f* to increase/decrease the relative strength (Beaumont et al. 2006, Butler et al. 2014, Appendix). This simplification allows for a relative comparison between materials of different strengths without having to incorporate other flow laws (Beaumont et al. 2006, Jamieson et al. 2007, Karato 2010). The scaling approach is also valid for a considerable range of *f* values, even for the reference flow laws, owing to the significant experimental uncertainties associated with the laboratory-determined flow-law parameters (Beaumont et al. 2006, Jamieson et al. 2007, Karato 2010, Butler et al. 2014; Appendix). The use of variations in *f* among models to achieve different combinations of stiff and pliable layers is described below (Section 2.8).

Strain-softening is included in the brittle regime to represent the formation of weak faults. The effective internal angle of friction is decreased linearly from 15˚ to 2˚ as the effective strain increases from 50% to 150%. The models are not particularly sensitive to the range of strain over which materials undergo strain softening (Huismans and Beaumont 2007). The low strain-softened angle of internal of friction is partly a result of the resolution of the finite element grid, such that with higher resolution a larger value would give equivalent results.

2.7.4 Thermal Properties

The initial steady-state temperature of the system is determined by the constant basal heat flux (q = 22 mW m^{-2}), the radiogenic heat production in the crust (A_r), and the thermal conductivity (K). The surface heat flow is q_s = 63.5 mW m^{-2} for radiogenic heat production in the upper crust of 1.5 µW m^{-3} and 0.5 µW m^{-3} in the lower crust (Hasterok and Chapman 2011). The

temperature at the base of the lithosphere is 1350˚C, and the Moho temperature is 600˚C. The thermal conductivity is scaled up in the sub-lithospheric mantle so that heat transport is equal to that of low Rayleigh number convection and the temperature gradient is adiabatic.

2.8 Model Results

As noted above, we describe selected model results from three series. The first models are laterally uniform, like those used by Chenin and Beaumont (2013). The second series shows an example where Control 1 dominates, and the third correspondingly shows where Control 2 wins. Both the second and third series juxtapose lithospheres of varying strengths. The models are classified as Type 1- 4 according to their inherited weak zones (Figure 2.4a).

There are a large number of factors that will influence the behavior of the models and we have specifically chosen to keep them as simple as possible while demonstrating the two controls. All models have an initial laterally homogeneous temperature regime which allows us to focus on the role of material properties, specifically the rheology, and not temperature *per se,* on the model results. We choose to use only the Wet Quartzite (Gleason and Tullis 1995) and Wet Olivine (Karato and Wu 1993) flow laws, and change layers from stiff to pliable, and the converse, by selecting different scaling factors, f (Equation 2.4). This approach is equivalent to choosing a stronger/weaker rheology for layers of the lithosphere (Figure 2.2b; Butler et al. 2014, Appendix). Specifically, choosing a small f will ensure stress in a layer is below yield and, therefore, flow is pliable with a small-n power-law exponent (Equation 2.4). Conversely, large f values will increase the flow stress to the Drucker-Prager yield (Equation 2.5), and the layer will be stiff with pseudo-viscous flow, equivalent to a very large n power-law exponent. For example, where both the upper and lower crust have a scaling factor f = 1 and the WQz flow law, the upper crust will be stiff and the lower crust will be pliable because of the temperature increase with depth. In contrast, a WQz flow law with scaling factor f = 10, for example, approximates a mixed quartz-feldspar controlled crust, or 'dry' quartz. The scaling factor can also represent dehydration in the mantle; WOl x 5 corresponds to low water content (<0.001 wt% H_2O) and is significantly stronger than water-saturated peridotite with WOl x 1.

We use the following notation 10-1 | 10-3 to describe *f*-scaling factors in our models. The 10-1 signifies the left lithosphere, with a crust of WQz x 10 and a mantle lithosphere of WOl x 1. The 10-3 denotes the right lithosphere with a crust of WQz x 10 and a mantle lithosphere of WOl x 3. We combine this notation with the consequences of the *f*-scaling for the stiff (S) and pliable (P) layering of the upper and lower crust, and the upper and lower mantle lithosphere, SP-PP | SP-SP, to give 10SP-1PP | 10SP-3SP. This example completely describes the same *f*-scaling model and its S-P layering in which the lithosphere to the left of the lithospheric boundary has a stiff upper crust and a pliable lower crust, upper and lower mantle lithosphere, whereas the lithosphere to the right of the boundary consists of a stiff upper crust, a stiff upper mantle lithosphere and a pliable lower crust and mantle lithosphere.

2.8.1 Model Results: Laterally Uniform Models

The models in this series have a similar geometry to those described by Chenin and Beaumont (2013). They are used to investigate the growth of necking instabilities at inherited embedded crustal weaknesses and a central mantle weak zone with a Type 4 geometry (Figure 2.4a), but in an otherwise laterally homogeneous layered lithosphere. In general, the results of Chenin and Beaumont (2013) showed that weak zones in a stiff layer preferentially localize deformation, whereas localization is absent or delayed in pliable layers. We illustrate this result by contrasting a Type 4 model where the Central Mantle Weak Zone (C-MWZ) is located in a stiff upper mantle lithosphere with a model where the C-MWZ is located in a pliable upper mantle lithosphere (Figure 2.5).

Where the C-MWZ is embedded in a stiff upper mantle lithosphere (Model 1.1 10SP-3SP | 10SP-3SP) strain localizes at the C-MWZ at 13 Ma (Figure 2.5c). Although there is some initial deformation at the CWZ's (Figure 2.5c), necking localizes more rapidly at the C-MWZ in the stiff upper mantle lithosphere and the CWZ's are abandoned (Figure 2.5d, e).

In contrast, where the C-MWZ is located in a pliable mantle lithosphere (Figure 2.5g) (Model 1.2 10SP-1PP | 10SP-1PP) the CWZs are fully activated after 13 Ma. The C-MWZ is essentially ignored and rifting localizes at one of the CWZ's (Figure 2.5i, j). Note, these models only differ in the *f*-scaling of the mantle lithosphere where $f = 1$ gives a P layer and $f = 3$ gives an S-layer.

These results illustrate the same behavior as seen in Chenin and Beaumont (2013). For laterally homogeneous models there is no spatial variation in background strain rate; therefore, Control 2 operates equally everywhere, leaving Control 1 as the winner.

2.8.2 Model Results: Control 1 Wins

In the laterally heterogeneous models, Control 1 wins where localization develops in a stiff layer on the side of the model that has the lower background strain rate. We have investigated a large range of models and find that this only occurs where there is a small difference in the background strain rates between the two sides. This indicates that for Control 1 to win special circumstances are required. Model 2.1 (10SP-1.3PP | 3.5SP-2SP; Figure 2.6a-f) is an example where Control 1 wins. It is a Type 3 model (Figure 2.4a); the MWZ's are symmetrical around the lithospheric boundary, with the left and right one respectively embedded in pliable and stiff upper mantle lithospheres. The background strain rates in the upper mantle are similar on both sides, but slightly higher (by $< 1.0 \times 10^{-16}$ s^{-1}) on the left side of the boundary. The necking instability at the right mantle weak zone (R-MWZ) in the stiff layer initializes and outcompetes the slower necking instability at the left mantle weak zone (L-MWZ) by 16.0 Ma (Figure 2.6), even though the background strain rate is larger in the left. Rifting finally occurs on the right side at 24 Ma (Figure 2.6f).

A small change in rheology flips the dominant control to Control 2. In Model 2.2 (10SP-1.3PP | 3.5SP-2.5SP; Figure 2.6g-l) the right mantle lithosphere is stronger than in Model 2.1, WOl x 2.5 instead of WOl x 2. This reduces the background strain rate in the right mantle lithosphere, thereby making the strain rate contrast higher than 1×10^{-16} s^{-1}, and localization develops at the L-MWZ (Figure 2.6g-l). The R-MWZ localizes a small amount of deformation, but by 13.0 Ma (Figure 2.6j) it is clear that the L-MWZ is localizing deformation more efficiently and that this will result in rifting in the left lithosphere (Figure 2.6).

These two examples illustrate that Control 1 can win for very specific conditions, where the background strain rates are nearly equal. However, wherever a significant strain-rate contrast is present Control 2 will take over, and rifting will take place in the pliable lithosphere under a higher strain rate. Further examples of this are presented in the next section.

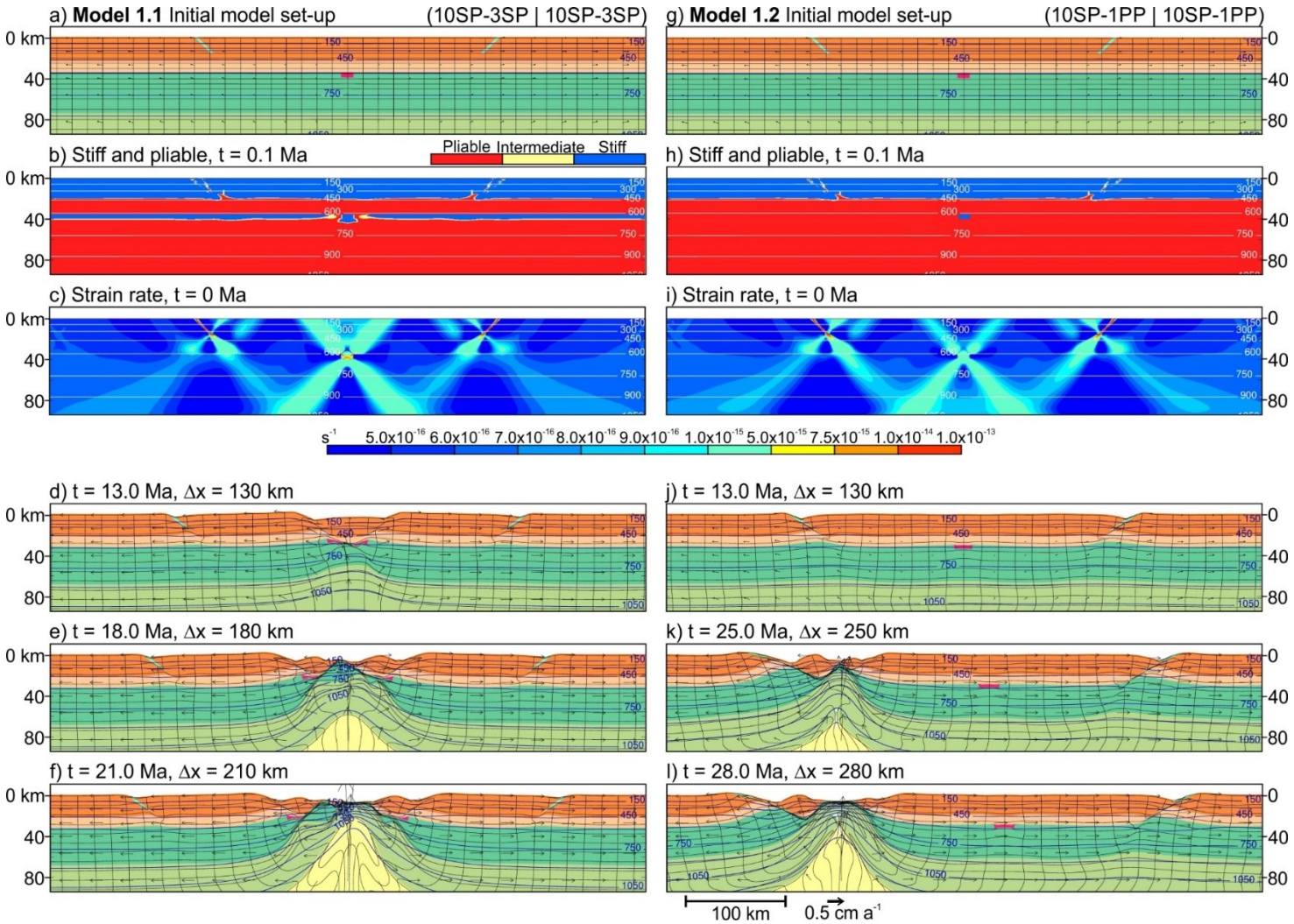

Figure 2.5. Models 1.1 and 1.2: Localization at the site of embedded weak zones (light blue and pink) in a laterally homogeneous lithosphere. a) intial model design for Model 1.1, a MWZ is located in a stiff upper mantle lithosphere. b) the total stress relative to the yield stress is plotted. Pliable materials (red) are at a shear stress <80% of the yield stress, whereas materials are that are considered stiff (blue) are at >95% of the yield stress and are mostly at yield. d-f) The C-MWZ is the site of localization and final breakup takes place at its location. g-l) C-MWZ located in a pliable upper mantle lithosphere. The C-MWZ is ignored in favor of the L-CWZ, which is the final locus of breakup. Isotherms (in °C) are shown in blue in the deformation plots and white in the stiff and pliable and strain rate plot. A representation of the Lagrangian grid can be seen in black.

2.8.3 Model Results: Control 2 Wins

The models presented below illustrate that deformation preferentially localizes in areas with higher background strain rates (Control 2). First, we describe Type 1 and Type 2 models which localize away from the lateral boundary, even where there is a C-MWZ in the case of the Type 2 model. Second, a Type 3 model is presented that illustrates that Control 2 dominates over Control 1. Third, a Type 4 model, like Model 1.1 but with a lateral boundary, is presented. Lastly, we present a Type 2 model where localization takes place at the C-MWZ at the boundary, but the effects of Control 2 determine how the asymmetry evolves.

2.8.3.1 Type 1 Model: No Weak Zones, and Type 2 Model: One Central Mantle Weak Zone

Model 3.1 (Figure 2.7) is a Type 1 model with no weak zones whatsoever. Its characteristics, (10SP-1PP | 10SP-3SP), result in a strong upper crust and stiff upper mantle on the right side (Figure 2.7b). Although Control 1 would predict localization in the stiff right lithosphere, it instead develops in the left lithosphere (Figure 2.7d) at 20 Ma. Control 2 wins because the background strain rate is at least one order of magnitude higher in the left lithosphere (Figure 2.7c). Before localization, the weaker left lithosphere undergoes pure shear extension and thins, whereas the stronger right lithosphere translates like a nearly rigid block and does not thin significantly. After a symmetrical plug forms, the stiff upper crust necks rapidly and breakup occurs at 29 Ma and 290 km of extension (Figure 2.7d-f).

The Type 2 model (Figure 2.7), Model 3.2 (5SP- 1PP | 10SP-3PP) behaves in the same way as Model 3.1, even though it has a C-MWZ at the lithospheric boundary. As in Model 1.2, the C-MWZ is located in a pliable upper mantle lithosphere (Figure 2.7h) and is similarly ignored. Instead, Control 2 wins owing to the much higher strain rate in the left lithosphere (Figure 2.7i), similar to Model 3.1. Localization at 20 Ma is followed by breakup at 29 Ma producing a similar rift to the Type 1 model, Model 3.1 (Figure 2.7). These models show that where there are no weak zones, or the C-MWZ is in a pliable layer, Control 2 wins and rifting takes place in the weaker lithosphere with the higher strain rate.

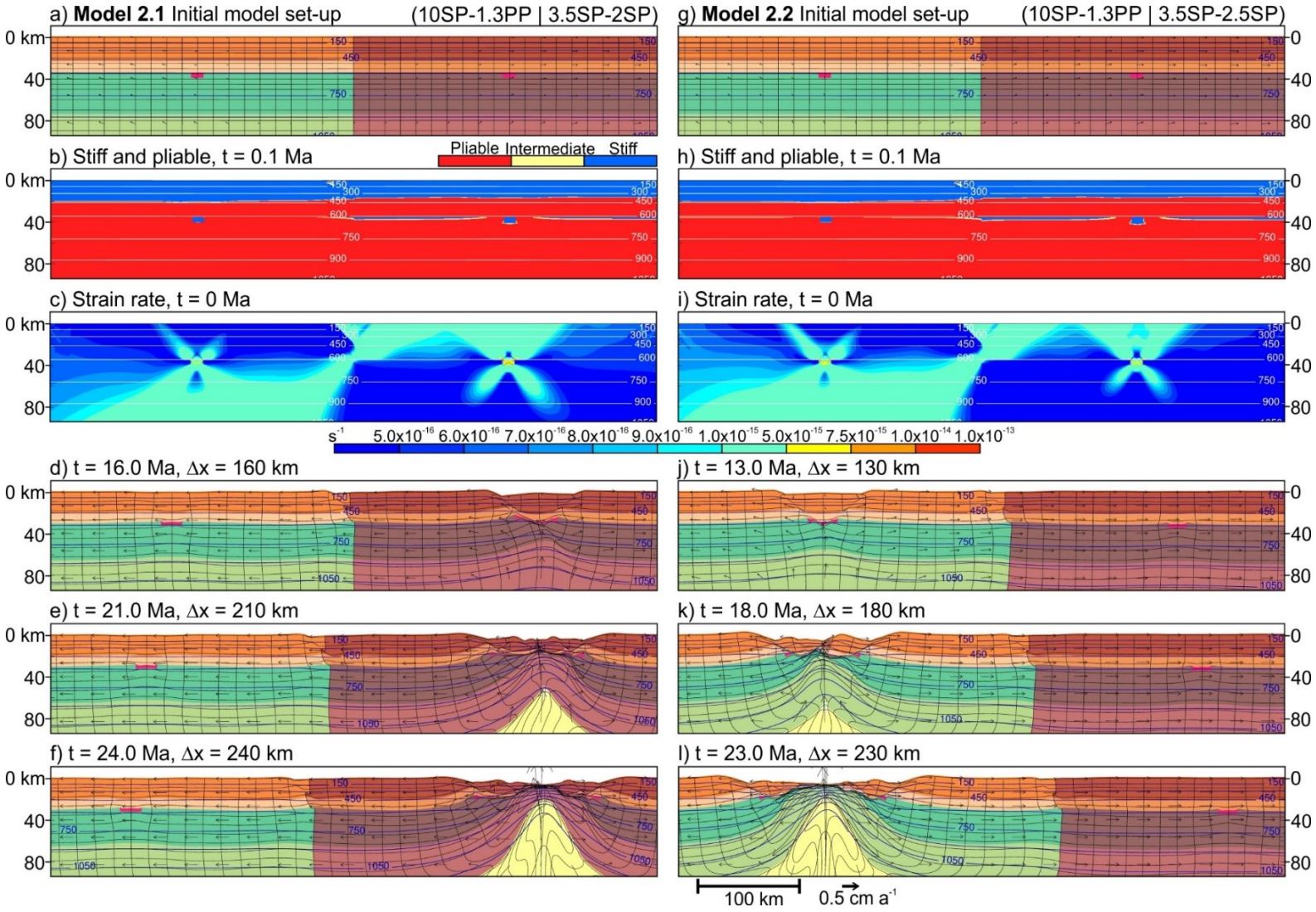

Figure 2.6. Model 2.1 (10SP-1.3PP | 3.5SP-2SP) and Model 2.2 (10SP-1.3PP | 3.5SP-2.5SP). Both models are Type 3 with the R-MWZ in a stiff layer and the L-MWZ (both pink) under a higher strain rate. a-f) Where the background strain rate contrast in the upper mantle lithosphere is less than 1.0 x 10^{-16} s^{-1} Control 1 wins and the right lithosphere rifts. g-l) A slight increase in strength in the right lithosphere results in a larger background strain rate contrast and Control 2 wins, rifting the left lithosphere.

2.8.3.2 Type 3 Model: Two Mantle Weak Zones

Model 3.3 (10SP-1PP | 10SP-3SP; Figure 2.8) is a Type 3 model (Figure 2.4). It contrasts the effects of Controls 1 and 2. The R-MWZ is located in a thin stiff layer in the upper mantle lithosphere (Figure 2.8b), which could localize rapid necking under Control 1. On the other hand, the L-MWZ is located in pliable upper mantle lithosphere that has a higher strain rate (Figure 2.8c), implying that if Control 2 is dominant it should localize deformation, similar to Model 2.2.

Control 2 is clearly dominant as a symmetric plug localizes around the L-MWZ at 10 Ma (Figure 2.8d). The stiff crust and pliable upper mantle lithosphere neck rapidly, allowing the lower mantle lithosphere to be exhumed by 20 Ma (Figure 2.8f). The R-MWZ remains undeformed throughout the rifting process, even though it is in a stiff layer. This result differs slightly from Model 2.2 where the R-MWZ localized some deformation.

2.8.3.3 Type 4 Model: Crustal Weak Zones and a Mantle Weak Zone in a Stiff Layer

Type 4 models (Figure 2.4a) are equivalent to those presented by Chenin and Beaumont (2013) except they include a lateral boundary (Figure 2.9). Model 3.4 (5SP-3SP | 10SP-5SP) has continuous stiff layers in both mantle and crust (Figure 2.9b). These characteristics are very similar to Model 1.1 (Figure 2.5b), which clearly demonstrated the role of Control 1 at the C-MWZ in the mantle stiff layer. However, in Model 3.4 the background strain rate is much higher in the left lithosphere (Figure 2.9c) which from the outset fosters more rapid localization at the L-CWZ than at the C-MWZ (Figure 2.7c). This allows Control 2 to win by rifting at the L-CWZ (Figure 2.9d-f) with final breakup at 20 Ma. Some deformation has localized in the left side of the C-MWZ, but its right side and the R-CWZ remain essentially undeformed in the translated but near-rigid right lithosphere.

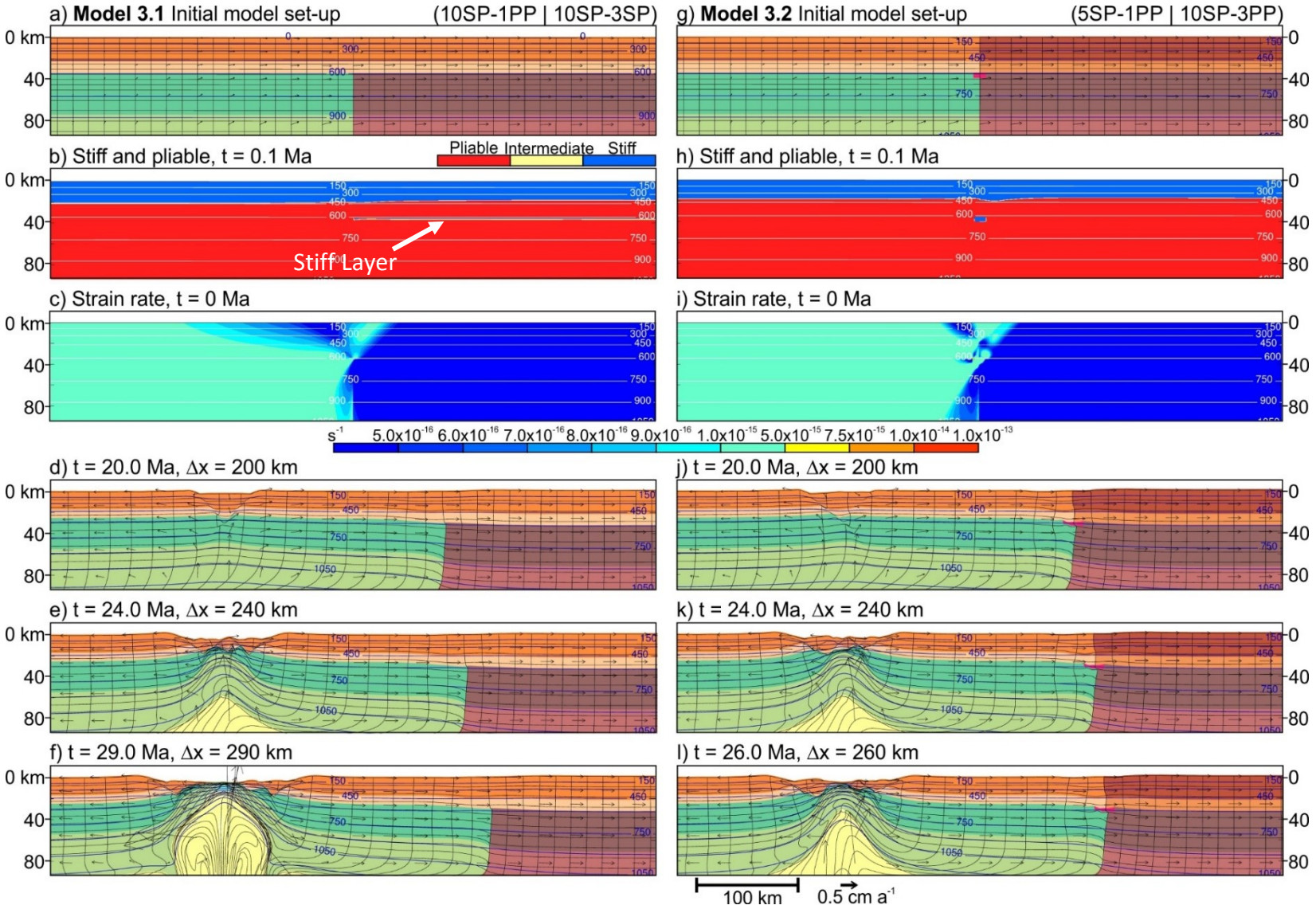

Figure 2.7. Models 3.1 and 3.2. Rifting away from the lithospheric boundary. a-f) Type 1 model without any weak zones with scaling factors of 10-1 | 10-3. Localization in the left lithosphere under a higher strain rate. g-l) Type 2 model with a C-MWZ in a pliable upper mantle lithosphere with scaling factors of 5-1 | 10-3. Although a C-MWZ is present, localization occurs away from the lithospheric boundary

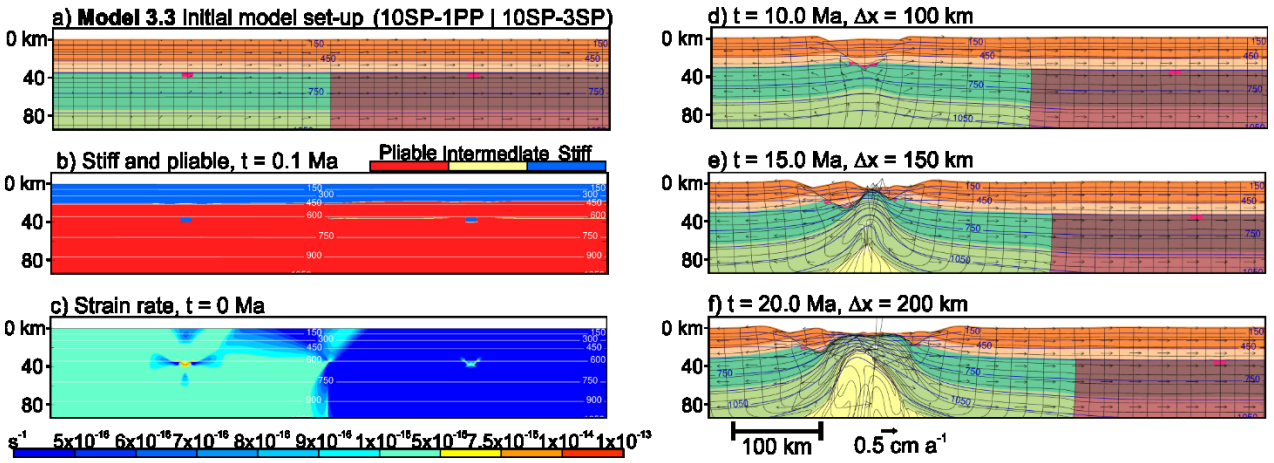

Figure 2.8. Model 3.3. Localization at weak zones in the lithosphere with a higher strain rate. a-f) Type 3 model with 2 MWZ. R-MWZ is located in a thin stiff layer, L-MWZ is under a higher strain rate. Rifting takes place at the L-MWZ and leaves the R-MWZ undeformed. This Model is similar to Model 2.2, although the strain rate contrast is significantly larger in Model 3.3, because of a larger strength contrast.

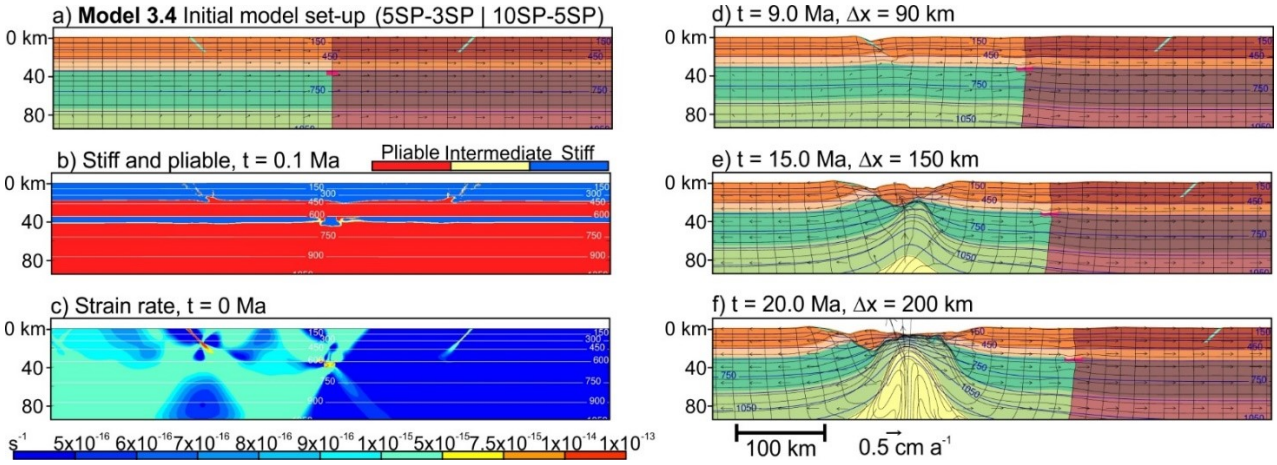

Figure 2.9. Model 3.4. Type 4 model (5SP-3SP | 10SP-5SP) with identical weak zones to the homogeneous models (Model 1.1 and Model 1.2). The C-MWZ is located in a stiff layer. At 9 Ma a basin has formed at the L-CWZ located in a higher strain rate area. The C-MWZ is undergoing small amount of necking, but the necking instability at the L-CWZ grows more efficiently and is the location of breakup.

2.8.3.4 Type 2 Model: Localization at the Lithospheric Boundary

Where a C-MWZ is located at the lithospheric boundary in a stiff layer, and it is the only weak zone in the model, deformation localizes there and a rift forms right on the boundary between the contrasting lithospheres (Figure 2.10). Model 3.5 (3SP-3SP | 10SP-3SP) has continuous crustal and mantle stiff layers (Figure 2.10b) and illustrates this case in which the rift localizes at the C-MWZ under Control 1, as in Model 1.1 (Figure 2.5a). However, Control 2

actually wins. The left half of the C-MWZ is located in lithosphere with the higher background strain rate (Figure 2.10c). The deformation localizes in this left side of the C-MWZ and the right side is ignored owing to the contrast in the background strain rate. A significant shear zone develops by 10 Ma that intersects the left side of the C-MWZ (Figure 2.10d). The final rift at 19 Ma is highly asymmetric with a ~ 80 km narrow right margin and ~120 km wider left margin. Model 3.5 nicely illustrates the competition between Controls 1 and 2. In this case, however, they cooperate such that Control 1 determines localization in the stiff layer at the C-MWZ, but Control 2 takes over and controls the asymmetric rifting. As a result, the final geometry is quite different from Model 1.1.

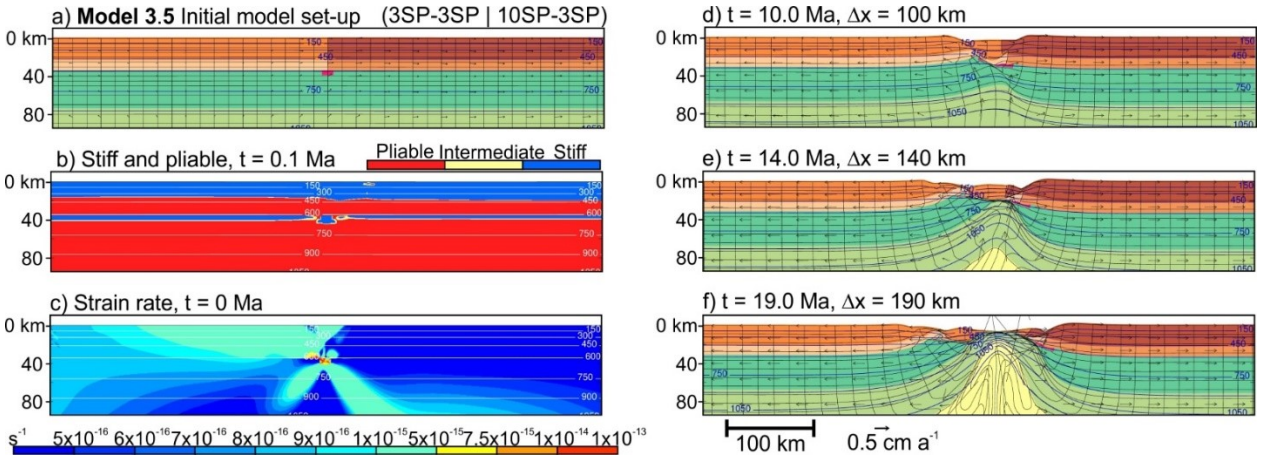

Figure 2.10. Model 3.5. Localization at the boundary where a C-MWZ is present. b) The C-MWZ is located in a stiff upper mantle lithosphere. c) The strain rate is higher left of the boundary. d) Deformation after 10 Ma. A discrete crustal-scale shear has developed at the C-MWZ. e) The stiff crust necks rapidly after localization and significant upper mantle lithosphere and asthenospheric mantle is upwelling. f) Breakup occurs after 19 Ma. The final rift has exhumed upper mantle lithosphere on both rifted margins. All deformation is located in the weaker lithosphere, which was under a higher strain rate. The right side of the C-MWZ has remained undeformed.

2.9 Discussion

The results presented above illustrate the two proposed dominant controls on rifting: Control 1, the distribution of stiff and pliable layers in the lithosphere, and Control 2, the background strain rate within the lithosphere. These controls determine where deformation localizes in the presence of heterogeneities such as finite weak zones and/or contrasting lithospheric properties. We first discuss how Control 1 and 2 compete in the different models,

and then place them in the context of a summary diagram (Figure 2.11). We then compare the location of localization in our models with previous analogue and numerical models.

2.9.1 Control 1 vs. Control 2

Control 1 is the only relevant control in a laterally homogeneous lithosphere because the background strain rate distribution is laterally uniform. In this case, weak zones embedded in stiff layers win, and the system evolves under Control 1 (Chenin and Beaumont 2013). As shown by Model 1.1 (Section 2.8.1), stiff mantle lithosphere necks rapidly where a weak zone is embedded within it, resulting in a narrow rift with only minor offset rift basins (Figure 2.5a-f) (e.g. Baikal Rift; Delvaux et al. 1995). In contrast, a pliable mantle lithosphere, Model 1.2, delays rifting, giving the shear zones localized at the CWZ's more time to create deep offset basins and, in this case, to become the primary rift (Figure 2.5g-l).

Where a lithospheric boundary and related compositional contrasts are introduced, the background stain rate becomes different in the two sides. The consequences are best illustrated by Type 3 models containing a MWZ on each side of the boundary, and with contrasting stiff and pliable upper mantle lithospheres. Model 2.1 (Figure 2.6) shows that Control 1 can win and localize deformation at the MWZ in the stiff upper mantle lithosphere where the strain rate contrast between the two sides is small. Where there is only a small change, however, for example, WOl x 2 to WOl x 2.5 (Model 2.2) and the strain rate contrast is increased, Control 2 wins, and rifting occurs at MWZ in the upper mantle lithosphere under a higher strain rate (Figure 2.6).

The background strain rate contrast between the right and left upper mantle lithospheres in Model 2.1 is small, less than $1x10^{-16}$ s^{-1}, which allows enough time for the necking instability at the MWZ in the stiff upper mantle lithosphere to grow and eventually outpace the necking instability at the MWZ in the pliable lithosphere, even though the background strain rate in the stiff upper-mantle lithosphere is less. This is a modified "hare and tortoise" competition in which the hare, the necking instability at the R-MWZ in a stiff layer, cannot be much slower at the start of extension than the tortoise if it is to win. The amount of deformation at the R-MWZ's in Model 2.2 (Figure 2.6g-l) and Model 3.3 (Figure 2.8), which are

both Type 3 models, illustrates this. The lower strain rate contrast in Model 2.2 allows for the hare (R-MWZ in stiff layer) to keep up with the tortoise (L-MWZ under higher strain rate) longer, localizing a small amount of deformation, but in Model 3.5 the larger strain rate contrast outcompetes the hare from the start and the R-MWZ remains completely undeformed.

Although we have not investigated the sensitivity of these results to the size and strength of the MWZ's, we suspect that Control 1 may win for larger strain rate contrasts where the MWZ's are smaller. The reasoning is that the necking instabilities at both MWZ's must develop from a smaller initial state, giving the hare (necking of a weak zone in a stiff layer) a better chance to speed up and overtake the tortoise (necking of a weak zone in a pliable layer under higher strain rate).

The summary diagram (Figure 2.11) shows model outcomes in relation to model properties and the background strain rate contrast, that is the difference in the background stain rates between the two sides. For example, where a Type 3 model with two MWZ's is under a low a strain rate contrast, $< 1 \times 10^{-16}$ s^{-1} (bottom right corner), Control 1 dominates and the necking instability grows fastest at the MWZ in a stiff layer (Model 2.1). As the strain rate contrast is increased, Control 2 wins and the necking instability at the MWZ in the pliable upper mantle lithosphere grows faster (Model 2.2).

Similarly, in the second column (Figure 2.11), Control 2 changes the location of localization between Model 1.1 and Model 3.4, which have a similar model design (Figure 2.5b and Figure 2.9b). The C-MWZ is located in a stiff upper mantle lithosphere in both models, and under Control 1 localizes deformation where the strain rate contrast is zero. On the other hand, the C-MWZ in Model 3.4 is ignored in favor of the necking instability at the L-CWZ located in the lithosphere with the higher strain rate and Control 2 wins, even though the C-MWZ is located in a stiff upper mantle lithosphere.

The results of all models in the third series, Models 3.1- 3.5, suggest that the strain-rate feedback grows a necking instability more efficiently than the stiffness of a layer wherever a significant strain-rate contrast is present, thereby changing the location of deformation from the stiff lithosphere to the lithosphere under the higher strain rate.

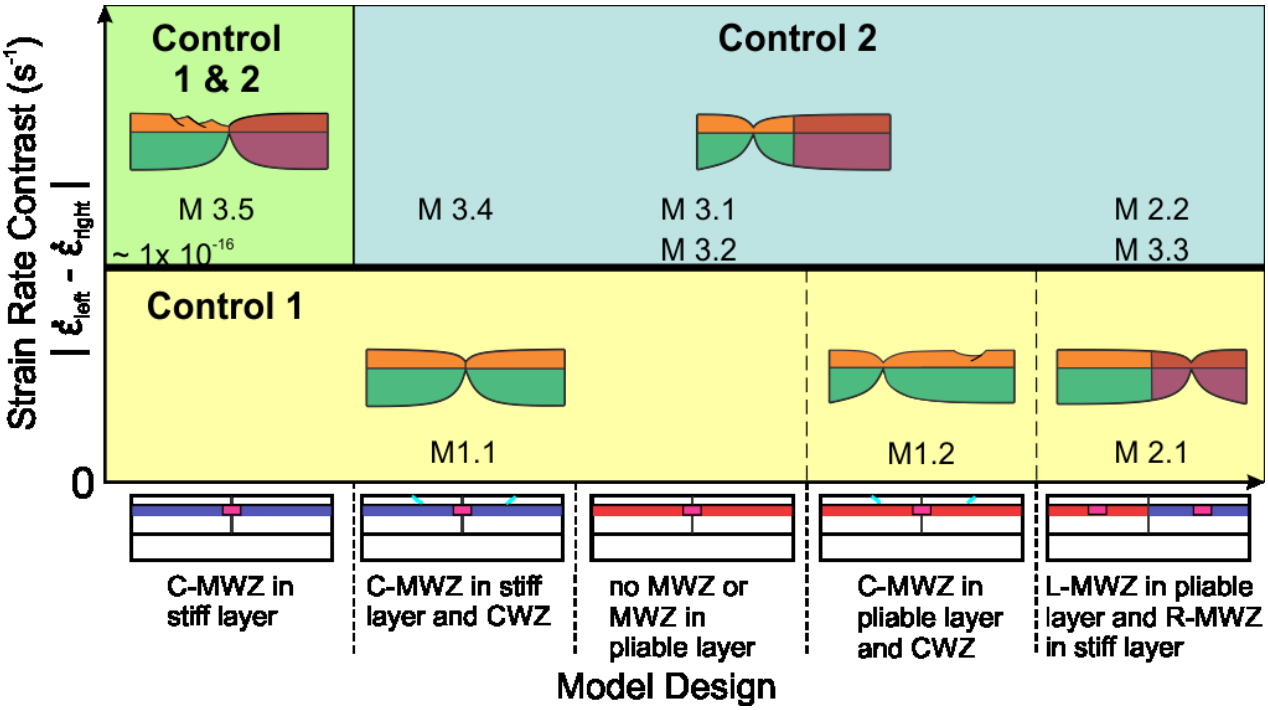

Figure 2.11. Summary of all results presented in the paper. The outcome of models with different weak zone configurations, in combination with stiff and pliable layering, changes depending on the strain rate contrast. For example, the second column represents a Type 4 model with 2 CWZ's and a C-MWZ in a stiff upper mantle lithosphere. where the strain rate contrast is < 1.0 x 10^{-16} s^{-1} control 1 dominates and rifting takes place at the C-MWZ (Model 1.1), but where the strain rate contrast is larger Control 2 takes over and rifting occurs in the lithosphere under the higher strain rate (Model 3.4). All models presented in the results were placed on the diagram in their respective columns. M1.1 stands for Model 1.1 etc.

The circumstances under which Control 1 wins in models that include a lithospheric boundary were difficult to find, indicating that it is a special case that applies only where the background strain rates in the two sides are similar. A small change to the scaling factor of the right mantle lithosphere increased the strain rate contrast and allowed Control 2 to win (Series 2).

We have focused on models with full rifting velocities of 1 cm a^{-1}. At higher or lower rifting velocities, and therefore different background strain rates, the models are likely to behave in a different manner because the distribution of stiff and pliable layers will change. An investigation of the velocity sensitivity is beyond the goals of the present research. We do, however, believe Controls 1 and 2 will operate in the same manner. This implies that once the

stiff vs pliable distribution has been established in any given model, the model behavior can be predicted on the basis of the controls.

It is also difficult to draw particular conclusions concerning the length of time required to achieve lithospheric breakup. In general, necking of a stiff layer under Control 1 will minimize this time, whereas rifting takes longer under Control 1 for a pliable lithosphere (Chenin and Beaumont 2013). Correspondingly, higher background strain rates, for example from higher rifting velocities, will also accelerate breakup in pliable layers under Control 2 by comparison with lower background strain rates. However, time to breakup does not correlate strongly with Control 1 or Control 2.

2.9.2 Other Mechanisms that Change the Strain Rate in the Lithosphere

In our simple models, lateral lithospheric-scale heterogeneity was introduced only by changing the strength of adjacent lithospheres across a vertical boundary. Previous modeling suggests that our results can be extended to other forms of heterogeneity, such as a heterogeneous temperature (Bassi 1991, 1995, Bassi et al. 1993, Huerta and Harry 2007) or thickness distribution (Bassi et al. 1993, Bonini et al. 2007, Corti et al. 2013a). These heterogeneities affect the strength of the lithosphere and, therefore, the strain rate distribution. An increased geotherm results in an overall weakening of the lithosphere (Bassi 1995). Similarly, a thickened lower crust weakens the lithosphere (Bassi 1991, Corti et al. 2013a) because the top of the upper mantle lithosphere will be deeper and hotter, with less potential to be in the stiff regime.

Comparing our results with previous analogue and numerical models brings with it difficulties. Analogue models may include a weakness at the lithospheric boundary, whether this is intended or not, because of the way they are constructed, which may result in significant faulting at the boundary. Nor are we able to make inferences on which layers are respectively stiff and pliable from the information provided in most cases. These analogue models (Chemenda et al. 2002, Bonini et al. 2007, Corti et al. 2013a) may also be limited by the amount of extension they can accommodate, causing the location of final breakup to be unclear, and the absence of a thermal evolution. Nevertheless, we have attempted a comparison. Some

previous analogue models were designed to represent specific natural rifts, including the Baikal Rift (Chemenda et al. 2002, Corti et al. 2011), the West Antarctica Rift System (Bonini et al. 2007), and the East African Rift System (Corti et al. 2007). In a more general study, Corti et al. (2013b) used analogue models to test the effects of lateral strength contrasts, the depth of the brittle-viscous transition, and the presence of a weak zone extending from the lower crust to the base of the mantle lithosphere, on rift geometry as applied to rifting along the edge of a craton. Generally, in these models a weak zone at the boundary results in a boundary fault dipping away from the strong lithosphere, creating an asymmetric rift similar to our Model 3.5 (Chemenda et al. 2002, Corti et al. 2013a). However, in the absence of a weak zone, localization is distributed throughout the weaker lithosphere with possible minor faulting in the stronger lithosphere as in our Model 3.1 (Chemenda et al. 2002, Corti et al. 2013a).

Previous research using numerical models adopted either a laterally changing crustal and/or mantle thickness (Bassi 1991, 1995, Huerta and Harry 2007), or a 50-400 km wide weak region surrounded by stronger lithosphere (Corti et al. 2007, Gorczyk et al. 2013) to model the effect of a lithospheric boundary. As noted above, increasing the crustal thickness raises the Moho temperature and lowers the strength of the lithosphere as a whole, as does thinning the mantle lithosphere. Bassi (1995), for example, concluded that where the lithosphere is hot (Moho >770˚C) localization happens in the transition zone between the normal and thickened crust. Still, in the absence of a superimposed weak zone, the largest amount of thinning actually develops ~150 km away from normal thickness lithosphere. Huerta and Harry (2007) observed a similar result in models with weak, hot lithosphere placed next to a thicker, cold, strong lithosphere. Our Model 3.2 is similar to these, where most of the left crust and mantle lithosphere are pliable (Figure 2.7h).

Models that include a 50-400 km wide weak region (Corti et al. 2007, Gorczyk et al. 2013) show results most similar to ours. Strain localizes in the weaker mobile belt in all cases, but the models with the wider weak zones (200 - 400 km), in particular, resemble our results where Control 2 wins and rifting takes place away from the lithospheric boundary in the lithosphere under the higher strain rate. Overall these numerical models support our predictions that other strength contrasts in addition to those caused by material properties, for

example, a temperature contrast and/or changes in lithospheric layer thickness, can also effectively change the strain rate distribution, and determine the location of initiation of necking instabilities under Control 2.

2.10 Applications

Control 2 dominates for nearly all cases we have investigated where a lithospheric boundary is present, and this results in localization in the lithosphere under the higher background strain rate. We apply this result to an end-member case, rifting where a craton is involved. In addition, we suggest that lateral lithospheric contrasts across boundaries can result in asymmetric margins. We compare our model results with the Basin and Range Province, the Baikal Rift, and the Camamu-Gabon rifted margin.

2.10.1 Application 1: Craton Preservation

The cratonic cores of continents are generally underlain by thick Archean lithosphere that has survived largely undeformed for >2.5 Ga (Griffin et al. 1999, Artemieva and Mooney 2001, Gung et al. 2003). Endurance of Archean lithosphere has been attributed to its neutral buoyancy owing to an isopycnal state, and high viscosity and yield strength, all of which likely originate from high levels of dehydration and melt depletion (<0.001wt % H_2O) and low heat flow (Jordan 1975, 1978, Lenardic and Moresi 1999, Griffin et al. 2009b, Karato 2010).

Cratons are interpreted to have been assembled from distinct units, possibly by a primitive form of plate tectonics (e.g. Griffin et al. 1999, Sleep 2005), and it is likely that cratons include weak zones corresponding to sutures. Consequently cratons, which are cold and likely stiff, should be susceptible to localization and rapid growth of necking instabilities at the weak zones under Control 1, as suggested by Chenin and Beaumont (2013). The persistence of cratons indicates these weak zones are ignored during rifting that involves cratons, and this needs to be explained. The answer appears to be that cratons that surround themselves with weaker lithosphere 'buy protection' from rifting via Control 2. Deformation will localize in the weaker surrounding lithosphere with the higher strain rate, leaving the cratonic nucleus undeformed, even though instabilities should grow faster in stiff cratons under Control 1 (Model 3.4, Figure 2.9). This explanation is similar to that proposed by Yoshida (2012) and may

also apply to cratons under compression that are surrounded by subduction zones (Lenardic et al. 2000).

Although not truly a craton, the Colorado Plateau in the southwestern United States behaves in this manner. The Basin and Range and Colorado Plateau were accreted to the cratonic core of North America during the Proterozoic as a series of juvenile volcanic arcs (Whitmeyer and Karlstrom 2007), and the Colorado Plateau is still underlain by Proterozoic lithosphere today (Livaccari and Perry 1993, Lee et al. 2001). However, the lithosphere under the Basin and Range province was severely altered after initial accretion by processes inferred to include: 1) rifting at ~600 Ma (Burchfiel et al. 1992); 2) rehydration by the subducting Farallon slab during the Laramide Orogeny (Humphreys et al. 2003), and 3) extensive heating and resulting magmatism when the Farallon slab was removed (Humphreys 1995, Sine et al. 2008).

The Colorado Plateau was largely unaffected by these processes and is still mostly underlain by a high velocity mantle lithosphere (Humphreys et al. 2003). It also has a heat flow of 50 - 60 mW m^{-2}, which is relatively low compared to the adjacent Basin and Range Province and Rio Grande rift (Parsons 1995). Additionally, a low conductivity, high density, strong lower crust has been interpreted to support the Colorado Plateau and to contribute to its persistence (Wannamaker et al. 2008, Bashir et al. 2011). These factors suggest a strong lithosphere similar to our right lithosphere in Model 3.4. The comparison is made more realistic by the relict NE-SW shear zones that cross-cut the Colorado Plateau, which play a role equivalent to the CWZ in Model 3.4. For example, the Yavapai-Mazatzal suture serves as a conduit for recent volcanism and may be weak (Karlstrom and Humphreys 1998, Whitmeyer and Karlstrom 2007, Bashir et al. 2011).

During the Cenozoic, the Basin and Range has extended to 200% of its original width and is the archetype of a wide rift, leaving the Colorado Plateau to the east largely undeformed (Jones et al. 1992, Wernicke and Snow 1998, McQuarrie and Wernicke 2005). It could be argued that the earliest extension within the core complexes (~36-16 Ma) was close to the edge of the Colorado Plateau, but this clearly did not persist (Jones et al. 1992, Parsons 1995, Wernicke and

Snow 1998, McQuarrie and Wernicke 2005). More recent E-W extension was distributed over more than 1000 km (McQuarrie and Wernicke 2005). Seismic and magnetotelluric profiles show that crustal thinning is most advanced 100-150 km away from the Colorado Plateau in the northern and central Basin and Range (Figure 2.12) (Zandt et al. 1995, Sine et al. 2008, Wannamaker et al. 2008, Wernicke et al. 2008).

Therefore, the Basin and Range is comparable to more pliable versions of Model 3.1 (Figure 2.7) if there were no inherited weak zones, or model Model 3.4 (Figure 2.9) if there were inherited weak zones. Even though the suture zones in the Colorado Plateau may be weak, the Basin and Range is under a much higher strain rate than the Colorado Plateau and it absorbs all of the deformation. The final geometries of the rift and our model result differ only because Model 3.4 has a strong crust, whereas the Basin and Range is extremely hot and is therefore more pliable. It has long been established that hot lithosphere or thickened viscous crust results in distributed deformation (Buck 1991). Were we to choose a more pliable crust and lithosphere for the left lithosphere a wide rift would be expected, similar to the Basin and Range (Chenin and Beaumont 2013). Although technically not a craton, the Proterozoic Colorado Plateau is protected by the hot and pliable lithosphere of the Basin and Range. The same case is evident for the modern East African rift system where the rifts are primarily confined to the younger, weaker lithosphere that surrounds the cratons (Ebinger 1989, 2005, Foster and Ebinger 1997, Ebinger et al. 1997, Klerkx et al. 1998).

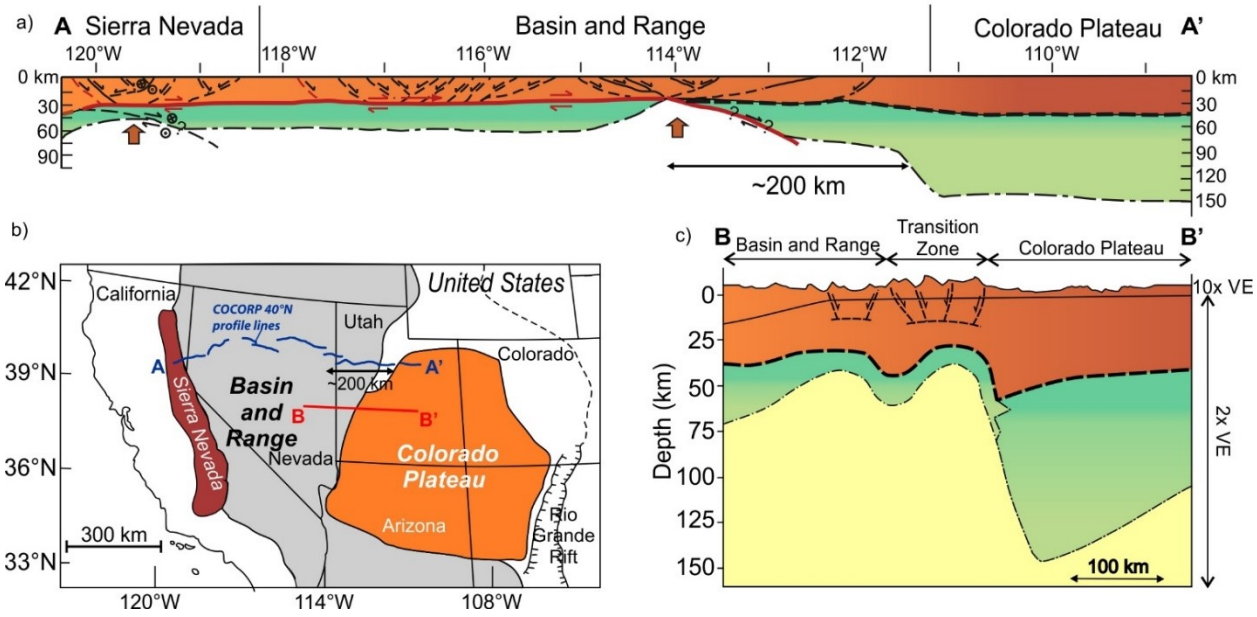

Figure 2.12. Preservation of the Colorado Plateau. a) An interpretive cross-section along the COCORP 40°N line which shows the significant change in lithospheric thickness between the Basin and Range and Colorado Plateau. Maximum thinning is located approximately 200 km away from the Colorado Plateau. Deformation is distributed in the Basin and Range, which is hot, weaker and under a higher strain rate (Modified from Wernicke et al., 2008). b) Map of the southeastern United States showing the locations of the 2 cross-sections. c) Interpretive cross-section in the central Basin and Range from a magnetotelluric profile. The mantle lithosphere under the Colorado Plateau is interpreted to be significantly thicker than under the Basin and Range and thinning is focused in the Transition Zone and the eastern Basin and Range.

2.10.2 Application 2: Asymmetric Margins

Asymmetric conjugate margins were first thought to be a key indicator of extension by simple shear (Wernicke 1985, Lister et al. 1986). Additionally, it was suggested that they are the result of slow spreading where cooling leads to shifting of strain localization (England 1983, Kusznir and Park 1987). Other suggested mechanisms include multiple phases of rifting (Tett and Sawyer 1996) and decoupling of the crust and mantle lithosphere because of a viscous lower crust (Brun and Beslier 1996).

Based on our results, we propose that the presence of lateral lithospheric strength contrasts is another factor that leads to asymmetric margins. In the models presented, Model 1.1 (Figure 2.5) can be interpreted as rifting at a boundary as a result of the C-MWZ in a stiff layer in the limiting case where there was no strength contrast across the boundary. This leads to a nearly symmetric margin. Model 3.5 (Figure 2.10) illustrates a similar case where there is a

small strength contrast across the boundary. In the latter case, Control 1 initiates the necking instability, but Control 2 results in distributed deformation in the lithosphere under the higher strain rate. Comparison of these two models shows that in Model 3.5 the rifted margin is asymmetric, with a narrow side where there is a lower strain rate and a wide side in the higher strain rate lithosphere.

An example conjugate margin of this type is the Camamu-Gabon margin in the central South Atlantic (Figure 2.13). The Congo and Sao Francisco cratons were connected during the Proterozoic by the Trans-Amazonian orogeny and only rifted apart during the Late Jurassic to Early Cretaceous (Barbosa and Sabaté 2004, Li et al. 2008, Wit et al. 2015). Immediately to the south of the connected region, the conjugate margins developed at the boundary between the Sao Francisco craton and Proterozoic lithosphere. The Brazilian margin adjacent to the Sao Francisco craton is very narrow (Figure 2.13a), and the crust thins from 30 km to less than 4 km over a distance less than 60 km (Chang et al. 1992, Rosendahl et al. 2005, Blaich et al. 2010, 2011). In contrast, the Gabon margin, which is underlain by Proterozoic basement, thins gradually over ~200 km. Figure 2.13 shows a comparison of Model 3.5 (shown with reversed polarity) with an interpreted seismic profile that spans the conjugate margin (Blaich et al. 2010).

An example of an asymmetric continental rift is the Baikal Rift System located on the boundary between the Archean Siberian craton and the Proterozoic Sayan-Baikal fold belt. It extends ~ 1500 km in a NE-SW direction (Delvaux et al. 1995, 1997). There is a thickness contrast between the >100 km thick lithosphere underlying the Siberian craton and the 60-80 km of mantle lithosphere beneath the Sayan-Baikal fold belt along the entire rift (Ionov et al. 1995, Petit and Déverchère 2006).

Deformation started in the southern end of the rift at 27 Ma and was mostly strike-slip (Delvaux et al. 1995). The highly asymmetric central Baikal basin has been undergoing orthogonal extension from 10-7 Ma and is now <100 km wide (Delvaux et al. 1997). Sedimentation started at 27 Ma under a transpressional regime and sediments thicknesses reach up to 9-km thick beneath the central Lake Baikal.

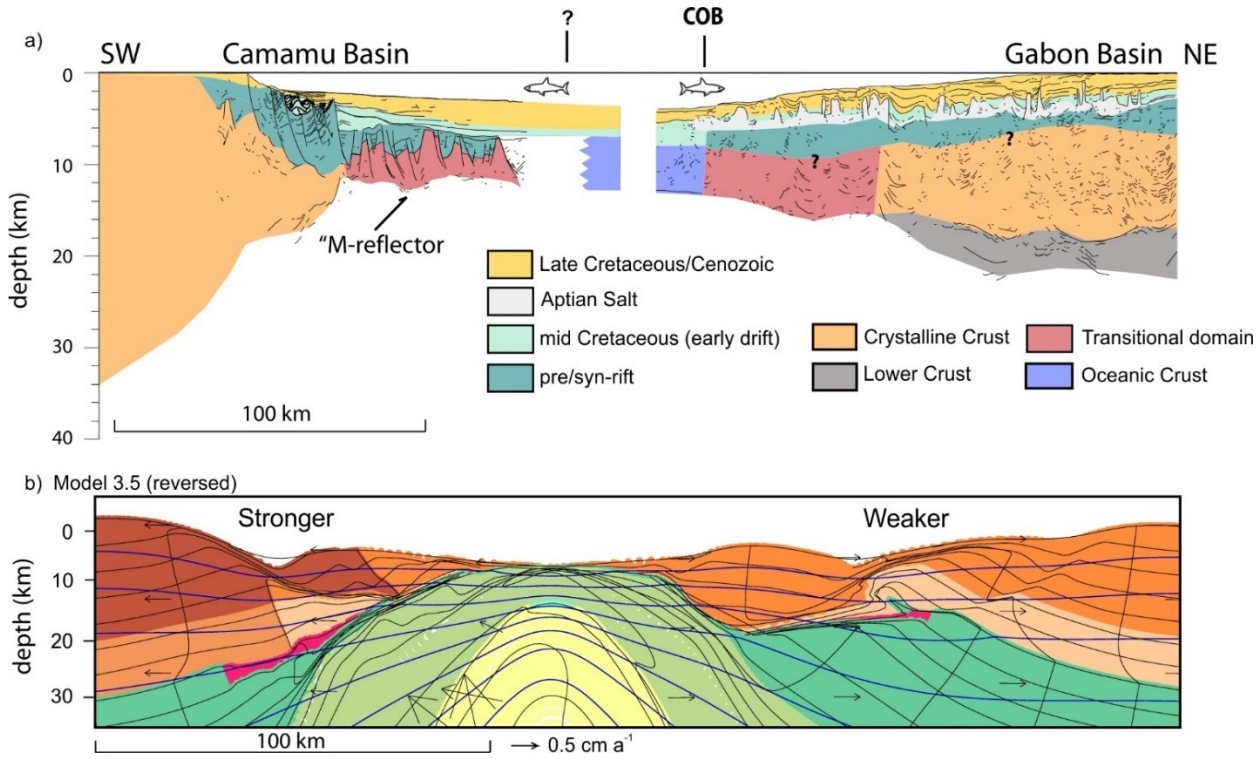

Figure 2.13. Model 3.5 compared with the Camamu-Gabon margin. a) Interpreted seismic cross-section across the Camamu-Gabon conjugate margin, which lies on the boundary between the Sao Francisco craton and a Proterozoic mobile belt. The Camamu margin is narrow and the crust rapidly thins towards the continent-ocean transition. The Gabon margin extends for over 200 km (Blaich et al. 2010). b) Model 3.5 at 19.0 Ma shown with reversed polarity. The stronger crust thins from over 30 km to less than 5 km in ~80 km. The weaker crust on the other side thins gradually over 150 km. Note the model is shown at end of syn-rift extension and there is no sediment, whereas the seismic cross-section above shows current configuration.

An inherited weak zone has been interpreted at the boundary (Petit and Déverchère 2006, Corti et al. 2013a). Similar to Model 3.5 (Figure 2.10), deformation is accommodated by a high-angle boundary fault on the stronger Siberian lithosphere side.

In contrast, further north and south along strike the rift widens and curves away from the edge of the Siberian craton (Corti et al. 2011). This is interpreted to represent the transition from orthogonal extension along the central Baikal rift to broad zones of oblique to transcurrent motion to the northwest and southeast (Chemenda et al. 2002, Petit and Déverchère 2006, Corti et al. 2011). Given the evidence for thick, cold, cratonic lithosphere beneath the Siberian craton and warmer, thinner lithosphere beneath the Sayan-Baikal fold belt (Ionov 2002), the evidence for a weak zone at the boundary (Chemenda et al. 2002), and the slow (~0.5 cm a^{-1}) spreading rate, the setting of the central Baikal Rift is similar to that of

Model 3.5 at 14 Ma (Figure 2.10e) and also similar to the restored Camamu-Gabon conjugate margins (Figure 2.13). By all indications the central Baikal Rift is asymmetric, consistent with asymmetry developed at a lithospheric boundary, initially under Control 1. The broader oblique to transcurrent regions in the weaker Sayan-Baikal fold belt may be cases where Control 2 prevails, as in the Basin and Range and Colorado Plateau examples (e.g. Models 3.1 and 3.4) (Corti et al. 2013a).

2.11 Conclusions

We investigated the effect of inherited small-scale weak zones and lateral boundaries, for example caused by fossil sutures, in localizing deformation and seeding necking instabilities in the lithosphere during extension. We propose that weak zones interact with the intrinsic rheological layering of the lithosphere in two ways, leading to two controls; Control 1) is the stiff and pliable behavior of the lithosphere (Chenin and Beaumont 2013), and; Control 2) is the background strain rate of a lithosphere under extension. These controls stem from the growth rates of necking instabilities in a layered lithosphere. Control 1 expresses the effect of nonlinearity in the growth rate such that necking develops much faster in stiff layers (power-law exponent, n > 1000) than in pliable layers (power-law flow exponent n ~2-5). A useful analogy is with the Mars Caramel bar in which the chocolate is stiff, whereas the caramel is pliable. The effect of Control 2 is to amplify the growth of necking instabilities according to the magnitude of the background strain rate, which is defined as the strain rate in the absence of inherited heterogeneities.

Control 1 operates in a uniform lithosphere where the background strain rate is laterally uniform. However, where lithospheric strength varies laterally the background strain rate will also vary. Control 2 is now involved and predicts that necking will develop fastest where the background strain rate is greatest. Controls 1 and 2 therefore compete in a 'hare and tortoise' manner to grow necking instabilities. We have used simple 2D finite element models of lithospheric extension to test these concepts. Our conclusions are:

1) Models 1.1 and 1.2 have laterally uniform lithosphere and demonstrate that necking develops faster where a weak zone is located in a stiff layer than where it is in a pliable layer (Chenin and Beaumont 2013); that is Control 1 operates.

2) Models 2.1 and 2.2 concern weak zones embedded symmetrically on either side of a lateral lithospheric boundary. The results show that Control 2 wins in general, but where the background strain rates in the two regions of the model are similar, Control 1 can win, causing rifting to localize at the weak zone in a stiff layer.

3) Other models are used to show that Control 2 also wins under other circumstances. This holds true where: 1) there are no weak zones whatsoever (Model 3.1); 2) the C-MWZ is in a pliable upper mantle lithosphere (Model 3.2); 3) one MWZ is present in a stiff upper mantle lithosphere, and the other MWZ is in an upper mantle lithosphere under a higher background strain rate (Model 3.3); 4) localization occurs at a CWZ under a high background strain rate even though a C-MWZ is in a stiff upper mantle lithosphere (Model 3.4); and, 5) where a C-MWZ localizes deformation at the lithospheric boundary most deformation is located in the lithosphere under the higher strain rate.

4) These results can be applied to show that cold, stiff cratons, which should rift rapidly under Control 1, avoid deformation if they are embedded in weaker lithosphere. Under these circumstances the strain rate is higher in the weaker lithosphere and Control 2 wins.

5) A second application of the results shows that rifts that localize at the boundary between two different types of lithosphere may develop into very asymmetric conjugate margins if Controls 1 and 2 operate on opposite sides of the boundary.

2.12 Acknowledgements

Concerning the AGU data policy the manuscript is based on results computed from a numerical model (http://geodynamics.oceanography.dal.ca/sopale_nested.html) and the literature cited. This research was funded by an NSERC Discovery Grant and Canada Research Chair in Geodynamics to CB. We thank Douglas Guptill for his computing support in regard to the development of SOPALE-nested and the associated graphics programs. Reviews by

colleagues Rebecca Jamieson, Charlotte Keen and Nick Culshaw are gratefully acknowledged. SOPALE was originally developed at Dalhousie University by Philippe Fullsack.

Chapter 3 Rifting Strong Cratons

3.1 Introduction

The existence of cratons that are over 2 billion years old is remarkable, considering that present-day oceanic lithosphere is recycled within 200 million years (Carlson et al. 2005, Lee et al. 2011). Cratons were formed through high degrees of melt extraction (30-40%; Pearson and Nowell 2002) from hot Archean lithosphere (1450°C-1600°C) at relatively low pressures (<5 GPa) implying that they formed at shallower depths (<150 km) than the maximum depth (200-250 km) from which xenoliths were transported to the surface at a later time (Kelemen et al. 1998, Canil 2004, Lee 2006, Pearson and Wittig 2008, Wittig et al. 2008). On the surface Archean rocks are mainly represented by greenstone belts and high grade gneiss terranes. These are located in the cores of continents and have escaped recycling back into the sublithospheric mantle (Windley 1981, Goodwin 1996). The underlying mantle lithosphere is composed mainly of highly depleted and dehydrated peridotites (Griffin et al. 2003a, Carlson et al. 2005). Cratons are substantially thicker than younger lithosphere (200-250 km vs. 100-130 km) and this requires that they currently have a cold geothermal gradient. These distinct characteristics result in a highly viscous, thick and strong cratonic keel (Carlson et al. 2005, Lee et al. 2011). Rheological and modeling studies suggest that the survival of cratons to the present is due to their neutral gravitational buoyancy and high viscosity with respect to the convecting mantle below (Section 3.2). Cratons are further protected by the presence of surrounding younger, weaker lithosphere (Chapter 2; Lenardic et al. 2000, 2003, Corti et al. 2007, Yoshida 2010, 2012, Gorczyk et al. 2013).

However, there is evidence that some initially strong cratons have subsequently thinned and rifted (Section 3.3). Xenoliths and xenocrysts derived from the cratonic mantle lithosphere (CML) indicate that its composition is not homogeneous with depth (Griffin et al. 2003a, Lee et al. 2011). Instead, the geochemical data indicate that the composition of the CML can be changed through metasomatism involving interaction of peridotite with fluids and/or melts from the sublithospheric mantle (Section 3.3.1). The modified characteristics of metasomatized cratons may weaken them sufficiently to allow them to rift. The second part of this thesis investigates the effects of metasomatism as a mechanism to weaken and rehydrate cratons.

These effects may include: 1) an increase in CML density; 2) an increase in temperature, and; 3) rehydration. The last two effects lower the viscosity of CML, allowing it to deform more easily. It has been proposed that the integrated strength of the CML can decrease through these effects (Tang et al. 2013b, Liao and Gerya 2014, Wang et al. 2015). This may cause convective erosion of the lower CML and thin the cratonic lithosphere significantly. Additionally, metasomatism may be a factor in the formation of intracratonic basins (Section 3.4) by reducing the buoyancy of the cratonic lithosphere, which then requires isostatic subsidence and creates accommodation for sediments.

Understanding the stability and destruction of CML is a fundamental part of understanding plate tectonics, but also has economic importance. For example, the formation of diamonds is limited to high pressures coupled with low temperatures and is therefore closely linked to the existence, survival, and destruction of cratons (Haggerty 1999). Additionally, intracratonic basins may host hydrocarbons (Mann et al. 2001, Yang et al. 2005) or uranium and other mineral deposits (Groves and Bierlein 2007).

This chapter starts by reviewing recent advances in the understanding of craton formation, stability, and destruction. Metasomatism is highlighted as an important weakening mechanism, which may lead to craton thinning and a reduction in its integrated strength. Finally, a link between metasomatism and intracratonic basins is proposed.

3.2 Craton Characteristics and Stability

Cratons are the oldest surviving continental lithosphere (>2.5 Ga) and form the cores of the present-day continents (Hoffman 1989, Goodwin 1996, Lee et al. 2011). Archean cratonic crust is generally believed to be underlain by Archean mantle lithosphere with characteristics that are distinctly different from younger lithosphere, such as a lower density, higher degree of dehydration and a colder geotherm (Griffin et al. 2003a). Although the mechanism of craton formation is still debated (Griffin et al. 2003a, Carlson et al. 2005, Lee et al. 2011, and references therein), there is a general agreement, based on xenolith data, that they formed after a high degree (30-40%) of melting of primitive mantle (Lee et al. 2011). For comparison, melting at modern mid-ocean ridges leads only to about 7% melt extraction (Katz et al. 2003).

The mantle lithosphere in general is composed mainly of peridotites (>95%), which range in composition from harzburgites (olivine + orthopyroxene) to lherzolites (olivine + orthopyroxene + clinopyroxene). A small amount of eclogite (garnet + clinopyroxene + omphacite), the high pressure equivalent of basalt, may be present in the mantle lithosphere (Schulze 1989). However, eclogite has a higher density (3560 kg m^{-3}) and seismic velocity (Vp ~8.7 km s^{-1}) than peridotite (3310-3380 m^{-3}, Vp ~8.3 km s^{-1}; Bousquet et al. 1997, Carlson 2005) and if large bodies (km-scale) were present in the mantle lithosphere, they should be discernible in seismic studies. Although it has been looked for beneath African cratons (James et al. 2001, Gao 2002), so far the only inferred subcratonic eclogite bodies are below the Slave Craton in Canada, where 10-km thick seismic reflectors with sharp boundaries are visible at ~70 km depth (Bostock 1998, Carlson et al. 2005).

The range in peridotite compositions is a function of the degree of melt extraction from a primitive mantle, on which the later effects of metasomatism have been superimposed. During initial melt extraction, peridotites are progressively depleted in clinopyroxene and garnet or spinel, leaving behind olivine and orthopyroxene (Lee et al. 2011). This effectively decreases the FeO, Al_2O_3, and CaO contents, and increases the Mg# (atomic Mg/(Mg + Fe)) (Figure 3.1) and lowers the overall density (Poudjom Djomani and O'Reilly 2001, Griffin et al. 2003a, 2009b). Primitive mantle has a density of ~3378 kg m^{-3} (Mg# 89), whereas Archean lithosphere can have a density as low as 3310 kg m^{-3} (Mg# 94) (e.g. Poudjom Djomani and O'Reilly 2001, Griffin et al. 2009b). The linear trend between lithosphere age and depletion in Al_2O_3 and CaO (Figure 3.1a) suggests that the high degree of melt extraction is the primary cause of the compositional difference between Archean and younger lithosphere. However, Archean and Proterozoic peridotites do not fall on the modern oceanic peridotite trend (Figure 3.1b, black arrows), which describes the current formation of oceanic lithosphere by melt extraction. This difference is ascribed to the high Archean geothermal gradient (Turcotte 1980, Turcotte and Schubert 1982, Christensen 1985). Geochemical interpretations of xenolith data suggest that CMLs formed at temperatures between 1450°C and 1600°C at a shallower depth (<5 GPa; ca 150 km) than the depths indicated from xenolith data (6-8 GPa; ca. 200-250 km) (Herzberg 2004, Lee et al. 2011). Specifically, the high Mg# and high MgO content reflect a high

percentage of melt extraction, the low total FeO content suggests high temperatures, and the major and trace elements indicate melting in the absence of garnet at pressures ≤ 5 GPa (Kelemen et al. 1998, Canil 2004, Lee 2006, Wittig et al. 2008). The high degree of melt extraction from CML left behind highly depleted and dehydrated peridotites (Mg# 92-95; <0.01 wt% H_2O) with a low density (~3331 kg m^{-3}) (Poudjom Djomani and O'Reilly 2001, Griffin et al. 2003a, Karato 2010).

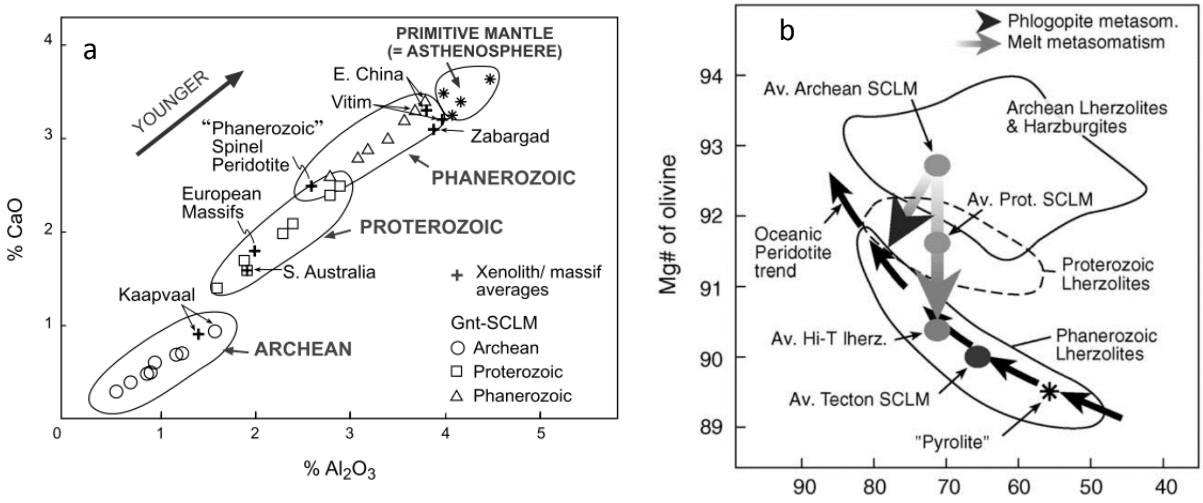

Figure 3.1. Geochemical data showing the compositional relationship between lithospheres of different ages. (Griffin et al. 2003). a) CaO vs. Al_2O_3. Melt extraction depletes the residue in Al_2O_3 and CaO, resulting in a near - linear trend from primitive mantle to Archean lithosphere. Recent xenolith evidence suggests that this trend can be reversed by melt metasomatism. b) Mg# vs modal % olivine. Archean peridotites can have Mg# up to 94, whereas Phanerozoic peridotites have Mg# of 89-92. The black arrows indicate the oceanic peridotite trend, whereas the downward arrows indicate the effects of melt metasomatism and fluid-metasomatism (grey and black arrow heads, respectively). The alteration of CML by metasomatism is highly dependent on the composition of the fluid/melt that is involved.

Seismic tomography studies provide evidence for the existence of a thick (200-250 km), high seismic velocity cratonic root (Goes and Lee 2002, Godey et al. 2004, Begg et al. 2009), which agrees with data from xenolith studies (Griffin et al. 1999, 2003a). Some studies suggest the cratonic root could extend to a depth of 400 km (Artemieva and Mooney 2001). The discrepancy is probably the result of the distinction between the thermal lithosphere and the chemical lithosphere (Artemieva 2009, O'Reilly and Griffin 2010, Lee et al. 2011). The chemically distinct lithosphere is depleted with respect to the sublithospheric mantle and marks the maximum depth from which xenoliths are derived, whereas the thermal lithosphere corresponds to the region that is cooler than the sublithospheric mantle. The difference

between the thermal and chemical lithosphere is referred to as the thermal boundary layer (TBL; Figure 3.2a). Although not chemically distinct, like the chemical boundary layer (CBL; Figure 3.2a), this thermal boundary layer, part of the sublithospheric mantle, does not fully participate in sublithospheric mantle convection (e.g. Cooper and Conrad 2009, Artemieva 2009). In this thesis we assume that the thermal and chemical lithosphere have the same thickness (250 km).

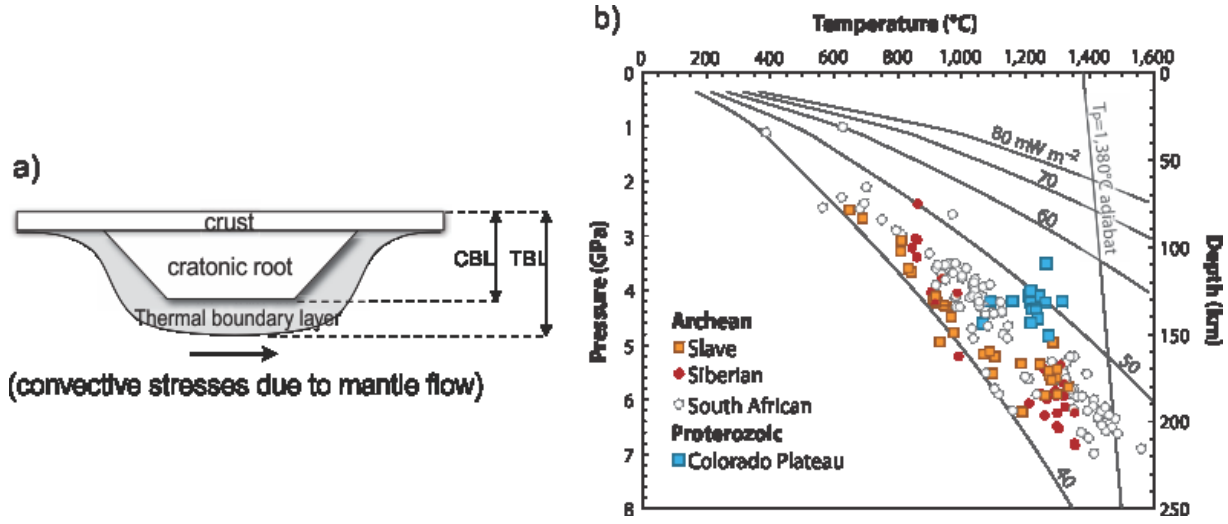

Figure 3.2. Thermal constraints on cratonic lithosphere. a) The chemically distinct cratonic root (chemical boundary layer, CBL) is surrounded by a thermal boundary layer (TBL), which does not participate in convection of the sublithospheric flow because of its low temperature. b) Xenolith data indicating the varying geotherms in Archean and Proterozoic lithospheres. (Lee et al. 2011). The P-T data are plotted on geotherms corresponding to a range of surface heat fluxes. The Colorado Plateau is Proterozoic in age and illustrates the difference in temperature between Archean and Proterozoic lithosphere.

The high seismic velocity of cratonic roots is due mainly to the cooler temperature of CML relative to younger continental lithosphere, and partly to the high Mg# in the mantle lithosphere (Kaban et al. 2003, Lee 2003, Schutt and Lesher 2006). Heat flow measurements for crustal domains with different ages illustrate the large differences in thermal regimes (Figure 3.2b). On average, cratonic domains are characterized by a lower heat flow (~40 mW m^{-2}) than that of Proterozoic (50-60 mW m^{-2}) and tectonically active Phanerozoic domains (~80 mW m^{-2}) (Nyblade and Pollack 1993, Nyblade 1999, Artemieva and Mooney 2001). The low heat flow is partly due to low radiogenic heat production in Archean crust, owing to its depletion in radioactive elements (Mareschal and Jaupart 2012). The heat flow is also closely related to the

temperature distribution required by the thick thermal boundary layer of the CML. If the base of thick CML is between 1300°C and 1400°C, the mantle heat flux must be proportionately less than that through younger, thinner, thermally stable lithosphere (Nyblade and Pollack 1993, Nyblade 1999). Continental geotherms can be constrained further by thermobarometry on xenoliths that have been brought to the surface by volcanic eruptions. Figure 3.2b shows xenolith pressure-temperature data for several cratons as well as the Proterozoic Colorado Plateau. Data from Archean cratons fall between the geotherms calculated for a surface heat flow of 40 mW m^{-2} and 50 mW m^{-2}. The difference in heat flow between Archean and younger lithosphere is illustrated by the slightly hotter Proterozoic Colorado Plateau (Figure 3.2b).

Seismic studies across North America demonstrate that the seismic velocity depends on the composition and temperature of the mantle lithosphere. From the tectonically active west to the stable Archean and Proterozoic shield areas in the center, the velocity increases abruptly by 10% at 100 km depth (e.g Goes and Lee 2002, Godey et al. 2004). A 2% increase in seismic velocity can be explained by a 120°C decrease in temperature or a chemical depletion of either 7.5% in FeO or 15% in Al_2O_3 (Godey et al. 2004). By applying this relationship to the North American data, Godey et al. (2004) calculated that the lithosphere beneath the stable parts of central North America may be colder by 440°C at 100 km depth and depleted in FeO by ~4% compared to western North America. These large differences hint at the characteristics that are important for craton survival.

The persistence of Archean lithosphere until the present day is partly explained by its cold geotherm and high degree of melt extraction. The bottom of the mantle lithosphere is susceptible to erosion, either by convection or shear stress, but the cold geotherm induces a viscosity contrast between the CML, the surrounding continental mantle lithosphere, and the convecting asthenosphere below. The CML viscosity is also increased as a result of high dehydration (Karato 2010); the viscosity of dehydrated peridotite can increase by a factor of ~140 at a constant stress relative to its hydrated state (Hirth and Kohlstedt 1996), further increasing CML strength. Finally, the low density that results from the high depletion in FeO gives the CML chemical buoyancy. However, this positive buoyancy is largely balanced by the

negative thermal buoyancy owing to the cold temperatures, so that cratonic lithosphere is neutrally buoyant to a first approximation (Jordan 1975).

Modeling studies (Lenardic et al. 2000, 2003, Yoshida 2010, 2012) indicate that, apart from their intrinsic characteristics, cratons inadvertently protect themselves by being surrounded by weaker lithosphere. Although cratons have a high integrated strength and have an upper mantle lithosphere in the frictional-plastic regime (Control 1, Section 2.6), a surrounding weaker lithosphere will rift preferentially if the strain rate contrast is sufficiently high (Control 2, Chapter 2). These factors combined contribute to the longevity of cratons, but are not sufficient by themselves. Numerous modeling studies have focused on determining the dominant characteristics needed to make cratons strong enough that they do not participate in sublithospheric mantle convection. Lenardic and Moresi (1999) found that positive chemical buoyancy was insufficient to explain the longevity of cratonic roots; instead they concluded that a high viscosity contrast with the asthenosphere (10^3), caused by dehydration and the effects of temperature-dependent viscosity, can provide root stability. Similar results were obtained in other modeling studies (e.g Lenardic et al. 2000, 2003, Sleep 2003, O'Neill et al. 2008, Beuchert and Podladchikov 2010, Wang et al. 2014). Additionally, where a lateral viscosity contrast or yield strength contrast with surrounding lithosphere is present, the craton was found to be less susceptible to the effects of mantle convection (Lenardic et al. 2000, 2003, Yoshida 2010, 2012).

Having established that cratons are strong and difficult to deform because of the combined effects of a high viscosity and chemical buoyancy, the question remains as to how some cratons can undergo deformation and even rifting. Chapter 4 investigates how much weakening of the CML, where most of the lithospheric strength is located (e.g. Burov 2011, François et al. 2012), may be needed to rift a craton. The next section reviews some mechanisms proposed to explain craton weakening and natural examples of altered, thinned and rifted cratons.

3.3 Craton Destruction and Rifting

Even though cratons are strong, there are places where there is evidence that they have thinned (e.g. Kaapvaal, Griffin et al. 2003b; Tanzania, Koornneef et al. 2009; North China Craton, Tang et al. 2013). Xenolith data in particular are useful in determining the timing and extent of lithospheric thinning. For example, data from xenoliths from the North China Craton suggest that the lithosphere under the eastern part of the craton has been entirely replaced by a young oceanic-type mantle lithosphere, whereas the west North China Craton is still underlain by a cratonic root (Menzies et al. 2007).

Mechanisms proposed to thin craton lithospheres are: 1) basal traction, and; 2) convective removal of the CML (Figure 3.3). Basal traction relies on shear stresses induced by sublithospheric mantle flow (Sleep 2003). However, the shear traction is probably not strong enough to completely destroy cratonic lithosphere because the shear stresses decrease significantly as the craton thins and the protecting thermal boundary layer increases (Cooper and Conrad 2009). Convective removal is driven by density contrasts (Lee et al. 2011). Temperature differences in the lithosphere, for example, cause density contrasts as a result of differential thermal expansion that could lead to convective removal (Figure 3.3b). Rayleigh-Taylor instabilities are the result of a gravitationally unstable configuration where a higher density material is underlain by a lower density material. A perturbation can cause the denser material to sink, and evolve into an instability as lower density material replaces the sinking denser material. These instabilities can exist on multiple scales. Small scale Rayleigh-Taylor instabilities can erode the lithosphere from below (Huang 2003, Korenaga 2004). Larger-scale instabilities, for example those caused by orogenically thickened lithosphere, may result in delamination of the lower part of the lithosphere (Figure 3.3b) (Downey et al. 2011). Edge-driven convection is important where a thickness contrast leads to upwelling of asthenosphere under the thin lithosphere and downwelling under the thick lithosphere, a process that may take CML down with it (King and Anderson 1998, Sleep 2007, van Wijk et al. 2010, Kaislaniemi and van Hunen 2014). Edge-driven convection has been suggested as the cause of recent thinning of the lithosphere beneath the Proterozoic Colorado Plateau, which is thicker than

those of the Basin and Range on the west and the Rio Grande rift on the east (West et al. 2004, van Wijk et al. 2010, Crow et al. 2010, Levander et al. 2011).

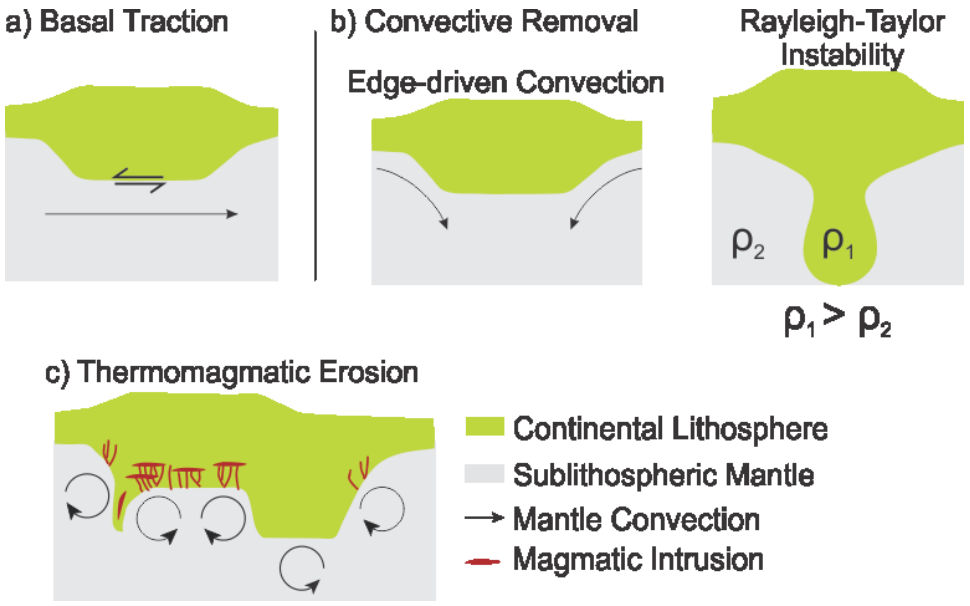

Figure 3.3. Mechanisms to thin the lithosphere. a) Shear stresses on the base of the lithosphere can remove the lower mantle lithosphere through basal traction. b) Density driven flows can cause delamination, Rayleigh-Taylor instabilities, and edge-driven convection. c) Melt infiltration may weaken the CML and cause convective removal. Additional small-scale convection cells can be produced by an uneven base of the lithosphere. Modified from Lee et al. (2011).

The composition of the CML through time and the timing of lithosphere removal can be investigated by analyzing xenoliths from different episodes of magmatism (Griffin et al. 2003a, Menzies et al. 2007). Thinning of many originally thick lithospheres seems to have occurred in the relatively recent past (e.g. Cretaceous for Kaapvaal Craton, Griffin et al. 2003b, Devonian for Wyoming Craton, Carlson et al. 2004, Cretaceous for North China Craton, Menzies et al. 2007, Paleogene for Tanzania Craton, Aulbach et al. 2008). This suggests that these cratons and shields were stable to depths of over 250 km for most of their history. Therefore, something had to change to make them more susceptible to thinning. Cooper and Conrad (2009) calculated the thickness of a chemically distinct craton root in convecting sublithospheric mantle with different Rayleigh numbers. Their results indicate that at present the maximum thickness of chemically distinct lithosphere is 225 km, which is similar to the thickness estimates of many cratons (Rudnick et al. 1998). An increased thickness of the thermal

boundary layer is predicted for increased vigour of convection so it is unlikely that increased vigour of convection cells result in convective removal of CML (Cooper and Conrad 2009). Instead of changes to the sublithospheric mantle, we consider that widespread refertilization of CML by mantle fluids and melts is integral to weakening and eventually thinning the cratonic lithosphere (Figure 3.3c).

3.3.1 Mantle Metasomatism as a Weakening and Thinning Agent

Mantle metasomatism is the compositional change of mantle lithosphere as a result of interaction with melts or fluids. Even where CML is stable with regard to the convecting sublithospheric mantle, it can be altered by externally derived melts or fluids. The sources of metasomatic fluids and melts can be low-degree partial melting, mantle plumes, and fluids or melts released from nearby subducting slabs (O'Reilly and Griffin 2013, Tang et al. 2013b). The high salinity and presence of ringwoodite included in Mesozoic diamonds from the Slave Craton supports the subducting slab under western North America at the time as a primary source for fluids (Weiss et al. 2015). Fluids may also be released by magma crystallisation at the base of or within the CML (O'Reilly and Griffin 2013). Metasomatism may decrease its mechanical strength (by hydration) and/or increase its density (by refertilization), allowing it to be convectively removed.

Evidence for mantle metasomatism is mainly provided by mantle xenoliths and xenocrysts that are brought to the surface by alkali basalts and kimberlites. Kimberlites originate in the CML and are well studied owing to their significance for diamond exploration. Alkali basalts are more typical of fertile Phanerozoic domains or, more importantly for this project, areas where old cratonic mantle lithosphere has been thinned (e.g. North China Craton; Griffin et al. 1998).

Data from xenocrysts and xenoliths indicate that there are different types of metasomatism depending on whether fluid or melt is involved (Rudnick et al. 1998, Carlson et al. 2005, O'Reilly and Griffin 2013). 1) Fluid-related metasomatism can result in the addition of minerals not integral to peridotites (e.g. amphibole, mica, carbonates, apatite, sulfides, titanite, ilmenite and zircon) (modal metasomatism; Harte 1983) or trace-element changes (cryptic

metasomatism; Dawson 1984). 2) Silicate melt metasomatism results in addition of phases already common in some peridotites (e.g. garnet and clinopyroxene) at the expense of olivine, and has only recently been recognized (Griffin et al. 2003a, 2009b, Carlson et al. 2005, Lee et al. 2011).

A large variety of physical effects resulting from fluid and melt metasomatism can have far-reaching effects on the stability of CML. Alteration by fluid metasomatism is highly dependent on the type of fluid, which may have a high CO_2 and/or H_2O content (O'Reilly and Griffin 2013). Fluid metasomatism may partly rehydrate the mantle lithosphere, which can decrease the viscosity by a factor of 140 (Hirth and Kohlstedt 1996). Fluids may also lower the solidus temperature of peridotite enough to produce small amounts of melt (only in an oxidized environment) (Taylor and Green 1988, Zhang and Herzberg 1994, Kawamoto and Holloway 1997, Foley 2008), which can in turn enhance the strain rate by a factor of 25 at a melt fraction of 7% (Hirth and Kohlstedt 1995). Recent petrological studies of major and trace-element characteristics in xenoliths and xenocrysts (e.g. Carlson et al. 2005, Griffin et al. 2009, Tappe et al. 2011, Tang et al. 2013) suggest that interaction with silicate melts during metasomatism can reverse the trends that are usually the result of different degrees of melt extraction. This refertilization leads to an increase in density of the CML from its depleted, low density state of 3335 kg m^{-3} to a more fertile state of 3378 kg m^{-3}, equivalent to a decrease in Mg# from 92 to 89 (Lee 2003). The advection and crystallisation of hot melt can heat wall rock peridotites and decrease the viscosity owing to the temperature-dependent power-law flow.

3.3.2 Reactive Front Metasomatism

In order to test the effectiveness of mantle metasomatism as a process to weaken and destabilize the CML in numerical models, we need to know its extent and spatial distribution. Xenoliths brought to the surface in kimberlites only provide a depth profile through the lithosphere sampled by the vertical kimberlite pipe. The lateral extent of altered wall rock cannot be reconstructed from these data (O'Reilly and Griffin 2013). Fortunately, the spatial scale and style of mantle metasomatism can be directly observed in exposed ultramafic massifs. In particular, at the Lherz massif in the French Pyrenees, a large body (1.5 km^2) of lherzolite is interleaved with foliated lenses of harzburgite (Bodinier et al. 1990, Le Roux et al. 2007, 2009).

The observed decrease in Mg# from 92 in the harzburgites to 90.5 in the lherzolites in the massif could be explained by different degrees of melt extraction. However, the constant fabric orientations in the harzburgites suggests that the lherzolite was not tectonically emplaced, but replaced the depleted harzburgite by melt metasomatism (Le Roux et al. 2007). This interpretation is supported by the major element data trends from the different lithologies, which differ from those predicted by melt extraction models (Figure 3.4).

Furthermore, in the Lherz massif, the rare earth element (REE) data suggest that pervasive melt metasomatism was preceded by cryptic metasomatism. Harzburgite over 20 m away from the contact with the lherzolites is only slightly enriched in light rare earth elements (LREE) relative to a chondrite normalization and was not cryptically metasomatized. Closer to the contact, on the other hand, the harzburgite is enriched in both heavy rare earth elements (HREE) and LREE. This pattern indicates that small, volatile-rich melt fractions preceded the

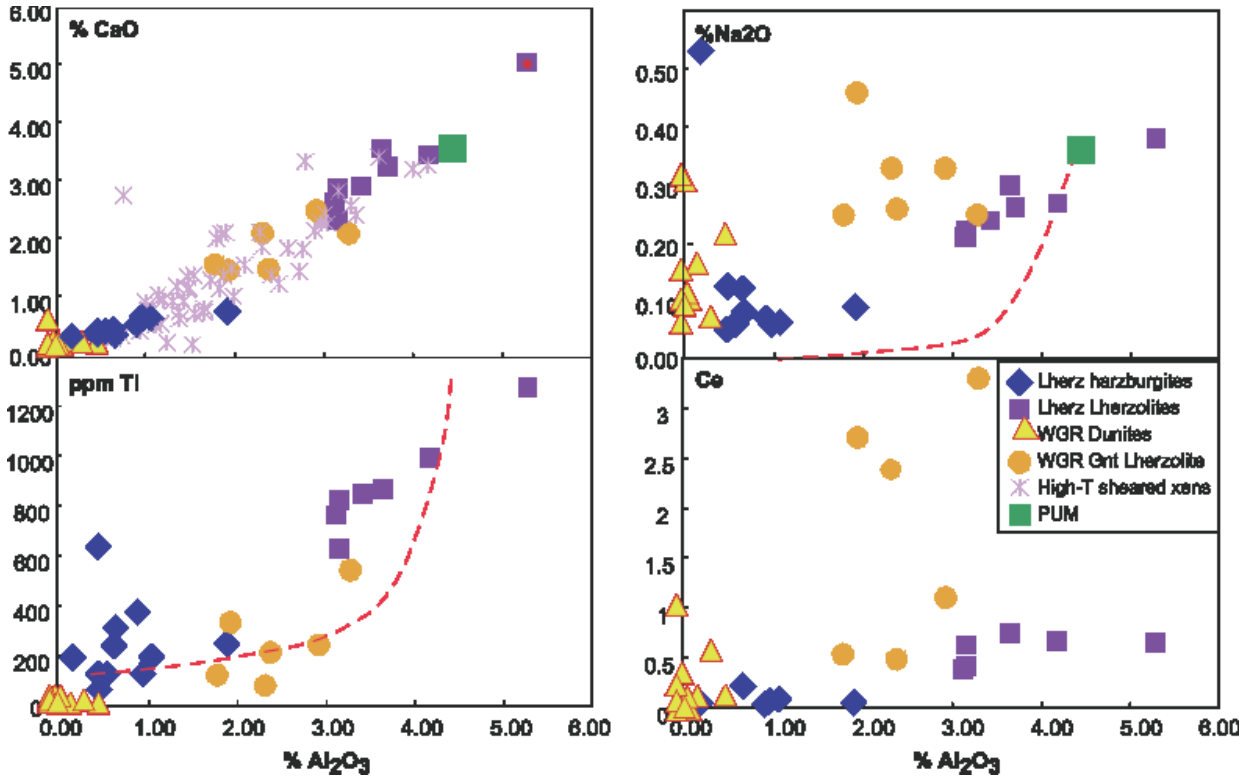

Figure 3.4. Geochemical analyses of harzburgites and lherzolites from the Lherz Massif (data from Le Roux et al. (2007) and Western Gneiss Region (WGR; data from Beyer et al. 2006). The red dashed line is the expected distribution if peridotites formed only by removal of melt from primitive upper mantle (PUM; green square). The harzburgites (blue diamonds) generally have low Al_2O_3 and have not undergone extensive metasomatism. The lherzolites (purple squares) do not follow the melt extraction curve and are enriched in Na_2O and Ti. (O'Reilly and Griffin 2013).

advance of melt metasomatism (Harte et al. 1993, Vernières et al. 1997). The REE pattern of lherzolites away from the contact resembles that of orogenic lherzolites found elsewhere and suggests interaction with silicate melts (Le Roux et al. 2007). Similar relationships are found in the ~300 km^2 Ronda massif in Spain, where a kilometer-scale reactive front between recrystallized spinel lherzolites and the original garnet lherzolite domain can be mapped (Lenoir et al. 2001, Soustelle et al. 2009).

Major- and trace-element data from xenoliths and xenocrysts in kimberlites indicate that different metasomatic processes operate at different depths. At depths <150 km the dominant alteration is the result of fluid metasomatism, and at depths >150 km melt-related metasomatism dominates (Griffin et al. 2003a, Begg et al. 2009, O'Reilly and Griffin 2013). The most efficient way to move significant amounts of melt throughout the lower mantle lithosphere is through cracks caused by overpressured fluids (O'Reilly and Griffin 2013 and references therein). Grain-boundary infiltration is also an efficient mechanism for silicate melt movement (Watson et al. 1990) and may cause the reactive front to move up to 20-50 m a^{-1} (Bodinier et al. 1990, Le Roux et al. 2007). Dissolution of peridotites during melt-wall rock reaction enhances porosity and allows further infiltration (Bodinier et al. 1990, Vernières et al. 1997, Van Den Bleeken et al. 2010). As the buoyant melt rises and moves through the lithosphere, it cools and crystallizes (Watson et al. 1990). During crystallization, metasomatic fluids are expelled and continue to interact with shallower less metasomatized peridotites.

Geophysical data may be able to expand the scale on which we can determine the extent of metasomatized mantle lithosphere. Highly depleted compositions are less dense, but have higher seismic velocities than lithologies that are more Fe-rich (Anderson 1989). Nevertheless the effects of temperature are probably more easily discernible on a small scale than those resulting from density changes (Kaban et al. 2003, Lee 2003, Schutt and Lesher 2006). High conductivity zones indicating the presence of melt or fluid, potentially detectable by magnetotelluric imaging, could also indicate mantle metasomatism (Wannamaker et al. 2008, Dong et al. 2014).

3.3.3 Varying Degrees of Metasomatism in Cratons

As more analyses are completed on mantle xenoliths and xenocrysts it is becoming evident that mantle metasomatism is a widespread phenomenon (e.g. Tang et al. 2013). Figure 3.5 shows the distribution of depleted harzburgites, depleted lherzolites, fertile lherzolites, metasomatized lherzolites and melt-metasomatized peridotites, for five different regions ranging in age from Archean to Phanerozoic, as interpreted from xenolith geochemistry. Eastern China is considered Phanerozoic in this context as it has been deformed in recent times. It is clear from this figure that the abundance of depleted lithologies increases with tectonic age, once again indicating the uniqueness of Archean mantle lithosphere.

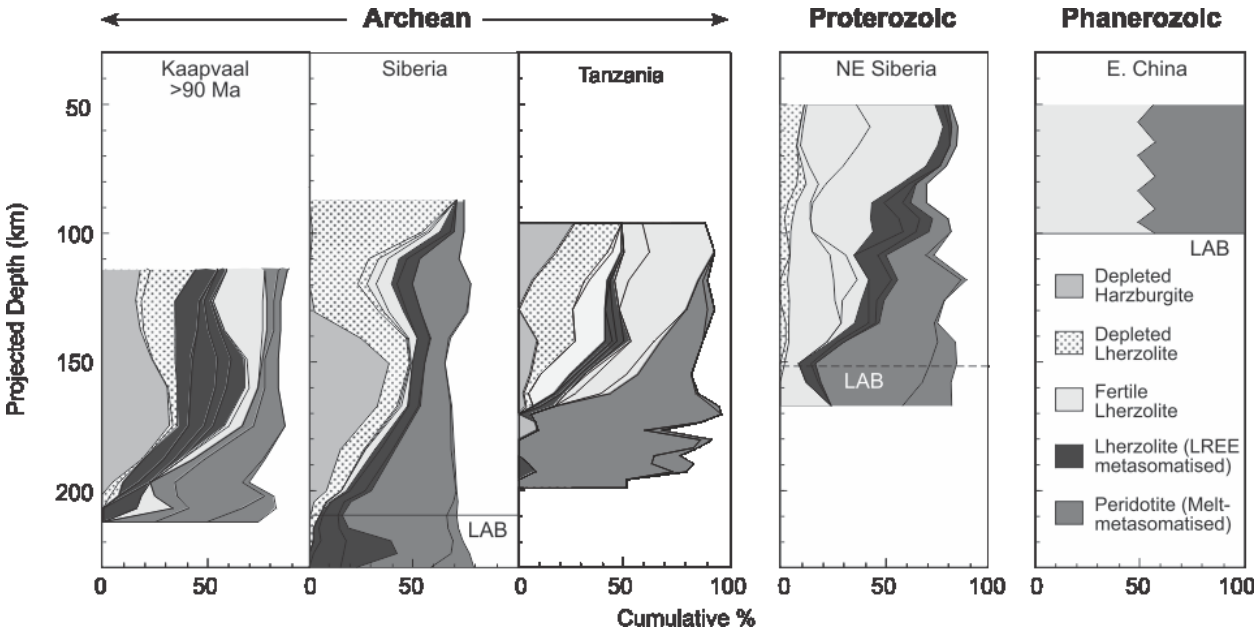

Figure 3.5. Chemical tomography sections representing Archean, Proterozoic and Phanerozoic lithosphere. Lithologies are constructed from major and trace element characteristics from xenoliths and xenocrysts. The lithosphere-asthenosphere boundary (LAB) is defined as the maximum depth where low-Y garnets (found in depleted lithosphere) are found. (O'Reilly et al. 2001, Griffin et al. 2003a).

The same data indicate variations in the degree of metasomatism; for example, the Siberian Craton is one of the least metasomatized cratons (Figure 3.5). Seismic velocity studies agree with the chemical tomography section in Figure 3.5 and suggest that high velocity lithosphere extends to a depth of 200-250 (Priestley and Debayle 2003). Even so, melt

metasomatism in xenoliths can be identified to depths as shallow as 80 km from geochemical data (Griffin et al. 1999).

The eruption and crystallization of magmas at different times and locations gives insight into the evolution of the lithosphere through time. The Kaapvaal craton is well suited to study thinning of CML. Kimberlites from the Kaapvaal craton are known for their diamond occurrences and are therefore studied in detail. Two separate groups (Figure 3.6) of xenoliths with different ages suggest that the lithosphere was over 200 km thick before 90 Ma and had an average Mg# 93 (Group 2). It was then thinned by 30 km and the shallower part of the mantle lithosphere entirely made up by fertile lherzolites with Mg# 92. After metasomatism and thinning it now resembles the Proterozoic xenocrysts from Northern Botswana (Figure 3.6).

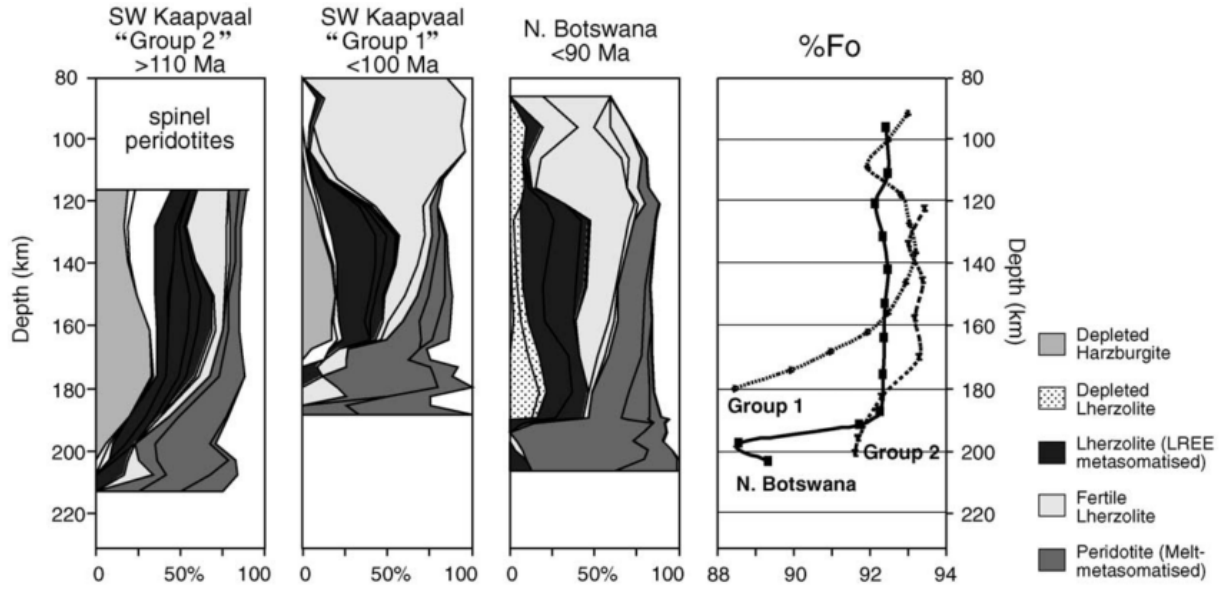

Figure 3.6. Chemical tomography of the Kaapvaal craton and northern Botswana, which lies in a Proterozoic domain. (Griffin et al. 2003).

The most extreme case of a thinned CML can be found in the eastern North China Craton (Figure 3.5). Xenoliths from Ordovician kimberlites suggest a cratonic melt-depleted mantle lithosphere was present to a depth of 180 km and heat flow was ~40 mW m^{-2} at the time of their eruption (Menzies et al. 2007). In contrast, Mesozoic and Cenozoic xenoliths and volcanics suggest a more fertile melt source and a heat flow of ~80 mW m^{-2} (Menzies et al.

2007, Zhang 2009, Zhang et al. 2009). There is debate about the amount of Archean lithosphere that is still present underneath the craton, but it is clear that a dramatic alteration of the mantle lithosphere has taken place.

3.4 Intracratonic Basins

Many cratons are overlain by intracratonic (also known as cratonic or intracontinental) basins that cannot directly be associated with active tectonic margins (Dickinson 1978). They are generally large (>150 000 km^2), have a roughly circular shape, and do not have major faults along their borders (Xie and Heller 2009, Allen and Armitage 2012). Examples include the Congo Basin above the Congo Craton in Africa (Buiter et al. 2012), the Williston, Illinois, Oklahoma, Michigan and Hudson Bay basins overlying the Laurentian Shield in North America (Kaminski and Jaupart 2000), the Parana and Paraiba basins overlying the Amazonian Shield and Sao Francisco Craton in South America, respectively (Soares et al. 1978, Julià et al. 2008, Xie and Heller 2009, Allen and Armitage 2012), and the Ordos Basin on the western North China Craton (Yang et al. 2005, Xu et al. 2008). The presence of sediment packages up to 6 km thick and spanning large timescales vouches for a long subsidence history. This is much longer than predicted by simple thermal subsidence alone (Kaminski and Jaupart 2000).

The subsidence curves for most cratonic basins show an exponential decay similar to oceanic basins (Xie and Heller 2009, Allen and Armitage 2012), except for their much longer duration and the lack of rapid initial subsidence (Figure 3.7). Superimposed on the long-term subsidence are shorter periods of uplift represented by unconformities of both long and short duration (horizontal segments in Figure 3.7), followed by exceptionally rapid subsidence, which separate the stratigraphy into megasequences (Sloss 1963, Kingston et al. 1983, Xie and Heller 2009, Armitage and Allen 2010). These data suggest that something other than thermal subsidence must have been responsible for the formation of intracratonic basins.

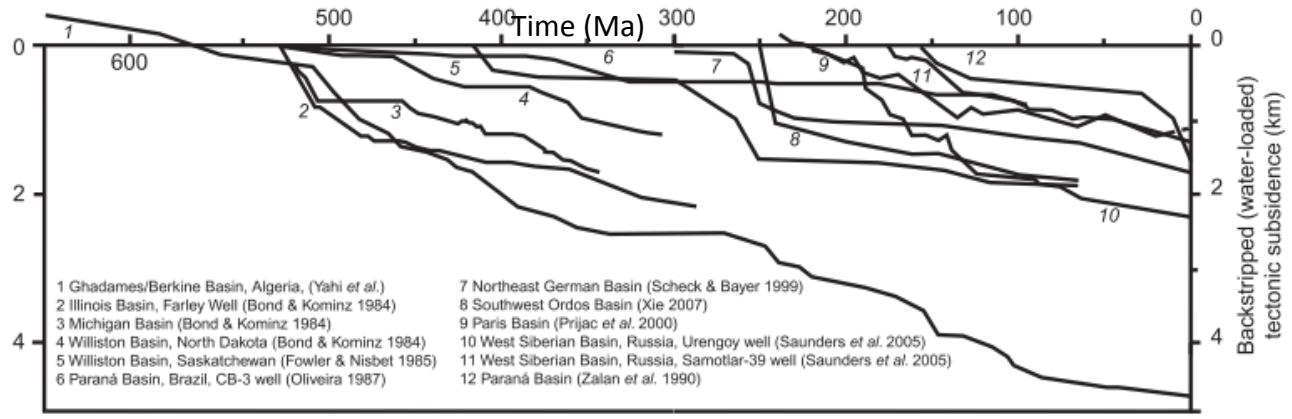

Figure 3.7. Subsidence curves for several cratonic basins (Allen and Armitage 2012, with data from Xie and Heller 2009). Unconformities, which indicate uplift and erosion, are shown as horizontal lines. Unconformities are generally followed by a time of rapid subsidence.

Several mechanisms have been suggested to explain the subsidence of these basins: 1) thinning of the lithosphere at a low strain rate (Armitage and Allen 2010, Allen and Armitage 2012); 2) downward mantle flow causing subsidence (dynamic topography) (Pysklywec and Quintas 2000, Crosby et al. 2010); 3) phase changes changing the density of either the crust or mantle lithosphere (Hartley and Allen 1994, Downey and Gurnis 2009); 4) magmatic underplating (Gvirtzman and Garfunkel 1997), and; 5) cooling after plume activity (Kaminski and Jaupart 2000).

Seismic tomography and gravity anomalies can provide insight into the deep temperature and density structure of the lithosphere underlying cratonic basins and thereby narrow down probable mechanisms. The Congo Basin, for example, has accumulated 1 km of sediment in the Mesozoic-Cenozoic, although there is no evidence for extensional or compressional events to cause subsidence (Daly et al. 1992, Giresse 2005). Seismic tomography data (as compiled by Buiter et al. 2012) discount the possibility of downward mantle flow associated with delaminated lithosphere (as suggested by Downey et al. 2011) and show that the Congo basin is still underlain by a ~300 km thick high-velocity mantle. The negative Bouguer anomaly in the basin can be explained by the low density of the Mesozoic-Cenozoic sedimentary units in the basin (Buiter et al. 2012), which should be isostatically balanced to explain the current elevation (~400 m above sea level) (Buiter et al. 2012). This raises the

possibility of a higher density region in the crust or mantle lithosphere (Downey and Gurnis 2009), although its nature and extent are unknown.

I suggest that even where metasomatism does not weaken the cratonic lithosphere enough to rift it, increasing its density by refertilization may still have effects on the surface. Slow subsidence could be explained by a gradual increase in density of the CML, whereas rapid uplift could result from delamination or convective removal of part of the lithosphere. Rapid subsidence would follow as the lithosphere regains isostatic balance. The total subsidence of a basin that is the result of refertilization, and filled with sediment can be approximated by a local isostatic balance equation (Equation 3.1).

$$d_S = (\Delta\rho \times d_{ML}) / (\rho_{SLM} - \rho_S) \quad (3.1)$$

Where d_S is the depth of sediments filling the basin, $\Delta\rho$ the change in density in the CML, d_{ML} the thickness of CML, ρ_{SLM} the density of the sublithospheric mantle, and ρ_S the density of the sediments. The tradeoff between increasing the CML density and replacing it with less dense sediments easily results in a basin ~5-6 km deep. For example, if we take $\Delta\rho$ = 43 k gm^{-3}, d_{ML} = 215 km, ρ_{SLM} = 3378 kgm^{-3} and ρ_S = 2200 kgm^{-3} then d_S = 7.85 km (Figure 3.8). In this case, we assume no convective removal has taken place.

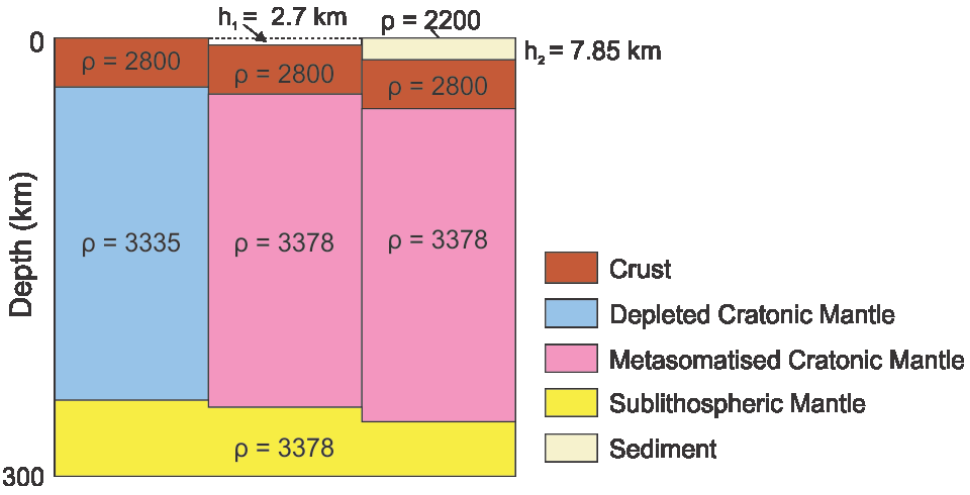

Figure 3.8. Isostasy of a metasomatized lithosphere. Isostatic readjustment after refertilization results in a basin 2.7 km deep without any sediment loading. The depth to the top of the crust is increased to 7.85 km when sediments with a density of 2200 kg m^{-3} are added. The effects of temperature changes and convective removal of the mantle lithosphere are not taken into account in this diagram.

The Ordos Basin on the western North China Craton is a key location to understand the effects of mantle refertilization on intracratonic basin formation, owing to its proximity to the well-known Mesozoic alteration and thinning of the adjacent eastern North China Craton. The Ordos Block has a complex tectonic history, but was stable and acted as an intraplate cratonic basin in the late Mesozoic. At that time large-scale thinning of the eastern North China Craton was in full progress (Menzies et al. 2007). In the Cenozoic some extension took place on the edges of the Ordos Block along old suture zones (Yinchuan-Hetao and Shanxi rift systems), but it is internally undeformed (Zhang et al. 1998). Although the western North China Craton is still underlain by a 150 km thick lithosphere, limited xenolith data indicate that the lithospheric mantle is late Archean to Early Proterozoic in age and has experienced multiple metasomatic events (Xu et al. 2008, Tang et al. 2013b). This is further supported by seismic and conductivity data (Jiang et al. 2013, Dong et al. 2014).

3.5 Summary

The low density (~3331 kg m^{-3}) and high dehydration of cratonic mantle lithosphere (CML) are interpreted to reflect the high degree of Archean melt extraction that formed them. These characteristics, combined with a cold geotherm, make CML strong with a high viscosity and integrated lithospheric strength. Thus, to weaken and thin a craton and ultimately rift it, I appeal to the recently proposed process of refertilization through melt metasomatism. Refertilization of CML can lead to an increase in density (Mg#), an increase in H_2O content, and an increase in temperature, and may lead to convective removal and thin cratonic lithosphere. Evidence for mantle metasomatism is mainly provided by xenolith and xenocryst data, reinforced by observations from exposed ultramafic massifs. The field data suggest that a reactive melt front is preceded by hot fluids, which alter the trace-element compositions (HREE and LREE) of the wall-rock.

Chapter 3 has been designed as an introduction to and motivation for Chapter 4, where I investigate the amount of metasomatic weakening needed to rift a craton that is initially protected by a “standard” lithosphere. The models are more complex than those of Chapter 2, and now include contrasts in thermal properties (Moho at 600°C in “standard” lithosphere, Moho at 450°C in craton lithosphere), thickness (140 km vs. 250 km), density (3360 kg m^{-3} vs

3335 kg m^{-3}), and viscosity (craton is cooler and more dehydrated than the standard lithosphere). Melt injected during metasomatism increases the volume, temperature, H_2O content, and density of the CML. This process is highly simplified with respect to the corresponding natural processes as described in this chapter, but represents all of the major contributing physical processes. In the models, I explicitly consider melt metasomatism. This simplification is justified by considering that the effects of fluid metasomatism may also increase the density and temperature of the CML peridotites (Griffin et al. 2009), although possibly to a lesser degree. Since fluids precede the melt metasomatism reaction front in nature, rehydration of the mantle lithosphere is likely, although not necessarily the result of melt metasomatism, as in the models. Therefore, I implicitly include the effects of fluids in rehydrating the CML as part of the modelled melt-metasomatism process.

In the modeling, up to 30% melt is added to the original volume, which is the same amount of melt extraction thought to have been required to form the CML (Bernstein et al. 2007, Pearson and Wittig 2008). By the end of metasomatism, the CML has the same density and temperature-dependent viscosity as the sublithospheric mantle. There are two ways in which we can add the melt: 1) throughout the CML at the same time, and; 2) assuming a reactive front mechanism, which metasomatises one 20-km thick layer at a time. The effect of metasomatism over 3 Ma, 10 Ma, 30 Ma, or 50 Ma time intervals is investigated. I think 3 Ma for each 20-km layer is a reasonable estimate for the reactive front models, whereas 30-50 Ma is more likely for the whole lithosphere.

My ultimate goal is to rift an initially strong “protected” craton, such as seems to have happened to the North China Craton in the Mesozoic. However, another side-effect of metasomatism may be isostatic readjustment leading to subsidence and/or uplift of the surface, resulting in the formation and erosion of intracratonic basins.

Chapter 4 Metasomatism and the Weakening of Cratons: How to Create Intracratonic Basins and Rift Cratons

4.1 Preface

This chapter is a draft of the paper "How to rift strong cratons: metasomatism and the intracratonic basin connection" by Stefanie Wenker and Christopher Beaumont. An edited version will be submitted to the journal *Earth and Planetary Science Letters.* SOPALE, the numerical modeling software used in this research was originally developed by Fullsack (1995) and expanded as SOPALE-nested by Beaumont et al. (2009) to include the nested domain. Its features were further expanded by numerous contributions by the Dalhousie Geodynamics Group. The numerical code needed for melt-addition and metasomatism was developed by C. Beaumont and programmed by D. Guptill specifically for this project (Appendix A). Stefanie Wenker was responsible for the design, computation and analysis of the numerical models, as well as writing the corresponding manuscript. These steps of the process were completed with guidance, discussions, and collaboration with C. Beaumont.

4.2 Abstract

Cratons are strong and their preservation demonstrates that they resist deformation and fragmentation. Yet several cratons are rifting now, or have rifted in the past. We suggest that cratons need to be weakened before they can rift. Specifically, metasomatism of the depleted dehydrated craton mantle lithosphere is a potential weakening mechanism. We use 2D numerical models to test the efficiency of simulated silicate-melt metasomatism and rehydration to weaken craton mantle lithosphere roots. This process effectively increases root density through a melt-peridotite reaction, and reduces root viscosity by increasing the temperature and rehydrating the cratonic mantle lithosphere. The models are designed to investigate when a craton is sufficiently weakened to undergo rifting and is no longer protected by adjacent standard Phanerozoic lithosphere. We find that cratons only become vulnerable to rifting after significant melt metasomatism (~30% by volume) and thinning of progressively more gravitationally unstable cratonic mantle lithosphere from >250 km to ~100 km. Furthermore, our results indicate rifting of cratons depends on the timing of extension, with

respect to metasomatism. The key effect is the associated increase in temperature which must have time to reach peak values in the uppermost mantle lithosphere.

An additional effect is that the craton surface subsides isostatically to balance the increasing density of craton mantle lithosphere where it is moderately metasomatized. We suggest that subsidence and subsequent uplift of intracratonic basins, and cratonic rifting constitute evidence of progressive metasomatism of cratonic mantle lithosphere.

4.3 Introduction

Cratons are distinctly different from Phanerozoic lithosphere (Griffin et al. 2009b), which participates in tectonics actively, and is recycled continuously. The high yield strength of cold cratonic mantle lithosphere (CML), combined with the secondary effects of high viscosity and neutral buoyancy (Jordan 1975), has been used to argue in favor of the longevity of cratons. This argument is supported by studies of CML rheology (Hirth and Kohlstedt 1996, Griffin et al. 2009b, Karato 2010) and geodynamical studies (Doin et al. 1997, Lenardic and Moresi 1999, Lenardic et al. 2003, Sleep 2003, O'Neill et al. 2008, Beuchert and Podladchikov 2010, François et al. 2012, Yoshida 2012, Wang et al. 2014). Additionally, it has been shown that strong lithosphere is protected against deformation by surrounding weaker lithosphere (Yoshida, 2010, 2012; Lenardic et al., 2000, 2003; Gorczyk et al., 2013; Corti et al., 2007; Wenker and Beaumont, sub.). Under these circumstances the weak lithosphere, with an overall lower integrated strength, will deform with a higher strain rate during extension than the stronger CML and, therefore, necking instabilities may grow faster in this weaker, pliable lithosphere (Control 2 of Wenker and Beaumont, sub.).

Since cratons are already strong and protected by surrounding weaker lithosphere, why do they thin and eventually rift? This certainly occurred in the case of the North China Craton (Menzies et al. 2007, Tang et al. 2013a), the Tanzanian Craton (Foster and Ebinger 1997, Ebinger et al. 1997), and the North Atlantic Craton, which is apparently cut by the Labrador Sea (Tappe et al. 2007, 2011, Sand et al. 2009, St-Onge et al. 2009).

In the past 20 years, geochemical data from xenoliths and xenocrysts have provided evidence that even if a cratonic root is stable, it may be altered by fluid and/or melt

metasomatism (Rudnick et al. 1998, Carlson et al. 2005, Griffin et al. 2009b, Lee et al. 2011). This widespread process can cause refertilization, rehydration, and increase the geothermal gradient, and may partly counteract the characteristics that allow cratons to survive (O'Reilly et al. 2001, Lee 2003, Schutt and Lesher 2010). Refertilization leads to an increase in the density of originally depleted mantle. Rehydration results in a decrease in the bulk viscosity by a factor of up to 140 at constant stress (Hirth and Kohlstedt 1996), and a temperature increase decreases the temperature-dependent viscosity, and may also induce fractional melting, further decreasing the viscosity (Hirth and Kohlstedt 1995). As a whole, metasomatism alters the rheology of the mantle lithosphere and may lead to destabilization of the cratonic root (Schutt and Lesher 2010). We propose that this type of weakening is required in order to rift an originally strong craton.

Here we use 2D-numerical models to investigate the stability of cratonic lithosphere under extension after varying degrees of metasomatism. The 2D models comprise welded adjacent regions of "standard" and "cratonic" lithosphere. Both regions contain small inherited weaknesses that represent the vestiges of previous tectonic processes. In simple terms they can be interpreted as weak sutures, shear zones, or inherited preferred orientations (Tommasi and Vauchez 2001, Manatschal et al. 2015). The models are used to investigate where extension localizes in the model and under what circumstances rifting shifts from the standard lithosphere to the craton as the CML is progressively weakened by melt metasomatism. In particular, we add basaltic melt to the CML which increases its density from 3335 kg m^{-3} (Mg# 92) to 3378 kg m^{-3} (Mg# 89) (Lee 2003, Bernstein et al. 2007), reduces the viscosity by a factor 5 as a result of rehydration, and increases temperature (by up to 250°C) from the heat released by cooling and crystallization of the melt. This metasomatism may result in convective removal of part of the CML. Metasomatism takes place under non-extensional boundary conditions, and the models are only tested for rifting at specified times near the end of or after metasomatism.

We present four M-type models in which 30% melt is added to the CML as a whole over 3 Ma, 10 Ma, 30 Ma and 50 Ma, respectively. These models illustrate convective removal in an extreme end-member as well as the effects of heat diffusion as a function of the duration of metasomatism. We next illustrate the more geologically realistic effects of progressive

metasomatism (reactive front metasomatism) in the RF model by metasomatising 20 km thick layers from the bottom up sequentially. This process is thought to be responsible for the geochemical trends seen in the Lherz and Ronda Massifs (Lenoir et al. 2001, Le Roux et al. 2007, 2009, Soustelle et al. 2009). Finally, we present the case for a link between refertilization of CML and the formation and evolution of intracratonic basins.

4.4 What Makes Cratons Vulnerable to Rifting

Many of the modeling studies that investigated the long term stability of cratons focused on thermal erosion by convective mantle removal (Doin et al. 1997, Shapiro et al. 1999, Sleep 2003, Wang et al. 2014) and delamination (Gorczyk et al. 2012, 2013). These processes have been suggested for the Colorado Plateau (Levander et al. 2011, Bashir et al. 2011), North China Craton (Gao et al. 2009), and the North Atlantic Craton (Tappe et al. 2007, 2011, Sand et al. 2009). Here we take the view, supported by studies of craton longevity noted above, that these processes may thin the CML, but not weaken it sufficiently to cause rifting where it is surrounded by weaker lithosphere. Instead we consider the effects of melt interaction with depleted CML peridotite, a process that reverses the internal characteristics that make cratons strong.

Widespread refertilization of CML is supported by major and trace element data, and Sr, Nd, and Os isotopic compositions from xenoliths (Griffin et al. 2009b, O'Reilly and Griffin 2013, Tang et al. 2013b). Metasomatism is the interaction of fluids and melts with the CML (Foley 2008, O'Reilly and Griffin 2013, Zheng et al. 2015). Here we focus on "stealth" metasomatism, where basaltic melts react with harzburgites to form lherzolites (O'Reilly and Griffin 2013). This type of metasomatism rehydrates the CML, increases the density by increasing the FeO concentration (Schutt and Lesher 2006), and increases the temperature of the CML. The rehydration component decreases the viscosity of CML, making it easier to deform, and also decreases the melting temperature, although generally not enough to induce significant melting at high pressures (Foley 2008, Lee et al. 2009, Zheng et al. 2015). The refertilization component increases the CML density and may make it gravitationally unstable (Griffin et al. 2003b). The delivery of melts to the CML results in an increase in temperature (O'Reilly and

Griffin 2013), which on the one hand reduces the negative buoyancy effect of increasing the density, but on the other hand weakens the CML by decreasing the viscosity.

4.5 Brief Summary of Modeling Methods

The calculations (described in detail in Appendix A) are made with an arbitrary Eulerian-Lagrangian finite-element method using the software SOPALE-nested (Fullsack 1995, Beaumont et al. 2009). Deformation is described by frictional-plastic and thermally activated power-law viscous rheologies that are scaled by a scaling factor *f* to change the relative strength among models and as the models evolve (Appendix A). The crust is described by the "Wet" Quartzite (WQz) flow law (Gleason and Tullis 1995) and the mantle lithosphere and sublithospheric mantle are described by a "Wet" Olivine (WOl) rheology (Karato and Wu 1993).

The upper-mantle-scale 2D models (Figure 4.1) comprise adjacent regions of thermally stable standard (left) and cratonic lithosphere (right) containing small weak regions designed to initiate necking instabilities where the model extends under velocity boundary conditions. Extensional boundary conditions are only applied after metasomatism has altered the mantle lithosphere. The timing of rifting tests varies between the models, and is specified in the results section.

The thickness, thermal regime, and rheology change across the vertical lithospheric boundary at the center of the model. The crust has a uniform thickness of 35 km, the standard lithosphere is 140-km thick, and the cratonic lithosphere is 250-km thick. The base of the CML geometry is inclined to reflect any prior flow and thinning of the CML and to represent an initially stable system. The thermal parameters within each lithosphere differ (Table A.1) and result in Moho temperatures of 600°C in the standard lithosphere and 450°C in the cratonic lithosphere. The base of both lithospheres is initially at 1350°C.

In the modeling section we investigate what degree of weakening makes cratons vulnerable to rifting and we parameterize the weakening of the CML in terms of melt metasomatism. There are ten 20-km thick layers in the CML and one 15-km thick top layer (just below the Moho). This gives us the flexibility to metasomatise the whole lithosphere concurrently, or just one layer at a time. The degree of metasomatism decreases toward the

central lithospheric boundary over a horizontal distance of 200 km, and the 50-km wide region of the cratonic lithosphere adjacent to the boundary does not have any melt added. This design represents the case where metasomatism is confined to the interior of the craton and avoids complexities caused by metasomatism spanning the boundary with the standard lithosphere.

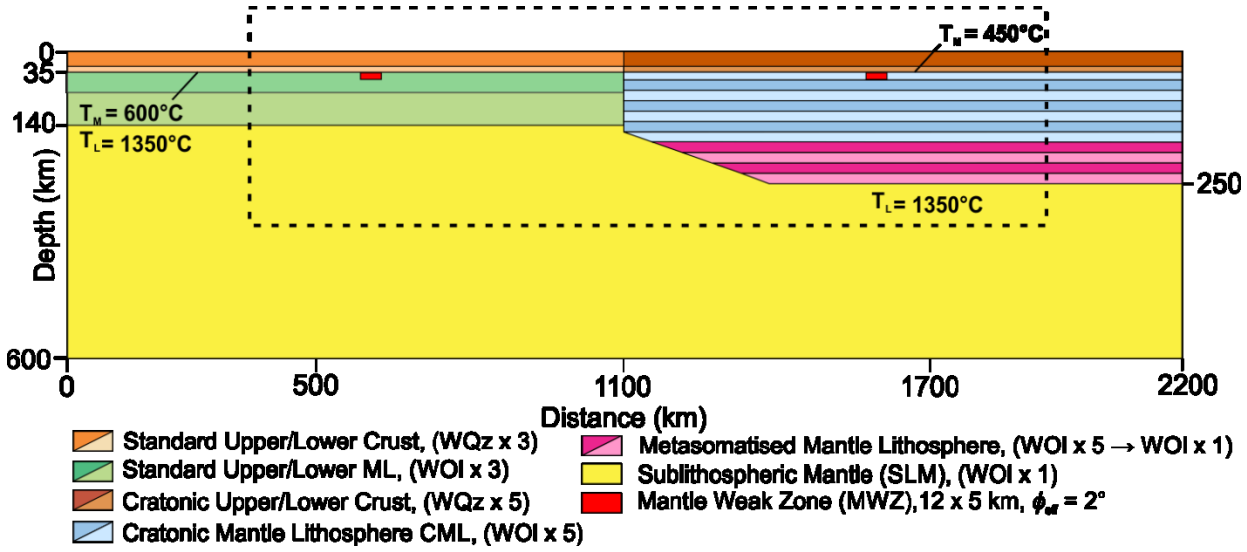

Figure 4.1. Model design. The standard lithosphere on the left is 140 km thick and has a Moho temperature of 600°C. In contrast, the cratonic lithosphere is 250 km thick and has a Moho temperature of 450°C. The boundary between the standard and cratonic lithosphere is located at 1100 km. Two mantle weak zones (12 x 10 km) with identical properties are embedded at equal distances from the boundary, one in each lithosphere. The standard lithosphere has a crust governed by the WQz x 3 flow law (see Appendix A for explanation of *f*-scaling) and a mantle lithosphere rheology of WOl x 3. Cratonic lithosphere has a crust with WQz x 5 and mantle lithosphere that starts at WOl x 5. As metasomatism proceeds (pink), the CML becomes more hydrated; this weakening corresponds to a linear change in model mantle lithosphere rheology to WOl x 1. The inclined base of the CML adjacent to the standard lithosphere is designed to reflect any prior flow and thinning of the CML and to represent an initially stable system. The higher resolution domain is outlined by the dashed box. ML = mantle lithosphere. Temperature distributions presented in the results section are taken at x = 500 km for the standard lithosphere and x = 1700 km for the cratonic lithosphere.

4.6 Refertilizing Cratons in the Numerical Models

Parameterized melt metasomatism is calculated for each time step (see Appendix A for details). We add uniformly distributed basaltic melt at 1300°C and at a steady volumetric rate to selected layers in the CML. Our focus is the effect of the melt as it permeates the CML layers, and we therefore do not specify how and where melt is produced, which could be from a mantle plume or melting in the mantle wedge above a subducting slab located beyond our right model boundary. We also assume that the melt percolates rapidly to the layer that is being

metasomatized, such that the percolation timescale for the Darcy flow is negligible by comparison with the duration of metasomatism (McKenzie 1989, Vernières et al. 1997, Ranalli et al. 2007). In most models, a total of 30% by volume of melt is added to specified layers at a uniform rate determined by the duration of metasomatism. We aim to refertilize the CML from depleted (Mg# 92) to a fertile sublithospheric mantle composition (Mg# 89), and we choose 30% melt addition as it the same amount of melt extraction that is thought to have formed CML from Archean primate mantle (Lee 2003, Griffin et al. 2003a, Bernstein et al. 2007). For each timestep the increment of melt added to each layer at the given initial temperature is treated in a self-consistent manner in terms of heat and mass balance. We assume that the melt crystallizes and cools to the ambient temperature during each timestep. Heat is conserved as the hot melt is added and cools, and mass is conserved during reaction with the peridotite. The associated change in volume during the reaction is enforced on the model layer (Appendix A).

In summary, the addition of melt has three effects. 1) As hot melt cools and crystallizes all heat released, including latent heat, is absorbed by the CML, thereby increasing its temperature, decreasing its viscosity, and causing minor melting if the temperature is high enough. 2) The melt reacts with the peridotite to make it less depleted as measured by the Mg# (Lee 2003), which progressively increases its density from 3335 kg m^{-3} (Mg# 92) to a specified maximum of 3378 kg m^{-3} (Mg# 89). By the time 30% by volume of melt has been added to the CML its material density is equal to that of the sublithospheric mantle (Bernstein et al. 2007). 3) The CML is incrementally rehydrated by linearly changing the scaling factor in the viscous flow law from WOl x 5 to WOl x 1 as the 30% melt increment is added, so that it evolves from an effectively dry to a hydrated rheology (Appendix A).

4.7 Rifting Cratons in the Models

4.7.1 Stability of the Initial Model Configuration

All models were run for an initial phase of 1 Ma before metasomatism was started to isostatically balance the two adjacent lithospheres. This produces a stable system with a weak component of edge-driven convection (Figure 4.2a). A reference model was also computed for 100 Ma without any metasomatism, to assess the stability of the initial geometry. We want to

make sure that any convective instability in the metasomatism models presented in the next sections is the result of the changes in the CML during metasomatism and not a consequence of the initial geometry (Sleep 2003, 2007). The result at 100 Ma (Figure 4.2b) shows a minimal amount of buoyant lower lithosphere counterflow (<100 km) at the vertical lithospheric boundary, and some smoothing of the initially inclined base of the CML. No vigorous convection of the sublithospheric mantle is seen and there is no thinning of the thickest part of the CML. We conclude that any destabilization of the CML in the models greater than this minor flow is the result of the metasomatism.

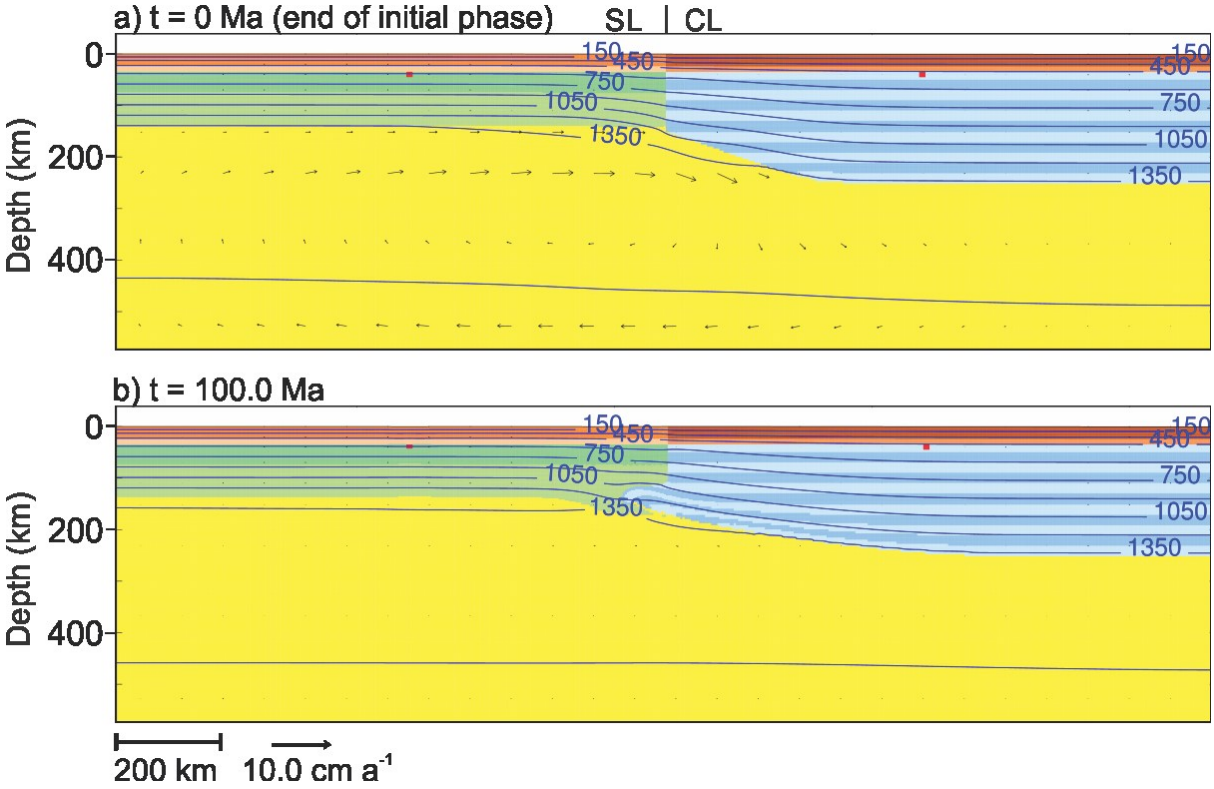

Figure 4.2 Initial model design and reference model after 100 Ma. a) Model after the initial phase of 1 Ma, this is t = 0 Ma for all the models in the results section. b) Reference model after 100 Ma. Only a small amount of buoyant counterflow has developed at the vertical lithospheric boundary. Velocities in the convecting mantle are less than 1 cm a^{-1} and no CML is removed by basal shear. Temperature contours (blue) are shown in °C. The boundary between the standard lithosphere (SL) and the cratonic lithosphere (CL) is shown.

4.7.2 Rifting Tests

No rifting is attempted in the basic models until a later specified time. Instead, they are computed progressively through the metasomatism phase and beyond with zero velocity boundary conditions on the lithosphere. The susceptibility to rifting and the position of the

localization and necking instabilities is tested using the 'restart' facility of SOPALE-nested. Any of the output files generated during the model computation can be used as an initial state from which to test the effects of rifting by 'restarting' with uniform velocity boundary conditions (+/- 0.5 cm a^{-1}) applied to the lithosphere at the model boundaries. By performing a series of these rifting tests we determine where and under what circumstances the localization of rifting relocates from the standard lithosphere, which is initially weaker, to the craton. The purpose of this approach is to understand how natural systems may behave if lithospheric extension starts during metasomatism or after it has finished. The timing of rifting tests corresponds to maximum weakening factors, such as the time at which the Moho reaches its maximum temperature, or when the CML first reaches its final thickness. The results of the rifting tests are discussed below. The time reported is referenced to the start of metasomatism (Figure 4.2a).

4.7.3 Simultaneous Metasomatism of the Whole Cratonic Mantle Lithosphere

M-type models (Table 4.1) investigate the effects of metasomatism where the whole CML (all 11 layers) is simultaneously metasomatized over 3 Ma (M3), 10 Ma (M10), 30 Ma (M30), and 50 Ma (M50) intervals, respectively. The rate of melt addition is calculated such that at the specified end time 30% of the original volume has been added in melt. In nature the rate of melt addition is a result of the permeability and availability of melt, but flow can be as rapid as 20-50 m a^{-1} (Bodinier et al. 1990, Le Roux et al. 2007). These models are regarded as the simplest archetypes and are used to establish the basic behavior of the models. We take M30 as the most likely duration and present its results in some detail, followed by a comparison with the M3, M10, and M50 cases. The primary difference among these models is the rate at which the density of the CML increases and the viscosity decreases versus the time available for the heat from the melt to diffuse. All of these model receive the same total volume of melt.

In the M30 model, by the time that 25% melt has been added (25 Ma) a gravitational instability has started to develop at the bottom left edge of the metasomatically thickened CML (Figure 4.3a). Delamination caused by this Rayleigh-Taylor instability has thinned approximately half of the craton by the end of metasomatism (30 Ma; Figure 4.3b). The convective velocities at the bottom of the CML have increased (up to 15 cm a^{-1}) by comparison with the initial edge-

driven convection (<1 cm a^{-1}). The "delamination front" propagates rapidly across the CML in ~6 Ma and thins the CML to the model boundary (Figure 4.3c). The residual cratonic lithosphere is now 120 km thick above the thinned region (Figure 4.3c).

Model	Max Moho Temp. (°C)	Time of Max thinning (Ma)	Moho Temp. at Max Thinning (°C)	Rifting tests and position of localization Ma (S vs C)			
M-Type							
M3	635	10	605	3(S)	5(S)	10(C)	
M10	625	17	595	10(S)	15(S)	17(S)	
M30	600	37	585	30(S)	37(S)		
M50	580	59	565	50(S)	56(S)		
Sensitivity tests							
M(T)3	630	-	-	5(S)			
M(H)3	450	-	-	-			
M(F)3	450	-	-	-			
M(H-F)3	450	-	-	20(S)			
M(U)3	620	-	-	3(S)			
RF-Type							
RF33-3	665	28	450	27(S)	30(S)	33(S)	39(S)
Sensitivity tests				-			
RF(T)33-3	685	-	-	33(S)			
RF(H)33-3	450	-	-	33(S)			
RF(F)33-3	450	100*	450	33(S)			
RF(H-F)33-3	450	100*	450	33(S)			
RF(SL2)33-3	665	28	450	33(S)			
RF(SL3)33-3	665	28	450	33(C)			
RF(25%)33-3	640	60	550	-			
RF(20%)33-3	615	-	-	-			
S-Type				Maximum Subsidence km		Ma	
S3	525	-	-	1.07		3	
S30	510	-	-	1.24		80	
SRF33	545	-	-	1.21		80	

Table 4.1. Model result summary. In rifting test column, S stands for localization in the standard lithosphere and C stands for localization in the cratonic lithosphere. The time in Ma is the time at which rifting was tested. * Models were computed to 100 Ma, but more thinning is expected after this time.

The temperature at the Moho has increased from 450°C to 600°C at 30 Ma (Figure 4.4c). This temperature increase is mainly a consequence of heating by the melt and there has been sufficient time for heat to diffuse upward into the crust so that the temperature at 25 km depth

has increased from 345°C to 440°C. However, the 30 Ma timescale is not long enough for significant heat to have been lost through the surface. The evolution of the temperature (Figure 4.4c) demonstrates the maximum temperature increase at 160 km depth and a minor increase in the surface geothermal gradient and the surface heat flux that begins at 25 Ma and peaks at 37 Ma. After metasomatism, the convective removal of lower CML affects the temperature of the lower 20 km of the residual lithosphere (~100-120 km depth; Figure 4.4c).

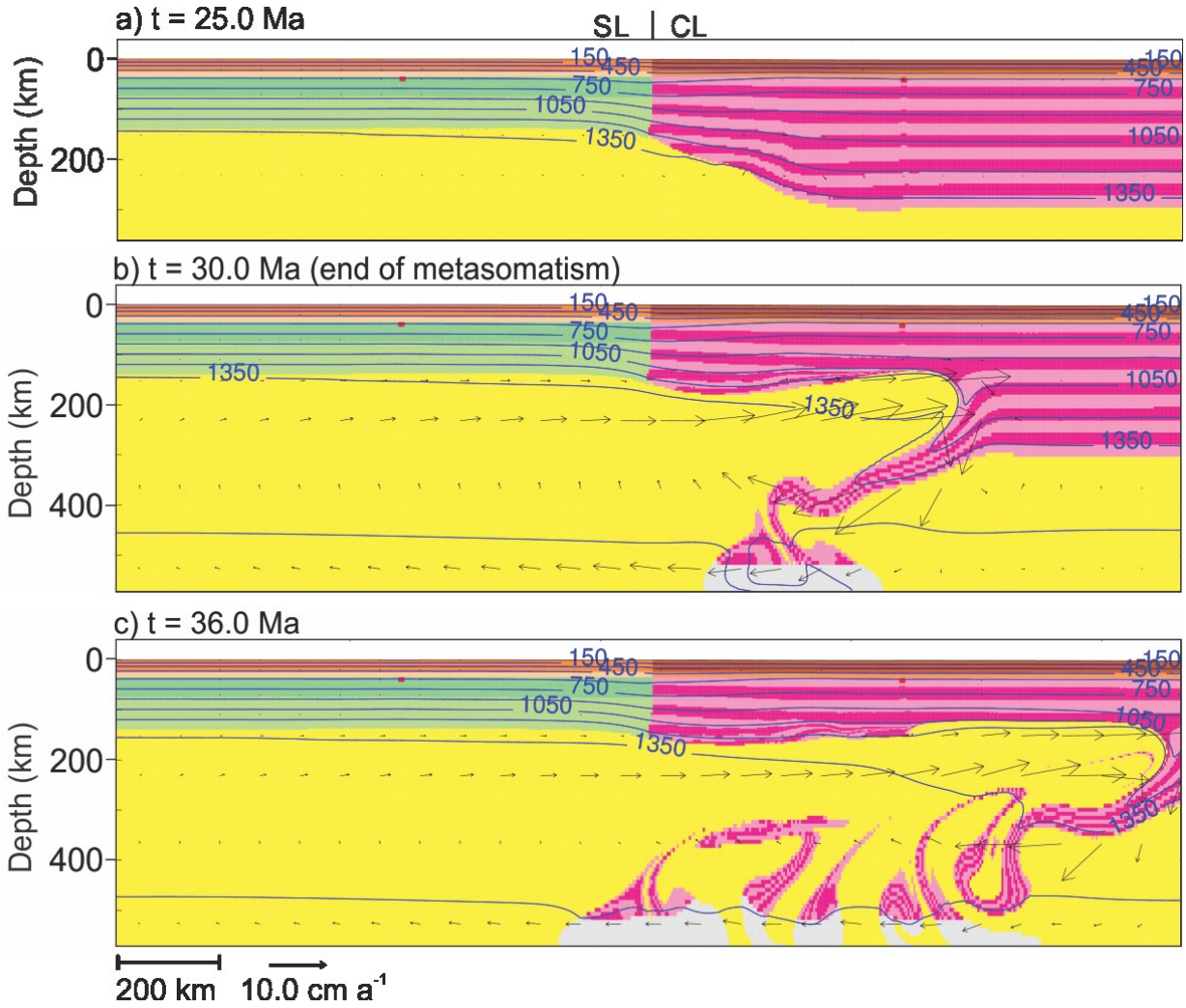

Figure 4.3. Convective removal of the CML in the M30 model. a) At 25 Ma the CML is starting to become unstable. b) At the end of metasomatism (30Ma) the delamination front is propagating and thinning the craton. c) Lithospheric thinning is complete at 36 Ma and in some places leaves the craton lithosphere thinner than the standard lithosphere.

In models M3, M10 and M50 (Figure 4.5), thinning and removal of the lower CML evolves in a similar manner to that in M30 (Figure 4.3), except that initiation of the Rayleigh-Taylor instability scales with the duration of metasomatism. In the M3 and M10 models the

initiation of the Rayleigh-Taylor instabilities happens right at the end or soon after metasomatism ends. In contrast, the instability develops 5 Ma before the end of metasomatism in the M50 model. In this case approximately half of the CML has delaminated by the end of metasomatism (Figure 4.5e).

The duration of metasomatism changes the amount of heat that diffuses. This is evident from the decreasing maximum Moho temperature with a longer duration of metasomatism (Table 4.1). M3 reaches the highest Moho temperature of all the M-type models as soon as metasomatism finishes (635°C; Figure 4.4a). The crustal geothermal gradient only starts noticeably increasing at this time and reaches its maximum by 10 Ma. In contrast, in M50 the crustal geothermal gradient has already reached its maximum by 50 Ma (Figure 4.4d). The temperature profiles of M30 and M50 have a similar character for their respective times at the end and after metasomatism (Figure 4.4c,d). Thinning of the CML is indicated by the sharp increase to 1350°C in the M30 and M50 profiles at 140 km depth. The deeper temperature decrease (225 km) is the result of the delaminating cold CML, which advects its temperature regime downwards as it delaminates. For all M-models, when the CML has reached its final thickness the temperature profile has stabilized again and resembles the starting thermal gradient, but with a vertically condensed distribution at a higher temperature (Figure 4.4, blue lines).

All M-type models were subjected to rifting tests. Model M30 was subjected to rifting tests at t1 = 30 Ma, t2 = 37 Ma. The strain rate and deviatoric stress are shown in Figure 4.6 for M30 and M3. In both of the M30 tests extension localizes in the standard lithosphere, resulting in necking and final breakup. Of all the M-type models, only in the rifting test for M3 at t3 = 10 Ma does localization relocate to the craton (Figure 4.6d,h). Right after metasomatism ends in M3, the Moho temperature is higher in the craton lithosphere than in the standard lithosphere (635°C vs. 600°C). However, the cratonic lithosphere is still under a lower strain rate than the standard lithosphere (Figure 4.6c). Only when the cratonic lithosphere has thinned to ~100 km does the strain rate become higher in the cratonic lithosphere, localizing deformation (Figure 4.6d). Evidently the craton is protected by its low strain rate throughout most of the metasomatism and convective removal of the CML.

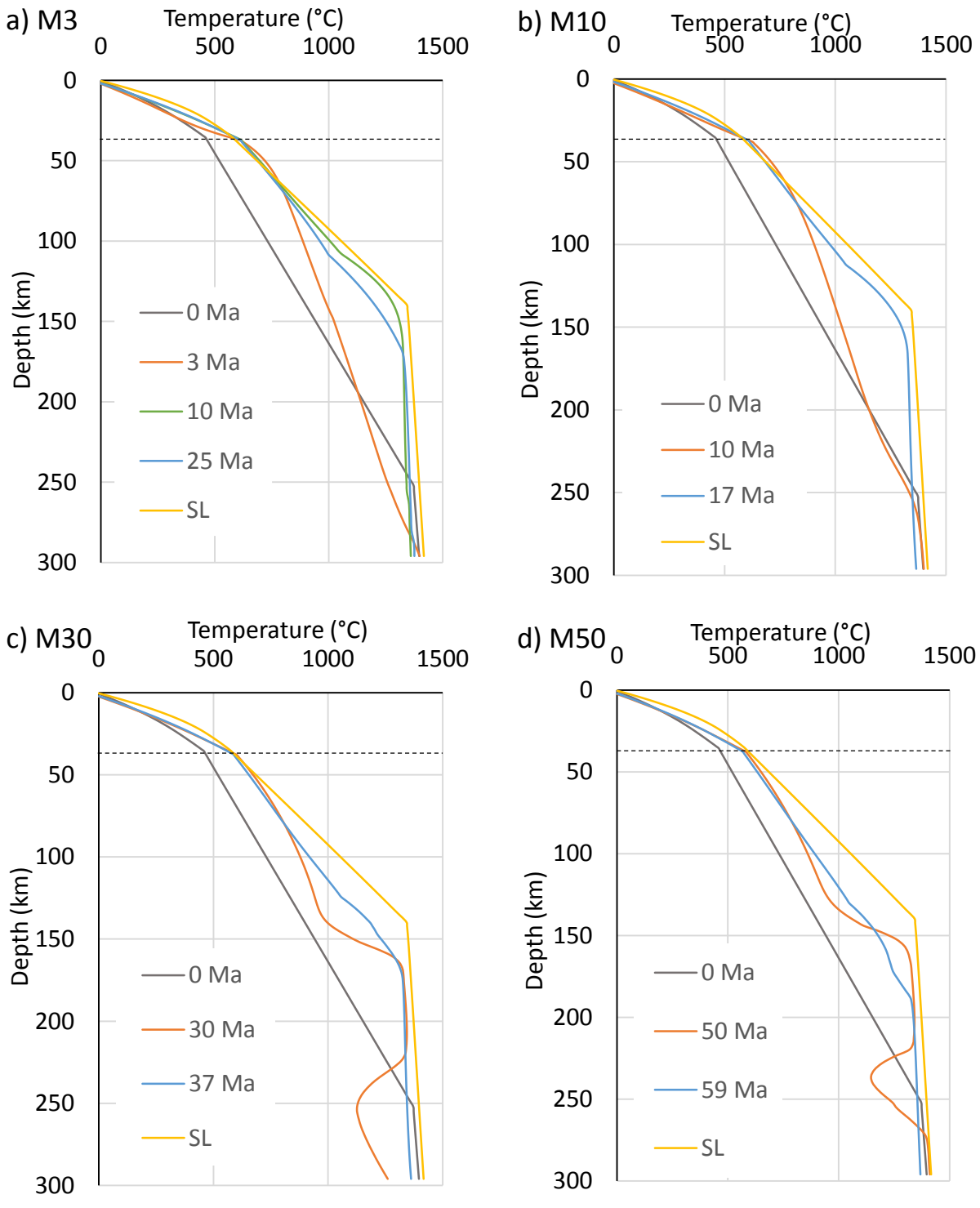

Figure 4.4. Temperature evolution with time for M-type models. a-d) Temperature evolution at x = 1700 km for M3, M10, M30 and M50. Standard lithosphere (SL) temperature distribution at x = 500 km. Moho depth is indicated by the dashed black line. For discussion see text.

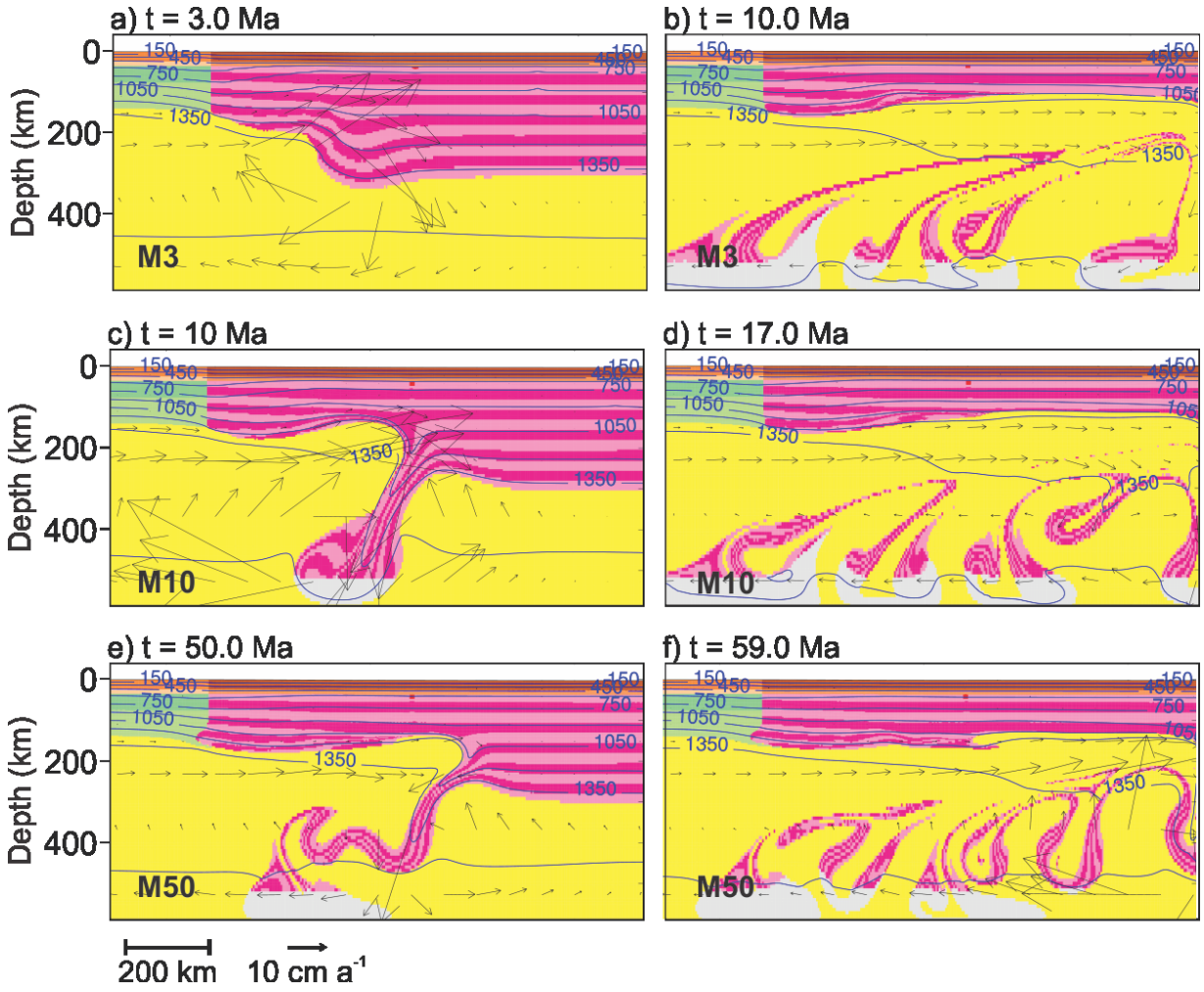

Figure 4.5. Model evolution for M3, M10, and M50. Only the evolution of the cratonic lithosphere is shown. a) A convective instability has started to form by the end of metasomatism (3 Ma). b) Maximum thinning of the CML in M3 has finished by 10 Ma. c) At the end of metasomatism in M10, a large part of the CML has delaminated. d) Thinning of the CML has reached the model boundary by 17 Ma. e) Thinning of the CML for the M50 model is further advanced as metasomatism is completed than in the other M-type models. By the end of metasomatism approximately half of the CML has delaminated. f) Maximum thinning is complete by 59 Ma.

The evolution in the relative strengths of the two lithospheres can be understood in terms of the effect of the evolving effective viscosity on the state of stress (Figure 4.6e-h). The stress is high in the stiff (brittle) standard upper mantle lithosphere. Although originally under high stress, the stress in the cratonic upper mantle lithosphere is lower at the end of metasomatism than in the standard lithosphere (Figure 4.6e,g). Heat diffusion after the end of metasomatism also affects the stress distribution. In the sequential deviatoric stress panels for M30 (Figure 4.6e,f) and M3 (Figure 4.6g,h) an increase in the deviatoric stress is discernible in

the upper CML as heat diffuses into the crust and the Moho temperature decreases. Nevertheless, there is an overall decrease in the integrated strength of the CML as the lower CML thins and is heated by upwelling sublithospheric mantle. In M3 the increase in the viscosity associated with the decreasing temperature at the Moho is insufficient to increase the integrated strength of the cratonic lithosphere, and the overall decrease in the integrated strength of the CML is sufficient so allow the cratonic lithosphere to rift.

The results for all the M-type rifting tests are listed in Table 4.1; the last column lists the results of the rifting tests in the following way: time(S) or time (C) for rifting in the standard (S) or cratonic (C) lithosphere, respectively. Tests were timed to correspond to the maximum Moho temperature (end of metasomatism) and when maximum thinning was achieved. The results show that rifting only localizes in the craton when the craton has thinned substantially and the Moho temperature in the cratonic lithosphere is similar to or higher than in the standard lithosphere.

4.7.4 Results of Propagating Reaction Front Models

It is highly improbable that the whole mantle lithosphere gets metasomatized at the same time and at the same rate as assumed in the M-type models. A closer approximation to gradual upward migration of metasomatism is the reaction front (RF33-3) model, where metasomatism happens one layer at a time, evolving progressively from the bottom to the top of the CML in 33 Ma. Metasomatism is active for 3 Ma in each layer and the layer receives the full 30% melt by volume in this time. The main difference with respect to the comparable M30 model is that the metasomatism propagates upward, therefore, lower regions of the CML are maximally weakened long before metasomatism starts in the upper layers. This evolution results in the development of multiple smaller scale convective instabilities in RF33-3, which peel away successive layers of the CML (Figure 4.7a-d) more slowly than in M30 where there is only one major thinning event (Figure 4.3). The upward propagating metasomatism front also means that the critical heating and weakening of the upper CML just below the Moho does not occur until close to 33 Ma.

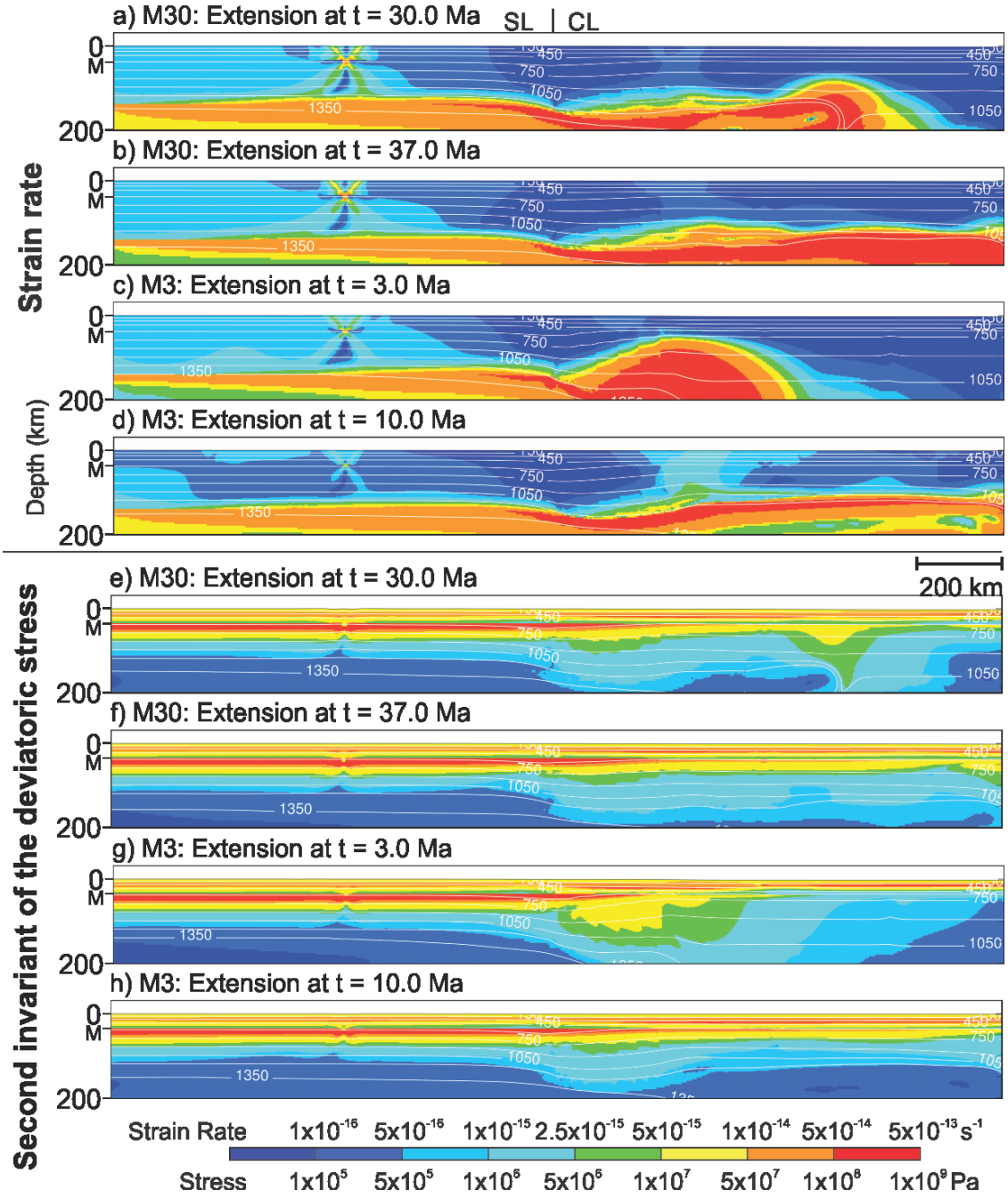

Figure 4.6. Rifting tests for M30 and M3. a) Strain rate plot of M30 at t1 = 30 Ma. Extension at the end of metasomatism for M30 does not weaken the craton lithosphere enough to rift the craton. A higher strain rate in the standard lithosphere leads to rifting in the standard lithosphere. b) Strain rate plot of M30 at t2 = 37 Ma. As the crust gets hotter and the CML thins (37 Ma), the craton lithosphere becomes weaker. c) Strain rate plot of M3 at t1 = 3.0 Ma (end of metasomatism). The CML has not thinned by the end of metasomatism in the M3 model, and even though the Moho is hotter than in the standard lithosphere, rifting localizes in the standard lithosphere. d) Strain rate plot at t2 = 10 Ma. Heat has diffused into the crust and the cratonic lithosphere has become weaker than the standard lithosphere. The red areas in the lower parts of the strain rate plots represent the delamination front. e,f) Deviatoric stress evolution for M30. The upper CML is under a lower stress than the standard upper mantle lithosphere. g,h) Deviatoric stress evolution for M3. As heat diffuses into the crust the stress in the upper CML increases. Temperature contours (°C) are shown in white. M = Moho.

The final thickness of the CML in RF33-3 (Figure 4.7d) is similar to the final thickness in M30 (Figure 4.3), but the Moho temperature is significantly hotter at the end of metasomatism in the RF33-3 model (665°C vs 600°C). The Moho temperature does not start increasing until after 27 Ma and has increased from 470°C to 540°C by 30 Ma (Figure 4.8). After the last layer has finished metasomatism the Moho temperature has reached 665°C.

Even after the 4th layer of the CML has metasomatized completely (12 Ma) there is only a small temperature deviation at 160-200 km depth from its original state (Figure 4.8; orange line). The character of this deviation marks the local increase (over a 20 km depth slice) in temperature during the metasomatism interval and a similar deviation can be seen for the 27 Ma, 30 Ma, and 33 Ma profiles, which represent the end of metasomatism for the 9th, 10th, and 11th layers, respectively. The maximum Moho temperature in the CML is higher in RF33-3 than in M30 as a result of heat diffusion from the 10th layer, before and after the start of metasomatism in the 11th layer.

Rifting tests were performed at t1 = 27 Ma, t2 = 30 Ma, t3 = 33 Ma, and t4 = 39 Ma (Table 4.1). The results show that even though the CML has thinned to 120-100 km by 27 Ma, rifting localizes in the standard lithosphere (Figure 4.9a). The Moho temperature increases to 540°C by 30 Ma, yet the strain rate remains higher in the standard lithosphere (Figure 4.9b). Even when metasomatism has finished, and the Moho temperature is higher than the Moho temperature in the standard lithosphere, localization occurs in the standard lithosphere (Figure 4.9d).

The stress distribution clearly shows the weakening effects of temperature in this case (Figure 4.9e-g). Where the cratonic upper mantle lithosphere is relatively cold, it remains strong (high stress) indicating that the viscosity is high. The stress in the cratonic upper mantle lithosphere is ~2 orders of magnitude lower after the final layer has metasomatized (Figure 4.9g).

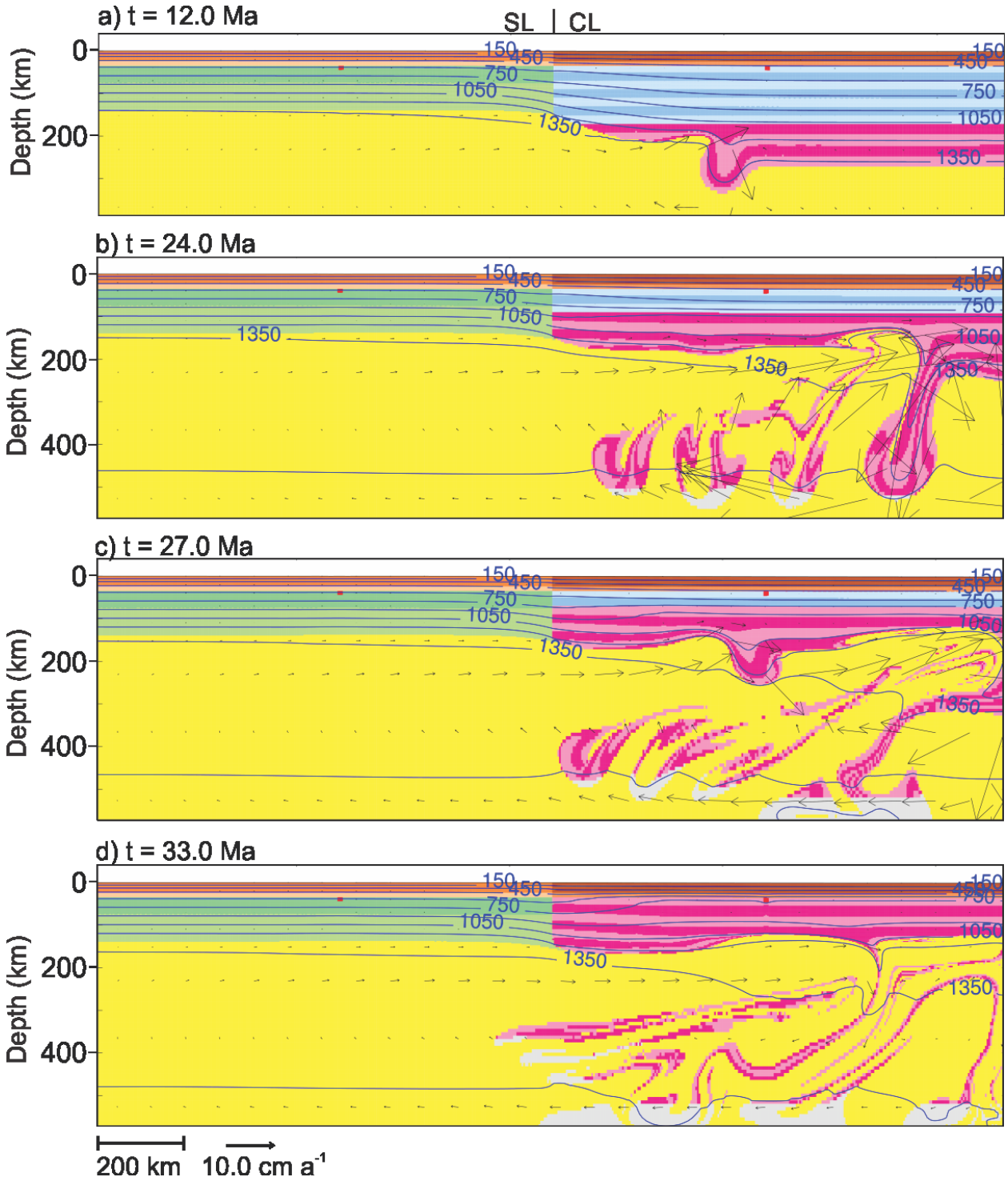

Figure 4.7. RF33-3 Metasomatism. The layers are sequentially metasomatized for 3 Ma at a time (pink layers). a) The instability starts after the 4th layer has completed metasomatism. b-c) Delamination is characterized by smaller instabilities than in the M30 model. d) Final thinning results in a 100-120km thick CML.

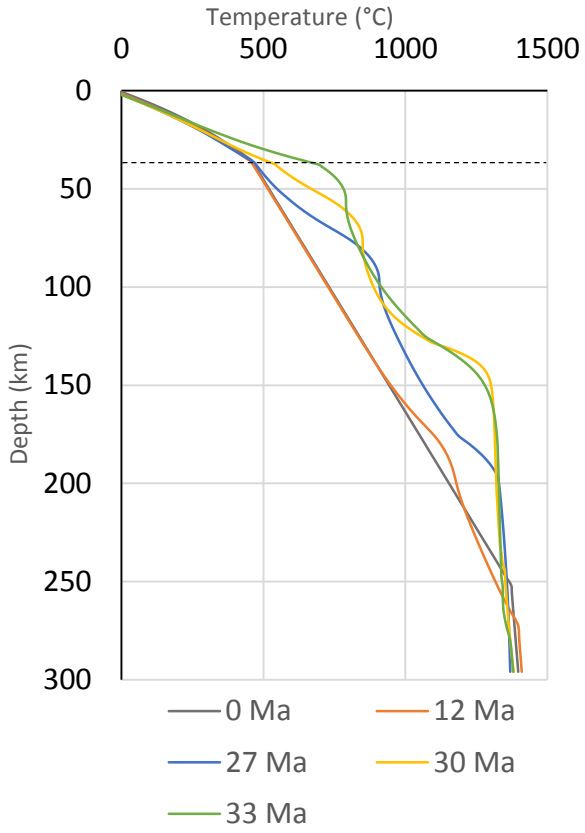

Figure 4.8. Temperature evolution of RF33-3 at x= 1700 km. A small temperature deviation from the 0 Ma profile can be seen after the 4th layer of the CML has finished metasomatising; 12 Ma. The temperature at the Moho (black dashed line) has not discernably increased by 27 Ma and only reaches its maximum after the top layer metasomatises (33 Ma).

4.7.5 Sensitivity of Reaction Front Models to the Components of Metasomatism

Model RF33-3 and the M-Type models demonstrate the total combined effects of metasomatism in regard to rendering the craton vulnerable to rifting, but we are also interested in the sensitivity of the results to the three contributing effects, namely: rehydration, refertilization, and increasing temperature. The series of models M( )3 and RF( )33-3 (Table 4.1) are used to investigate which effect dominates, and whether all three effects are required for craton rifting. The models are synthetic in that all three effects will occur together in natural systems and therefore suppressing one or more of them is not physically realistic. However, in the numerical models this is possible by: 1) decreasing the specific heat and latent heat of the melt by a factor 1.0 x 10^{-5} so that any heat added is negligible; 2) maintaining a constant density of the mantle peridotite during the reaction with the melt, and; 3) not changing the *f*-scaling of the olivine viscous flow law which suppresses the simulated rehydration.

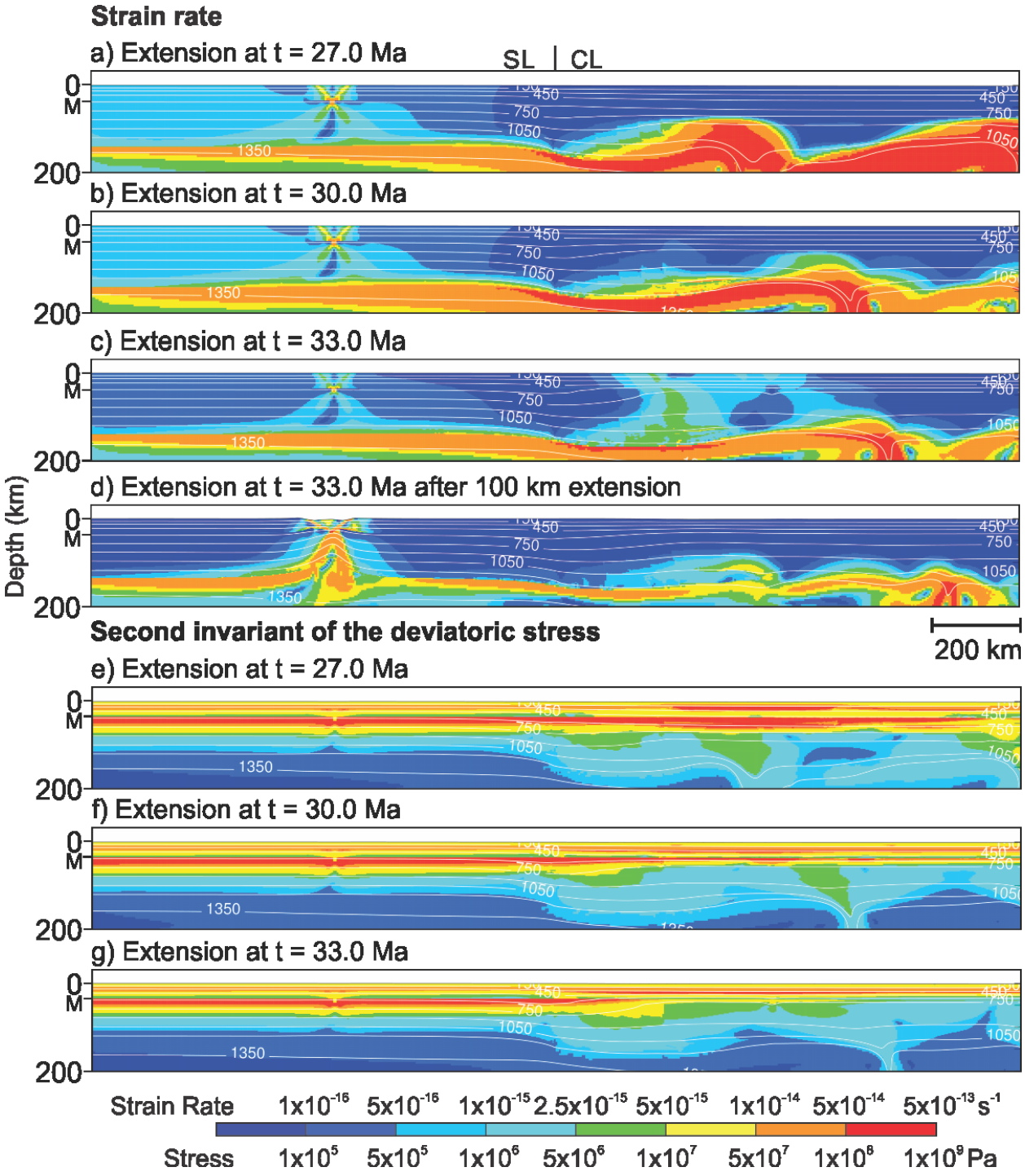

Figure 4.9. Rifting tests for RF33-3. a) Strain rate at 27.0 Ma. Although the CML has thinned to <150 km the strain rate is still higher in the standard lithosphere. b) The Moho temperature has reached 540°C at 30 Ma, but the strain rate is higher in the standard lithosphere. c,d) After metasomatism of the layer immediately beneath the Moho, the strain rate distribution has changed, but not enough to favor rifting in the cratonic lithosphere. e-g) The second invariant of the deviatoric stress illustrates the weakening of the craton. At 27.0 Ma the Moho temperature is 450°C and the upper layers have WOI x 5 and thus the upper CML is still strong and has a high deviatoric stress. As the Moho temperature increases and the *f*-factor decreases the upper CML becomes weaker (less viscous) and is under a lower deviatoric stress.

In model RF(T)33-3 only the effect of heating by the melt and the volume increase is retained. The results (Figure 4.10a) show an increase in Moho temperature to 685°C. By 33 Ma buoyant counterflow has started to smooth out the original inclined base of the CML. This temperature increase is even higher than in the RF33-3 model. In model RF(F)33-3 only the refertilization is retained (Figure 4.10b), which changes only the density. The viscosity of the CML has not changed at all and it takes a long time for the convective instability to start (100 Ma) in the viscous CML. In model RF(H)33-3 only the rehydration is included. The results (Figure 4.10c) are similar to RF(T)33-3, although the counterflow is enhanced with respect to the RF(T)33-3 model. The lower layers of the CML are more susceptible to buoyant counterflow in this case, since they are already at a relatively high temperature and thus have a lower viscosity. Finally, Model RF(H-F)33-3 demonstrates the combined effect of rehydration and refertilization. As the CML becomes denser and less viscous, small Rayleigh-Taylor instabilities form (Figure 4.10d) similar to the RF33-3 model. However, the extent of the delamination is much less than in the RF33-3 model. At 38 Ma the delaminating and thinning zone is only 80 km wide in the center of the CML. The colder upper CML remains stable and the final CML thickness is ~200 km. This result demonstrates the importance of the contribution from the heating by the melt.

The RF( )33-3 series of models was rift tested at t = 33 Ma. Neither hydration nor refertilization acting alone or in combination weakens the cratonic lithosphere sufficiently to rift it (Figure 4.11c,d), and the craton remains protected by the standard lithosphere. The temperature increase in RF(T)33-3 does weaken the cratonic lithosphere so that the strain rate is at least an order of magnitude higher in the cratonic mantle lithosphere immediately after metasomatism ends (Figure 4.11a). However, as heat diffuses the integrated strength of the cratonic lithosphere increases sufficiently for the MWZ in the standard stiff upper mantle lithosphere to localize a necking instability (Figure 4.11e,f). Rifting once again localizes in the standard lithosphere (Figure 4.11b).

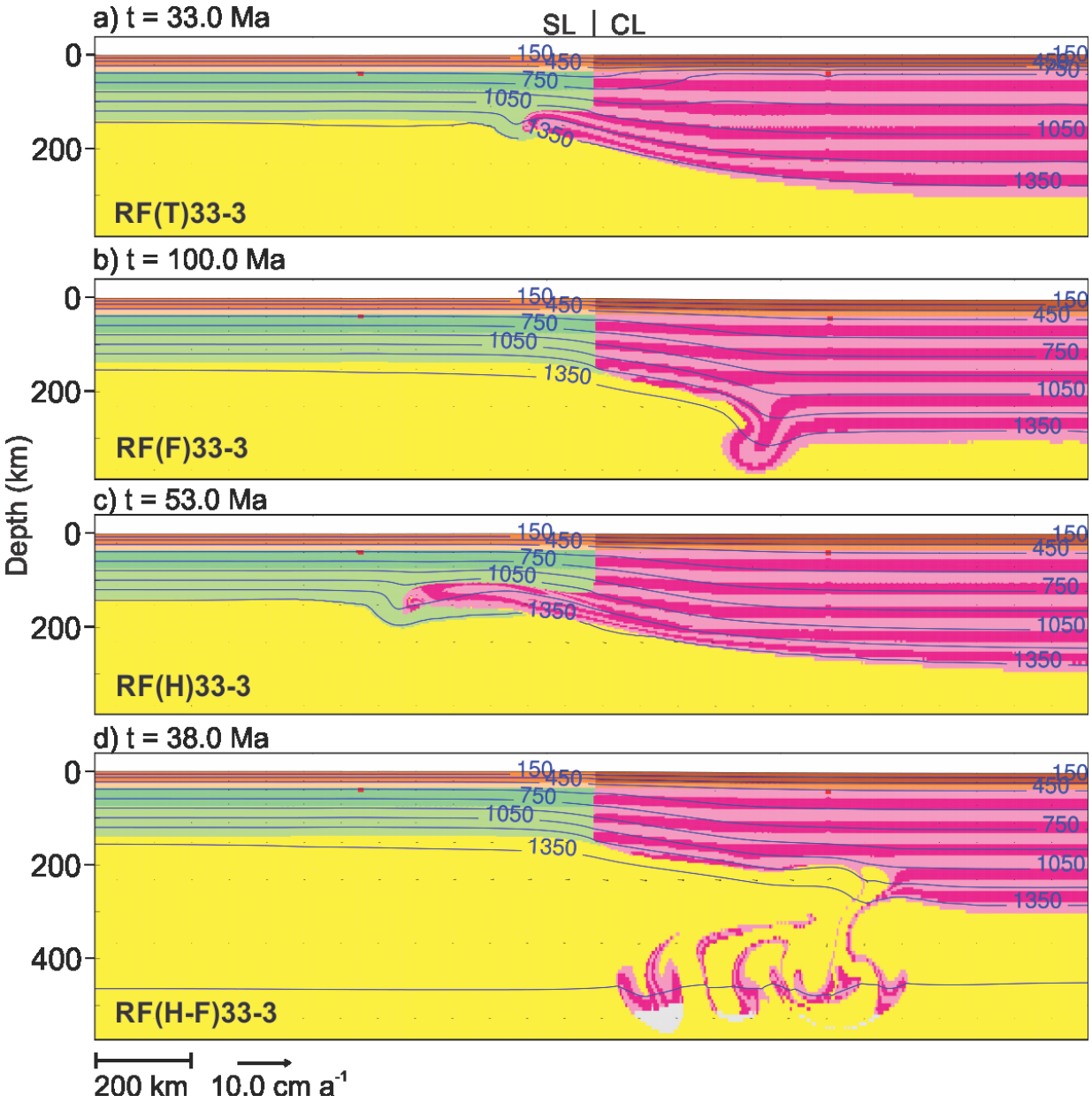

Figure 4.10. Sensitivity tests for the RF( )3-33 series. a) RF(T)33-3. A temperature increase in the CML results in buoyant counterflow at the vertical lithospheric boundary. The Moho temperature has increased to 685°C. b) RF(F)33-3. Where the CML is refertilized, but the viscosity does not change, delamination eventually occurs. c) RF(H)33-3. Hydration of the CML results in extensive counterflow. The lower layers, which are hotter than the upper layers, are incorporated into the counterflow more readily than the upper layers. d) RF(H-F)33-3. This model resembles the RF33-3 model, as small parts of CML delaminate. However the final thinning is not as extensive as in RF33-3.

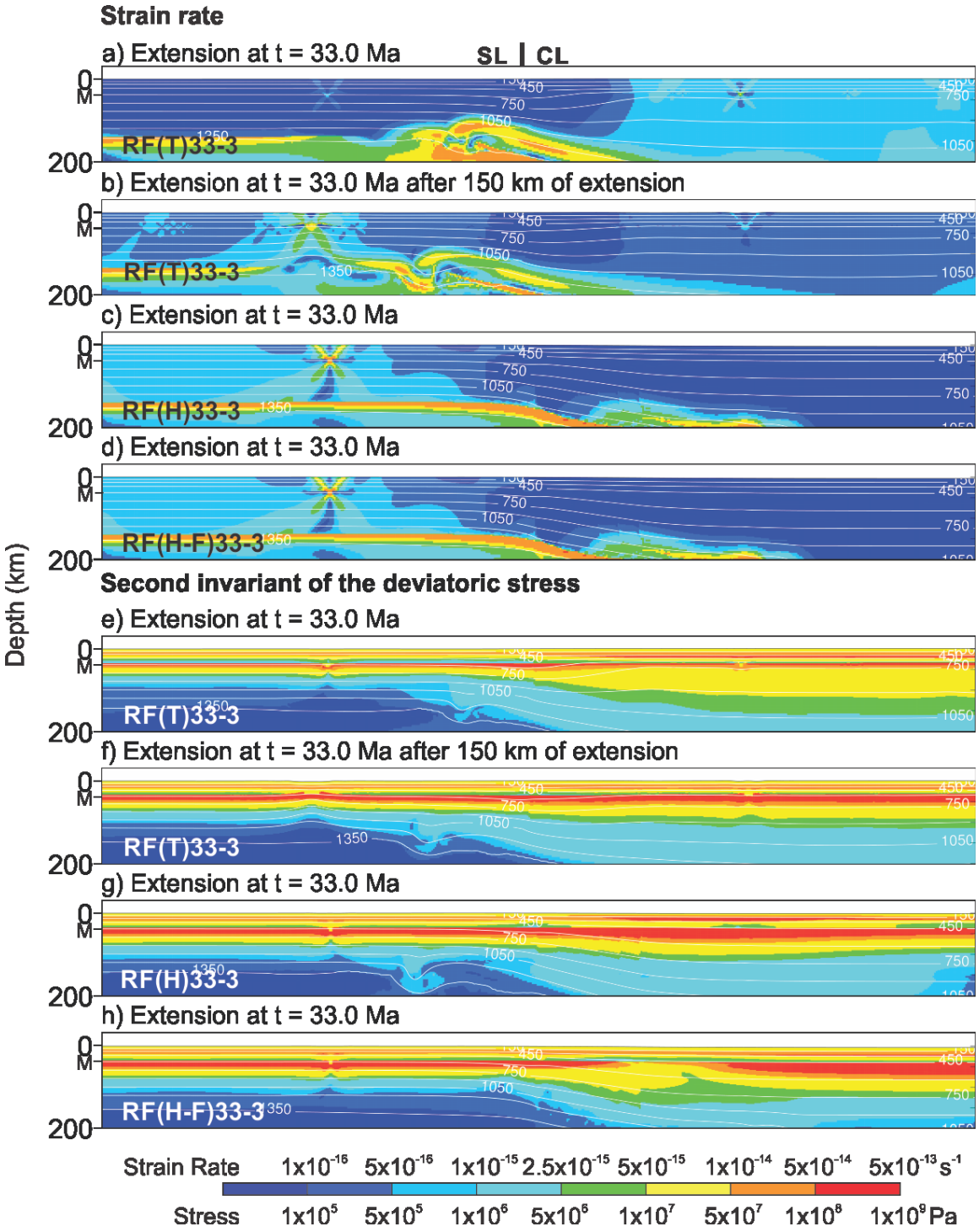

Figure 4.11. Rifting tests of the RF( )33-3 series. All panels show extension at t = 33.0 Ma. a) The temperature increase in RF(H)33-3 results in a higher strain rate in the cratonic lithosphere. b) Rifting localizes in the standard lithosphere as heat diffuses and the integrated strength of the CML increases. c,d) Neither rehydration by itself (RF(H)33-3), nor rehydration and refertilization combined (RF(H-F)33-3) weaken the cratonic lithosphere enough to make the strain rate higher in the cratonic lithosphere. e-h) The increase in temperature (RF(T)33-3) decreases the stress throughout the upper CML more than in the RF(H)33-3 model. RF(H-F)33-3 has a local low stress zone in the upper mantle lithosphere.

The stress distributions illustrate the effects on the viscosity and strength distribution in the metasomatized lithosphere. The temperature increase (RF(T)33-3; Figure 4.11e) results in an overall decrease in stress in the upper CML as the viscosity has decreased. Rehydration, results in overall lowering of the strength of the CML, but since the temperature has remained relatively cold, a thick high stress layer can still be seen, indicating the upper CML is still strong (Figure 4.11g). In RF(H-F)33-3 the only change to the stress distribution (Figure 4.11h) where compared with RF(H)33-3 is the decrease in stress in the region where the lithosphere has been thinned by up to 80 km. Since the overall strength is a result of the integrated stress, the thinner lithosphere results in a lower integrated strength. Similar tests were performed for the M( )3 series models. The results are similar to the results presented above and are summarized in Table 4.1.

4.7.6 Limited Melt Underplating of the Crust

Melt underplating of the crust has been proposed as a mechanism to weaken the cratonic lithosphere and eventually lead to rifting (Zhang 2012). The U model is designed with a metasomatising region around the MWZ in the upper CML 35 km thick and 100 km wide. It is fully metasomatized (30% melt addition) in 3 Ma (Figure 4.12a,b). The Moho temperature in the cratonic lithosphere is 620°C at the end of metasomatism (Figure 4.12b), whereas it is 600°C in the standard lithosphere. At 10 Ma, heat has dissipated into the surrounding cratonic lithosphere. The Moho temperature has decreased to 560°C (Figure 4.12c), but the crustal temperature has increased (from 380°C to 415°C at 25 km depth).

Two rifting tests were conducted at t1 = 3.0 Ma and t2 = 10.0 Ma for comparison with the M3 model. The Moho temperature in the metasomatized region is higher than in the standard lithosphere at 3.0 Ma. Nevertheless, where the lithosphere is extended, the strain rate is much higher in the standard lithosphere (Figure 4.12d). A similar result is obtained for rifting at t2 (Figure 4.12e). The stress distribution does change significantly in the period after metasomatism. At 3.0 Ma the stress in the metasomatized region is lower than in the standard lithosphere (Figure 4.12f). The high temperature in the metasomatized region results in a low viscosity, and thus it is also under relatively low stress. At 10 Ma, the decreased temperature partly restores the higher viscosity and the stress in the upper CML has increased back to > 1 x

10^8 Pa. In summary, even though melt underplating of the crust can increase the temperature and decrease the strength locally, the weakening effect is insufficient to shift localization from the standard lithosphere to the cratonic lithosphere.

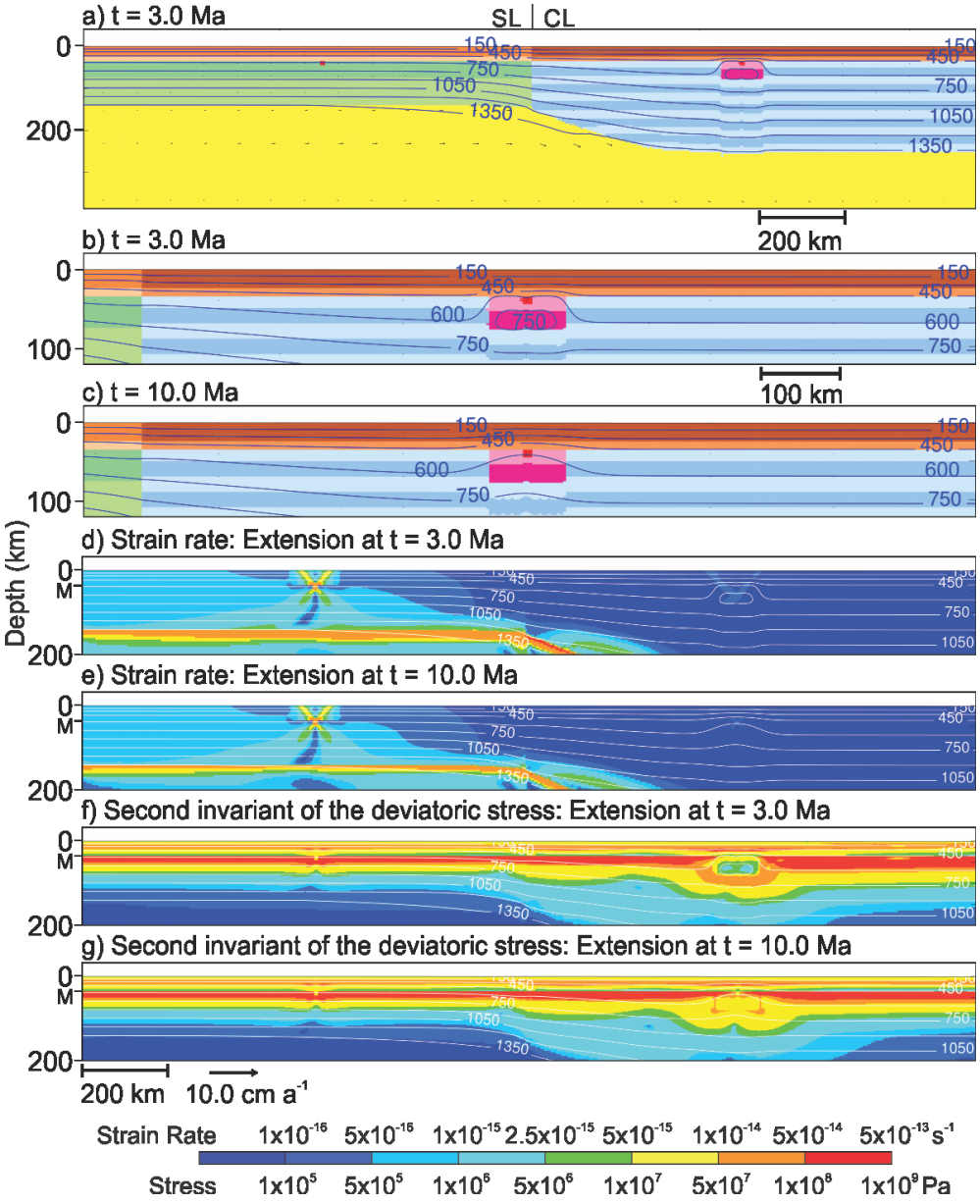

Figure 4.12. Limited melt underplating of the crust at the MWZ (M(U)3). a) The metasomatized region has finished metasomatism at 3 Ma and the Moho temperature is 620°C. Downward displacement of the isotherms at depth in the CML is a consequence of melt thickening of the upper CML in the U region. b,c) Close up of the metasomatized region showing the dissipation of heat after metasomatism. The Moho temperature has decreased to 560°C by 10 Ma. The horizontal scale is different from the other panels shown in this figure. d,e) Rifting tests at t1 = 3.0 Ma and t2 = 10 Ma. The strain rate is higher in the standard lithosphere. f) The deviatoric stress in the metasomatized region is much lower at the end of metasomatism. The high temperatures decrease the viscosity in the vicinity of the metasomatized region. g) After heat dissipation of 7 Ma the increased stress in the upper mantle lithosphere indicates that the viscosity has increased as temperature decreased.

4.7.7 Sensitivity to the Strength of the Standard Lithosphere

The strength contrast between the standard lithosphere and the CML at the time of extension is the ultimate control on the location of rifting. All the models presented above have a standard lithosphere with the same rheology (WQz x 3 and WOl x 3). The rifting tests presented below illustrate the importance of the strength of the standard lithosphere with respect to the cratonic mantle lithosphere (Figure 4.13).

In RF(SL2)33-3 the crustal strength has been increased (WQz x 4), and the strain rate distribution (Figure 4.13a) is similar to that of RF33-3 (Figure 4.11c). The strength contrast is not diminished sufficiently and rifting localizes in the standard lithosphere (Figure 4.13b). In contrast, in RF(SL3)33-3 the strain rate distribution is in favor of localization in the cratonic lithosphere (Figure 4.13c). In this case, both the standard crust (WQz x 4) and mantle lithosphere (WOl x 4) are stronger than in RF33-3. These results indicate that it is easier to rift a craton where it is adjacent to a lithosphere with a similar integrated strength. This is consistent with the results from Chapter 2.

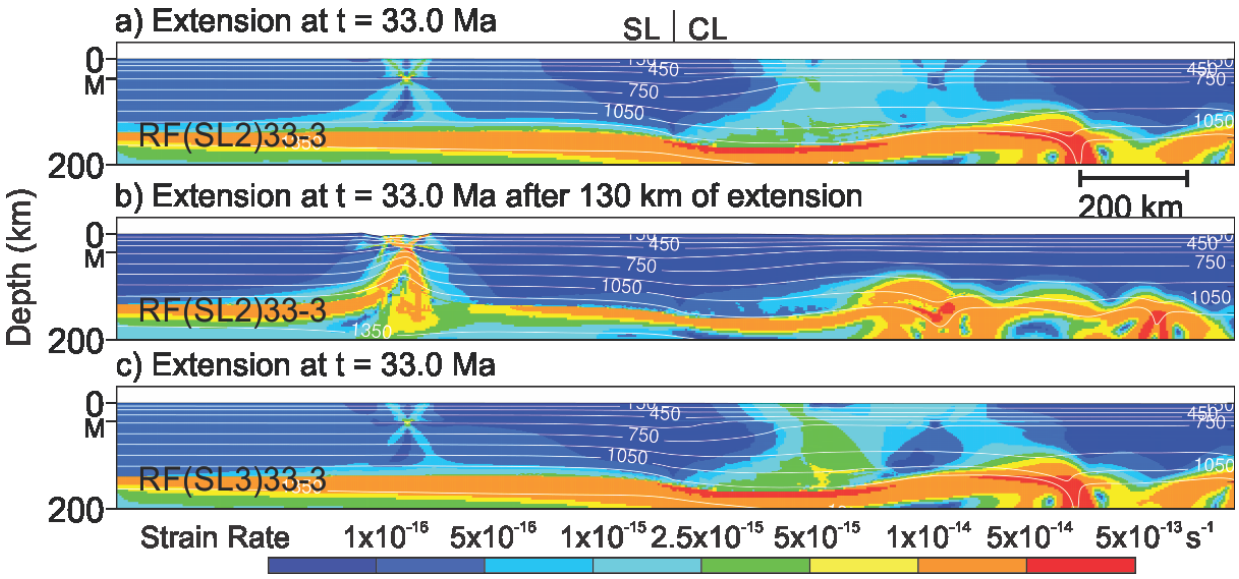

Figure 4.13. Rifting tests for RF33-3 with a stronger standard lithosphere (SL). a) The standard crust in RF(SL2)33-3 is stronger than in the reference RF33-3 model (WQz x 4 vs. WQz x 3, see Appendix for detailed explanation of scaling the flow laws). b) Rifting localizes in the standard lithosphere for RF(SL2)33-3. c) Where the standard lithosphere has a crustal rheology of WQz x 4 and the mantle lithosphere is WOl x 4 RF(SL3)33-3 the strain rate is higher in the cratonic lithosphere and it will rift.

4.7.8 Sensitivity to the Volume of Melt Added

The addition of 30% melt by volume in RF33-3 results in large-scale delamination of the CML and a temperature increase throughout the CML. Two tests with 20% (RF(20%)33-3) and 25% (RF(25%)33-3) melt addition were computed to test the sensitivity of these results to the amount of melt added. In RF(20%)33-3 20% melt by volume is added to each layer over 3 Myr. The decrease in melt volume results in a smaller increase in density (28.7 kg m^{-3} vs. 43 kg m^{-3}), a smaller degree of rehydration, and a smaller increase in temperature (Table 4.1). The smaller increase in density does not result in a Rayleigh-Taylor instability in RF(20%)33-3 (Figure 4.14a).

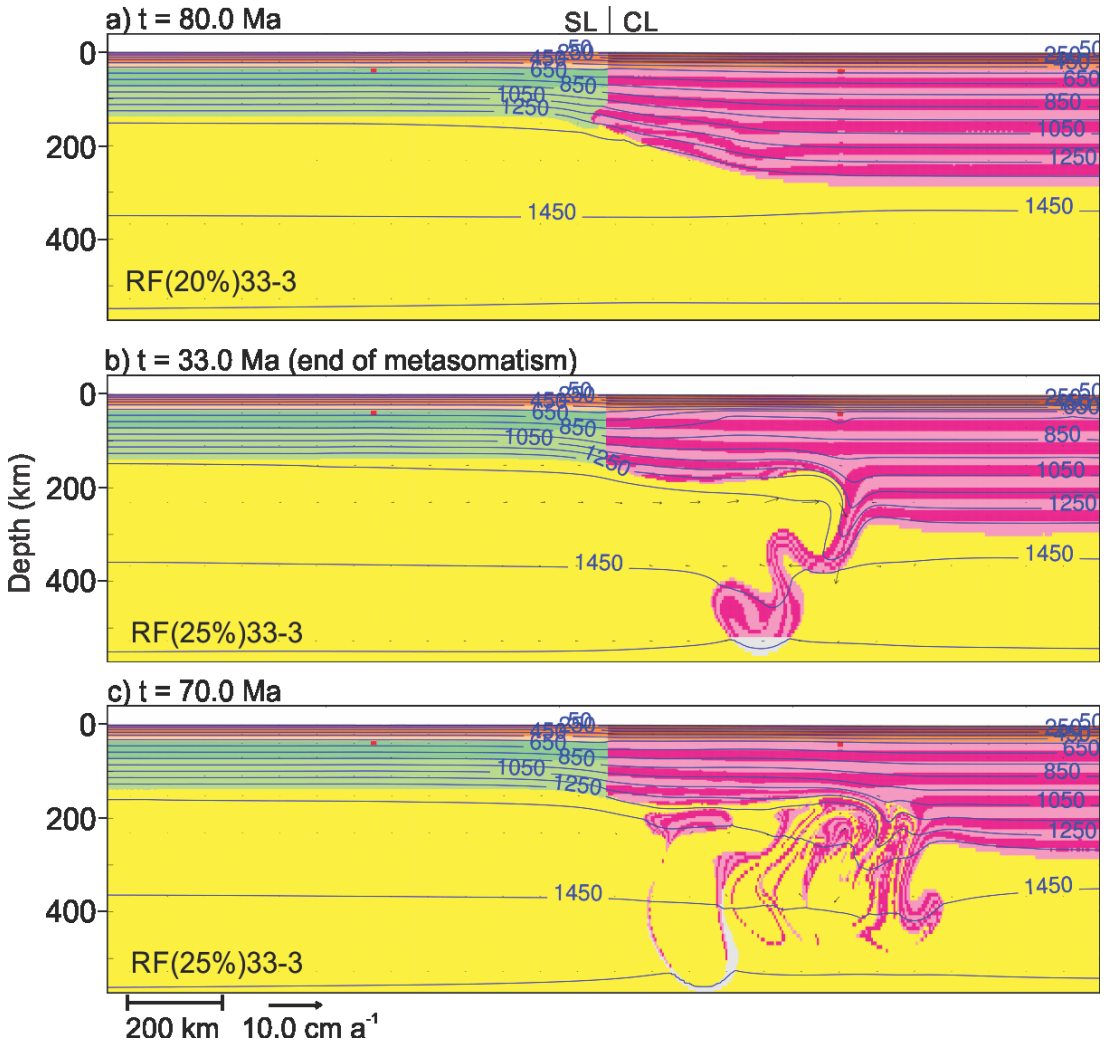

Figure 4.14. Sensitivity to the volume of melt. a) The total amount of melt added by the end of metasomatism is 20% in RF(20%)33-3. No CML thinning has developed by 80 Ma. b,c) The total amount of melt added by the end of metasomatism is 25% in RF(25%)33-3. A Rayleigh-Taylor instability has started, but by 70 Ma the CML has not thinned to the same extent as RF33-3.

Where 25% melt is added, the density increase of 35.8 kg m^{-3} does result in a Rayleigh-Taylor instability (Figure 4.14b). However, the convective removal is more limited than in RF33-3, where the CML thinned to ~120 km by 27 Ma (Figure 4.7c). The convective instability in the sublithospheric mantle is smaller than in RF33-3 and the delamination front only propagates to the center of the cratonic lithosphere by 70 Ma (Figure 4.14c). It is clear that the total amount of melt added dictates the temperature and amount of convective thinning, and thus strength, of the cratonic lithosphere.

4.8 Discussion

4.8.1 Weakening by Metasomatism; Does it Allow Cratons to Rift?

The abundance of lherzolite in the lower mantle lithosphere of many cratons has recently been interpreted as evidence of widespread silicate melt metasomatism of depleted harzburgites. Here we suggest that this process may eventually lead to weakening of the craton by increasing the temperature and/or by delamination of the CML and its replacement by fertile sublithospheric mantle. The M3, M10, M30, M50, and RF33-3 models illustrate that the timing of extension relative to metasomatism is very important. Heat diffusion is the controlling factor in this respect. All the M-type models (Section 4.7.3), have a similar evolution relative to the duration of metasomatism. The time available for heat to diffuse is the remaining control that makes the model behaviors different. In M3 the exceptionally short duration of metasomatism precludes significant heat diffusion during metasomatism and results in a generally hot upper cratonic lithosphere by the time significant thinning has occurred. By comparison, in the M10, M30, and M50 models heat diffusion into the crust has decreased the Moho temperature sufficiently so that it is no longer much hotter than the standard lithosphere Moho and rifting only takes place in the standard lithosphere.

RF33-3 supports this interpretation. The CML has thinned by 90 km at 24 Ma. However, the rifting test at 27 Ma (Figure 4.9a,d) shows that the strain rate is higher in the standard lithosphere. The upper CML is still strong as indicated by the high stress. As the upper layers get metasomatized, the Moho temperature starts increasing (Figure 4.8) and the stress in the upper CML decreases. Even at the end of metasomatism of the last layer in RF33-3 (Figure 4.7d)

the CML has not weakened sufficiently to rift and the standard lithosphere rifts instead (Figure 4.9c,f).

The sensitivity tests illustrate the effectiveness of temperature to decrease the viscosity and weaken the CML (Figure 4.11). At the end of metasomatism in RF(T)33-3 the upper 100 km of the cratonic lithosphere has a higher temperature than the standard lithosphere, and the strain rate is higher in the cratonic lithosphere (Figure 4.11a). Rifting still localizes in the standard lithosphere after 130 km of extension. The increase in temperature has decreased the viscosity in the crust sufficiently so that the crust is decoupled from the CML. Although the strain rate is higher in the cratonic lithosphere when extension starts, the low viscosity results in slow, pliable, necking. At the same time, heat diffusion results in an increased integrated strength in the CML, and this finally results in localization at the MWZ in the standard stiff upper mantle lithosphere. It is unlikely that temperature alone will increase as much in natural systems as it did in this model, without the other associated effects. Nevertheless, these models illustrate that the integrated strength of the CML is highly dependent on its temperature regime and that hotter melt, for example from a plume, may shift localization to the cratonic lithosphere.

In all models that were metasomatized by 30% melt and included all the effects of metasomatism, the CML was thinned by ~100-150 km. This suggests that metasomatism can be responsible for thinning of the cratonic mantle lithosphere in natural settings. Rifting of the cratonic lithosphere was only achieved in a limited number of models and only when an improbable amount of melt and heat were added to the CML in a short period of time (e.g. M3). Small amounts of local melt addition, such as in the melt underplating model (Section 4.7.6; Figure 4.12) do not weaken the craton enough so that it becomes weaker than the standard lithosphere. This suggests that large-scale metasomatism of the CML is needed to lead to rifting the craton. Melt underplating could be effective if convective removal has thinned the CML prior to underplating. In this case the thickness of the CML would be similar to standard lithosphere and underplating could increase the temperature in a small region enough to localize deformation in the cratonic lithosphere. Similarly, localized metasomatism that weakens and reduces the integrated strength of a vertical column with the same depth extent

as the CML, may localize deformation in the cratonic lithosphere. In this case, regional metasomatism may not be necessary.

Sensitivity tests where the strength of the standard lithosphere is altered to decrease the strength contrast illustrate that the properties of any lithosphere surrounding cratons in reality play a major role in the amount of weakening needed to rift a craton. If the craton is surrounded by similar strength lithosphere, a lesser amount of weakening than that needed to weaken the cratons in our reference model design may be sufficient to rift the craton. The strength of the standard lithosphere could also be affected by a different temperature regime than in our models. If the Moho temperature in the standard lithosphere is closer to 500-550°C, less heating of the CML would be required to make the CML weaker than standard lithosphere. On the other hand, the melt addition tests clearly show that when less melt is added, convective removal and the temperature increase throughout the CML is limited (Figure 4.14).

Overall, in most models rifting localized in the standard lithosphere. This is true, even for models with large amounts of convective removal of the CML and with a higher Moho temperature in the CML than in the standard lithosphere. This result underlines how difficult it is to rift an initially strong craton, and is consistent with the observations that imply very few cratons have rifted in the last 2-2.5 Ga.

4.8.2 Comparison with other Model Research

There are many modelling studies that focus on stability of the craton for over 2 Ga, which is largely attributed to a high viscosity contrast with the adjacent lithosphere and underlying sublithospheric mantle. Here we investigate the opposite problem. Even though cratons are highly viscous, strong, and surrounded by weaker lithosphere, there is evidence that they rift. In the case of the North China Craton and North Atlantic Craton, rifting did not initiate until the late Mesozoic (Menzies et al. 2007, Tappe et al. 2007), and was preceded by extensive thinning of the CML (Wu et al. 2006, Tappe et al. 2007).

Mantle plume-continent interaction leading to continental breakup has been well studied with geodynamical models (review in Buiter and Torsvik 2014), but only a few models consider plumes as a mechanism to thin the CML (Guillou-Frottier et al. 2012, Wang et al.

2015). Recent modelling by Wang et al. (2015) suggests that plumes have a limited thinning effect when a chemically distinct, strong, and depleted cratonic root is present. In contrast, where rheological weakening and a decrease in the buoyancy of the cratonic root are included, representing the effects of melt metasomatism, a more dramatic thinning is seen, especially around the edges of the craton. Although their models indicate that melt metasomatism decreases the stability of CML, the changes were made instantaneously and not gradually over a time interval as in our models. As demonstrated by the M30 and RF33-3 models the amount of thinning and the size of the instabilities depend on the distribution of metasomatism in time and space. By metasomatising the lithosphere instantaneously (Wang et al. 2015), larger instabilities are favored. Furthermore, no extensional boundary conditions were applied and thus the Wang et al. (2015) models do not give insight into rifting of cratons. The only craton rifting numerical model that includes a weak layer within the CML (Liao and Gerya 2014) is laterally homogeneous and does not take into account any protection provided by adjacent weaker lithosphere.

A lateral boundary between a craton or strong lithosphere and weaker lithosphere has been included in some analogue (Chemenda et al. 2002, Corti et al. 2013a) and numerical models (Huerta and Harry 2007, Corti et al. 2007, Gorczyk et al. 2013, Wenker and Beaumont sub). These studies agree that rifting of laterally heterogeneous lithosphere will localize in the weaker lithosphere, although a decrease in the strength/strain rate contrast may result in some deformation in the stronger lithosphere (Corti et al. 2013a, Wenker and Beaumont, sub). None of these include a weakening effect of any sort in CML.

Our modeling approach is unique in that we consider: 1) the heat and mass balance of melt that is added over a specified metasomatism time interval with associated volume change, heating, rehydration and refertilization; 2) the competition between localization of deformation in weaker/younger lithosphere and localization in the craton, and; 3) the effect of applying extensional boundary conditions after metasomatism has resulted in some convective removal.

4.8.3 Comparison with Natural Examples

The presence of thin (80-km thick) “oceanic” lithospheric mantle has long been recognized under the eastern North China Craton, although the specific mechanisms and causes of the precursor delamination are still debated (Menzies et al. 2007). Alteration of the CML was most likely linked to tectonic events that included the collision between the North China Block and South China Block (Late Permian-Triassic), southeast-directed subduction followed by collision of the Yangtze block with the North China Craton, and more recent Pacific subduction (Tian et al. 2009, Wei et al. 2012). Although we do not take these complexities into account in our models, we implicitly assume that melt was generated through processes caused by tectonic events of this type.

Xenoliths from Ordovician kimberlites suggest that a cratonic depleted mantle lithosphere was present to a depth of 180 km and that heat flow was ~40 mW m^{-2} (Griffin et al. 1998, Menzies et al. 2007). In contrast, Mesozoic and Cenozoic xenoliths and volcanics suggest a more fertile melt source (Menzies and Xu 1998). The exact timing of delamination with respect to extension is not well constrained. Magmatism was spread over a 100 Ma time interval (Xu et al. 2009), but peak heat flow (80 mW/m^2) was reached in the Cretaceous and correlates with peak magmatism (Wu et al. 2006, He 2015). Our results suggest that there should be a lag between heat diffusion from melt infiltration and increased surface heat flux. This may mean that melt infiltration in the mantle lithosphere began before there was any surface magmatism.

The North China Craton has undergone periods of extension as is evident from extensional basins overlying the craton (Menzies and Xu 1998, Menzies et al. 2007). The stress regime changed from compressional in the Triassic-Late Jurassic to extensional in the Early to Mid-Cretaceous.

Other examples of rifted cratons are the North Atlantic Craton (Tappe et al. 2007), which is crosscut by the Labrador Sea, and the Tanzania Craton, which has been metasomatically altered and only recently started to deform and (Le Gall et al. 2008, Koornneef et al. 2009).

4.9 Metasomatism and Intracratonic Basins

Surface subsidence and formation of sedimentary basins away from tectonically active plate boundaries remains an unsolved geodynamic problem. Many mechanisms have been proposed for the development of the enigmatic intracratonic basins (Chapter 3): 1) thermal subsidence owing to cooling of the lithosphere (Haxby et al. 1976, Sleep and Sloss 1980, Kaminski and Jaupart 2000); 2) thinning of the lithosphere at a low strain rate (Armitage and Allen 2010, Allen and Armitage 2012); 3) downward mantle flow causing subsidence (dynamic topography) (Pysklywec and Quintas 2000, Crosby et al. 2010); 4) phase changes changing the density of either the crust or mantle lithosphere (Hartley and Allen 1994, Downey and Gurnis 2009); 5) magmatic underplating, and; 6) cooling after plume activity (Kaminski and Jaupart 2000). Although these processes explain some of the observations, there is a lingering doubt that any of them truly solve the puzzle (e.g. Buiter et al. 2012). Here we add another mechanism and suggest that metasomatism of the underlying mantle lithosphere may result in protracted subsidence of the surface and form intracratonic sedimentary basins. This effect will be maximized in cases where the underlying lithosphere is cratonic and therefore highly depleted and susceptible to density increases during metasomatism. However, any depleted mantle lithosphere will respond to some degree to metasomatism.

The actual response can be quite complex. Increased density alone will result in subsidence, but addition of melt and heat will counteract this effect and result in surface uplift if the density increase is insufficient to compensate for the heating. Buoyant uplift above a mantle plume has a similar effect. In addition, large amounts of metasomatism will produce lithospheric instabilities as in the M and RF models, resulting in uplift during the replacement of lower lithosphere by less dense sublithospheric mantle, another effect that competes with subsidence.

Analysis of the movement of the surface of the M and RF models (Figure 4.15a) provides predictions of what might happen above cratons that are subjected to a single cycle of profound metasomatism, and in the absence of dynamical uplift by plumes. In cases where there is no removal of the lower lithosphere the surface subsides uniformly in the center of the

metasomatized region. Representative 1D subsidence curves for the basin center are shown in Figure 4.15.

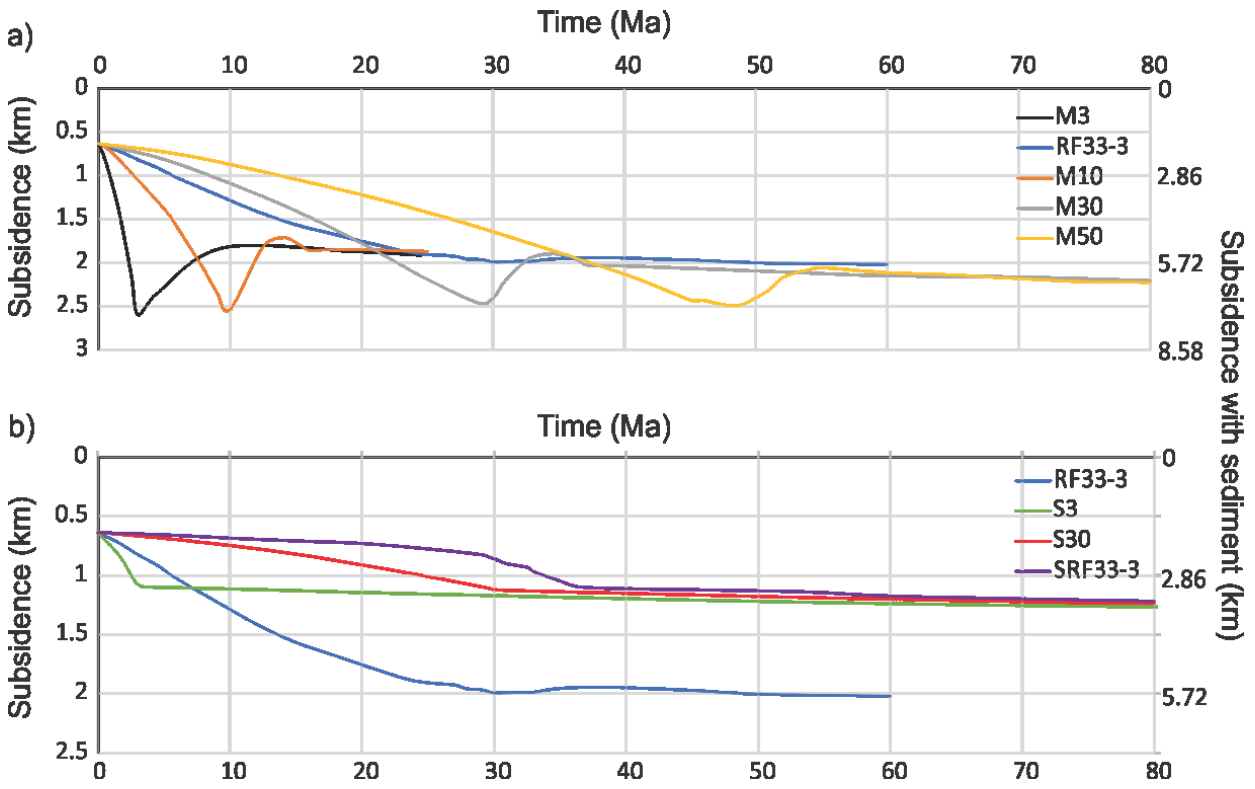

Figure 4.15. Subsidence curves for the center of the craton (x = 1700 km) for the metasomatism models. a) M-Type models and RF33-3. Rapid subsidence during refertilization (phase 1) is followed by rapid uplift (phase 2). Phase 3 is thermal subsidence. b) Subsidence models (total 10% melt) and the RF33-3 model as a comparison. The axis on the right corresponds to subsidence with sediment loading (ρ = 2200 kg m^{-3}) in the basin.

For the M models the main subsidence, phase 1, develops on the timescale of the metasomatism as would be expected. The increase in density outweighs the effect of melt addition and thermal expansion. The rebound of the surface (Figure 4.15) or a hiatus in subsidence in the M models, phase 2, is a consequence of removal of the lower lithosphere (e.g. Figure 4.3 and Figure 4.5). As noted above this delamination sweeps across the craton from its edge which results in diachronous phase 2 uplift. The corresponding behavior for model RF33-3 is also shown (Figure 4.15a,b), phase 2 is much smaller and happens at the end of metasomatism. This is a result of the smaller size of the instabilities that thin the CML in the RF33-3 model. The terminal monotonic subsidence, phase 3, corresponds to the long term cooling of the cratonic lithosphere and has a timescale that depends on its residual thickness

after metasomatism and possible delamination. The total subsidence achieved during this phase is relatively small compared with phase 1.

The M and RF models provide examples of putative intracratonic basin subsidence resulting from an extreme bout of metasomatism. The results show that realistic amounts of subsidence are predicted, resulting in 2-km deep sedimentary basins in the absence of sediment or water loading and approximately 6 km where sediments fill the basin. However, we also suggest that most intracratonic basins may result from multiple episodes of minor metasomatism. Models S3 to S30 and SRF33-3 illustrate the effect of one episode of this more limited metasomatism (Figure 4.15b). S3 is equivalent to M3 but has only 10% of melt added during the 3 Ma metasomatism. S30 is the same except the metasomatism lasts 30 Ma. SRF33-3 is equivalent to RF33-3 but also with 10% melt added. As expected these models lead to reduced overall subsidence (Figure 4.15b), and phase 2 is totally absent because no instabilities develop in the lower CML. Phase 3 starts as soon as metasomatism has finished and leads to slow prolonged subsidence. The total thermal subsidence is relatively small.

4.9.1 Testing the Metasomatic Origin of Intracratonic Basins

Having advanced the hypothesis that intracratonic basins subside isostatically as a result of metasomatism of the underlying lithosphere, it is necessary to list the types of data that could be used to test model predictions. Here we focus on intracratonic basins formed on thick, depleted cratonic lithosphere. Figure 4.16 is a cross-section of a hypothetical intracratonic basin that was subjected to 2 episodes (E1, E2) of moderate metasomatism (each 10% melt, as in the S models above). The two sides of the diagram show the contrasting cases where the lower lithosphere was and was not removed (Figure 4.16b,c) following the second episode. Timescales for the phases of each episode will depend on the duration of the metasomatism. The adjacent panels (Figure 4.16b,d) show the subsidence history. The model predicts two phases of fairly rapid but limited subsidence during metasomatism (P1), two phases of thermal subsidence as the lithosphere cools (P3), and an unconformity (U) in one basin resulting from removal of the lower lithosphere during phase 2. The thermal subsidence phases are long (> 200 Ma e-folding timescale) when the lithosphere remains thick (~250 km) and short (~ 50 Ma e-folding timescale) when the lithosphere is thin (100-140 km).

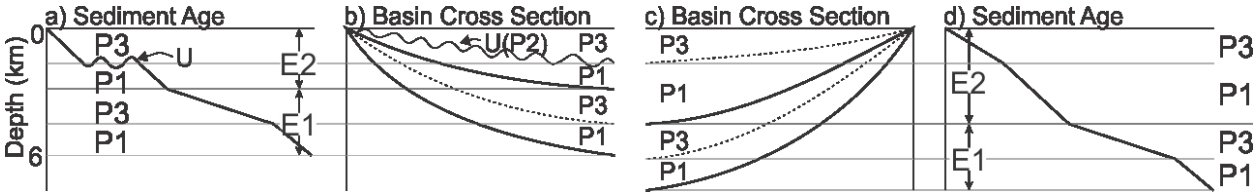

Figure 4.16. Hypothetical subsidence curves. a,b) Sediment age with depth and basin cross section in a case where the CML undergoes two episodes of metasomatism (E1, E2) and delamination (P2) results in uplift and an unconformity (U) between phase 1 (P1) and phase 3 (P3). c,d) The same metasomatism does not result in convective removal and the final thickness of the sediment package is thicker than in (a,b).

The most convincing test of subsidence caused by metasomatism is that mantle xenoliths from volcanics in the intracratonic basin show that the CML was metasomatized at times corresponding to phase 1 subsidence, or at least a change in CML fertility that corresponds to phase 1 subsidence. This test will be more complicated in the case of dynamical uplift above a plume, in which case subsidence may be delayed until the plume is removed and the subsidence therefore develops later than metasomatism. Evidence of other magmatism (e.g. kimberlites, lamproiites, alkali basalts) is also useful provided it can be linked to mantle lithosphere metasomatism. There should also be a phase of enhanced surface heat flow that should be detectable, particularly against a background of low surface heat flow from cratonic lithosphere, using thermochronometers from the basin sediments and the basement. Data providing constraints on the properties of the CML are also needed, namely: seismic evidence of refertilization of the CML; gravity and geoid anomaly observations demonstrating a mass excess in the mantle below the basin that is correlated with its extent, and; magnetotelluric measurements of mantle conductance in cases where the metasomatism is recent and melts may remain, or the CML is hydrated, and as a result shows enhanced conductance.

The best natural examples of intracratonic basins to investigate in regard to metasomatism are those on cratonic lithosphere where other basin-forming mechanisms such as rifting and flexure can be excluded during the time interval of interest. Three potentially good examples are the Congo (Giresse 2005, Crosby et al. 2010, Buiter et al. 2012), Parana (Pysklywec and Quintas 2000, Julià et al. 2008) and Ordos (Yang et al. 2005) basins. The best North American examples, Williston, Michigan and Illinois basins (Kaminski and Jaupart 2000) are also potential candidates, although they overlie older crustal rifts and Proterozoic lithosphere. The Colorado Plateau is also interesting owing to its uplift (Roy et al. 2009) and

convincing evidence of mantle lithosphere refertilization since the Carboniferous (Crow et al. 2010). It is also worth investigating whether Lake Victoria on the Tanzania craton is a nascent intracratonic basin.

A full investigation of the merits of these basins as cases that do and do not support the metasomatism hypothesis is beyond the scope of this thesis but preliminary follow-up work will be done for publication.

4.10 Conclusions

Cratons need to be weakened if they are to rift. The amount of weakening required depends on the overall strength of the surrounding lithosphere. Weakening can occur through refertilization (increase in density) and rehydration (decrease in viscosity), but temperature increases from local melt cooling and crystallization are most effective at decreasing the strength of CML. The model results indicate that significant melt infiltration is needed to weaken cratons enough to localize rifting within them. Even after melt metasomatism has heated the CML so that the Moho temperature is higher than in the standard lithosphere, and has thinned the CML by 100-120 km, rifting localized in the standard lithosphere in most models. This result is consistent with the survival of non-rifted cratons since 2-2.5 Ga. To rift a craton successfully, the extensional stresses need to be applied at the right time. If the lithosphere is under extension when it is still thick (>250 km), even if it is hot, the integrated strength of the craton will be higher than that of the standard lithosphere and the latter will rift. Our results show that the craton needs to be both hotter and weaker than the standard lithosphere in order for rifting to localize there. Mantle metasomatism can result in significant thinning and heating and may eventually result in removal of the craton mantle lithosphere. Refertilization changes the isostatic balance of the craton and may create accommodation space, forming intracratonic basins. Uplift and erosion, followed by protracted subsidence as identified in the stratigraphy of these basins may be explained by delamination (uplift) and subsequent cooling of the hot sublithospheric mantle.

Chapter 5 Discussion and Conclusions

5.1 Numerical Modeling of a Heterogeneous Lithosphere under Extension

The models presented in this thesis are designed to investigate the overarching question: how do lithospheric heterogeneities affect the distribution of deformation in an extending lithosphere? Forward numerical modeling can provide constraints on the behavior of a complex lithosphere when it cannot be observed readily in nature. The work in this thesis is a unique example of modeling heterogeneity. The models throughout this thesis indicate the importance of the background strain rate and consider multiple factors that may change the strain rate distribution of an extending lithosphere. Part 1 of the thesis provides an application of the fundamental theories of the growth of necking instabilities by considering competition between necking instabilities in a laterally heterogeneous lithosphere where a strength contrast results in a strain rate contrast. The second part of the thesis uses the concept of the control of strain rate on the localization of deformation and rifting developed in Part 1, and applies it to rifting of a craton. In this case the strain rate contrast is a result of thermal, thickness, and rheological contrasts.

5.1.1 Stiff and Pliable Layers in a Laterally Heterogeneous Lithosphere

The relatively simple models presented in Chapter 2 provide the opportunity to interpret the change in stiff and pliable layer distribution where a strength contrast is present in the lithosphere. The relation between the stiff and pliable layering and the brittle and viscous behavior of a laterally homogeneous lithosphere was explained in Section 1.2.2. Where under sufficient stress, brittle layers are equivalent to stiff layers and viscous layers are equivalent to pliable layers (Figure 1.3c). The distribution of stiff and pliable layers in a laterally heterogeneous lithosphere is complicated by the change in brittle and viscous layering across the lithospheric boundary. For example, in the homogeneous models Model 1.1 and Model 1.2 (Section 2.8.1; Figure 2.5), the scaling factor of the mantle lithosphere varies from WOl x 3 to WOl x 1, thereby changing the upper mantle lithosphere from stiff to pliable. The same change in scaling factors across the vertical boundary for Model 3.1 (10-1 | 10-3) (Section 2.8.3.1; Figure 2.7) results in a similar stiff and pliable distribution; the left upper mantle lithosphere is pliable, whereas the right upper mantle lithosphere has a stiff layer. In contrast, in Model 3.2

(5-1 | 10-3) (Section 2.8.3.1; Figure 2.7) the upper mantle lithosphere is pliable on both sides of the boundary, even though the right lithosphere has the same scaling factors that resulted in a stiff upper mantle lithosphere in Models 1.1 and 3.1. The decrease in strength of the crust in the left lithosphere from WQz x 10 (Model 3.1) to WQz x 5 (Model 3.2) has thus changed the stiff vs. pliable behavior of the upper mantle lithosphere in the right upper mantle lithosphere.

This change in stiff and pliable behavior in the presence of a weaker crust is the result of the distribution of stress as induced by the force that is extending the lithosphere. The amount of stress the lithosphere is under is determined by the amount of force that is applied to it. In all the models presented in this thesis this force is a result of the velocity boundary conditions. Even though the velocity boundary conditions remain constant throughout rifting at 1 cm a^{-1}, the forces on each boundary required to satisfy the velocity boundary condition change over time. In particular, after a necking instability has localized and the strain rate feedback is operating efficiently, the force required to extend the lithosphere decreases as it becomes "easier" to extend the material under a higher strain rate with decreasing viscosity. Similarly in a laterally heterogeneous lithosphere, any weaker regions require less force to accommodate extension than any adjacent stronger regions.

The forces required to extend the lithosphere at 1 cm a^{-1} are balanced across the model for each timestep and therefore, the integrated stress of each distinct lithosphere is equal and can be described by Equation 5.1.

$$F = \int_0^L \sigma dL = \int_0^L \eta_{eff}\, 2\dot{\varepsilon}\, dL \tag{5.1}$$

where F is the force applied at the boundary, and L is the lithospheric thickness. This means that the integrated stress in a laterally heterogeneous lithosphere is lower than if a strong laterally homogeneous lithosphere was under the same extensional boundary conditions, since the overall force required to extend the weaker lithosphere in the composite is less. The pliable right upper mantle lithosphere of Model 3.2 can be explained by the presence of the weaker lithosphere to the left of the boundary. The brittle upper mantle lithosphere is under insufficient stress to be at yield and does not behave as a stiff layer.

There has been debate about the magnitude of the forces required to rift the lithosphere (e.g. Kusznir and Park 1987, Buck et al. 1999, Buck 2004). It seems that calculated forces for thick or strong lithospheres are generally an order of magnitude larger than those inferred to operate in nature (Forsyth and Uyeda 1975, Solomon et al. 1975). The answer may lie in the heterogeneous nature of the lithosphere. Heterogeneous lithospheres like the ones considered here require smaller forces to extend them than equivalent pristine ones. The presence of any inherited finite weak zones decreases the yield strength and can intiate a necking instability, after which the strain rate feedback decreases the force required for continued extension.

5.1.2 It is (Almost) All About the Strain Rate

The models presented in Chapter 2 establish that the strain rate is a major control on the localization of deformation. In those models the strain rate was influenced only by the strength of the adjacent lithosphere as controlled by scaling of the flow-laws, whereas the temperature and thickness of the adjacent lithospheres were equal on both sides of the vertical boundary. It is much easier to understand that a lithosphere is "weaker" where it has a lower viscosity, which is controlled only by the scaling factor. Chapter 4 introduces thermal and thickness contrasts. Initially, it is clear that the standard lithosphere is weaker than the craton, but as soon as metasomatism alters the characteristics that are ascribed to craton survival, determining the weaker lithosphere becomes much more complex.

The ultimate goal of Chapter 4 is to understand when the cratonic lithosphere is weakened enough so that it has become the weaker lithosphere, and will rift. Mantle metasomatism is proposed to be the main mechanism responsible for rendering the cratonic lithosphere weaker and under a higher strain rate after convective removal of the CML and an increase in temperature. To my knowledge, no other study exists that includes the effects of metasomatism in such a comprehensive way. My sensitivity tests illustrate the importance of including the multiple weakening effects associated with mantle metasomatism, and in particular point to the addition of heat as a critical factor. Extension of the lithosphere still results in localization in the standard lithosphere when the cratonic mantle lithosphere (CML)

becomes denser and less viscous as a result of refertilization and rehydration (Section 4.7.5; Figure 4.11).

The weakening effects of temperature are clearly shown in Figure 4.11a,d. By just increasing the temperature of the originally cold CML the thickness of the high stress layer in the upper CML has decreased and the strain rate is now higher in the cratonic lithosphere. The differences between the effects of temperature and the scaling factor (f) can be seen in Figure 5.1. A 200 K increase in temperature, from 800 K to 1000 K, results in a viscosity decrease of 2 orders of magnitude, whereas a decrease in scaling factor from 5 to 1 results in a viscosity decrease of less than 1 order of magnitude. The temperature dependence of viscosity is even more pronounced in the lower temperature regimes.

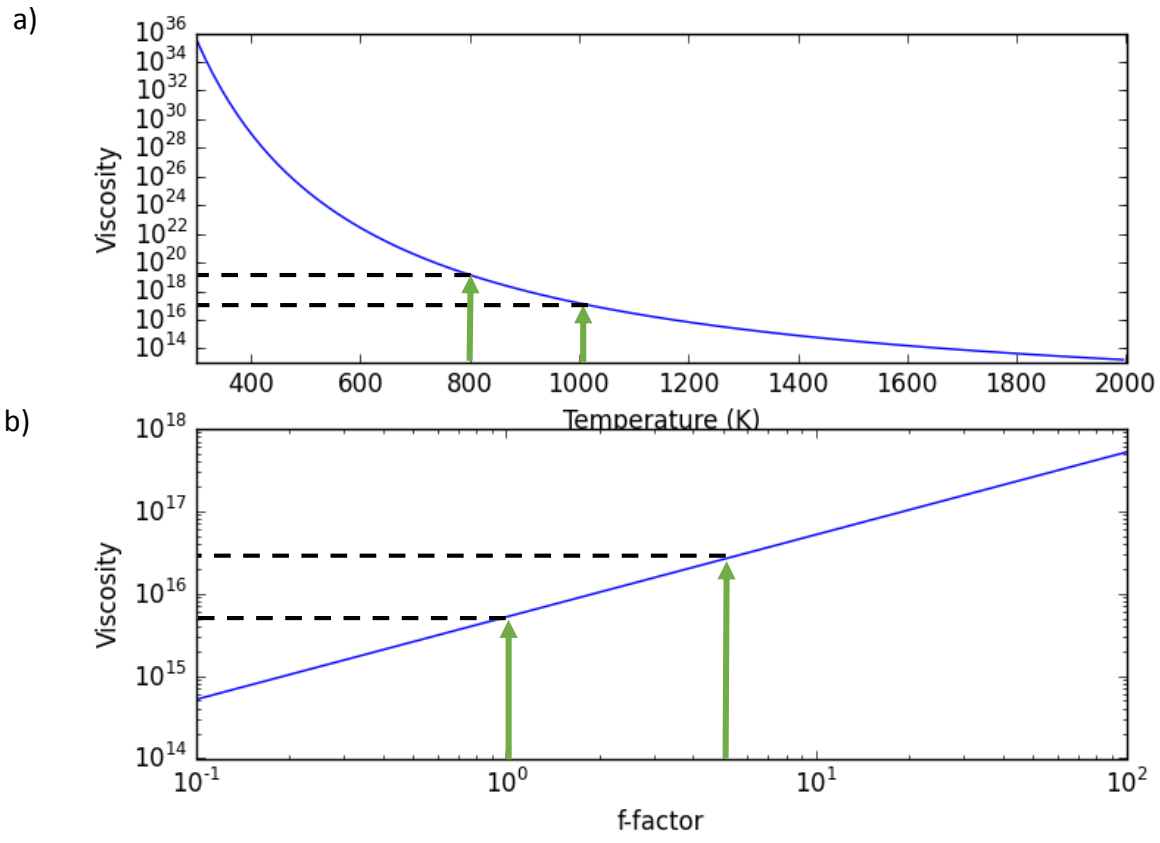

Figure 5.1. Viscosity variation with temperature and scaling factor of the Wet Olivine flow law (Karato and Wu 1993). a) Viscosity vs. Temperature (in K). A temperature increase of 200 K, from 800 K to 1000 K, results in a viscosity decrease of 2 orders of magnitude. b) Viscosity vs. scaling factor at a constant temperature of 1223 K (950°C). A decrease in scaling factor from 5 to 1 results in a viscosity decrease of a factor of 8.

Nevertheless, a temperature increase does not necessarily lead to rifting. The Moho temperature was higher in the cratonic lithosphere than in the standard lithosphere in most M-type models and in RF33-3, but rifting localized in the cratonic lithosphere only in the M3 model. The temperature is highest by the end of metasomatism in RF33-3 (665°C), and the CML is 120-100 km thick, but localization still takes place in the standard lithosphere. The difficulty of rifting a craton even after significant weakening may be part of the reason why cratons are still a part of our geological record today. Rifting of cratons such as the North Atlantic Craton and the North China Craton may therefore only be possible because of small integrated strength contrasts between them and the lithosphere that surrounds them, or as a consequence of profound, relatively rapid metasomatism.

5.2 Future Research Directions

In all extending models presented in the thesis a velocity boundary condition of 1 cm a^{-1} was used. This applied velocity has a direct consequence for the strain rate of the lithosphere. Therefore, the results on the control of strain rates in a heterogeneous lithosphere from Chapter 2 need to be expanded to include a range of velocity boundary conditions. Furthermore, a higher extensional velocity increases the force exerted on the lithosphere, which may change the stiff and pliable layering of the lithosphere. Similarly, constant force boundary conditions can give additional insight into the competition between the stiff and pliable behavior of the lithosphere. In this case, extension will speed up as the strain-rate feedback acts on any necking instabilities.

The model results in this thesis can be used only as a first order approximation to natural examples, owing to the complexity and 3D nature of nearly all natural examples. For example, the southern edge of the Siberian craton, which is bordered by the Baikal rift, is highly curved and the width of the Baikal rift seems to be linked to this curvature (Chemenda et al. 2002, Petit et al. 2008, Corti et al. 2013a). Oblique extension may also have affected this pattern, but cannot be modeled with 2D models. New 3D models have been developed in the past 5 years, but generally have a lower resolution as a result of their high computational cost (e.g. Thieulot 2011, Allken et al. 2012, Brune and Autin 2013). A more comprehensive

understanding of the effects of lithospheric heterogeneity will result from 3D modelling in the future.

Finally, the connection between the formation of intracratonic basins and mantle metasomatism can be investigated further. The subsidence history inferred from sediment cores and seismic observations can be correlated with the evidence for and timing of melt metasomatism from xenoliths. Heat flow estimates from metamorphosed basement rocks can constrain the timing of maximum heat flow. The time of peak heat flow should lag behind the time of maximum melt metasomatism, as it takes time for the heat to diffuse to the surface. Geophysical data, such as magnetotelluric and gravity constraints, can give additional insight into the current state of the CML. Of particular interest are the Ordos Basin on the western part of the North China Craton, the Parana Basin in South America, Lake Victoria on the Tanzania Craton, the Colorado Plateau, and the Congo Basin on the Congo Craton.

5.3 Conclusions

1) The heterogeneity that results from the multi-stage tectonic history of the continental lithosphere affects the way it behaves under extension. In particular, the distribution of stiff and pliable layers, the strength of the lithosphere and equivalently the strain rate, affects the growth rate of necking instabilities. Necking instabilities therefore grow faster in weaker lithosphere under a higher strain rate in most model configurations that were tested for Chapter 2. Thus, strong lithosphere is protected from deformation where surrounded by weaker lithosphere.

2) The models presented in Chapter 2 illustrate how asymmetric margins may result from a lithospheric strength contrast. Deformation is localized at the lithospheric boundary, but is more distributed in the weaker lithosphere under the higher strain rate than in the strong lithosphere under a lower strain rate. The final result is an asymmetric conjugate margin pair, where the margin underlain by stronger lithosphere is narrow (50 km) and the margin underlain by weaker lithosphere is wide (150 km).

3) Cratons that are initially strong and protected by surrounding weaker lithosphere need to be weakened significantly in order to rift. I propose that fluid and/or melt metasomatism may be the weakening mechanism responsible for rifting of the North China, the Tanzania, and the North Atlantic cratons. Refertilization (increasing density), rehydration (increasing H_2O content), and an increasing geothermal gradient (increasing temperature) are a consequence of metasomatism and result in convective removal and significant thinning (100-150 km) of the cratonic mantle lithosphere (CML) in some of the models presented.

4) The craton rifting models illustrate the importance of the timing of extension with respect to metasomatism. Heat diffusion weakens the crust, but also decreases the Moho temperature. Rifting only localizes in the craton when extension occurs relatively soon after an increase in temperature. The cratonic lithosphere has to be hotter, but also thinner, than the standard lithosphere to rift. The reactive front model had the hottest Moho temperature, but only localized rifting in the cratonic lithosphere where the strength contrast between the standard and cratonic lithosphere was decreased.

5) Sensitivity tests for the metasomatism models illustrate the effects of the individual components of metasomatism. Even if the CML is thinned by 30 km, when the density causes the CML to become gravitationally unstable and rehydration decreases the viscosity, the cratonic lithosphere does not become vulnerable to rifting in the absence of a temperature increase. This is because increasing temperature has a much greater effect on reducing viscosity than hydration (Figure 5.1).

6) Cratons are more susceptible to rifting and do not have to be weakened to the same extent as in my M-type and RF33-3 models if the adjacent lithosphere is stronger (or alternatively if the craton is weaker) than in my initial model design. The smaller the strain rate contrast between the cratonic and standard lithosphere, the less weakening is required to rift the craton.

7) The complex subsidence histories of intracratonic basins can be explained by the effects of mantle metasomatism. Gradual subsidence is expected where melt metasomatism increases CML density by refertilization. Uplift and erosion are expected following partial delamination of CML. A third subsidence phase corresponds to protracted cooling of the hot metasomatized lithosphere.

Appendix A Modeling Methods

A.1 Overview of SOPALE-Nested Software

We use a 2D upper-mantle-scale model comprising adjacent regions of standard and cratonic lithosphere subject to extension under specified velocity boundary conditions. We calculate the model evolution using an Arbitrary-Lagrangian-Eulerian (ALE) finite element method, which can accommodate large amounts of deformation, using the software SOPALE-nested. The code solves the thermo-mechanically coupled, incompressible viscous-plastic creeping (Stokes) flow equations and has thermally activated power-law viscous rheologies.

For each timestep, the force balance equations, for a quasi-static incompressible creeping flow, are solved in two dimensions (Equations A.1 and A.2) on the Eulerian grid. These are coupled to the energy balance equation (Equation A.3) through the temperature-dependent viscosity and density and constrained by mechanical and thermal boundary conditions.

$$\frac{\partial \sigma_{ij}}{\partial x_i} - \frac{\partial P}{\partial x_i} + \rho g = 0 \qquad i,j = 1,2 \qquad (A.1)$$

$$\frac{\partial v_i}{\partial x_i} = 0 \qquad i = 1,2 \qquad (A.2)$$

$$\rho C_p \left(\frac{\partial T_K}{\partial t} + \frac{\partial T_K}{\partial x_i}\right) = K(T_K)\frac{\partial^2 T_K}{\partial x_i^2} + A_R + v_2\, \alpha(T_K)\, g T_K \rho \quad i = 1,2 \qquad (A.3)$$

where σ_{ij} is the deviatoric stress tensor, x_i spatial coordinates, P is the pressure (mean stress), ρ the density, g the gravitational acceleration, v_i a component of velocity, C_p the specific heat, T_K the absolute temperature, t time, $K(T_K)$ the thermal conductivity, A_R radioactive heat production per unit volume, and $\alpha\ (T_K)$ the volumetric thermal expansivity.

All models have a high resolution nest embedded in the large scale domain. The solution for the velocity and thermal field are first found for the 2200 x 600 km domain. The solution is then used as the boundary condition for the nested domain around the center of the model from 300-2100 km and 360 km deep. A two-way connection is maintained by the Lagrangian

tracking particles, which are shared between the two solutions; the particles in the nested domain always obey the higher resolution solution.

A.2 Model Design

The large-scale model has basal and side boundaries with free slip in the horizontal and vertical directions, respectively, and no basal vertical velocity. Extension of the lithosphere is defined by horizontal velocities of 0.5 cm a^{-1} on the right and left horizontal boundaries (total 1 cm a^{-1}). A small horizontal flux of material into the sub-lithospheric mantle allows for conservation of mass, and there is no material flux through the base. The model (Figure 4.1) juxtaposes a "standard" 140 km thick lithosphere with a 250 km thick "cratonic" lithosphere (Artemieva and Mooney 2001, Griffin et al. 2009b). Two Mantle Weak Zones (MWZ) of 12 x 10 km are embedded in the upper mantle lithosphere equidistant from the lithospheric boundary. The MWZ are 500 km away from the lithospheric boundary and have a reduced internal angle of friction of 2˚ to represent the effect of inherited plastic strain softening. The size and position of the weak zones was chosen to represent simplified residual mantle weaknesses; elsewhere, annealing in the hotter viscous parts of the lithosphere (Yamasaki et al. 2006), where grain regrowth is efficient, is assumed to have removed strength contrasts associated with grain size reduction in lithospheric-scale sutures, although some form of heterogeneity (e.g. compositional) may remain (Vauchez et al. 2012).

The base of the cratonic mantle lithosphere (CML) is tapered over a horizontal distance of 300 km to represent the effect of a history of destabilization of the edge of the craton by various processes and to reduce the tendency for vigorous edge driven convection (EDC), which is not the subject of this investigation. In addition, the models are computed for an initial spin-up phase of 1 Ma with no extension to achieve a statistical convective equilibrium between the lithospheres and the sublithospheric. The model was also tested for an initial 100 Ma to demonstrate stability against EDC and convective CML removal (Figure 4.2). There is only minimal deformation of the lower boundary of the lithospheres during this phase which demonstrates initial stability against EDC convective erosion of the CML owing to disequilibrium in the initial conditions, a requirement emphasized by Sleep (2007). Destabilization of the CML

during the main phase of the computations is therefore the result of the metasomatism, not the initial conditions.

A.3 Material Properties

The deformation mechanism is determined by the state of stress in the flow. Flow is viscous (Equation A.4) where stress is lower than the frictional-plastic yield stress. In contrast, where stress is on the frictional-plastic yield envelope, described by the pressure-dependent Drucker-Prager yield criterion (Equation 5), material deforms in a plastic (stiff) manner.

$$\eta = f\, A^{-1/n} (\dot{\mathrm{I}}_2')^{\frac{1-n}{2n}} \exp\left(\frac{Q + PV^*}{nRT_K}\right) \qquad (A.4)$$

$$J_2' = P \sin\phi_{\mathrm{eff}} + C \cos\phi_{\mathrm{eff}} \qquad (A.5)$$

In power-law flow (Equation A.4), *f* is the viscosity scaling factor which modifies the relative strength of viscous materials with respect to the reference flow law, *f* =1, as explained below, A is the pre-exponential scaling factor, $\dot{\mathrm{I}}_2' = \left(\frac{1}{2}\dot{\epsilon}_{ij}'\dot{\epsilon}_{ij}'\right)$ is the second invariant of the deviatoric strain rate tensor $\dot{\epsilon}_{ij}'$, n is the power law exponent, Q is the activation energy, V^* is the activation volume, *R* is the universal gas constant. In Equation (5), J_2' = $\left(\frac{1}{2}\sigma_{ij}'\sigma_{ij}'\right)^{1/2}$ is the square root of the second invariant of the deviatoric stress σ_{ij}', C is the cohesion, ϕ_{eff} is the effective internal angle of friction taking account of hydrostatic fluid pressure (using $Psin\,\phi_{\mathrm{eff}} = (P - P_f)sin\,\phi$ where P_f is the pore-fluid pressure), which gives $\phi_{\mathrm{eff}} \sim 15^\circ$ where $\phi = 30°$. Parameter values are given in Table A.1.

Only two laboratory-determined flow-law are used in these models. We use “Wet” Quartzite (WQz) (Gleason and Tullis 1995) for the crust and “Wet” Olivine (WOl) (Karato and Wu 1993) for the mantle. These flow laws are scaled with the scaling factor *f* to increase/decrease the relative strength (Butler et al. 2014, Appendix). This simplification allows for a relative comparison between materials of different strengths without having to incorporate other flow laws (Beaumont et al. 2006, Jamieson et al. 2007, Karato 2010).

Property	Symbol	Value
Frictional-plastic parameters		
Internal angle of friction (˚)	ϕ_{eff}	15 → 2
Over strain range of (%)	ε	50-150
Crust cohesion (Pa)	C_{Crust}	$1{\cdot}10^{7}$
Mantle cohesion (Pa)	C_{Mantle}	$2{\cdot}10^{6}$
Crust: Wet Quartzite	WQz	
Power law exponent	n_{Crust}	4
Activation energy (J mol^{-1})	Q	$223{\cdot}10^{3}$
Initial constant (tensor invariant) ($Pa^{-n}s^{-1}$)	A	$8.574{\cdot}10^{-28}$
Scaling factor	f_{Crust}	variable
Crustal density (kg m^{-3})	ρ_S	2800
Mantle: Wet Olivine	WOl	
Power law exponent	$n_{ML} = n_{SML}$	3
Activation energy (J mol^{-1})	Q	$430{\cdot}10^{3}$
Activation Volume (m^3 mol^{-1})	V^*	$12{\cdot}10^{-6}$
Initial constant (tensor invariant) ($Pa^{-n}s^{-1}$)	A	$1.7578{\cdot}10^{-14}$
Standard mantle lithosphere density (kg m^{-3})	ρ_{UML1}	3360
Cratonic mantle lithosphere density (kg m^{-3})	ρ_{UML2}	3335
Sub-lithospheric mantle density (kg m^{-3})	ρ_{SLM}	3378
Standard Moho temperature (˚C)	T_{Moho}	600
Cratonic Moho temperature (˚C)	T_{CMoho}	450
Base of lithosphere temperature (˚C)	T_L	1350
Basal heat flux (mW m^{-2})	q	21-22
Standard lithosphere surface heat flux (mW m^{-2})	q_s	62.5
Cratonic lithosphere surface heat flux (mW m^{-2})	q_c	38.6
Radiogenic Heat Production	A_R	
Standard upper crust (μW m^{-3})	$A_{R_{UCS}}$	1.5
Standard lower crust (μW m^{-3})	$A_{R_{LCS}}$	0.5
Cratonic upper crust (μW m^{-3})	$A_{R_{UCC}}$	0.6
Cratonic lower crust (μW m^{-3})	$A_{R_{LCC}}$	0.2
Coefficient of thermal expansion (˚C^{-1})	$\alpha(T)$	$3.2{\cdot}10^{-5}$ → $3.9{\cdot}10^{-5}$
Over temperature range (˚C)		500-2000
Crust thermal conductivity (W m^{-1}˚C^{-1})	K_{Crust}	2.25
Standard mantle lithosphere thermal conductivity (W m^{-1}˚C^{-1})	$K_{MLS}(T)$	2.7
Cratonic mantle lithosphere thermal conductivity (W m^{-1}˚C^{-1})	K_{MLC}	5.3
Sub-lithospheric mantle thermal conductivity (W m^{-1}˚C^{-1})	$K_{SLM}(T)$	3-40
Over temperature range (˚C)		1323-1423
Melt Metasomatism		
Heat capacity peridotite (J Kg^{-1} ˚C^{-1})	Cp_1	1100
Latent heat of crystallization peridotite (J Kg^{-1} ˚C^{-1})	L_1	$4.0{\cdot}10^{5}$
Peridotite liquidus, intermediate temperature and solidus (˚C)	T_{1L}, T_{1i}, T_{1S},	1900, 1750, 1600
Peridotite melt coefficient high, low for	X_{1h}, X_{1l}	0.6, 04
Temperature of the melt (˚C)	T_m	1300
Heat Capacity melt (J Kg^{-1} ˚C^{-1})	Cp_2	1480
Latent heat of crystallization melt (J Kg^{-1} ˚C^{-1})	L_2	$4.0{\cdot}10^{5}$
Melt liquidus, intermediate temperature and solidus (˚C)	T_{2L}, T_{2i}, T_{2S},	1250, 1075, 725
Melt coefficient high, low	X_{2h}, X_{2l}	0.6, 04

Table A.1. Model Parameters for Chapter 4

The scaling approach is also valid for a considerable range of *f* values, even for the reference flow laws, owing to the significant experimental uncertainties associated with the laboratory-determined flow-law parameters (Beaumont et al. 2006, Jamieson et al. 2007, Karato 2010, Butler et al. 2014).

The models presented have a constant scaling factor of WQz x 3 for the standard crust and WQz x 5 for the cratonic crust. Scaling factors of *f* = 3 and 5 approximate a mixed quartz-feldspar controlled crust, or 'dry' quartz with increasing feldspar content. We scale the flow laws for the mantle lithospheres to represent dehydration. In most models, the standard lithosphere has WOl x 3 to account for the moderate dehydration expected in Proterozoic or Phanerozoic mantle lithosphere (Griffin et al. 2009b). The CML starts with an effective viscosity of WOl x 5 corresponding to low water content (<0.001 wt% H_2O), and close to the 'dry' olivine flow law (Karato, 2010, Butler et al. 2014, Appendix). As the CML is metasomatized the scaling factor decreases to 1 (as explained below) linearly with the olivine Mg#, 92 to 89, so that it reaches WOl x 1 by the end of metasomatism at Mg# 89. This reproduces a decrease in the viscosity expected with rehydration of the CML. The question here is whether the scaling of the olivine flow law should be more complex than the linear variation with olivine Mg#. We adopted the linear scaling to keep things simple but if the water content or the viscosity changes in a more complex manner with Mg # we can approximate this effect. Other complications concern fugacity and choice of V^* value. Uncertainties in these effects may render more complex scaling of *f* of no real value.

Strain-softening is included in the brittle regime to represent the formation of weak faults. The effective internal angle of friction is decreased linearly from 15˚ to 2˚ as the effective strain increases from 50% to 150%. The models are not particularly sensitive to the range of strain over which materials undergo strain softening (Huismans and Beaumont 2007). The requirement for a low strain-softened angle of internal of friction is a consequence of the resolution of the computational finite element grid, such that with higher resolution grid a larger value would give equivalent results.

A.4 Thermal Properties

The initial 2D steady-state temperature of the system is determined by the insulated side boundaries, the basal heat flux, the radioactive heat production in the crust (A_r), and the thermal conductivity ($K(T_K)$). These parameters are different for the standard and cratonic lithospheres (Table A.1) and are selected so that the temperature at their base is 1350˚C. The standard lithosphere has a higher geothermal gradient (surface heat flow is 62.5 mW m^{-2}) than the cratonic lithosphere (surface heat flow of 38.6 mW m^{-2}). The basal heat flux changes from 20 to 22 mW m^{-2} at the center of the model. The standard lithosphere has a radioactive heat production of 1.5 μW m^{-3} in the upper crust and 0.5 μW m^{-3} in the lower crust (Hasterok and Chapman 2011) and the Moho temperature is 600˚C. The cratonic crust has a lower radiogenic heat production of 0.6 μW m^{-3} and 0.2 μW m^{-3} for the upper and lower crust, respectively, and the Moho temperature is 450˚C.

The choice of thermal expansivity of the mantle lithospheres and sublithospheric mantle is important because it determines the thermal buoyancy which directly competes with the effects of depletion on material density, particularly in the CML which is designed to be isopycnic. Uniform values of thermal expansivity for the mantle in the range 3.0-3.2 x 10^{-5} deg^{-1} are commonly used, but there is increasing evidence that thermal expansivity depends on temperature (Bouhifd et al. 1996). We approximate this temperature dependence such that for T < 500 K $\alpha(T_K) = 3.1 \times 10^{-5}$ K^{-1} and for T> 2000 K $\alpha(T_K) = 3.9 \times 10^{-5}$ K^{-1} and varies linearly between these temperatures. The high temperature expansivity has been reduced by comparison with the Bouhifd et al. (1996) value to account for the secondary effect of pressure on thermal expansivity (Katsura et al. 2009).

During time stepping, the heat conservation equation A.3 is solved with the same boundary conditions as those described above.

A.5 Metasomatism in the Models

To simulate the refertilization of CML through a process of stealth metasomatism (O' Reilly 2014), uniformly distributed basaltic melt is injected at a given temperature, T_{BM}, and a steady fractional volumetric rate, R_{BM}, to selected layers in the CML for a given time interval,

t_{BM}. Our focus is the effect of the melt as it percolates the CML layers, and we therefore do not specify the production of melt, but it could derive from a mantle plume or melting in the mantle wedge above a subducting slab. There are 11 horizontal layers in the CML each one of which can be metasomatized independently during each model timestep. We use a simple reaction model between the depleted peridotite and the basaltic melt in which both the heat and mass of the metasomatized layer are conserved. There are three effects: 1) as hot melt rapidly cools and crystallizes all heat released, including latent heat, is absorbed by the CML layer, thereby increasing its temperature and decreasing its viscosity; 2) the melt reacts with the peridotite to make it less depleted as measured by the Mg# (Lee 2003) which progressively increases its density from 3335 kg m^{-3} (Mg# 92) to a specified maximum of 3378 kg m^{-3} (Mg# 89) when 30% by volume of melt has been added, at which point its material density is equal to that of the sublithospheric mantle (Table A.1), and; 3) the CML is incrementally rehydrated by changing the scaling factor in the viscous flow law from "Wet" Olivine WOl x 5 to a WOl x 1 as the 30% melt is added. In addition to heat conservation as the hot melt is added, mass is conserved during the reaction with the peridotite and the associated change in volume during the reaction is enforced on the model layer.

As pieces of detached CML sink, the material properties are changed to those of the sublithospheric mantle (density 3378 kg m^{-3}, WOl x 1) after they reach a depth of 500 km. These pieces of CML can only reach this depth after delamination and this is normally close to the end of metasomatism. The 500 km depth was chosen to minimize interference with current delamination by previously delaminated CML.

A.5.1 Conservation of Heat

Basaltic melt is injected at a specified temperature, T_{BM}, and can therefore be at a higher or lower temperature than the surrounding lithospheric layer and can cause an increase or decrease in the temperature. We take into account cooling of the basaltic melt to the local ambient temperature of the lithosphere, which may include the release of latent heat when melt solidifies. For each Eulerian element in the finite element model the heat released by a fractional volume ΔV_2 of the melt, referred to as material 2, is equal to:

$$Q_2 = \Delta V_2(Cp_2\rho_2\Delta T + rX_2\rho_2 L_2) \quad (A.6)$$

where Cp_2 is the specific heat capacity of the basaltic melt, ΔT the difference in temperature between the melt and the ambient temperature, r ratio between the actual temperature change and the total temperature change of the region (see below), X_2 the melt fraction and L_2 the latent heat of crystallization. The other variables are the same as described above.

There are four specified cooling intervals based on Annen et al. (2006) (Figure A.1): 1) specific heat released during cooling to the liquidus temperature of material 2; 2) specific and latent heat released between the liquidus and the intermediate temperature (Annen et al. 2006); 3) specific and latent heat released between the intermediate temperature and the solidus temperature of material 2, and; 4) specific heat released below the solidus temperature. The intermediate temperature reflects changes in melt fraction with temperature that has two linear segments (Figure A1).

The total heat released by cooling of material 2 is absorbed by material 1, the peridotite, and is described by a similar equation:

$$Q_1 = (\Delta V_1 + V_1^I)(Cp_1\rho_1\Delta T + rX_1\rho_1 L_1) \quad (A.7)$$

Q_1 is the heat absorbed by material 1, ΔV_1 is the change in volume calculated from the mass balance equation, V_1^I the initial volume of the element at the beginning of the timestep, Cp_1 the specific heat capacity of material 1, ρ_1 the density of material 1, X_1 the melt fraction for either a low or high temperature region between the solidus and liquidus, and L_1 the latent heat of fusion for material 1. The temperature regions are defined in the same manner as for the heat released, but with parameters specific to material 1. However, in these models the temperature never goes above the solidus temperature of peridotite and so the temperature of material 1 only changes because specific heat is absorbed (Hirschmann 2000). The thermal parameters of material 1 are constant, although heat is technically absorbed by the evolving peridotite. This simplification is justified because the density of the peridotite increases by a very small amount..

A.5.2 Conservation of Mass and Rehydration

The original material is the depleted CML, a peridotite with WOl x 5 and a density of 3335 kg m^{-3} (corresponding to Mg# 92). The basaltic melt is injected at a constant rate calculated by the total volume change required divided by the length of time over which metasomatism is occurring. Metasomatism occurs over specified time intervals and will increase the initial volume by a specified amount, 30% in most cases for the models used here.

The basaltic melt (material 2) reacts with the peridotite (material 1) to give the new material a less depleted character (i.e. increase in Fe), thereby increasing material 1's density. Although the temperature at which material 2 is injected dictates all of it to be melt, it is injected with the density of the solid. We justify this by asserting that the melt crystallizes in less time than a model time step and therefore has a solid density by the end of the timestep. The density of material 1 increases incrementally from 3335 kg m^{-3} to 3378 kg m^{-3} over the total time of melt injection. This represents a decrease in Mg# of 93 to 89 (Lee 2003, Lee et al. 2011). The volume change of material 1, required by the mass balance during the reaction is described by the following equation:

$$\Delta V_2 \rho_2 + V_1^I \rho_1^I = \rho_1^F V_1^I (1 + \Delta V_1) \qquad (A.8)$$

Where ΔV_2 is the constant volume of material 2 added per timestep, ρ_2 the density of material 2, V_1^I the Volume of material 1 at the beginning of the timestep, ρ_1^I and, ρ_1^F the initial density and final density for material 1 during this timestep, and ΔV_1 the fractional change in volume 1.

The scaling factor f is linearly decreased from WOl x 5 to WOl x 1 to simulate rehydration over the range of metasomatism. The CML becomes more deformable as the viscosity of the mantle lithosphere decreases. In nature rehydration would have the additional effect of lowering the solidus temperature. This is not taken into account in the models presented, however the decrease in melting temperature of the peridotite is still insufficient to produce melt in the CML (Hirschmann 2000).

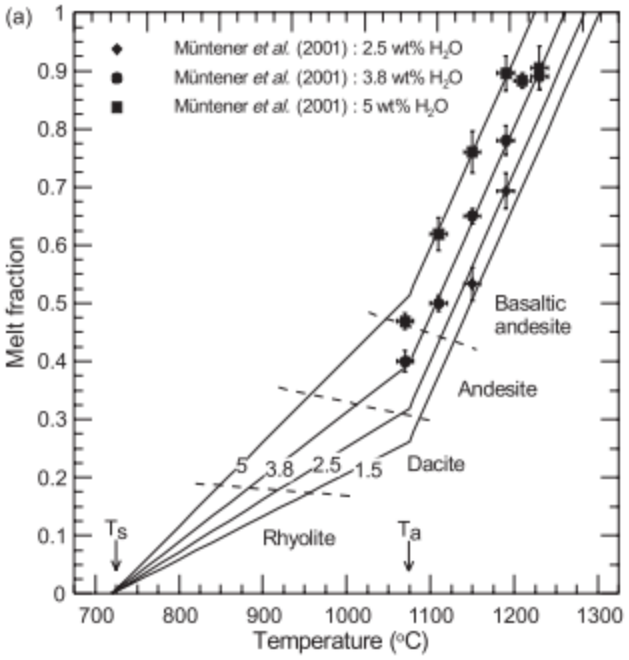

Figure A.1. Melt Fractions. (Annen et al. 2006)

References

Allen, P.A., and Armitage, J.J. 2012. Cratonic basins. *In* Tectonics of Sedimentary Basins: Recent Advances. *Edited by* C. Busby and A. Azor. Blackwell Publishing Ltd. pp. 602–620.

Allken, V., Huismans, R.S., and Thieulot, C. 2012. Factors controlling the mode of rift interaction in brittle-ductile coupled systems: A 3D numerical study. Geochemistry Geophysics Geosystems **13**(5): Q05010. doi: 10.1029/2012GC004077.

Annen, C., Blundy, J.D., and Sparks, R.S.J. 2006. The genesis of intermediate and silicic magmas in deep crustal hot zones. J. Pet. **47**(3): 505–539. doi: 10.1093/petrology/egi084.

Armitage, J.J., and Allen, P.A. 2010. Cratonic basins and the long-term subsidence history of continental interiors. J. Geol. Soc. London. **167**(1): 61–70. doi: 10.1144/0016-76492009-108.

Artemieva, I.M. 2009. The continental lithosphere: Reconciling thermal, seismic, and petrologic data. Lithos **109**(1-2): 23–46. doi: 10.1016/j.lithos.2008.09.015.

Artemieva, I.M., and Mooney, W. 2001. Thermal thickness and evolution of Precambrian lithosphere: A global study. J. Geophys. Res. **106**(B8): 16387–16414.

Aulbach, S., Rudnick, R.L., and McDonough, W.F. 2008. Li-Sr-Nd isotope signatures of the plume and cratonic lithospheric mantle beneath the margin of the rifted Tanzanian craton (Labait). Contrib. to Mineral. Pet. **155**: 79–92. doi: 10.1007/s00410-007-0226-4.

Axen, G.J. 2004. Mechanics of low-angle normal faults. *In* Rheology and Deformation of the Lithosphere at Continental Margins. *Edited by* G.D. Karner, B. Taylor, N.W. Driscoll, and D.L. Kohlstedt. Columbia University Press, New York. pp. 46–91.

Baldridge, W.S., Keller, G.R., Haak, V., Wendlandt, E., Jiracek, G.R., and Olsen, K.H. 1995. The Rio Grande rift. *In* Continental rifts: Evolution, Structure, Tectonics. *Edited by* K.H. Olsen. Elsevier, Amsterdam, Holland. pp. 233–275.

Barbosa, J.S.F., and Sabaté, P. 2004. Archean and Paleoproterozoic crust of the São Francisco Craton, Bahia, Brazil: geodynamic features. Precambrian Res. **133**(1-2): 1–27. doi: 10.1016/j.precamres.2004.03.001.

Bashir, L., Gao, S.S., Liu, K.H., and Mickus, K. 2011. Crustal structure and evolution beneath the Colorado Plateau and the southern Basin and Range Province: Results from receiver function and gravity studies. Geochemistry Geophysics Geosystems **12**(6): Q06008. doi: 10.1029/2011GC003563.

Bassi, G. 1991. Factors controlling the style of continental rifting: insights from numerical modelling. Earth Planet. Sci. Lett. **105**: 430–452.

Bassi, G. 1995. Relative importance of strain rate and rheology for the mode of continental extension. Geophys. J. Int. **122**: 195–210.

Bassi, G., Keen, C.E., and Potter, P. 1993. Contrasting styles of rifting: models and examples from the eastern Canadian margin. Tectonics **12**(3): 639–655.

Beaumont, C., Jamieson, R.A., Butler, J.P., and Warren, C.J. 2009. Crustal structure: A key constraint on the mechanism of ultra-high-pressure rock exhumation. Earth Planet. Sci. Lett. **287**(1-2): 116–129. doi: 10.1016/j.epsl.2009.08.001.

Beaumont, C., Nguyen, M.H., Jamieson, R.A., and Ellis, S. 2006. Crustal flow modes in large hot orogens. *In* Channel Flow, Ductile Extrusion and Exhumation in Continental Collision Zones. *Edited by* R.D. Law, M.P. Searle, and L. Godin. Geological Society, London, Special Publications. pp. 91–145. doi: 10.1144/GSL.SP.2006.268.01.05.

Begg, G.C., Griffin, W.L., Natapov, L.M., O'Reilly, S.Y., Grand, S.P., O'Neill, C.J., Hronsky, J.M.A., Djomani, Y.P., Swain, C.J., Deen, T., and Bowden, P. 2009. The lithospheric architecture of Africa: Seismic tomography, mantle petrology, and tectonic evolution. Geosphere **5**(1): 23–50. doi: 10.1130/GES00179.1.

Behrendt, J.C., LeMasurier, W.E., Cooper, A.K., Tessensohn, F., Trehu, A., and Damaske, D. 1991. Geophysical studies of the West Antarctic rift system. Tectonics **10**(6): 1257–1273.

Benes, V., and Davy, P. 1996. Modes of continental lithospheric extension: experimental verification of strain localization processes. Tectonophysics **254**(1-2): 69–87. doi: 10.1016/0040-1951(95)00076-3.

Bernstein, S., Kelemen, P.B., and Hanghøj, K. 2007. Consistent olivine Mg# in cratonic mantle reflects Archean mantle melting to the exhauston of orthopyroxene. Geology **35**(5): 459–462. doi: 10.1130/G23336A.1.

Beuchert, M.J., and Podladchikov, Y.Y. 2010. Viscoelastic mantle convection and lithospheric stresses. Geophys. J. Int. **183**(1): 35–63. doi: 10.1111/j.1365-246X.2010.04708.x.

Blaich, O.A., Faleide, J.I., and Tsikalas, F. 2011. Crustal breakup and continent-ocean transition at South Atlantic conjugate margins. J. Geophys. Res. **116**(B1): B01402. doi: 10.1029/2010JB007686.

Blaich, O.A., Faleide, J.I., Tsikalas, F., Gordon, A.C., and Mohriak, W. 2013. Crustal-scale architecture and segmentation of the South Atlantic volcanic margin. *In* Conjugate Divergent Margins. *Edited by* W.U. Mohriak, A. Danforth, P.J. Post, D.E. Brown, G.C. Tari, M. Nemcok, and S.T. Sinha. Geological Society, London, Special Publications. pp. 167–183. doi: 10.1144/sp369.22.

Blaich, O.A., Faleide, J.I., Tsikalas, F., Lilletveit, R., Chiossi, D., Brockbankc, P., and Cobbold, P. 2010. Structural architecture and nature of the continent-ocean transitional domain at the Camamu and Almada Basins (NE Brazil) within a conjugate margin setting. Petrol. Geol. Conf. Ser. **7**: 867–883. doi: 10.1144/0070867.

Blaich, O.A., Tsikalas, F., and Faleide, J.I. 2008. Northeastern Brazilian margin: Regional tectonic evolution based on integrated analysis of seismic reflection and potential field data and modelling. Tectonophysics **458**(1-4): 51–67. doi: 10.1016/j.tecto.2008.02.011.

Van Den Bleeken, G., Müntener, O., and Ulmer, P. 2010. Reaction processes between tholeiitic melt and residual peridotite in the uppermost mantle: An experimental study at 0·8 GPa. J. Pet. **51**(1-2): 153–183. doi: 10.1093/petrology/egp066.

Bodinier, J.L., Vasseur, G., Vernieres, J., Dupuy, C., and Fabries, J. 1990. Mechanisms of mantle metasomatism: Geochemical evidence from the Lherz peridotite. Jour. Pet. **31**(3): 597–628.

Boillot, G., and Froitzheim, N. 2001. Non-volcanic rifted margins, continental break-up and the onset of sea-floor spreading: some outstanding questions. *In* Non-volcanic Rifting of Continental Margins: A Comparion of Evidence from Land and Sea. *Edited by* R.C.L. Wilson, R.B. Whitmars, B. Taylor, and N. Froitzheim. Geological Society, London, Special Publications. pp. 9–30. doi: 10.1144/GSL.SP.2001.187.01.02.

Boillot, G., Grimaud, S., Mauffret, A., Mougenot, D., Kornprobst, J., Mergoil-Daniel, J., and Torrent, G. 1980. Ocean-continent boundary off the Iberian margin: A serpentinite diapir west of the Galicia Bank. Earth Planet. Sci. Lett. **48**(1): 23–34. doi: 10.1016/0012-821X(80)90166-1.

Boillot, G., Recq, M., Winterer, E.L., Meyer, A.W., Applegate, J., Baltuck, M., Bergen, J.A., Comas, M.C., Davies, T.A., Dunham, K., Evans, C.A., Girardeau, J., Goldberg, G., Haggerty, J., Jansa, L.F., Johnson, J.A., Kasahara, J., Loreau, J.P., Luna-Sierra, E., Moullade, M., Ogg, J., Sarti, M., Thurow, J., and Williamson, M. 1987. Tectonic denudation of the upper mantle along passive margins: a model based on drilling results (ODP leg 103, western Galicia margin, Spain). Tectonophysics **132**: 335–342. doi: 10.1016/0040-1951(87)90352-0.

Bonini, M., Corti, G., Ventisette, C. Del, Manetti, P., Mulugeta, G., and Sokoutis, D. 2007. Modelling the lithospheric rheology control on the Cretaceous rifting in West Antarctica. Terra Nov. **19**(5): 360–366. doi: 10.1111/j.1365-3121.2007.00760.x.

Bos, B., and Spiers, C.J. 2002. Frictional-viscous flow of phyllosilicate-bearing fault rock: Microphysical model and implications for crustal strength profiles. J. Geophys. Res. **107**(B2): 2028. doi: 10.1029/2001JB000301.

Bostock, M.G. 1998. Mantle stratigraphy and evolution of the Slave province. J. Geophys. Res. **103**(B9): 21183–21200.

Bouhifd, M.A., Andrault, D., Fiquet, G., and Richet, P. 1996. Thermal expansion of forsterite up to the melting point. Geophys. Res. Lett. **23**(10): 1143–1146. doi: 10.1029/96GL01118.

Bousquet, R., Goffé, B., Henry, P., Le Pichon, X., and Chopin, C. 1997. Kinematic, thermal and petrological model of the Central Alps: Lepontine metamorphism in the upper crust and eclogitisation of the lower crust. Tectonophysics **273**(1-2): 105–127. doi: 10.1016/S0040-1951(96)00290-9.

Brun, J.P. 2002. Deformation of the continental lithosphere: Insights from brittle-ductile models. *In* Deformation Mechanisms, Rheology and Tectonics: Current Status and Future Perspectives. *Edited by* S. De Meer, M.R. Drury, J.H.P. De Bresser, and G.M. Pennock. Geological Society, London, Special Publications. pp. 355–370. doi: 10.1144/GSL.SP.2001.200.01.20.

Brun, J.P., and Beslier, M.O. 1996. Mantle exhumation at passive margins. Earth Planet. Sci. Lett. **142**(1-2): 161–173. doi: 10.1016/0012-821X(96)00080-5.

Brune, S., and Autin, J. 2013. The rift to break-up evolution of the Gulf of Aden: Insights from 3D numerical lithospheric-scale modelling. Tectonophysics **607**: 65–79. doi: 10.1016/j.tecto.2013.06.029.

Buck, W.R. 1991. Modes of continental lithospheric extension. J. Geophys. Res. **96**: 161–178.

Buck, W.R. 1993. Effect of lithospheric thickness on the formation of high- and low-angle normal faults. Geology **21**(10): 933. doi: 10.1130/0091-7613(1993)021<0933:EOLTOT>2.3.CO;2.

Buck, W.R. 2004. Consequences of asthenospheric variability on continental rifting. *In* Rheology and Deformation of the Lithosphere at Continental Margins. *Edited by* G.D. Karner, B. Taylor, N.W. Driscoll, and D.L. Kohlstedt. Columbia University Press New York. pp. 1–30.

Buck, W.R., Lavier, L., and Poliakov, A.N.B. 1999. How to make a rift wide. Philos. Trans. **357**: 671–693. doi: 10.1098/rsta.1999.0348.

Buiter, S.J.H., Steinberger, B., Medvedev, S., and Tetreault, J.L. 2012. Could the mantle have caused subsidence of the Congo Basin? Tectonophysics **514-517**: 62–80. doi: 10.1016/j.tecto.2011.09.024.

Buiter, S.J.H., and Torsvik, T.H. 2014. A review of Wilson Cycle plate margins: A role for mantle plumes in continental break-up along sutures? Gondwana Res. **26**(2): 627–653. International Association for Gondwana Research. doi: 10.1016/j.gr.2014.02.007.

Burchfiel, B.C., Cowan, D.S., and Davis, G.A. 1992. Tectonic overview of the Cordilleran orogen in the western United States. *In* The Cordilleran Orogen: Conterminous U.S. The Geology of North America, The Geolog. *Edited by* B.C. Burchfiel, P.W. Lipman, and M.L. Zoback. Geological Society of America, Boulder, Colorado. pp. 407–479.

Burov, E.B. 2011. Rheology and strength of the lithosphere. Mar. Petrol. Geol. **28**(8): 1402–1443. doi: 10.1016/j.marpetgeo.2011.05.008.

Butler, J.P., Beaumont, C., and Jamieson, R.A. 2014. The Alps 2: Controls on crustal subduction and (ultra)high-pressure rock exhumation in Alpine-type orogens. J. Geophys. Res. **119**(7): 5987–6022. doi: 10.1002/2013JB010799.

Canil, D. 2004. Mildly incompatible elements in peridotites and the origins of mantle lithosphere. Lithos **77**(1-4): 375–393. doi: 10.1016/j.lithos.2004.04.014.

Carlson, R.W., Irving, A.J., Schulze, D.J., and Hearn, B.C. 2004. Timing of Precambrian melt depletion and Phanerozoic refertilization events in the lithospheric mantle of the Wyoming Craton and adjacent Central Plains Orogen. Lithos **77**(1-4): 453–472. doi: 10.1016/j.lithos.2004.03.030.

Carlson, R.W., Pearson, D.G., and James, D.. E. 2005. Physical, chemical, and chronological characteristics of continental mantle. Rev. Geophys. **43**(1): RG1001. doi: 10.1029/2004RG000156.

Castro, A. 1987. The northeastern Brazil and Gabon basins: a double rifting system associated with multiple crustal detachment surfaces. Tectonics **6**(6): 727–738.

Chalmers, J.A. 1997. The continental margin off southern Greenland: along-strike transition from an amagmatic to a volcanic margin. J. Geol. Soc. London. **154**(3): 571–576. doi: 10.1144/gsjgs.154.3.0571.

Chalmers, J.A., and Pulvertaft, T.C.R. 2001. Development of the continental margins of the Labrador Sea: a review. *In* Non-volcanic Rifting of Continental Margins: A Comparion of Evidence from Land and Sea. *Edited by* R.C.L. Wilson, R.B. Whitmarsh, B. Taylor, and N. Froitzheim. Geological Society, London, Special Publications. pp. 77–105. doi: 10.1144/GSL.SP.2001.187.01.05.

Chang, H.K., Kowsmann, R.O., Figueiredo, A.M.F., and Bender, A. 1992. Tectonics and stratigraphy of the East Brazil Rift system: an overview. Tectonophysics **213**(1-2): 97–138. doi: 10.1016/0040-1951(92)90253-3.

Chemenda, A., Déverchère, J., and Calais, E. 2002. Three-dimensional laboratory modelling of rifting: application to the Baikal Rift, Russia. Tectonophysics **356**(4): 253–273. doi: 10.1016/S0040-1951(02)00389-X.

Chen, W.-P., Hung, S.-H., Tseng, T.-L., Brudzinski, M., Yang, Z., and Nowack, R.L. 2012. Rheology of the continental lithosphere: Progress and new perspectives. Gondwana Res. **21**(1): 4–18. doi: 10.1016/j.gr.2011.07.013.

Chenin, P., and Beaumont, C. 2013. Influence of offset weak zones on the development of rift basins: Activation and abandonment during continental extension and breakup. J. Geophys. Res. **118**: 1–23. doi: 10.1002/jgrb.50138.

Chian, D., Louden, K.E., and Reid, I. 1995. Crustal structure of the Labrador Sea conjugate margin and implications for the formation of nonvolcanic continental margins. J. Geophys. Res. **100**(B12): 24239–24253. doi: 10.1029/95JB02162.

Chorowicz, J. 2005. The East African rift system. J. African Earth Sci. **43**(1-3): 379–410. doi: 10.1016/j.jafrearsci.2005.07.019.

Christensen, U.R. 1985. Thermal Evolution Models for the Earth. J. Geophys. Res. **90**(4): 2995–3007.

Coney, P.J. 1980. Cordilleran metamorphic core complexes: An overview. Geol. Soc. Am. Mem. **153**: 7–31. Geological Society of America.

Cooper, C.M., and Conrad, C.P. 2009. Does the mantle control the maximum thickness of cratons? Lithosphere **1**(2): 67–72. doi: 10.1130/L40.1.

Corti, G., Calignano, E., Petit, C., and Sani, F. 2011. Controls of lithospheric structure and plate kinematics on rift architecture and evolution: An experimental modeling of the Baikal rift. Tectonics **30**: 1–16. doi: 10.1029/2011TC002871.

Corti, G., Iandelli, I., and Cerca, M. 2013a. Experimental modeling of rifting at craton margins. Geosphere **9**(1): 138–154. doi: 10.1130/GES00863.1.

Corti, G., Ranalli, G., Agostini, A., and Sokoutis, D. 2013b. Inward migration of faulting during continental rifting: Effects of pre-existing lithospheric structure and extension rate. Tectonophysics **594**: 137–148. doi: 10.1016/j.tecto.2013.03.028.

Corti, G., van Wijk, J., Cloetingh, S., and Morley, C.K. 2007. Tectonic inheritance and continental rift architecture: Numerical and analogue models of the East African Rift system. Tectonics **26**(6). doi: 10.1029/2006TC002086.

Crosby, A.G., Fishwick, S., and White, N. 2010. Structure and evolution of the intracratonic Congo Basin. Geochemistry Geophysics Geosystems **11**(6): 1–20. doi: 10.1029/2009GC003014.

Crow, R., Karlstrom, K., Asmerom, Y., Schmandt, B., Polyak, V., and DuFrane, S.A. 2010. Shrinking of the Colorado Plateau via lithospheric mantle erosion: Evidence from Nd and Sr isotopes and geochronology of Neogene basalts. Geology **39**(1): 27–30. doi: 10.1130/G31611.1.

Daly, M.C., Lawrence, S.R., Diemu-Tshiband, K., and Matouana, B. 1992. Tectonic evolution of the Cuvette Centrale, Zaire. J. Geol. Soc. London. **149**(4): 539–546. doi: 10.1144/gsjgs.149.4.0539.

Davis, M., and Kusznir, N. 2004. Depth-dependent lithospheric stretching at rifted continental margins. *In* Rheology and Deformation of the Lithosphere at Continental Margins. *Edited by* G.D. Karner, B. Taylor, N.W. Driscoll, and D.L. Kohlstedt. Columbia University Press New York. pp. 92–137.

Davison, I. 1997. Wide and narrow margins of the Brazilian South Atlantic. J. Geol. Soc. London. **154**: 471–476. doi: 10.1144/gsjgs.154.3.0471.

Dawson, J.B. 1984. Contrasting types of upper-mantle metasomatism. Kimberlites II. Elsevier, Amsterdam: 289–294.

Delvaux, D., Moeys, R., Stapel, G., Melnikov, A., and Ermikov, V. 1995. Palaeostress reconstructions and geodynamics of the Baikal region, Central Asia, Part I. Palaeozoic and Mesozoic pre-rift evolution. Tectonophysics **252**: 61–101. doi: 10.1016/0040-1951(95)00090-9.

Delvaux, D., Moeys, R., Stapel, G., and Petit, C. 1997. Paleostress reconstructions and geodynamics of the Baikal region, central Asia, Part 2. Cenozoic rifting. Tectonophysics **282**: 1–38.

Dickinson, W.R. 1978. Plate tectonic evolution of sedimentary basins. *In* Plate Tectonics and hydrocarbon accumulation. *Edited by* W.R. Dickinson and H. Yarborough. AAPG Department of Educational Activities.

Doin, M.-P., Fleitout, L., and Christensen, U. 1997. Mantle convection and stability of depleted and undepleted continental lithosphere. J. Geophys. Res. **102**(B2): 2771. doi: 10.1029/96JB03271.

Dong, H., Wei, W., Ye, G., Jin, S., Jones, A.G., Jing, J., Zhang, L., Xie, C., Zhang, F., and Wang, H. 2014. Three-dimensional electrical structure of the crust and upper mantle in Ordos Block and adjacent area: Evidence of regional lithospheric modification. Geochemistry Geophysics Geosystems **15**(6): 2414–2425. doi: 10.1002/2014GC005270.

Dore, A.G., Lundin, E.R., Fichler, C., and Olesen, O. 1997. Patterns of basement structure and reactivation along the NE Atlantic margin. J. Geol. Soc. London. **154**(1): 85–92. doi: 10.1144/gsjgs.154.1.0085.

Downey, N., Gurnis, M., and Avouac, J. 2011. Subsidence history and geodynamic evolution of the cratonic Congo basin. *In* Geophysical Research Abstracts. EGU General Assembly 2011. p. 3881.

Downey, N.J., and Gurnis, M. 2009. Instantaneous dynamics of the cratonic Congo basin. J. Geophys. Res. **114**(6): 1–29. doi: 10.1029/2008JB006066.

Dunbar, J., and Sawyer, D. 1989. How preexisting weaknesses control the style of continental breakup. J. Geophys. Res. **94**(88): 7278–7292.

Ebinger, C. 1989. Tectonic development of the western branch of the East African rift system. Geol. Soc. Am. Bull. **101**: 885–903.

Ebinger, C. 2005. Continental break-up: the East African perspective. Astron. Geophys. **46**: 2.16–2.21.

Ebinger, C., Djomani, Y.P., Mbede, E., Foster, A., and Dawson, J.B. 1997. Rifting Archaean lithosphere: the Eyasi-Manyara-Natron rifts, East Africa. J. Geol. Soc. London. **154**(6): 947–960. doi: 10.1144/gsjgs.154.6.0947.

Emerman, H., and Turcotte, L. 1984. A back-of-the-envelope approach to boudinage mechanics. Tectonophysics **110**: 333–338.

England, P. 1983. Constraints on extension of continental lithosphere. J. Geophys. Res. **88**: 1145–1152.

Fletcher, R.C., and Hallet, B. 1983. Unstable extension of the lithosphere: A mechanical model for basin-and-range structure. J. Geophys. Res. **88**(B9): 7457–7466. doi: 10.1029/JB088iB09p07457.

Foley, S.F. 2008. Rejuvenation and erosion of the cratonic lithosphere. Nat. Geosci. **1**: 503–510. doi: 10.1038/ngeo261.

Forsyth, D., and Uyeda, S. 1975. On the Relative Importance of the Driving Forces of Plate Motion. Geophys. J. R. Astron. Soc. **43**: 163–200. doi: 10.1111/j.1365-246X.1975.tb00631.x.

Foster, A., and Ebinger, C. 1997. Tectonic development of the northern Tanzanian sector of the East African Rift System. J. Geol. Soc. London. **154**: 689–700.

François, T., Burov, E., Meyer, B., and Agard, P. 2012. Surface topography as key constraint on thermo-rheological structure of stable cratons. Tectonophysics **602**: 106–123. doi: 10.1016/j.tecto.2012.10.009.

Fraser, S.I., Fraser, A.J., Lentini, M.R., and Gawthorpe, R.L. 2007. Return to rifts - the next wave: fresh insights into the petroleum geology of global rift basins. Petrol. Geosci. **13**(2): 99–104. doi: 10.1144/1354-079307-749.

Fullsack, P. 1995. An arbitrary Lagrangian-Eulerian formulation for creeping flows and its application in tectonic models. Geophys. J. Int. **120**(1): 1–23. doi: 10.1111/j.1365-246X.1995.tb05908.x.

Le Gall, B., Nonnotte, P., Rolet, J., Benoit, M., Guillou, H., Mousseau-Nonnotte, M., Albaric, J., and Deverchère, J. 2008. Rift propagation at craton margin. Distribution of faulting and volcanism in the North Tanzanian Divergence (East Africa) during Neogene times. Tectonophysics **448**(1-4): 1–19. doi: 10.1016/j.tecto.2007.11.005.

Gao, S.S. 2002. Mantle discontinuities beneath Southern Africa. Geophys. Res. Lett. **29**(10): 4–7. doi: 10.1029/2001GL013834.

Gartrell, A.P. 2000. Rheological controls on extensional styles and the structural evolution of the Northern Carnarvon Basin, North West Shelf, Australia. Aust. J. Earth Sci. **47**(2): 231–244. doi: 10.1046/j.1440-0952.2000.00776.x.

Geoffroy, L. 2005. Volcanic passive margins. C.R. Geosci. **337**: 1395–1408. doi: 10.1016/j.crte.2005.10.006.

Gerlings, J., Louden, K.E., and Jackson, H.R. 2011. Crustal structure of the Flemish Cap Continental Margin (eastern Canada): An analysis of a seismic refraction profile. Geophys. J. Int. **185**(1): 30–48. doi: 10.1111/j.1365-246X.2011.04931.x.

Ghosh, A.K. 1977. The influence of strain hardening and strain-rate sensitivity on sheet metal forming. J. Eng. Mater. Technol. **99**(3): 264–274. American Society of Mechanical Engineers.

Giresse, P. 2005. Mesozoic-Cenozoic history of the Congo Basin. J. African Earth Sci. **43**(1-3): 301–315. doi: 10.1016/j.jafrearsci.2005.07.009.

Gleason, G.C., and Tullis, J. 1995. A flow law for dislocation creep of quartz aggregates determined with the molten salt cell. Tectonophysics **247**(1-4): 1–23. doi: 10.1016/0040-1951(95)00011-B.

Godey, S., Deschamps, F., and Trampert, J. 2004. Thermal and compositional anomalies beneath the North American continent. J. Geophys. Res. **109**: B01308. doi: 10.1029/2002JB002263.

Goes, S., and Lee, S. Van Der. 2002. Thermal structure of the North American uppermost mantle inferred from seismic tomography. J. Geophys. Res. **107**(B3): B32050. doi: 10.1029/2000JB000049.

Goetze, C., and Evans, B. 1979. Stress and temperature in the bending lithosphere as constrained by experimental rock mechanics. Geophys. J. R. Astron. Soc. **59**(3): 463–478. doi: 10.1111/j.1365-246X.1979.tb02567.x.

Goodwin, A.M. 1996. Distribution and Tectonic Setting of Precambrian Crust. *In* Principles of Precambrian Geology. *Edited by* A.M. Goodwin. Academic Press. pp. 1–78.

Gorczyk, W., Hobbs, B., and Gerya, T. 2012. Initiation of Rayleigh–Taylor instabilities in intra-cratonic settings. Tectonophysics **514-517**: 146–155. doi: 10.1016/j.tecto.2011.10.016.

Gorczyk, W., Hobbs, B., Gessner, K., and Gerya, T. 2013. Intracratonic geodynamics. Gondwana Res. **24**(3-4): 838–848. doi: 10.1016/j.gr.2013.01.006.

Griffin, W.L., Andi, Z., O'reilly, S.Y., and Ryan, C.G. 1998. Phanerozoic evolution of the lithosphere beneath the Sino-Korean craton. *In* Mantle Dynamics and Plate Interactions in East Asia. *Edited by* M.F.J. Flower, S. Chung, C. Lo, and T. Lee. pp. 107–126.

Griffin, W.L., Kobussen, A.F., Babu, E.V.S.S.K., O'Reilly, S.Y., Norris, R., and Sengupta, P. 2009a. A translithospheric suture in the vanished 1-Ga lithospheric root of South India: Evidence from contrasting lithosphere sections in the Dharwar Craton. Lithos **112**: 1109–1119. doi: 10.1016/j.lithos.2009.05.015.

Griffin, W.L., O'Reilly, S.Y., Abe, N., Aulbach, S., Davies, R.M., Pearson, N.J., Doyle, B.J., and Kivi, K. 2003a. The origin and evolution of Archean lithospheric mantle. Precambrian Res. **127**(1-3): 19–41. doi: 10.1016/S0301-9268(03)00180-3.

Griffin, W.L., O'Reilly, S.Y., Afonso, J.C., and Begg, G.C. 2009b. The composition and evolution of lithospheric mantle: a re-evaluation and its tectonic implications. J. Pet. **50**(7): 1185–1204. doi: 10.1093/petrology/egn033.

Griffin, W.L., O'Reilly, S.Y., Natapov, L.M., and Ryan, C.G. 2003b. The evolution of lithospheric mantle beneath the Kalahari Craton and its margins. Lithos **71**: 215–241. doi: 10.1016/j.lithos.2003.07.006.

Griffin, W.L., Ryan, C.G., Kaminsky, F. V, Reilly, S.Y.O., and Natapov, L.M. 1999. The Siberian lithosphere traverse : mantle terranes and the assembly of the Siberian Craton. Tectonophysics **310**: 1–35.

Groves, D.I., and Bierlein, F.P. 2007. Geodynamic settings of mineral deposit systems. J. Geol. Soc. London. **164**: 19–30. doi: 10.1144/0016-76492006-065.

Guillou-Frottier, L., Burov, E., Cloetingh, S., Le Goff, E., Deschamps, Y., Huet, B., and Bouchot, V. 2012. Plume-induced dynamic instabilities near cratonic blocks: Implications for P-T-t paths and metallogeny. Glob. Planet. Change **90-91**: 37–50. doi: 10.1016/j.gloplacha.2011.10.007.

Gung, Y., Panning, M., and Romanowicz, B. 2003. Global anisotropy and the thickness of continents. Nature **422**: 707–711. doi: 10.1038/nature01557.1.

Gvirtzman, Z., and Garfunkel, Z. 1997. Vertical movements following intracontinental magmatism: An example from southern Israel. J. Geophys. Res. **102**(B2): 2645–2658. doi: 10.1029/96JB02567.

Haggerty, S.E. 1999. A diamond trilogy: Superplumes, supercontinents, and supernovae. Science **285**: 851–860. doi: 10.1126/science.285.5429.851.

Harte, B. 1983. Mantle peridotites and processes - the kimberlite sample. *In* Continental Basalts and Mantle Xenoliths. *Edited by* C.J. Hawkesworth and M.J. Norry. Shiva. pp. 46–91.

Harte, B., Hunter, R.H., and Kinny, P.D. 1993. Melt geometry, movement and crystallization, in relation to mantle dykes, veins and metasomatism. Philos. Trans. R. Soc. A Math. Phys. Eng. Sci. **342**(1663): 1–21. doi: 10.1098/rsta.1993.0001.

Hartley, R.W., and Allen, P.A. 1994. Interior cratonic basins of Africa: relation to continental break-up and role of mantle convection. Basin Res. **6**(2-3): 95–113. doi: 10.1111/j.1365-2117.1994.tb00078.x.

Hasterok, D., and Chapman, D.S. 2011. Heat production and geotherms for the continental lithosphere. Earth Planet. Sci. Lett. **307**(1-2): 59–70. doi: 10.1016/j.epsl.2011.04.034.

Haxby, W.F., Turcotte, D.L., and Bird, J.M. 1976. Thermal and mechanical evolution of the Michigan Basin. Tectonophysics **36**(1): 57–75.

Hayob, J.L., Essene, E.J., Ruiz, J., Ortega-Gutierrez, F., and Aranda-Gomez, J.J. 1989. Young high-temperature granulites from the base of the crust in central Mexico. Nature **342**: 265–268.

He, L. 2015. Thermal regime of the North China Craton: Implications for craton destruction. Earth-Science Rev. **140**: 14–26. Elsevier B.V. doi: 10.1016/j.earscirev.2014.10.011.

Herzberg, C. 2004. Geodynamic information in peridotite petrology. J. Pet. **45**(12): 2507–2530. doi: 10.1093/petrology/egh039.

Hibbard, J., and Waldron, J.W.F. 2009. Truncation and translation of Appalachian promontories: Mid-Paleozoic strike-slip tectonics and basin initiation. Geology **37**(6): 487–490. doi: 10.1130/G25614A.1.

Hirschmann, M.M. 2000. Mantle solidus: Experimental constraints and the effects of peridotite composition. Geochemistry Geophysics Geosystems **1**: 1–26. doi: 10.1029/2000GC000070.

Hirth, G., and Kohlstedt, D.L. 1995. Experimental constraints on the dynamics of the partially molten upper mantle: Deformation in the diffusion creep regime. J. Geophys. Res. **100**(B2): 1981–2001. doi: 10.1029/94JB02128.

Hirth, G., and Kohlstedt, D.L. 1996. Water in the oceanic upper mantle: implications for rheology, melt extraction and the evolution of the lithosphere. Earth Planet. Sci. Lett. **144**(1-2): 93–108. doi: 10.1016/0012-821X(96)00154-9.

Hoffman, P.F. 1989. Precambrian geology and tectonic history of North America. *In* The geology of North America: an overview. *Edited by* A.W. Bally and A.R. Palmer. Geological Society of America, Boulder, Colorado. pp. 447–512.

Huang, J. 2003. Controls on sublithospheric small-scale convection. J. Geophys. Res. **108**(B8): 1–13. doi: 10.1029/2003JB002456.

Huerta, A.D., and Harry, D.L. 2007. The transition from diffuse to focused extension: Modeled evolution of the West Antarctic Rift system. Earth Planet. Sci. Lett. **255**(1-2): 133–147. doi: 10.1016/j.epsl.2006.12.011.

Huet, B., Le Pourhiet, L., Labrousse, L., Burov, E., and Jolivet, L. 2011. Post-orogenic extension and metamorphic core complexes in a heterogeneous crust: the role of crustal layering inherited from collision. Application to the Cyclades (Aegean domain). Geophys. J. Int. **184**(2): 611–625. doi: 10.1111/j.1365-246X.2010.04849.x.

Huismans, R., and Beaumont, C. 2011. Depth-dependent extension, two-stage breakup and cratonic underplating at rifted margins. Nature **473**: 74–78. doi: 10.1038/nature09988.

Huismans, R.S., and Beaumont, C. 2003. Symmetric and asymmetric lithospheric extension: Relative effects of frictional-plastic and viscous strain softening. J. Geophys. Res. **108**(B10): 2496. doi: 10.1029/2002JB002026.

Huismans, R.S., and Beaumont, C. 2007. Roles of lithospheric strain softening and heterogeneity in determining the geometry of rifts and continental margins. *In* Imgaging, Mapping and Modelling Continental Lithosphere Extension and Breakup. *Edited by* G.D. Karner, G.D. Manatschal, and L.M. Pinheiro. Geological Society, London, Special Publications. pp. 111–138. doi: 10.1144/SP282.6.

Huismans, R.S., and Beaumont, C. 2008. Complex rifted continental margins explained by dynamical models of depth-dependent lithospheric extension. Geology **36**(2): 163. doi: 10.1130/G24231A.1.

Huismans, R.S., and Beaumont, C. 2014. Rifted continental margins : The case for depth-dependent extension. Earth Planet. Sci. Lett. **407**: 1–15. doi: 10.1016/j.epsl.2014.09.032.

Humphreys, E., Hessler, E., Dueker, K., Farmer, G.L., Erslev, E., and Atwater, T. 2003. How Laramide-age hydration of North American lithosphere by the Farallon slab controlled subsequent activity in the western United States. Int. Geol. Rev. **45**(7): 575–595. doi: 10.2747/0020-6814.45.7.575.

Humphreys, E.D. 1995. Post-Laramide removal of the Farallon slab,western United States. Geology **23**: 987–990.

Ionov, D. 2002. Mantle structure and rifting processes in the Baikal-Mongolia region: Geophysical data and evidence from xenoliths in volcanic rocks. Tectonophysics **351**: 41–60. doi: 10.1016/S0040-1951(02)00124-5.

Ionov, D.A., O'Reilly, S.Y., and Ashchepkov, I. V. 1995. Feldspar-bearing lherzolite xenoliths in alkali basalts from Hamar-Daban, southern Baikal region, Russia. Contrib. to Mineral. Pet. **122**: 174–190. doi: 10.1007/s004100050120.

James, D.E., Fouch, M.J., VanDecar, J.C., van der Lee, S., and Group, K.S. 2001. Tectospheric structure beneath southern Africa. Geophys. Res. Lett. **28**(13): 2485–2488. doi: 10.1029/2000GL012578.

Jamieson, R.A., Beaumont, C., Nguyen, M.H., and Culshaw, N.G. 2007. Synconvergent ductile flow in variable-strength continental crust: Numerical models with application to the western Grenville orogen. Tectonics **26**: TC5005. doi: 10.1029/2006TC002036.

Jiang, M., Ai, Y., Chen, L., and Yang, Y. 2013. Local modification of the lithosphere beneath the central and western North China Craton: 3-D constraints from Rayleigh wave tomography. Gondwana Res. **24**(3-4): 849–864. doi: 10.1016/j.gr.2012.06.018.

Jolivet, L., Lecomte, E., Huet, B., Denèle, Y., Lacombe, O., Labrousse, L., Le Pourhiet, L., and Mehl, C. 2010. The North Cycladic detachment system. Earth Planet. Sci. Lett. **289**(1-2): 87–104. doi: 10.1016/j.epsl.2009.10.032.

Jones, C.H., Wernicke, B.P., Farmer, G.L., Walker, J.D., Coleman, D.S., Mckenna, L.W., and Perry, F.V. 1992. Variations across and along a major continental rift: An interdisciplinary study of the Basin and Range Province, western USA. Tectonophysics **213**(1-2): 57–96. doi: 10.1016/0040-1951(92)90252-2.

Jordan, T. 1978. Composition and development of the continental tectosphere. Nature **274**: 544–548.

Jordan, T.H. 1975. The continental Tectosphere. Rev. Geophys. Sp. Phys. **13**(3): 1–12.

Julià, J., Assumpção, M., and Rocha, M.P. 2008. Deep crustal structure of the Paraná Basin from receiver functions and Rayleigh-wave dispersion: Evidence for a fragmented cratonic root. J. Geophys. Res. **113**(8): 1–23. doi: 10.1029/2007JB005374.

Kaban, M.K., Schwintzer, P., Artemieva, I.M., and Mooney, W.D. 2003. Density of the continental roots: Compositional and thermal contributions. Earth Planet. Sci. Lett. **209**(1-2): 53–69. doi: 10.1016/S0012-821X(03)00072-4.

Kaislaniemi, L., and van Hunen, J. 2014. Dynamics of lithospheric thinning and mantle melting by edge-driven convection: Application to Moroccan Atlas mountains. Geochemistry Geophysics Geosystems **15**(8): 3175–3189. doi: 10.1002/2014GC005414.

Kaminski, E., and Jaupart, C. 2000. Lithosphere structure beneath the Phanerozoic intracratonic basins of North America. Earth Planet. Sci. Lett. **178**(1-2): 139–149. doi: 10.1016/S0012-821X(00)00067-4.

Karato, S. 2010. Rheology of the deep upper mantle and its implications for the preservation of the continental roots: A review. Tectonophysics **481**(1-4): 82–98. doi: 10.1016/j.tecto.2009.04.011.

Karato, S., Paterson, M.S., and FitzGerald, J.D. 1986. Rheology of synthetic olivine aggregates: Influence of grain size and water. J. Geophys. Res. **91**(B8): 8151–8176. doi: 10.1029/JB091iB08p08151.

Karato, S., and Wu, P. 1993. Rheology of the upper mantle: A synthesis. Science **260**(5109): 771–778.

Karlstrom, K., and Humphreys, E. 1998. Influence of Proterozoic accretionary boundaries in the tectonic evolution of southwestern North America Interaction of cratonic grain and mantle modification events. Rocky Mt. Geol. **33**(2): 161–179.

Katsura, T., Shatskiy, A., Manthilake, M.A.G.M., Zhai, S., Fukui, H., Yamazaki, D., Matsuzaki, T., Yoneda, A., Ito, E., Kuwata, A., Ueda, A., Nozawa, A., and Funakoshi, K. ichi. 2009. Thermal expansion of forsterite at high pressures determined by in situ X-ray diffraction: The adiabatic geotherm in the upper mantle. Phys. Earth Planet. Inter. **174**(1-4): 86–92. doi: 10.1016/j.pepi.2008.08.002.

Katz, R.F., Spiegelman, M., and Langmuir, C.H. 2003. A new parameterization of hydrous mantle melting. Geochemistry Geophysics Geosystems **4**(9): 1–19. doi: 10.1029/2002GC000433.

Kawamoto, T., and Holloway, J.R. 1997. Melting Temperature and Partial Melt Chemistry of H2O-Saturated Mantle Peridotite to 11 Gigapascals. Science **276**: 240–243. doi: 10.1126/science.276.5310.240.

Kearey, P., Klepeis, K.A., and Vine, F.J. 2009. Global tectonics. *In* 3rd edition. *Edited by* P. Kearey, K.A. Klepeis, and F.J. Vine. John Wiley & Sons.

Kelemen, P.B., Hart, S.R., and Bernstein, S. 1998. Silica enrichment in the continental upper mantle via melt/rock reaction. Earth Planet. Sci. Lett. **164**(1-2): 387–406. doi: 10.1016/S0012-821X(98)00233-7.

Keller, G., and Baldridge, W. 1999. The Rio Grande rift A geological and geophysical overview. Rocky Mt. Geol. (1): 121–130.

King, S.D., and Anderson, D.L. 1998. Edge-driven convection. Earth Planet. Sci. Lett. **160**: 289–296.

Kingston, D.R., Dishroon, C.P., and Williams, P.A. 1983. Global basin classification system. Am. Assoc. Petrol. Geol. Bull. **67**(12): 2175–2193. doi: 10.1306/AD460936-16F7-11D7-8645000102C1865D.

Klerkx, J., Theunissen, K., and Delvaux, D. 1998. Persistent fault controlled basin formation since the Proterozoic along the Western Branch of the East African Rift. J. African Earth Sci. **26**(3): 347–361. doi: 10.1016/S0899-5362(98)00020-7.

Koornneef, J.M., Davies, G.R., Döpp, S.P., Vukmanovic, Z., Nikogosian, I.K., and Mason, P.R.D. 2009. Nature and timing of multiple metasomatic events in the sub-cratonic lithosphere beneath Labait, Tanzania. Lithos **112**: 896–912. doi: 10.1016/j.lithos.2009.04.039.

Korenaga, J. 2004. Physics of multiscale convection in Earth's mantle: Evolution of sublithospheric convection. J. Geophys. Res. **109**(B1): 1–11. doi: 10.1029/2003JB002464.

Korhonen, A.S. 1978. On the theories of sheet metal necking and forming limits. J. Eng. Mater. Technol. **100**(3): 303–309.

Kusznir, N.J., and Karner, G.D. 2007. Continental lithospheric thinning and breakup in response to upwelling divergent mantle flow: application to the Woodlark, Newfoundland and Iberia margins. *In* Imgaging, Mapping and Modelling Continental Lithosphere Extension and Breakup. *Edited by* G.D. Karner, G. Manatschal, and L.M. Pinheiro. Geological Society, London, Special Publications. pp. 389–419. doi: 10.1144/SP282.16.

Kusznir, N.J., and Park, R.G. 1987. The extensional strength of the continental lithosphere: its dependence on geothermal gradient, and crustal composition and thickness. *In* Continental Extensional Tectonics. *Edited by* M.P. Coward, J.F. Dewey, and P.L. Hancock. Geological Society, London, Special Publications. pp. 35–52. doi: 10.1144/GSL.SP.1987.028.01.04.

Laville, E., Pique, A., Amrhar, M., and Charroud, M. 2004. A restatement of the Mesozoic Atlasic Rifting (Morocco). J. African Earth Sci. **38**(2): 145–153. doi: 10.1016/j.jafrearsci.2003.12.003.

Lee, C.A. 2006. Geochemical/petrologic constraints on the origin of cratonic mantle. Archean Geodyn. Environ. **164**: 89–114. doi: 10.1029/164gm08.

Lee, C.-T.A. 2003. Compositional variation of density and seismic velocities in natural peridotites at STP conditions: Implications for seismic imaging of compositional heterogeneities in the upper mantle. J. Geophys. Res. **108**(B9): 2441. doi: 10.1029/2003JB002413.

Lee, C.-T.A., Luffi, P., and Chin, E.J. 2011. Building and Destroying Continental Mantle. Annu. Rev. Earth Planet. Sci. **39**(1): 59–90. doi: 10.1146/annurev-earth-040610-133505.

Lee, C.-T.A., Luffi, P., Plank, T., Dalton, H., and Leeman, W.P. 2009. Constraints on the depths and temperatures of basaltic magma generation on Earth and other terrestrial planets using new thermobarometers for mafic magmas. Earth Planet. Sci. Lett. **279**(1-2): 20–33. doi: 10.1016/j.epsl.2008.12.020.

Lee, C.-T.A., Yin, Q., Rudnick, R.L., and Jacobsen, S.B. 2001. Preservation of ancient and fertile lithospheric mantle beneath the southwestern United States. Nature **411**: 69–73. doi: 10.1038/35075048.

Lefort, J.P., and Max, M.D. 1984. Development of the Porcupine Seabight: use of magnetic data to show the direct relationship between early oceanic and continental structures. J. Geol. Soc. London. **141**(4): 663–674. doi: 10.1144/gsjgs.141.4.0663.

Lenardic, A., Moresi, L., and Muhlhaus, H. 2000. The role of mobile belts for the longevity of deep cratonic lithosphere: the crumple zone model. Geophys. Res. Lett. **27**: 1235–1238.

Lenardic, A., and Moresi, L.N. 1999. Some thoughts on the stability of cratonic lithosphere: Effects of buoyancy and viscosity. J. Geophys. Res. **104**(B6): 12747–12758. doi: 10.1029/1999JB900035.

Lenardic, A., Moresi, L.N., and Muhlhaus, H. 2003. Longevity and stability of cratonic lithosphere: Insights from numerical simulations of coupled mantle convection and continental tectonics. J. Geophys. Res. **108**(B6): 2303. doi: 10.1029/2002JB001859.

Lenoir, X., Garrido, C.J., Bodinier, J.L., Dautria, J.M., and Gervilla, F. 2001. The recrystallization front of the Ronda peridotite: Evidence for melting and thermal erosion of subcontinental lithospheric mantle beneath the Alboran basin. J. Pet. **42**(1): 141–158. doi: 10.1093/petrology/42.1.141.

Levander, A., Schmandt, B., Miller, M.S., Liu, K., Karlstrom, K.E., Crow, R.S., Lee, C.-T.A., and Humphreys, E.D. 2011. Continuing Colorado plateau uplift by delamination-style convective lithospheric downwelling. Nature **472**: 461–465. doi: 10.1038/nature10001.

Li, Z.X., Bogdanova, S.V., Collins, A.S., Davidson, A., De Waele, B., Ernst, R.E., Fitzsimons, I.C.W., Fuck, R.A., Gladkochub, D.P., Jacobs, J., Karlstrom, K.E., Lu, S., Natapov, L.M., Pease, V., Pisarevsky, S.A., Thrane, K., and Vernikovsky, V. 2008. Assembly, configuration, and break-up history of Rodinia: A synthesis. Precambrian Res. **160**(1-2): 179–210. doi: 10.1016/j.precamres.2007.04.021.

Liao, J., and Gerya, T. 2014. Influence of lithospheric mantle stratification on craton extension: Insight from two-dimensional thermo-mechanical modeling. Tectonophysics **631**: 50–64. doi: 10.1016/j.tecto.2014.01.020.

Lister, G.S., Etheridge, M.A., and Symonds, P.A. 1986. Detachment faulting and the evolution of passive continental margins Detachment faulting and the evolution of passive continental margins. Geology **14**: 246–250. doi: 10.1130/0091-7613(1986)14<246.

Livaccari, R.F., and Perry, F. V. 1993. Isotopic evidence for preservation of Cordilleran lithospheric mantle during the Sevier-Laramide orogeny, western United States. Geology **21**: 719–722.

Logatchev, N., and Florensov, N. 1978. The Baikal system of rift valleys. Tectonophysics **45**: 1–13.

Magnani, M.B., Miller, K.C., Levander, A., and Karlstrom, K. 2004. The Yavapai-Mazatzal boundary: A long-lived tectonic element in the lithosphere of southwestern North America. Geol. Soc. Am. Bull. **116**(7-8): 1137–1142. doi: 10.1130/B25414.1.

Magnavita, L., Davison, I., and Kusznir, N. 1994. Rifting, erosion, and uplift history of the Recôncavo-Tucano-Jatobá Rift, northeast Brazil. Tectonics **13**(2): 367–388.

Malvern, L.E. 1969. Introduction to the Mechanics of a Continuous Medium. Prentice-Hall International Inc.

Manatschal, G., Lavier, L., and Chenin, P. 2015. The role of inheritance in structuring hyperextended rift systems: Some considerations based on observations and numerical modeling. Gondwana Res. **27**(1): 140–164. doi: 10.1016/j.gr.2014.08.006.

Mann, P., Gahagan, L., and Gordon, M. 2001. Tectonic setting of the world's giant oil and gas fields. World Oil: 42–50.

Mareschal, J.-C., and Jaupart, C. 2012. Radiogenic heat production, thermal regime and evolution of continental crust. Tectonophysics. doi: 10.1016/j.tecto.2012.12.001.

Martinod, J., and Davy, P. 1992. Periodic instabilities during compression or extension of the lithosphere 1. Deformation modes from an analytical perturbation method. J. Geophys. Res. **97**(B2): 1999–2014. doi: 10.1029/91JB02715.

McKenzie, D. 1978. Some remarks on the development of sedimentary basins. Earth Planet. Sci. Lett. **40**(1): 25–32. doi: 10.1016/0012-821X(78)90071-7.

McKenzie, D. 1989. Some remarks on the movement of small melt fractions in the mantle. Earth Planet. Sci. Lett. **95**(1): 53–72.

McQuarrie, N., and Wernicke, B. 2005. An animated tectonic reconstruction of southwestern North America since 36 Ma. Geosphere **1**: 147–172. doi: 10.1130/GES00016.1.

Menzies, M., Xu, Y., Zhang, H., and Fan, W. 2007. Integration of geology, geophysics and geochemistry: A key to understanding the North China Craton. Lithos **96**(1-2): 1–21. doi: 10.1016/j.lithos.2006.09.008.

Menzies, M.A., and Xu, Y. 1998. Geodynamics of the North China craton. *In* Mantle dynamics and Plate Interactions in East Asia. *Edited by* M.F.J. Flower, S. Chung, C. Lo, and T. Lee. Wiley Online Library. pp. 155–165.

Mohriak, W., Nemčok, M., and Enciso, G. 2008. South Atlantic divergent margin evolution: rift-border uplift and salt tectonics in the basins of SE Brazil. Geol. Soc. London **294**: 365–398. doi: 10.1144/SP294.19.

Mohriak, W.U., and Leroy, S. 2012. Architecture of rifted continental margins and break-up evolution: insights from the South Atlantic, North Atlantic and Red Sea-Gulf of Aden conjugate margins. *In* Conjugate Divergent Margins. *Edited by* W.U. Mohriak, A. Danforth, P.J. Post, D.E. Brown, G.C. Tari, M. Nemcok, and S.T. Sinha. Geological Society, London, Special Publications. pp. 497–535. doi: 10.1144/SP369.17.

Nagel, T.J., and Buck, W.R. 2007. Control of rheological stratification on rifting geometry: a symmetric model resolving the upper plate paradox. Int. J. Earth Sci. **96**(6): 1047–1057. doi: 10.1007/s00531-007-0195-x.

Nyblade, A.A. 1999. Heat flow and the structure of Precambrian lithosphere. Lithos **48**: 81–91. doi: 10.1016/S0419-0254(99)80006-8.

Nyblade, A.A., and Pollack, H.N. 1993. A global analysis of heat flow from Precambrian terrains: Implications for the thermal structure of Archean and Proterozoic lithosphere. J. Geophys. Res. **98**(B7): 12207–12218. Available from http://dx.doi.org/10.1029/93JB00521.

Nye, J.F. 1953. The flow law of ice from measurements in glacier tunnels, laboratory experiments and the Jungfraufirn borehole experiment. Proc. R. Soc. A Math. Phys. Eng. Sci. **219**: 477–489. doi: 10.1098/rspa.1953.0161.

O'Neill, C.J., Lenardic, a., Griffin, W.L., and O'Reilly, S.Y. 2008. Dynamics of cratons in an evolving mantle. Lithos **102**: 12–24. doi: 10.1016/j.lithos.2007.04.006.

O'Reilly, S.Y., and Griffin, W.L. 2010. The continental lithosphere-asthenosphere boundary: Can we sample it? Lithos **120**(1-2): 1–13. doi: 10.1016/j.lithos.2010.03.016.

O'Reilly, S.Y., and Griffin, W.L. 2013. Mantle Metasomatism. *In* Metasomatism and the Chemical Transformation of Rock. *Edited by* D.E. Harow and H. Austrheim. Springer. pp. 471–533. doi: 10.1007/978-3-642-28394-9.

O'Reilly, S.Y., Griffin, W.L., Djomani, Y.P., and Morgan, P. 2001. Are lithospheres forever? Tracking changes in subcontinental lithospheric mantle through time. GSA Today **11**(4): 4–10.

Olsen, K.H., Baldridge, W.S., and Callender, J.F. 1987. Rio Grande rift: an overview. Tectonophysics **143**(1): 119–139.

Olsen, P., Kent, D. V, and Et-touhami, M. 2003. Chronology and stratigraphy of the Fundy and related Nova Scotia offshore basins and Morocco based on core and outcrop. AGS Conventional Core Workshop.

Olsen, P.E. 1997. Stratigraphic record of the early Mesozoic breakup of Pangea in the Laurasia-Gondwana rift system. Annu. Rev. Earth Planet. Sci. **25**: 337–401. doi: 10.1146/annurev.earth.25.1.337.

Pancha, A., Anderson, J.G., and Kreemer, C. 2006. Comparison of seismic and geodetic scalar moment rates across the Basin and Range province. Bull. Seismol. Soc. Am. **96**(1): 11–32. doi: 10.1785/0120040166.

Parsons, T. 1995. The Basin and Range Province. *In* Continental Rifts: Evolution, Structure and Tectonics. *Edited by* K.H. Olsen. pp. 277–324.

Pearson, D.G., and Nowell, G.M. 2002. The continental lithospheric mantle: characteristics and significance as a mantle reservoir. Philos. Trans. R. Soc. London A Math. Phys. Eng. Sci. **360**(1800): 2383–2410.

Pearson, D.G., and Wittig, N. 2008. Formation of Archaean continental lithosphere and its diamonds: the root of the problem. J. Geol. Soc. London. **165**(5): 895–914. doi: 10.1144/0016-76492008-003.

Péron-Pinvidic, G., and Manatschal, G. 2008. The final rifting evolution at deep magma-poor passive margins from Iberia-Newfoundland: a new point of view. Int. J. Earth Sci. **98**(7): 1581–1597. doi: 10.1007/s00531-008-0337-9.

Peron-Pinvidic, G., Manatschal, G., and Osmundsen, P.T. 2013. Structural comparison of archetypal Atlantic rifted margins: A review of observations and concepts. Mar. Petrol. Geol. **43**: 21–47. doi: 10.1016/j.marpetgeo.2013.02.002.

Petit, C., Burov, E., and Tiberi, C. 2008. Strength of the lithosphere and strain localisation in the Baikal rift. Earth Planet. Sci. Lett. **269**(3-4): 523–529. doi: 10.1016/j.epsl.2008.03.012.

Petit, C., and Déverchère, J. 2006. Structure and evolution of the Baikal rift: A synthesis. Geochemistry Geophysics Geosystems **7**(11): Q11016. doi: 10.1029/2006GC001265.

Pickup, S.L.B., Whitmarsh, R.B., Fowler, C.M.R., and Reston, T.J. 1996. Insight into the nature of the ocean-continent transition off West-Iberia from a deep-multichannel seismic reflection profile. Geology **24**(12): 1079–1082. doi: 10.1130/0091-7613(1996)024<1079.

Poudjom Djomani, Y., and O'Reilly, S. 2001. The density structure of subcontinental lithosphere through time. Earth Planet. Sci. Lett. **184**: 605–621.

Priestley, K., and Debayle, E. 2003. Seismic evidence for a moderately thick lithosphere beneath the Siberian Platform. Geophys. Res. Lett. **30**(3): 1–4. doi: 10.1029/2002GL015931.

Pysklywec, R.N., and Quintas, M.C.L. 2000. A mantle flow mechanism for the late Paleozoic subsidence of the Paraná Basin. J. Geophys. Res. **105**(B7): 16359–16370. doi: 10.1029/2000JB900080.

Ranalli, G., Piccardo, G.B., and Corona-Chávez, P. 2007. Softening of the subcontinental lithospheric mantle by asthenosphere melts and the continental extension/oceanic spreading transition. J. Geodyn. **43**(4-5): 450–464. doi: 10.1016/j.jog.2006.10.005.

Regenauer-Lieb, K., and Yuen, D.A. 2003. Modeling shear zones in geological and planetary sciences: solid- and fluid-thermal–mechanical approaches. Earth-Science Rev. **63**(3-4): 295–349. doi: 10.1016/S0012-8252(03)00038-2.

Reston, T.J. 2009. The structure, evolution and symmetry of the magma-poor rifted margins of the North and Central Atlantic: A synthesis. Tectonophysics **468**(1-4): 6–27. doi: 10.1016/j.tecto.2008.09.002.

Ring, U. 1994. The influence of preexisting structure on the evolution of the Cenozoic Malawi Rift (East African Rift System). Tectonics **13**(2): 313–326.

Rosenbaum, G., Regenauer-Lieb, K., and Weinberg, R.F. 2010. Interaction between mantle and crustal detachments: A nonlinear system controlling lithospheric extension. J. Geophys. Res. **115**(B11): B11412. doi: 10.1029/2009JB006696.

Rosendahl, B.R., Mohriak, W.U., Odegard, M.E., Turner, J.P., and Dickson, W.G. 2005. West African and Brazilian conjugate margins: Crustal types, architecture, and plate configurations. *In* Petroleum Systems of Divergent Continental Margin Basins: Houston, 25th Gulf Coast Section, Society Sedimentary Geology, Bob F. Perkins Research Conference. pp. 4–7.

Le Roux, V., Bodinier, J.L., Alard, O., O'Reilly, S.Y., and Griffin, W.L. 2009. Isotopic decoupling during porous melt flow: A case-study in the Lherz peridotite. Earth Planet. Sci. Lett. **279**(1-2): 76–85. doi: 10.1016/j.epsl.2008.12.033.

Le Roux, V., Bodinier, J.L., Tommasi, A., Alard, O., Dautria, J.M., Vauchez, A., and Riches, A.J. V. 2007. The Lherz spinel lherzolite: Refertilized rather than pristine mantle. Earth Planet. Sci. Lett. **259**(3-4): 599–612. doi: 10.1016/j.epsl.2007.05.026.

Roy, M., Jordan, T.H., and Pederson, J. 2009. Colorado Plateau magmatism and uplift by warming of heterogeneous lithosphere. Nature **459**: 978–982. doi: 10.1038/nature08052.

Royden, L., and Keen, C.E. 1980. Rifting process and thermal evolution of the continental margin of eastern Canada determined from subsidence curves. Earth Planet. Sci. Lett. **51**: 343–361.

Rudnick, R.L., McDonough, W.F., and O'Connell, R.J. 1998. Thermal structure, thickness and composition of continental lithosphere. Chem. Geol. **145**(3-4): 395–411. doi: 10.1016/S0009-2541(97)00151-4.

Sand, K.K., Waight, T.E., Pearson, D.G., Nielsen, T.F.D., Makovicky, E., and Hutchison, M.T. 2009. The lithospheric mantle below southern West Greenland: A geothermobarometric approach to diamond potential and mantle stratigraphy. Lithos **112**: 1155–1166. doi: 10.1016/j.lithos.2009.05.012.

Schmalholz, S.M., Schmid, D.W., and Fletcher, R.C. 2008. Evolution of pinch-and-swell structures in a power-law layer. J. Struct. Geol. **30**(5): 649–663. doi: 10.1016/j.jsg.2008.01.002.

Schulze, D.J. 1989. Constraints on the abundance of eclogite in the upper mantle. J. Geophys. Res. **94**(B4): 4205. doi: 10.1029/JB094iB04p04205.

Schutt, D.L., and Lesher, C.E. 2006. Effects of melt depletion on the density and seismic velocity of garnet and spinel lherzolite. J. Geophys. Res. **111**(5): 1–24. doi: 10.1029/2003JB002950.

Schutt, D.L., and Lesher, C.E. 2010. Compositional trends among Kaapvaal Craton garnet peridotite xenoliths and their effects on seismic velocity and density. Earth Planet. Sci. Lett. **300**(3-4): 367–373. Elsevier B.V. doi: 10.1016/j.epsl.2010.10.018.

Shapiro, S.S., Hager, B.H., and Jordan, T.H. 1999. Stability and dynamics of the continental tectosphere. Lithos **48**: 115–133.

Sibson, H. 1990. Conditions for fault-valve behaviour. *In* Deformation Mechanisms, Rheology and Tectonics. *Edited by* R.J. Knipe and E.H. Rutter. Geological Society, London, Special Publications. pp. 15–28.

Simon, K. 2007. Dynamical modelling of lithospheric extension and small-scale convection: Implications for magmatism during the formation of volcanic rifted margins. Dalhousie University.

Sine, C.R., Wilson, D., Gao, W., Grand, S.P., Aster, R., Ni, J., and Baldridge, W.S. 2008. Mantle structure beneath the western edge of the Colorado Plateau. Geophys. Res. Lett. **35**: 1–5. doi: 10.1029/2008GL033391.

Skaarup, N., Jackson, H.R., and Oakey, G. 2006. Margin segmentation of Baffin Bay/Davis Strait, eastern Canada based on seismic reflection and potential field data. Mar. Petrol. Geol. **23**(1): 127–144. doi: 10.1016/j.marpetgeo.2005.06.002.

Sleep, N.H. 2003. Survival of Archean cratonal lithosphere. J. Geophys. Res. **108**(B6): 1–29. doi: 10.1029/2001JB000169.

Sleep, N.H. 2005. Evolution of the continental lithosphere. Annu. Rev. Earth Planet. Sci. **33**: 369–393. doi: 10.1146/annurev.earth.33.092203.122643.

Sleep, N.H. 2007. Edge-modulated stagnant-lid convection and volcanic passive margins. Geochemistry Geophysics Geosystems **8**(12). doi: 10.1029/2007GC001672.

Sleep, N.H., and Sloss, L.L. 1980. The Michigan Basin. *In* Dynamics of Plate Interiors. *Edited by* A.W. Bally. Wiley Online Library. pp. 93–98.

Sloss, L.L. 1963. Sequences in the Cratonic Interior of North America. Geol. Soc. Am. Bull. **74**(2): 93. doi: 10.1130/0016-7606(1963)74[93:SITCIO]2.0.CO;2.

Smith, R. 1977. Formation of folds, boudinage, and mullions in non-Newtonian materials. Geol. Soc. Am. Bull. **88**(2): 312–320. doi: 10.1130/0016-7606(1977)88<312.

Snow, J., and Wernicke, B. 2000. Cenozoic tectonism, in the central Basin and Range: Magnitude, rate, and distribution of upper crustal strain. Am. J. Sci. **300**: 659–719.

Soares, P.C., Barbosa Landim, P., and Fulfaro, V.J. 1978. Tectonic cycles and sedimentary sequences in the Brazilian intracratonic basins. Geol. Soc. Am. Bull. **89**(2): 181–191. doi: 10.1130/0016-7606(1978)89<181:TCASSI>2.0.CO;2.

Solomon, S.C., Sleep, N.H., and Richardson, R.M. 1975. On the forces driving plate tectonics : Inferences from absolute plate velocities and intraplate stress. Geophys. J. R. Astron. Soc. **42**: 769–801. doi: 10.1111/j.1365-246X.1975.tb05891.x.

Sonder, L.J., and Jones, C.H. 1999. Western United States extension: How the west was widened. Annu. Rev. Earth Planet. Sci. **27**: 417–462. doi: 10.1146/annurev.earth.27.1.417.

Soustelle, V., Tommasi, A., Bodinier, J.L., Garrido, C.J., and Vauchez, A. 2009. Deformation and reactive melt transport in the mantle lithosphere above a large-scale partial melting domain: The Ronda peridotite Massif, Southern Spain. J. Pet. **50**(7): 1235–1266. doi: 10.1093/petrology/egp032.

van Staal, C.R., Barr, S.M., and Murphy, J.B. 2012. Provenance and tectonic evolution of Ganderia: Constraints on the evolution of the Iapetus and Rheic oceans. Geology **40**(11): 987–990. doi: 10.1130/G33302.1.

St-Onge, M.R., Van Gool, J.A.M., Garde, A.A., and Scott, D.J. 2009. Correlation of Archaean and Palaeoproterozoic units between northeastern Canada and western Greenland: constraining the pre-collisional upper plate accretionary history of the Trans-Hudson orogen. *In* Earth Accretionary Systems in Space and Time. *Edited by* P.A. Cawood and A. Kroner. Geological Society, London, Special Publications. pp. 193–235. doi: 10.1144/SP318.7.

Tang, Y.J., Zhang, H.F., Santosh, M., and Ying, J.F. 2013a. Differential destruction of the North China Craton: A tectonic perspective. J. Asian Earth Sci. **78**: 71–82. doi: 10.1016/j.jseaes.2012.11.047.

Tang, Y.-J., Zhang, H.-F., Ying, J.-F., and Su, B.-X. 2013b. Widespread refertilization of cratonic and circum-cratonic lithospheric mantle. Earth-Science Rev. **118**: 45–68. doi: 10.1016/j.earscirev.2013.01.004.

Tappe, S., Foley, S.F., Stracke, A., Romer, R.L., Kjarsgaard, B.A., Heaman, L.M., and Joyce, N. 2007. Craton reactivation on the Labrador Sea margins: 40Ar/39Ar age and Sr–Nd–Hf–Pb isotope constraints from alkaline and carbonatite intrusives. Earth Planet. Sci. Lett. **256**(3-4): 433–454. doi: 10.1016/j.epsl.2007.01.036.

Tappe, S., Pearson, D.G., Nowell, G., Nielsen, T., Milstead, P., and Muehlenbachs, K. 2011. A fresh isotopic look at Greenland kimberlites: Cratonic mantle lithosphere imprint on deep source signal. Earth Planet. Sci. Lett. **305**(1-2): 235–248. doi: 10.1016/j.epsl.2011.03.005.

Taylor, W.R., and Green, D.H. 1988. Measurement of reduced peridotite-C-O-H solidus and implications for redox melting of the mantle. Nature **332**(6162): 349–352. doi: 10.1038/332349a0.

Tett, D.L., and Sawyer, D.S. 1996. Dynamic models of multiphase continental rifting and their implications for the Newfoundland and Iberia conjugate margins. *In* Proceedings of the Ocean Drilling Program, Scientific Results. *Edited by* R.B. Whitmarsh, D.S. Sawyer, A. Klaus, and D.G. Masson. pp. 635–647.

Theunissen, K., Klerkx, J., Melnikov, A., and Mruma, A. 1996. Mechanisms of inheritance of rift faulting in the western branch of the East African Rift, Tanzania. Tectonics **15**(4): 776–790.

Thieulot, C. 2011. FANTOM: Two- and three-dimensional numerical modelling of creeping flows for the solution of geological problems. Phys. Earth Planet. Inter. **188**(1-2): 47–68. doi: 10.1016/j.pepi.2011.06.011.

Tian, Y., Zhao, D., Sun, R., and Teng, J. 2009. Seismic imaging of the crust and upper mantle beneath the North China Craton. Phys. Earth Planet. Inter. **172**(3-4): 169–182. doi: 10.1016/j.pepi.2008.09.002.

Tommasi, A., and Vauchez, A. 2001. Continental rifting parallel to ancient collisional belts: an effect of the mechanical anisotropy of the lithospheric mantle. Earth Planet. Sci. Lett. **185**: 199–210.

Turcotte, D.L. 1980. On the thermal evolution of the Earth. Earth Planet. Sci. Lett. **48**(1): 53–58.

Turcotte, D.L., and Schubert, G. 1982. Geodynamics: Applications of Continuum Physics to Geological Problems. John Wiley, New York.

Ussami, N., Karner, G., and Bott, M. 1986. Crustal detachment during South Atlantic rifting and formation of Tucano—Gabon basin system. Nature **322**: 629–632.

Vauchez, A., Tommasi, A., and Barruol, G. 1998. Rheological heterogeneity, mechanical anisotropy and deformation of the continental lithosphere. Tectonophysics **296**(1-2): 61–86.

Vauchez, A., Tommasi, A., and Mainprice, D. 2012. Faults (shear zones) in the Earth's mantle. Tectonophysics **558-559**: 1–27. doi: 10.1016/j.tecto.2012.06.006.

Vaughan, A.P.M., Leat, P.T., and Pankhurst, R.J. 2005. Terrane processes at the margins of Gondwana: introduction. *In* Terrane Processes at the Margins of Gondwana. *Edited by* A.P.M. Vaughan, P.T. Leat, and R.J. Prankhurst. Geological Society, London, Special Publications. pp. 1–21. doi: 10.1144/GSL.SP.2005.246.01.01.

van der Velden, A.J., van Staal, C.R., and Cook, F.A. 2004. Crustal structure, fossil subduction, and the tectonic evolution of the Newfoundland Appalachians: Evidence from a reprocessed seismic reflection survey. Bull. Geol. Soc. Am. **116**(11-12): 1485–1498. doi: 10.1130/B25518.1.

Vernières, J., Godard, M., and Bodinier, J.-L. 1997. A plate model for the simulation of trace element fractionation during partial melting and magma transport in the Earth's upper mantle. J. Geophys. Res. **102**(B11): 24771–24784. doi: 10.1029/97JB01946.

Versfelt, J., and Rosendahl, B. 1989. Relationships between pre-rift structure and rift architecture in Lakes Tanganyika and Malawi, East Africa. Nature **337**(26): 354–357.

Wang, H., van Hunen, J., and Pearson, D.G. 2015. The thinning of subcontinental lithosphere: The roles of plume impact and metasomatic weakening. Geochemistry Geophysics Geosystems **16**(4): 1156–1171. doi: 10.1002/2015GC005784.

Wang, H., van Hunen, J., Pearson, D.G., and Allen, M.B. 2014. Craton stability and longevity: The roles of composition-dependent rheology and buoyancy. Earth Planet. Sci. Lett. **391**: 224–233. doi: 10.1016/j.epsl.2014.01.038.

Wannamaker, P.E., Hasterok, D.P., Johnston, J.M., Stodt, J.A., Hall, D.B., Sodergren, T.L., Pellerin, L., Maris, V., Doerner, W.M., Groenewold, K.A., and Unsworth, M.J. 2008. Lithospheric dismemberment and magmatic processes of the Great Basin-Colorado Plateau transition, Utah, implied from magnetotellurics. Geochemistry Geophysics Geosystems **9**(5). doi: 10.1029/2007GC001886.

Watson, E.B., Brenan, J.M., and Baker, D.R. 1990. Distribution of fluids in the continental mantle. *In* Continental Mantle. *Edited by* M.A. Menzies. Clarendon Press Oxford. pp. 111–125.

Wei, W., Xu, J., Zhao, D., and Shi, Y. 2012. East Asia mantle tomography: New insight into plate subduction and intraplate volcanism. J. Asian Earth Sci. **60**: 88–103. doi: 10.1016/j.jseaes.2012.08.001.

Weinberg, R.F., Regenauer-Lieb, K., and Rosenbaum, G. 2007. Mantle detachment faults and the breakup of cold continental lithosphere. Geology **35**(11): 1035–1038. doi: 10.1130/G23918A.1.

Weiss, Y., McNeill, J., Pearson, D.G., Nowell, G.M., and Ottley, C.J. 2015. Highly saline fluids from a subducting slab as the source for fluid-rich diamonds. Nature **524**(7565): 339–342. doi: 10.1038/nature14857.

Welford, J.K., Shannon, P.M., O'Reilly, B.M., and Hall, J. 2012. Comparison of lithosphere structure across the Orphan Basin-Flemish Cap and Irish Atlantic conjugate continental margins from constrained 3D gravity inversions. J. Geol. Soc. London. **169**(4): 405–420. doi: 10.1144/0016-76492011-114.

Wenker, S., and Beaumont, C. (*Submitted*). Effects of lateral strength contrasts and inherited heterogeneities on necking and rifting of continents. J. Geophys. Res.

Wernicke, B. 1985. Uniform-sense normal simple shear of the continental lithosphere. Can. J. Earth Sci. **22**: 108–125.

Wernicke, B. 2009. The detachment era (1977-1982) and its role in revolutionizing continental tectonics. *In* Extending a Continent: Architecture, Rheology and Heat Budget. *Edited by* U. Ring and B. Wernicke. Geological Society, London, Special Publications. pp. 1–8. doi: 10.1144/SP321.1.

Wernicke, B., Davis, J.L., Niemi, N. a., Luffi, P., and Bisnath, S. 2008. Active megadetachment beneath the western United States. J. Geophys. Res. **113**(B11): B11409. doi: 10.1029/2007JB005375.

Wernicke, B., and Snow, J.K. 1998. Cenozoic Tectonism in the Central Basin and Range: Motion of the Sierran-Great Valley Block. Int. Geol. Rev. **40**(5): 403–410. doi: 10.1080/00206819809465217.

West, M., Ni, J., Baldridge, W.S., Wilson, D., Aster, R., Gao, W., and Grand, S. 2004. Crust and upper mantle shear wave structure of the southwest United States: Implications for rifting and support for high elevation. J. Geophys. Res. **109**. doi: 10.1029/2003JB002575.

Whitmeyer, S., and Karlstrom, K. 2007. Tectonic model for the Proterozoic growth of North America. Geosphere **3**: 220–259. doi: 10.1130/GES00055.1.

Whitney, D.L., Teyssier, C., Rey, P., and Buck, W.R. 2012. Continental and oceanic core complexes. Geol. Soc. Am. Bull. **125**(3-4): 273–298. doi: 10.1130/B30754.1.

van Wijk, J.W., Baldridge, W.S., van Hunen, J., Goes, S., Aster, R., Coblentz, D.D., Grand, S.P., and Ni, J. 2010. Small-scale convection at the edge of the Colorado Plateau: Implications for topography, magmatism, and evolution of Proterozoic lithosphere. Geology **38**(7): 611–614. doi: 10.1130/G31031.1.

Van Wijk, J.W., and Cloetingh, S. a P.L. 2002. Basin migration caused by slow lithospheric extension. Earth Planet. Sci. Lett. **198**: 275–288. doi: 10.1016/S0012-821X(02)00560-5.

Willett, S.D. 1992. Dynamic and kinematic growth and change of a Coulomb wedge. *In* Thrust Tectonics. *Edited by* K.R. McClay. Chapman and Hall. pp. 19–31.

Williams, H. 1964. The Appalachians in northeastern Newfoundland; a two-sided symmetrical system. Am. J. Sci. **262**(10): 1137–1158.

Williams, H. 1978. Tectonic lithofacies map of the Appalachian orogen. International Geological Correlation Programme, International Geodynamics Project, Maritime Resource Management Service, & Memorial University of Newfoundland.

Wilson, D., Aster, R., West, M., Ni, J., Grand, S., Gao, W., Baldridge, W.S., Semken, S., and Patel, P. 2005. Lithospheric structure of the Rio Grande rift. Nature **433**: 851–855. doi: 10.1038/nature03297.

Wilson, J. 1966. Did the Atlantic close and then re-open? Nature **211**(5050): 676–681.

Windley, B.F. 1981. Precambrian rocks in the light of the plate-tectonic concept. Dev. Precambrian Geol. **4**: 1–20.

Wit, M.J.D.E., Stankiewicz, J., and Reeves, C. 2015. Restoring Pan-African – Brasiliano connections : more Gondwana control, less Trans-Atlantic corruption. *In* West Gondwana: Pre-Cenozoic Correlations Across the South Atlanic Region. *Edited by* R.J. Pankhurst, R.A.J. Trouw, B.B. Brito Neves, and de W. M.J. The Geological Society of London 2008. pp. 399–412. doi: 10.1144/SP294.20.

Withjack, M., and Schlische, R. 2005. A review of tectonic events on the passive margin of eastern North America. *In* 25th annual Bob F. Perkins Research Conference: Petroleum Systems of Divergent Continental Margin Basins.

Wittig, N., Pearson, D.G., Webb, M., Ottley, C.J., Irvine, G.J., Kopylova, M., Jensen, S.M., and Nowell, G.M. 2008. Origin of cratonic lithospheric mantle roots: A geochemical study of peridotites from the North Atlantic Craton, West Greenland. Earth Planet. Sci. Lett. **274**(1-2): 24–33. doi: 10.1016/j.epsl.2008.06.034.

Wu, F.Y., Walker, R.J., Yang, Y.H., Yuan, H.L., and Yang, J.H. 2006. The chemical-temporal evolution of lithospheric mantle underlying the North China Craton. Geochim. Cosmochim. Acta **70**(19): 5013–5034. doi: 10.1016/j.gca.2006.07.014.

Xie, X., and Heller, P.L. 2009. Plate tectonics and basin subsidence history. Bull. Geol. Soc. Am. **121**(1-2): 55–64. doi: 10.1130/B26398.1.

Xu, Y., Li, H., Pang, C., and He, B. 2009. On the timing and duration of the destruction of the North China Craton. Chinese Sci. Bull. **54**(19): 3379–3396. doi: 10.1007/s11434-009-0346-5.

Xu, Y.G., Blusztajn, J., Ma, J.L., Suzuki, K., Liu, J.F., and Hart, S.R. 2008. Late Archean to Early Proterozoic lithospheric mantle beneath the western North China craton: Sr-Nd-Os isotopes of peridotite xenoliths from Yangyuan and Fansi. Lithos **102**(1-2): 25–42. doi: 10.1016/j.lithos.2007.04.005.

Yamasaki, T., O'Reilly, B., and Readman, P. 2006. A rheological weak zone intensified by post-rift thermal relaxation as a possible origin of simple shear deformation associated with reactivation of rifting. Earth Planet. Sci. Lett. **248**(1-2): 134–146. doi: 10.1016/j.epsl.2006.05.019.

Yang, Y., Li, W., and Ma, L. 2005. Tectonic and stratigraphic controls of hydrocarbon systems in the Ordos basin: A multicycle cratonic basin in central China. Am. Assoc. Petrol. Geol. Bull. **89**(2): 255–269. doi: 10.1360/10070404027.

Yoshida, M. 2010. Preliminary three-dimensional model of mantle convection with deformable, mobile continental lithosphere. Earth Planet. Sci. Lett. **295**(1-2): 205–218. doi: 10.1016/j.epsl.2010.04.001.

Yoshida, M. 2012. Dynamic role of the rheological contrast between cratonic and oceanic lithospheres in the longevity of cratonic lithosphere: A three-dimensional numerical study. Tectonophysics **532-535**: 156–166. doi: 10.1016/j.tecto.2012.01.029.

Zandt, G., Myers, S.C., and Wallace, T.C. 1995. Crust and mantle structure across the Basin and Range-Colorado Plateau boundary at 37°N latitude and implications for Cenozoic extensional mechanism. J. Geophys. Res. **100**(94): 10529–10548. doi: 10.1029/94JB03063.

Zhang, H. 2009. Peridotite-melt interaction: A key point for the destruction of cratonic lithospheric mantle. Chinese Sci. Bull. **54**: 3417–3437. doi: 10.1007/s11434-009-0307-z.

Zhang, H.F. 2012. Destruction of ancient lower crust through magma underplating beneath Jiaodong Peninsula, North China Craton: U-Pb and Hf isotopic evidence from granulite xenoliths. Gondwana Res. **21**(1): 281–292. doi: 10.1016/j.gr.2011.05.013.

Zhang, J., and Herzberg, C. 1994. Melting experiments on anhydrous peridotite KLB-1 from 5.0 to 22.5 GPa. J. Geophys. Res. **99**(B9): 17729–17742. doi: 10.1029/94JB01406.

Zhang, J.J., Zheng, Y.F., and Zhao, Z.F. 2009. Geochemical evidence for interaction between oceanic crust and lithospheric mantle in the origin of Cenozoic continental basalts in east-central China. Lithos **110**(1-4): 305–326. doi: 10.1016/j.lithos.2009.01.006.

Zhang, Y.Q., Mercier, J.L., and Vergdly, P. 1998. Extension in the graben systems around the Ordos (China), and its contribution to the extrusion tectonics of south China with respect to Gobi-Mongolia. Tectonophysics **285**: 41–75.

Zheng, J.P., Lee, C.-T.A., Lu, J.G., Zhao, J.H., Wu, Y.B., Xia, B., Li, X.Y., Zhang, J.F., and Liu, Y.S. 2015. Refertilization-driven destabilization of subcontinental mantle and the importance of initial lithospheric thickness for the fate of continents. Earth Planet. Sci. Lett. **409**: 225–231. doi: 10.1016/j.epsl.2014.10.042.

Ziegler, P.A., and Cloetingh, S. 2004. Dynamic processes controlling evolution of rifted basins. Earth-Science Rev. **64**(1-2): 1–50. doi: 10.1016/S0012-8252(03)00041-2.

Zuber, M.T., and Parmentier, E.M. 1986. Lithospheric necking: A dynamic model for rift morphology. Earth Planet. Sci. Lett. **77**: 373–383.